Controlling system dynamics through reservoir engineering

Dissertation

zur Erlangung des akademischen Grades

Doctor rerum naturalium
(Dr. rer. nat.)

vorgelegt

der Fakultät Mathematik und Naturwissenschaften
der Technischen Universität Dresden

von

David Walther Schönleber

geboren am 05.04.1988 in Tübingen

Eingereicht am 06. Februar 2017

Eingereicht am 06. Februar 2017

1. Gutachter: Prof. Dr. J.-M. Rost
2. Gutachter: Dr. A. Browaeys
3. Gutachter: Prof. Dr. R. Ketzmerick

Verteidigt am 19. Mai 2017

The following publications and manuscripts originated during my candidature:

1. ***Collective Excitation of Rydberg-Atom Ensembles beyond the Superatom Model***
   M. Gärttner, S. Whitlock, D. W. Schönleber, and J. Evers
   Phys. Rev. Lett. **113**, 233002 (2014)

2. ***Quantum Simulation of Energy Transport with Embedded Rydberg Aggregates***
   D. W. Schönleber, A. Eisfeld, M. Genkin, S. Whitlock, and S. Wüster
   Phys. Rev. Lett. **114**, 123005 (2015)

3. ***Pseudomodes and the corresponding transformation of the temperature-dependent bath correlation function***
   D. W. Schönleber, A. Croy, and A. Eisfeld
   Phys. Rev. A **91**, 052108 (2015)

4. ***Optomechanical interactions in non-Hermitian photonic molecules***
   D. W. Schönleber, A. Eisfeld, and R. El-Ganainy
   New J. Phys. **18**, 045014 (2016)

5. ***Non-Markovian dynamics in ultracold Rydberg aggregates***
   M. Genkin, D. W. Schönleber, S. Wüster, and A. Eisfeld
   J. Phys. B **49**, 134001 (2016)

6. ***Engineering thermal reservoirs with ultracold Rydberg atoms***
   D. W. Schönleber, C. D. B. Bentley, and A. Eisfeld
   arXiv 1611.02914 (2016)

7. ***Singlet Fission in weakly-interacting acene molecules***
   S. Izadnia, D. W. Schönleber, A. Eisfeld, A. Ruf, A. C. LaForge, and F. Stienkemeier
   submitted (2017)

The work presented in this thesis is based on publications two to six.

Contents

1 Introduction 1

2 Shaping environments for Rydberg aggregates 7
2.1 Introduction . . . 8
2.2 Basic concepts . . . 9
2.2.1 Rydberg atoms . . . 9
2.2.2 Interactions between Rydberg atoms . . . 13
2.2.3 Laser excitation and decay of Rydberg atoms . . . 19
2.2.4 Optical response of a Rydberg medium . . . 21
2.2.5 The embedded Rydberg aggregate . . . 25
2.3 Imaging excitation transport . . . 30
2.3.1 Using the environment as a probe . . . 31
2.3.2 Measurement-induced dephasing . . . 41
2.4 Simulating energy transport . . . 43
2.4.1 Effective model for excitation transport . . . 43
2.4.2 Gaussian disorder and dephasing . . . 48
2.4.3 Non-Gaussian disorder . . . 51
2.5 Tuning non-Markovianity of aggregate dynamics . . . 58
2.5.1 A measure for non-Markovianity . . . 60
2.5.2 Model system results . . . 61
2.6 Engineering aggregate states . . . 66
2.6.1 Numerical optimization and distance measures . . . 68
2.6.2 Bell-state preparation . . . 70
2.6.3 Thermal-state preparation . . . 71

3 Tuning displacement in non-Hermitian optomechanical resonators 79
3.1 Introduction . . . 80
3.2 System and model . . . 81
3.3 Steady-state solutions and their stability properties . . . 84
3.3.1 Steady-state analysis . . . 84
3.3.2 Stability analysis of the steady-state solutions . . . 88
3.4 Nonlinear dynamics . . . 90

4 Shifting individual modes between system and environment 93
4.1 Introduction . . . 94
4.2 Model system and analytic transformations . . . 96
4.2.1 Standard model for harmonic environments . . . 96
4.2.2 Model Hamiltonian with PM . . . 97
4.2.3 System-environment partitioning . . . 98
4.2.4 Calculation of the BCF . . . 99
4.2.5 Choice of initial environment states . . . 99
4.3 Numerical examples . . . 101
4.3.1 Evaluation of the transformed BCFs . . . 101
4.3.2 Corresponding SDs . . . 103

4.3.3 Corresponding system dynamics 104

5 Summary and outlook 107

A Supporting Information for Chapter 2 111
A.1 Calculation of radial Rydberg wave functions 111
A.2 Derivation of an effective model for excitation transport 113

B Supporting Information for Chapter 3 117
B.1 Rescaling of the optomechanical equations of motion 117
B.2 Optomechanical enhancement in the two-resonator model 117

C Supporting Information for Chapter 4 119
C.1 Microscopical definitions of BCF and SD 119
C.2 Environment transformation 120
C.3 Alternative derivation of the transformed BCF 121

Bibliography 125

Chapter 1

Introduction

The modeling of physical systems using mathematical terms plays an important role in scientific research. For a long time, this modeling was essentially restricted to analytically solvable models. Since the advent of computers, numerical simulations have facilitated the solution of increasingly complex models. These computer experiments with a simulated physical system are typically much less demanding in resources, time and effort than real experiments. When dealing with objects of the quantum world, however, classical computers face a severe challenge, termed the “exponential explosion” [1] or “exponential wall” [2]: the number of classical bits required to represent a quantum system increases exponentially with system size, rendering the direct simulation of large quantum systems (or even the storage of the state of such systems) intractable.

Fortunately, the comprehensive knowledge of all degrees of freedom of a quantum many-body system is not required in general. The formulation of concise research questions necessitates a narrowing down of attention on a small subset of the entirety of degrees of freedom, whose properties are to be investigated. This raises the notion of an *open quantum system* [3–5]: the few degrees of freedom of interest are defined as the *system*, which interacts with an *environment* consisting of the remaining degrees of freedom. Since the system dynamics represents the desired quantum dynamics, only the properties of the environment which affect the system dynamics are required to simulate the system. Such properties may include, inter alia, environment temperature or environment memory. (An environment is said to have memory or to be “non-Markovian” if its effect on the system depends on previous system dynamics.) Nevertheless, due to the unaltered exponential explosion in the system degrees of freedom and the immense numerical challenges in efficiently treating complex non-Markovian environments, numerical simulations of large open quantum systems remain largely inaccessible to classical computers.

Alternatives to numerical simulations of open quantum systems are thus called for. One means follows naturally from the open quantum system notion that the details of the environment do not matter, but only its effective action on the system: this gives rise to the possibility that the relevant environment properties can be realized using different physical implementations. Emulating the dynamics of one quantum system with another one is the central idea behind quantum simulation.

Quantum simulators mimic a less controllable or accessible target system by means of a more controllable or accessible counterpart [1, 6, 7]. They are needed whenever experimental or numerical investigation of the quantum system of interest is impeded by, for instance, lack of controllability or system size respectively. Their task is to implement the evolution of the target system using the simulator system, which requires that the Hamiltonians typically specifying the evolution of each system can be mapped onto one another. This ‘quantum simulation by emulation’ is often referred to as analog quantum simulation, as opposed to digital quantum simulation, where the evolution of a quantum system is reproduced by implementing unitary operators on the simulator via universal quantum gates [8]. Different platforms have been proposed for analog quantum simulation, such as neutral atoms, ions, and superconducting circuits, which can simulate, for example, condensed-matter spin models,

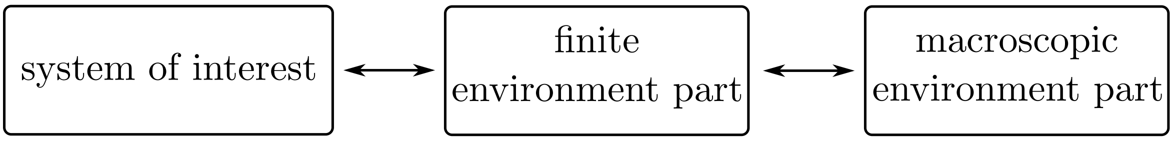

Figure 1.1: Schematic of the nested environment structure harnessed for reservoir engineering throughout this thesis. The system of interest is coupled to a finite environment part, which in turn is coupled to a macroscopic environment part. The environment can be controlled via the finite part, whose dynamics can be tuned.

disordered systems, and open quantum systems (see, e.g., Refs. [1, 7, 9–12]). In this thesis, we consider the latter aspect; the simulation of open quantum systems.

Finding a mapping between a target open quantum system and a simulator system can be a challenging task; however, open quantum system theory furnishes quantum simulation with a flexible tool: reservoir engineering [13].

Reservoir engineering is a general concept that considers the environment as a resource for tuning the system dynamics. It comprises the preparation of the system in specific states, or, appropriating more a general notion, the generation of certain system dynamics or properties. Reservoir engineering involves the design of the environment or its coupling to the system and can be applied in a variety of (quantum) systems [14] for entanglement generation and protection [15–28], ground state preparation [29], dissipative computation [30], and open quantum system simulation [9–11, 31–33]. In this thesis, we apply reservoir engineering both to prepare states and to design dynamics.

We consider reservoir engineering in the context of two distinct physical platforms. The first platform, and the main focus of this thesis, is ultracold Rydberg atoms. Rydberg atoms have (at least) one electron excited to a high principal quantum number [34]. They constitute well-controllable model systems useful for quantum simulation [9] and quantum information processing [35, 36]. We show that, by using reservoir engineering, one can implement an open quantum system simulator with Rydberg atoms. In addition, we demonstrate that reservoir engineering can be applied to prepare a variety of initial states for quantum simulation, for instance thermal states. The second platform is optomechanical. Here we use reservoir engineering to tune system properties, in this case the displacement and dynamics of the mechanical degree of freedom.

In both platforms, the environment harnessed for reservoir engineering exhibits a particular, nested structure depicted in Fig. 1.1: it consists of a finite part which in turn is coupled to a macroscopic part. Control over this environment is exercised via the finite part, whose dynamics can be tuned. Nested environment structures are not only convenient for reservoir engineering but also for the numerical treatment of open quantum systems, where they allow the emulation of complex environments [37–39]. Since in these numerical approaches only the system part is treated explicitly, nested environments provide great flexibility by allowing one to treat selected environment parts explicitly, i.e., as part of the system. When dealing with thermal environments, however, this immediately raises the question whether or not the system-environment partitioning is arbitrary. To pursue this question, we employ a harmonic environment model and show that differences in the system dynamics can arise if concepts like temperature are naively applied to different system-environment partitionings.

Having provided an outline of the thesis scope, we now provide more details on the results of this thesis. Each of the three different aspects of environment engineering using nested environments addressed above is covered in a separate chapter.

Shaping environments for Rydberg aggregates (Chapter 2)

Reservoir engineering with ultracold Rydberg atoms allows us to propose a setup for dipole-mediated quantum excitation transport simulations. Such transport occurs, for example, in light harvesting complexes; there, numerical investigation of excitation transport within the electronic degrees of freedom is impeded by the coupling to a complex finite-temperature environment of vibrational degrees of freedom [40, 41], which furthermore renders the environment non-Markovian [42, 43]. Since the presence of a complex environment also complicates experimental research [44, 45], quantum simulators are of great interest for excitation transport studies, as they provide a means to assess the impact of different environment effects by allowing control of environment properties.

Rydberg atoms are ideally suited to study dipole-mediated excitation transport: firstly, they feature strong, distance-dependent interactions, which allow one to realize excitation transport dynamics similar to the dynamics of groups, or aggregates, of molecules [46–49]. Secondly, the long lifetimes of Rydberg states when compared to the timescale of the transport render possible the experimental observation of excitation transport [50–52]. Thirdly, Rydberg atoms represent a platform which provides relative ease of experimental control. That is, optical trapping of cold atoms [53–55] enables control of atomic distances, which translates into control of interaction strengths; and optical addressability of Rydberg atoms permits control of excitation dynamics within the atoms.

We harness these properties of Rydberg atoms in our quantum simulator proposal. Specifically, we show that an ensemble of optically-driven ultracold atoms, which is coupled to a photonic continuum through spontaneous emission, provides a highly-tunable environment for a group, or aggregate, of Rydberg atoms interacting via transition-dipole coupling. This nested atomic environment allows us in particular to image excitation transport within the aggregate, that is, to distinguish between the two aggregate Rydberg states involved in the excitation transport. Besides, we shed light on the quantum back-action relating to information acquired on the aggregate through the imaging and decoherence: measuring the excitation location introduces dephasing to the aggregate dynamics. We derive an effective model for this dynamics, in which the properties of the environment atoms enter only via energy shifts of the aggregate atoms and additional dephasing terms, and investigate the impact of different environment effects such as site-energy disorder and decoherence on the transport. We furthermore show that non-Markovian excitation dynamics can be simulated with our setup. In addition, we apply reservoir engineering both to construct a thermal environment of tunable temperature for the aggregate and to demonstrate that pure eigenstates, such as Bell states, can be dissipatively prepared in the Rydberg atomic system.

Our setup expands the toolbox available for quantum simulation of excitation transport and allows investigation of the impact of a broad range of environment effects on the transport dynamics.

Tuning displacement in non-Hermitian optomechanical resonators (Chapter 3)

Reservoir engineering with optomechanical resonators allows the control of properties of the phononic, i.e., mechanical, degree of freedom. The setup we consider consists of two coupled non-Hermitian optical resonators, one of which supports a vibrational mechanical mode. The non-Hermiticity of the optical resonators arises from optical gain or loss experienced by the resonators. Singularities in the resonators' eigenenergy spectrum can arise as a consequence of introducing optical gain and loss; and controlling these singularities has facilitated the design of new devices such as single-mode microring lasers [56, 57]. Optomechanical systems, conversely, are promising platforms for high-precision sensing of forces, displacements, masses, and accelerations, as well as for quantum information processing, where they could realize light-matter interfaces [58]. Combining the two themes of optomechanics and non-Hermitian systems has been reported to yield a giant enhancement of the optomechanical coupling strength around the spectral singularities when compared to a gain-less structure [59]. This enhancement, which was found in resonators with balanced optical gain and loss, i.e., parity-time ($\mathcal{PT}$) symmetric resonators, might be valuable for phonon lasing applications [59]. Here we do not entertain this potential application but pursue the question of what advantages the additional ingredient of non-Hermiticity introduced in Ref. [59] provides for reservoir engineering with optomechanical structures.

We study the properties of the optomechanical system both analytically and numerically to assess the tunability of the mechanical mode via environment properties such as optical pumping power levels and frequencies, as well as material design parameters (gain and loss) of the optical resonators in the classical limit. We characterize the classical steady-state solutions and the stability properties of the mechanical mode in terms of the optical design parameters as well as the optical pumping power levels and frequencies, and detail the conditions under which an enhancement of the steady-state displacement of the mechanical mode can be obtained. In particular, we find that unstable solutions exist for certain gain-loss ratios, including those predicted in Ref. [59] to yield large enhancements. Introducing a more realistic modeling of optical gain including gain saturation, we show that, depending on the environment design parameters, excitation power levels and frequencies, different regimes of nonlinear dynamics such as fixed points and sustained oscillations are possible.

Our analysis provides new insight into the interplay between optical non-Hermiticity and optomechanical coupling.

Shifting individual modes between system and environment (Chapter 4)

The engineered environments of both physical systems (Rydberg aggregate and mechanical mode) considered here exhibit a particular, nested structure: the system degrees of freedom are coupled to a finite, controllable environment part which in turn is coupled to a macroscopic environment part (cf. Fig. 1.1). In the Rydberg system, the finite part corresponds to the laser-driven atoms and the macroscopic part to the spontaneous emission, which can be interpreted as a coupling to a photonic continuum. In the optomechanical system, the finite part consists of the optical resonators and the macroscopic part consists of gain and loss providing environments that are effectively described using a non-Hermitian representation.

The nested environment structure proves convenient for exerting control over the system, and in addition this structure is useful for environment modeling; notably for open quantum system models using harmonic oscillator environments [37–39, 60–63]. In the framework of harmonic environment modes linearly coupled to the system degrees of freedom, the characteristics of a thermal environment are specified through environment temperature and details of the system-environment coupling, encoded in a quantity called spectral density. This allows for the mapping of complex environments onto nested environment structures, thereby easing numerical or even implementations of quantum simulation. Given such a nested environment, by shifting particular modes from the environment to the system part — i.e., by changing the *system-environment partitioning* — the intricacy of the environment can be significantly reduced; for instance, a non-Markovian environment can be transformed into a Markovian (memory-less) one [60, 62, 63]. This 'reservoir engineering' procedure is typically performed in terms of the spectral density and does not incorporate temperature.

To investigate consequences of different system-environment partitionings in the presence of temperature, we consider a nested, harmonic environment: a system of interest coupled to a single harmonic mode, which in turn is coupled to a macroscopic environment of harmonic oscillators. The single mode can either be described as part of the system, or the environment. We show how the different partitionings can change the influence of the environment on the system of interest, which is quantified by a function called the bath correlation function. This function depends on temperature via the initial state of the environment, which might be chosen differently when considering the single mode to either be part of the system or of the environment. We analyze the impact of different initial states on the bath correlation function by numerically calculating this function, and find differences in the initial dynamics. These differences give rise to pronounced differences in the dynamics of a system, which, for simplicity, we choose to be a harmonic oscillator.

Our investigation using the example of a nested, harmonic environment shows that thermal environment transformations convenient for reservoir engineering come with a caveat: when temperature is incorporated as a property of the environment, different system-environment partitionings can be non-equivalent if the initial state of the environment is not preserved.

Chapter 2

Shaping environments for Rydberg aggregates

Abstract — Excitation transport through dipole-dipole interactions plays a prominent role in molecular aggregates, assemblies of molecules that appear, for instance, in the context of photosynthesis. In these systems, the fundamentally coherent transport mechanism competes with the coupling to a complex, non-Markovian, finite-temperature environment. This poses severe challenges for both numerical investigation and clean experimental studies. Here we propose an experimental setup for quantum simulation of excitation transport with Rydberg atoms. Rydberg atoms exhibit similar dipolar state-changing interactions as found in molecules, but are considerably simpler to study. Accordingly, we mimic the coherent excitation transport in the molecular aggregate using a Rydberg aggregate, i.e., an assembly of transition-dipole interacting Rydberg atoms. A set of optically-driven ultracold atoms in turn provides a highly-tunable environment for this aggregate through which various environment effects can be introduced. Specifically, we can control the degree of decoherence as well as non-Markovianity of the transport dynamics, and can even prepare thermal states in the Rydberg aggregate.

The work described in this chapter is based on the following publications [64–66]:

Quantum Simulation of Energy Transport with Embedded Rydberg Aggregates
D. W. Schönleber, A. Eisfeld, M. Genkin, S. Whitlock, and S. Wüster
Phys. Rev. Lett. **114**, 123005 (2015)

Non-Markovian dynamics in ultracold Rydberg aggregates
M. Genkin, D. W. Schönleber, S. Wüster, and A. Eisfeld
J. Phys. B: At. Mol. Opt. Phys. **49**, 134001 (2016)

Engineering thermal reservoirs with ultracold Rydberg atoms
D. W. Schönleber, C. D. B. Bentley, and A. Eisfeld
arXiv 1611.02914 (2016)

2.1 Introduction

Rydberg states, highly-excited electronic states with high principal quantum numbers n, already appeared in the early days of atomic spectroscopy and have played a role in atomic physics since [34]. Their relevance to astrophysical processes triggered mostly theoretical work in the beginning [67]. It was the advent of the tunable laser that stimulated a rapid growth of interest in Rydberg atoms in the 1970s, fueled by experiments facilitated by laser technology. Advances in the field of laser cooling and trapping allowed for a resurge of interest in the year 2000, when Rydberg atoms were proposed for applications in quantum information processing [68, 69].

It is the remarkable properties of Rydberg states that attracted immense research interest since their first appearance [70, 71]. The average distance of a rubidium Rydberg electron from the nucleus, for example, amounts to ~ 210 nm for $n \approx 55$ [71]. The binding energies associated with these extremely large electron orbits scale inversely with the electron orbit, rendering Rydberg states very loosely bound. Huge polarizabilities and very small energy spacings of adjacent levels give rise to strong and long-range interactions (as compared to ground-state atoms in gases [35]), of which the C_6 interaction coefficient associated with the van der Waals interaction most notably scales as n^{11}. Lastly, Rydberg states possess long lifetimes of the order of ~ 100 μs for $n \approx 55$ [72].

Due to their strong interactions, ensembles of Rydberg atoms feature collective states similar to the ones arising from coupled individual units in crystals [73, 74]. This was realized in the seminal works [68, 69], which proposed the use of Rydberg atoms to create quantum logic gates, utilizing what is called the dipole blockade [69]. That is, the energy of the doubly-excited Rydberg state in a system consisting of two interacting Rydberg atoms gets shifted due to the Rydberg-Rydberg interaction between the two atoms. Accordingly, the doubly-excited state of two atoms which are resonantly laser-excited to the Rydberg state is rendered off-resonant, and hence its excitation is inhibited. In a coherently-excited gas, the dipole blockade impedes the presence of more than a single Rydberg excitation in a certain region, called the blockade region, whose extent depends on the distance-dependent Rydberg-Rydberg interaction.

While the understanding and harnessing of the dipole blockade triggered much research on Rydberg atoms after the year 2001, we here focus on another manifestation of the strong interactions between Rydberg states in form of a modified optical response of a Rydberg medium (e.g., Refs. [75–78]). More specifically, in an atomic medium in which a level scheme including a Rydberg state is used to realize electromagnetically induced transparency [79, 80], the optical response of the medium to a probe laser beam depends on the interaction-induced energy shift of the Rydberg state. Reminiscent of the blockade region, the atomic medium is thus rendered opaque to the probe beam in the vicinity of a Rydberg excitation, which allows in particular for temporally and spatially-resolved, nondestructive imaging of Rydberg excitations [77, 81, 82].

Owing to their relative ease of experimental control, Rydberg atoms have been proposed for a variety of quantum simulation purposes, for instance as quantum simulators for quantum spin models [9, 83], electron-phonon interactions [84], multi-band materials [85], or topological insulators [86]. Admixing a small fraction of Rydberg state properties to the ground state of a cold atomic gas using off-resonant excitation ("Rydberg dressing"), long-lived but long-range interacting many-body systems can be obtained [87–93], which can implement, for example, spin models for quantum magnets [94–98]. Alternatively, microwave dressing opens up possibilities to realize interacting many-body systems with more than pairwise interactions [99, 100].

From the abundance of quantum simulation applications, our interest is directed towards a particular purpose: the simulation of dipole-mediated excitation transport in the presence of an environment. Dipole-mediated excitation transport was already discussed in the 1920s and 1930s in the context of gases [101, 102], crystals [73], and self-assembled organic dye aggregates, as well as photosynthetic light harvesting systems [103]. In Rydberg systems, dipole-mediated excitation transport was observed via collisional resonances first in thermal Rydberg vapor [104] and later on in “frozen” Rydberg gases [105, 106], i.e., low-temperature gases in which the motional degrees of freedom are essentially frozen out as the atoms cover only small distances relative to their separation on timescales relevant for experiment. These observations of excitation transport in Rydberg systems triggered further theoretical [47, 107–109] as well as experimental research [110], where increasing experimental control allowed for the observation of dipole-mediated excitation transport between both two spatially separated ensembles of Rydberg atoms [50] and single Rydberg atoms [51], and even excitation transport between three spatially separated single Rydberg atoms [52]. In gases, coherent [111] as well as diffusive [81] dipolar excitation transport have been observed.

In this chapter, we study a network of transition-dipole coupled Rydberg atoms, called Rydberg aggregate, embedded in a laser-driven, dissipative background gas from different perspectives. Section 2.2 reviews the essentials of Rydberg physics as concerns this thesis and introduces the system that we consider throughout this chapter. In Sec. 2.3 we then show how the background gas can be used to monitor excitation transport within the aggregate and how information-gain about the aggregate leads to dephasing of the aggregate dynamics. The back-action of the background gas on the aggregate we employ in Sec. 2.4 to provide controllable disorder and dephasing to the aggregate, thus realizing a quantum simulator for excitation transport. Section 2.5 extends this approach while at the same time reducing the complexity of the setup, showing that also non-Markovian aggregate dynamics can be achieved in a small aggregate interacting with a single background atom. Lastly, in Sec. 2.6 we apply reservoir engineering to construct a thermal environment with controllable temperature for the Rydberg aggregate and demonstrate that also pure eigenstates, such as Bell states, can be prepared in the Rydberg atomic system using this method.

2.2 Basic concepts

This section summarizes the basic concepts relevant for the description of the physical system that we consider throughout this chapter, namely the embedded Rydberg aggregate. Preceded by a brief historical introduction to Rydberg atoms, we review their properties in Sec. 2.2.1. An important property of Rydberg atoms that deserves special attention is their interactions, which is the topic of Sec. 2.2.2. In Sec. 2.2.3 we address the modeling of laser-excitation and radiative decay of Rydberg states, which allows us to discuss the optical response of a Rydberg medium in Sec. 2.2.4. Lastly, the concept of the embedded aggregate is introduced in Sec. 2.2.5.

2.2.1 Rydberg atoms

Rydberg atoms have at least one electron excited to a state with high principal quantum number n [34]. They were first recognized in the early days of atomic spectroscopy, when Johann J. Balmer succeeded in 1885 in finding a formula for the wavelengths of the spectral lines of hydrogen previously measured by Ångström, Huggins, and Vogel [112]. As we know today, the *Balmer formula* describes the wavelengths of light emitted in a transition from a higher principal quantum number $n' > n$ to the principal quantum number $n = 2$ in hydrogen. Soon after, in 1890, Johannes R. Rydberg found an expression for the wavenumbers, as opposed to wavelengths, of the spectral lines of different chemical elements, given by [34, 113]

$$\nu_\ell = \nu_{\infty\ell} - \frac{Ry'}{(n-\delta_\ell)^2}. \tag{2.1}$$

Here, $Ry' = 109721.6\ \mathrm{cm}^{-1}$ is the universal *Rydberg constant*, and $\nu_{\infty\ell}$ the series limits of the different ℓ series, namely the sharp, principal, and diffuse series, from which the naming s, p, d for angular momentum $\ell = 0, 1, 2$ originates. The integer n we recognize today as the principal quantum number, and δ_ℓ as the quantum defect.

The physical significance of Rydberg states only became clear in 1913 when Niels Bohr proposed his model of the hydrogen atom [114]. Bohr combined the notion of electrons surrounding (and presumably orbiting around) a positive charge, developed by Ernest Rutherford [115], with recent advances in the theory of energy radiation, specifically the assumption made by Max Planck [116] that radiation is emitted in quanta that are proportional to the the Planck constant h. Despite the mixing of quantum and classical concepts[1] and the resulting shortcomings, Bohr was able to recover the Rydberg formula for hydrogen, and with it an expression for the Rydberg constant in terms of fundamental constants such as electron mass m_e and charge e. His model provided a connection between the number n in the Rydberg formula and the radius of the electron orbit,

$$r = \frac{4\pi\varepsilon_0\hbar^2}{e^2 m_e} n^2 = a_0 n^2, \tag{2.2}$$

with $a_0 = 0.052917721$ nm denoting the *Bohr radius*, ε_0 the vacuum permittivity, and $\hbar$ the reduced Planck constant. Accordingly, atoms in states with high principal quantum number n, i.e., Rydberg states, have very large electron orbits. The binding energy of an electron with high principal quantum number n, in contrast, is very small, as the energy E_n of an electron is inversely proportional to the electron orbit,

$$E_n = -\frac{e^2}{8\pi\varepsilon_0}\frac{1}{a_0 n^2} = -\frac{Ry}{n^2}. \tag{2.3}$$

Note that $Ry = hcRy'$ with h the Planck constant and c the speed of light, such that Ry has units of energy. We now know that the classical notion of electrons contained in Bohr's model is not consistent with quantum theory; however, the basic observations on Rydberg atoms are retained within the understanding of quantum theory we hold today.[2] Specifically, the scaling of the binding energy as well as the scaling of the spatial extent of the Rydberg atom with principal quantum number n predicted by Bohr's model agrees with quantum mechanical findings.

With these remarks we conclude our historical introduction to Rydberg atoms; in the remainder of this chapter we will deal with quantum theory alone. Note that we set $\hbar = 1$ for notational convenience in the following.

Before we continue reviewing the basic concepts of Rydberg atom theory relevant for this thesis, we summarize the properties of Rydberg atoms. Table 2.1 lists the scalings of different

---

[1] According to Ref. [117, p. 111], William L. Bragg noted on a related topic: "On Mondays, Wednesdays and Fridays one uses the classical laws, on Tuesdays, Thursdays and Saturdays the laws of quantum physics".

[2] We note in passing that one should be careful with a 'cumulative' presentation of scientific progress [118], since a new theory might ascribe new meanings to concepts such as position, mass etc., thus rendering a straightforward comparison of theories (or paradigms) impossible. (The detection of incompatibility requires some comparability, though [119].) An example is given by Bohr, who noted in his work on the correspondence principle that this principle was not to diminish the differences between quantum and classical theory, but to be understood as an asymptotic agreement of statistical results only [120, p. 144].

Table 2.1: Properties of Rydberg atoms. The n dependence is adapted from Refs. [34, 72].

Property	Expression	n dependence	^{87}Rb $43s_{1/2}$ value
Binding energy[a]	$E_n = -\frac{Ry}{n^2}$	n^{-2}	$-8.559608(4)$ meV
Level spacing[a]	$E_{n+1} - E_n$	n^{-3}	100.049(1) GHz
Orbital radius[b]	$\langle r \rangle$	n^2	$2\,384.3\,a_0$
Polarizability[c]	α	n^7	-17.7 MHz cm^{2}V^{-2}
Dipole moment[b]	$\langle ns_{1/2}\lvert er \rvert np_{3/2}\rangle$	n^2	$1823\,ea_0$
Radiative lifetime[d]	τ_0	n^3	87 μs
Black-body lifetime[d]	τ_{bbr}	$\approx n^2$	88 μs
Effective lifetime[d]	$\tau_{\mathrm{eff}} = (\tau_0^{-1} + \tau_{\mathrm{bbr}}^{-1})^{-1}$		43.7 μs
Van-der-Waals coefficient[c]	C_6	n^{11}	1.697×10^{19} a.u.

[a] Numerical values taken from Ref. [122] (experiment).

[b] Numerical values obtained by numerically solving the radial Schrödinger equation (cf. Appendix A.1) using the quantum defects listed in Refs. [123, 124].

[c] Numerical values taken from Ref. [71] (theory).

[d] Numerical values calculated according to Eqs. (14) to (16) in Ref. [72] (theory), using $T = 300$ K. For a comparison of different theoretical lifetime predictions, see Ref. [125].

properties of Rydberg atoms with the principal quantum number n. Particularly notable are the scaling of the radiative lifetime and of the van der Waals interaction. The radiative lifetime scales as n^3, rendering highly-excited Rydberg states very long-lived (≈ 1.7 ms for $n = 110$ [121]). The van der Waals interaction scales remarkably, as n^{11}, giving rise to strong interactions among Rydberg atoms on distances typical for cold atomic gases. Furthermore, due to their huge polarizability scaling as n^7, Rydberg atoms are extremely sensitive to external fields.

Rydberg states of alkali atoms

Although Rydberg states exist in every atom, in this thesis, we focus on Rydberg states with a single highly-excited electron, which is the relevant case for alkali-metal atoms. More specifically, we focus on rubidium Rydberg states, one of the typical elements used in Rydberg experiments.

Alkali atoms are atoms with a single valence electron. In a highly-excited state that is localized far away from the core, the valence electron essentially sees a singly-charged core, leading to a hydrogen-like electronic structure. In contrast to hydrogen, the alkali atom core is of finite size, consisting of the nucleus and the closely-bound inner-shell electrons. Whenever the valence electron penetrates the core, it is exposed to the unshielded nuclear charge, which, together with core polarization, reduces its total energy (or, equivalently, increases its binding energy) [34]. Due to the centrifugal potential, electrons in states of high orbital angular momentum $\ell \geq 3$ do not penetrate the core, such that their energy is basically identical with hydrogen, while for low angular momentum $\ell < 3$, their energy is reduced as compared to hydrogen. The energy difference between Rydberg states of alkali atoms and hydrogen can be quantified by introducing an empirically observed *quantum defect* $\delta_{n\ell j}$ depending on the principal quantum number n, the orbital angular momentum ℓ, and the total angular momentum j of the Rydberg state into Eq. (2.3),

$$E_{n\ell j} = -\frac{Ry}{(n - \delta_{n\ell j})^2}. \tag{2.4}$$

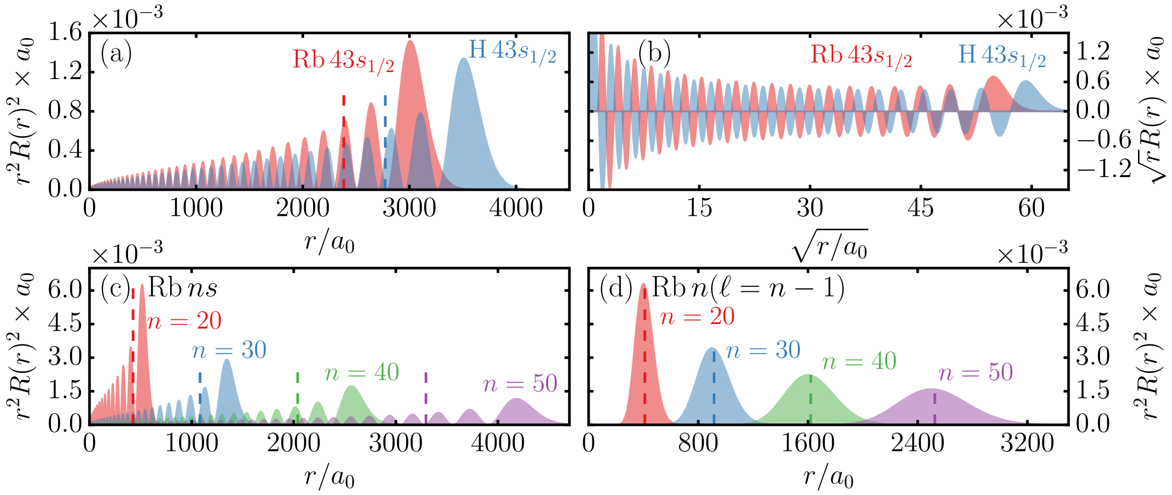

Figure 2.1: Radial probability densities and wave functions of Rydberg states (cf. [127]). (a) Radial probability density $r^2R_{n\ell j}(r)^2$ of the $|43s_{1/2}\rangle$ state of rubidium (red) and hydrogen (blue). (b) Radial wave function of the same states as in (a) as a function of the scaled radial variable $\sqrt{r}$. (c) Radial probability densities of rubidium Rydberg s states for different principal quantum numbers n. (d) Radial probability densities of circular rubidium Rydberg states with $\ell = n-1$ for different principal quantum numbers n. Color-matched dashed lines indicate the expectation value $\langle r\rangle$.

The quantum defect can be parametrized using the extended Rydberg-Ritz formula [126]

$$\delta_{n\ell j} = \delta_0 + \frac{\delta_2}{(n-\delta_0)^2} + \frac{\delta_4}{(n-\delta_0)^4} + \frac{\delta_6}{(n-\delta_0)^6} + \cdots . \tag{2.5}$$

The parameters $\delta_0, \delta_2, \ldots$ depend on the quantum numbers ℓ and j and are specific for each element; for rubidium, we only consider δ_0 and δ_2, whose values are listed in Refs. [123, 124]. The experimentally-obtained quantum defects are consistent with our reasoning above, i.e., that the energy of states with low angular momentum strongly deviates from the respective hydrogen energy, $\delta_0(\ell=0, j=1/2) = 3.1311804$ [123], while for high angular momentum the energy is essentially the same as hydrogen; $\delta_0(\ell=3, j=5/2, 7/2) = 0.016312$ [124]. The quantum defect is conventionally absorbed in the effective principal quantum number $n^\star_{n\ell j} = n - \delta_{n\ell j}$.

Given the difference in energy between the states of rubidium and hydrogen for low angular momentum quantum numbers, stemming from core penetration and polarization, it is clear that the wave functions of rubidium and hydrogen will also differ. The radial wave functions of rubidium Rydberg states can be calculated via the Schrödinger equation, using the eigenenergies (2.4) as well as an adapted core potential (also including spin-orbit coupling). Details on the calculation of the radial wave functions can be found in Appendix A.1.

In Fig. 2.1 we show radial probability densities and wave functions of Rydberg states. Figure 2.1(a) displays the radial probability density of the $43s_{1/2}$ state of both rubidium and hydrogen. The effect of the rubidium core on the Rydberg wave function can be clearly seen; the rubidium core potential decreases the wavelength of the radial oscillations relative to hydrogen. The corresponding wave functions as a function of the scaled radial variable $\sqrt{r}$ are depicted in Fig. 2.1(b), demonstrating that the oscillations of the wave function are approximately equally spaced as a function of the scaled coordinate. Note that we adopt the convention to take the sign of the wave function at small r to be positive, independent of n [34]. In Figs. 2.1(c) and (d), the radial probability densities of rubidium states, both $|s_{1/2}\rangle$ states (c) and circular states with $\ell = n-1$ (d) are shown for different principal quantum numbers n. The expectation value of the radial coordinate $\langle r \rangle$ is indicated by color-matched dashed lines, illustrating the n^2 scaling of the spatial extent of the wave function. We note in passing that circular states, i.e., states with $\ell = n - 1$, approach the classical limit of localized motion in a circular orbit [128]. This is illustrated by the radial probability density of circular rubidium Rydberg states displayed in Fig. 2.1(d), which is almost centered around the radial coordinate $a_0 n^2$ of the classical orbit.

In the following, we will be interested in rubidium Rydberg s and p states only.

2.2.2 Interactions between Rydberg atoms

In one way or another, almost all facets of Rydberg physics rely on the "strong and long-range" interaction of Rydberg atoms. In a simple picture, the interaction between two Rydberg atoms can be thought of as arising from the leading-order point-charge interaction between two separated atoms, where each atom consists of an ionic core and an electron and the distance between the core and the electron of each atom is much smaller than the separation of the two cores [129]. The Hamiltonian between two Rydberg atoms A and B is given by

$$\mathcal{H}_{\mathrm{AB}} = \mathcal{H}_{\mathrm{A}} \otimes I_{\mathrm{B}} + I_{\mathrm{A}} \otimes \mathcal{H}_{\mathrm{B}} + \mathcal{H}_{\mathrm{int}}, \tag{2.6}$$

where $\mathcal{H}_{\mathrm{A,B}}$ denote the single-atom Hamiltonians, $I_{\mathrm{A,B}}$ are the unit operators in subspace A and B respectively, and $\mathcal{H}_{\mathrm{int}}$ is the Hamiltonian quantifying the interaction between the two atoms. Ignoring higher-order multipole terms, the interaction Hamiltonian is essentially given by the dipole-dipole interaction operator, $\mathcal{H}_{\mathrm{int}} \simeq V_{\mathrm{dd}}(\boldsymbol{R})$;

$$V_{\mathrm{dd}}(\boldsymbol{R}) = \frac{1}{4\pi\varepsilon_0} \frac{\boldsymbol{\mu}_{\mathrm{A}} \cdot \boldsymbol{\mu}_{\mathrm{B}} - 3(\boldsymbol{\mu}_{\mathrm{A}} \cdot \hat{\boldsymbol{R}})(\boldsymbol{\mu}_{\mathrm{B}} \cdot \hat{\boldsymbol{R}})}{R^3}. \tag{2.7}$$

Here, $\hat{\boldsymbol{R}}$ is a unit vector pointing in the direction of $\boldsymbol{R}$, the vector connecting the cores of the two atoms A and B, and $R = |\boldsymbol{R}|$. The transition dipole moment operators $\boldsymbol{\mu}_{\mathrm{A,B}}$ are defined as $\boldsymbol{\mu}_{\mathrm{A,B}} = e\boldsymbol{r}_{\mathrm{A,B}}$, with the distance vector $\boldsymbol{r}_{\mathrm{A,B}}$ between core and electron of atom A and B respectively. In setting $\mathcal{H}_{\mathrm{int}} \simeq V_{\mathrm{dd}}(\boldsymbol{R})$, we assumed that (i) dipole interactions dominate higher-order multipole terms, (ii) modifications of the dipole-dipole interaction due to retardation do not play a role, and (iii) exchange effects due to wave function overlap are negligible [130, 131].

Assumption (i) is employed since higher-order multipole contributions are typically negligible for the interatomic separations we consider here [129, 132]. Higher-multipole terms lead to energy shifts that drop more quickly with R than those arising from dipole-dipole interaction [131, 133]. (For a discussion of quadrupole effects in Rydberg alkali systems we refer to Refs. [130, 131, 133–135].) Assumption (ii) is justified since the reduced wavelengths $\lambdabar = \lambda/(2\pi)$ of the relevant Rydberg-Rydberg transitions are much larger than the interatomic separations we consider [130] (e.g., $\lambdabar \sim 500\ \mu\mathrm{m}$ for the transition $|43s_{1/2}\rangle \rightarrow |43p_{3/2}\rangle$ in ^{87}Rb, cf. Tab. 2.1). Assumption (iii) is justified since interatomic distances we consider are larger than the LeRoy radius R_{LR},

$$R_{\mathrm{LR}} = 2\left(\sqrt{\langle\psi_{\mathrm{A}}|r^2|\psi_{\mathrm{A}}\rangle} + \sqrt{\langle\psi_{\mathrm{B}}|r^2|\psi_{\mathrm{B}}\rangle}\right), \tag{2.8}$$

with $|\psi\rangle \equiv |n\ell j m_j\rangle$. For distances smaller than the LeRoy radius, exchange interactions become non-negligible [130].

To evaluate the diatomic Hamiltonian (2.6), it is convenient to employ a pair state basis $|\psi_{\mathrm{A}}\rangle \otimes |\psi_{\mathrm{B}}\rangle \equiv |\psi_{\mathrm{A}}\,\psi_{\mathrm{B}}\rangle$. The dipole-dipole operator (2.7) in the diatomic Hamiltonian depends on the interatomic distance and couples pair states that comply with the dipole selection rules, $\langle\psi_\mathrm{A}\,\psi_\mathrm{B}|\,V_\mathrm{dd}(\boldsymbol{R})\,|\psi'_\mathrm{A}\,\psi'_\mathrm{B}\rangle \neq 0$. The solutions to the corresponding eigenvalue problem $\mathcal{H}_\mathrm{AB}\,|\Phi\rangle = E_\Phi\,|\Phi\rangle$ yield the new eigenstates (superpositions of the asymptotically distant eigenstates $|\psi_\mathrm{A}\,\psi_\mathrm{B}\rangle$) and eigenenergies. The energy difference between the eigenstate at a distance R as compared to the unperturbed pair state quantifies the Rydberg-Rydberg interaction $V(R)$ between the two Rydberg states. It is typically given as an expansion of the interatomic distance R, $V(R) \simeq \sum_n C_n/R^n$. The expansion coefficients C_n are called dispersion coefficients. Note that for more than two atoms, a binary interactions-based approach to the many-body Rydberg-Rydberg interaction might not be generally valid, in particular in the presence of resonant dipole interactions [136–138].

To gain insight into the interactions between Rydberg atoms, it is instructive to distinguish between two sets of pair states that are coupled by the transition dipole interaction (2.7): states that are energetically degenerate, and states which are not. We start with the discussion of interactions between degenerate states.

Resonant dipole-dipole interaction

If two pair states $|\psi_\mathrm{A}\,\psi_\mathrm{B}\rangle$ and $|\psi'_\mathrm{A}\,\psi'_\mathrm{B}\rangle$ have equal energy and are directly coupled by the transition dipole operator (2.7), one speaks of resonant dipole-dipole interaction. As a particular example relevant for this thesis, we consider the two pair states $|ns\,np\rangle$ and $|np\,ns\rangle$, which are intrinsically degenerate. Ignoring for a moment both Zeeman degeneracy and the coupling to other pair states, and factoring out the dependence on the interatomic distance from the transition matrix element, the dipole matrix element coupling these two states can be written as

$$\langle ns\,np|V_\mathrm{dd}(R)|np\,ns\rangle = \langle np\,ns|V_\mathrm{dd}(R)|ns\,np\rangle \equiv \frac{C_3}{R^3}, \tag{2.9}$$

where $C_3 \approx \mu^2_{ns,np}$ denotes the product of the dipole moments quantifying the transition strength of the transition $|ns\rangle \to |np\rangle$. (The approximate relationship between C_3 and the product of the dipole moments arises from the neglect of the angular momentum part of $V_\mathrm{dd}(R)$. The dipole moments can be determined using the radial wave functions calculated in Appendix A.1 via $\mu_{\psi_A,\psi_B} = \langle\psi_A|er|\psi_B\rangle$.) Considering the scaling of the dipole moments $\propto n^2$ (cf. Tab. 2.1) we see that the resonant dipole-dipole interaction scales as n^4.

Accordingly, the diatomic Hamiltonian (2.6) in the pair-state basis ($|ns\,np\rangle$, $|np\,ns\rangle$) can be written as

$$\mathcal{H}_\mathrm{AB} = \begin{pmatrix} 0 & C_3/R^3 \\ C_3/R^3 & 0 \end{pmatrix}, \tag{2.10}$$

and the corresponding eigenvalues (i.e., interaction-induced energy shifts) are given by $\pm C_3/R^3$. Since the eigenstates of Eq. (2.10) are not the pair states with localized p excitation but their superpositions $|\pm\rangle = (|ns\,np\rangle \pm |np\,ns\rangle)/\sqrt{2}$, excitation transport is induced by the dipole-dipole interaction. That is, a p excitation initially localized at atom A (pair state $|np\,ns\rangle$) will coherently oscillate between atom A and B, reminiscent of Rabi oscillations.

In a quantitative treatment of interactions between resonant pair states, the simplifications employed in the example above, namely the neglect of both Zeeman degeneracy and the coupling to other pair states, have to be abandoned. Below we comment on how the findings of the simplified example are modified in a quantitative treatment.

On the one hand, Zeeman-degenerate pair states have an important effect on the spatial dependence of the dipole-dipole interaction. In the absence of an external field, states with angular momentum $\ell > 0$ are degenerate. In particular, for light alkali atoms which have negligible spin-orbit coupling [139], the state $|n\ell\rangle$ exhibits a $(2\ell+1)$-fold degeneracy, whereas for heavy alkali atoms such as rubidium where spin-orbit coupling cannot be ignored, the

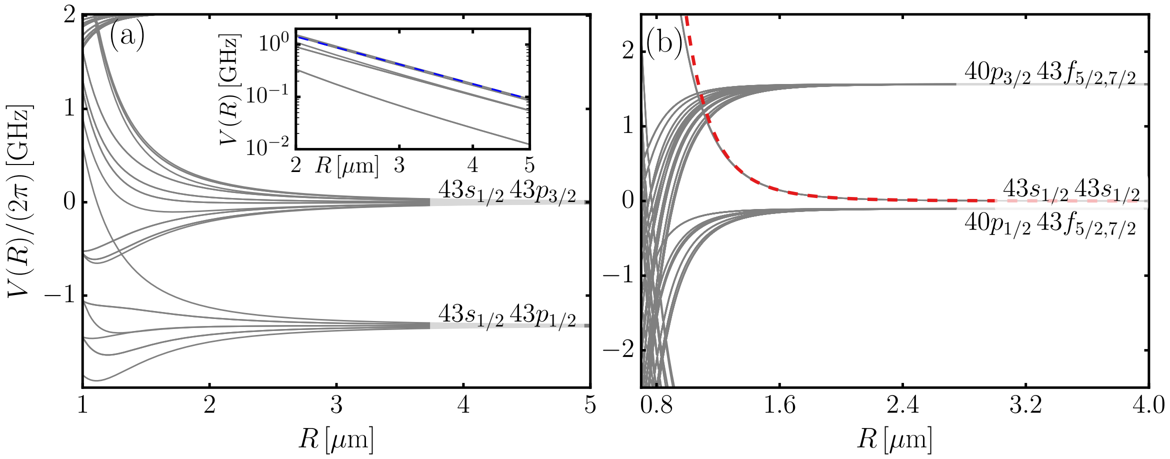

Figure 2.2: Potential energies (gray lines) as a function of the interatomic distance R, around the ^{87}Rb pair states $|43s_{1/2}\,43p_{3/2}\rangle$ and $|43p_{3/2}\,43s_{1/2}\rangle$ (a) and $|43s_{1/2}\,43s_{1/2}\rangle$ (b). The inset in (a) displays the potential energies around $|43s_{1/2}\,43p_{3/2}\rangle$ on double-logarithmic scale; the dashed blue line indicates a C_3/R^3 scaling with $C_3 = 2\pi \times 1.8$ GHz μm^3 for comparison. The angle θ between $\boldsymbol{R}$ and the quantization axis is set to zero. In (b), the dashed red line shows a C_6/R^6 fit to the potential curve (fit range $[1.5, 5]$ μm), confirming van der Waals-type interaction for $R \gtrsim 1.4$ μm. At small distances $R \sim 0.8$ μm, pair states become strongly mixed. This region is called the "spaghetti region" [145].

state $|n\ell j\rangle$ is $(2j+1)$-fold degenerate. The dipole-dipole interaction mixes states within the degenerate manifold, giving rise to spatially anisotropic interactions in general [132, 140–142]. In this case, the interaction between a pair of Rydberg atoms depends on angle between $\boldsymbol{R}$ and the quantization axis with respect to which the magnetic quantum number m_j is defined. There are certain geometrical arrangements, however, for which the interactions among the Rydberg atoms can be described by a distance-dependent part only, e.g., a linear chain of Rydberg atoms (cf. Refs. [139, 143, 144]).

On the other hand, coupling to other pair states can give rise to a deviation from the R^{-3} scaling of the potential curves. This is illustrated in Fig. 2.2(a), which shows the potential energies around the ^{87}Rb pair states $|43s_{1/2}\,43p_{3/2}\rangle$ and $|43p_{3/2}\,43s_{1/2}\rangle$. While the potential energies exhibit a R^{-3} dependence for distances $R \gtrsim 2$ μm (cf. inset), this is no longer the case for smaller distances where contributions from other pair states become non-negligible. We note that for the interatomic distances employed in the remainder of this thesis, deviations from the R^{-3} dependence of the resonant dipole-dipole interaction are negligible. Given that the coupling to other pair states can be treated perturbatively, the higher-order contributions to the resonant dipole-dipole interaction, which are of van der Waals type [139, 146], can be calculated using degenerate perturbation theory.

Van der Waals interaction and Förster resonance

We now discuss the interaction between non-degenerate pair states. To this end, it is instructive to consider a *toy model* [129, 132, 147–150], which is able to capture the essential features. Specifically, we consider a pair state, say $|ns\,ns\rangle$, coupled via the dipole-dipole interaction (2.7) to another pair state, say $|np\,(n-1)p\rangle$. Since the dipole-dipole interaction is invariant under exchange of the electronic states of atom A and B, the state $|(n-1)p\,np\rangle$ is also coupled to $|ns\,ns\rangle$. In taking only the states $|np\,(n-1)p\rangle$ and $|(n-1)p\,np\rangle$ into account, we assume that all other states $|ns\,np\rangle\,, |np, np\rangle\,, \ldots,$ are energetically far detuned, such that their contribution to the interaction energy of the state $|ns\,ns\rangle$ can be ignored.

Using the pair states $|ns\, ns\rangle$, $|np\,(n-1)p\rangle$, and $|(n-1)p\, np\rangle$, we can evaluate the dipole-dipole interaction (2.7) in the same way as in Eq. (2.9),

$$\langle ns\, ns|V_{\text{dd}}(R)|np\,(n-1)p\rangle = \langle ns\, ns|V_{\text{dd}}(R)|(n-1)p\, np\rangle \equiv \sqrt{D_\varphi}\frac{C_3}{R^3}, \tag{2.11}$$

where C_3 is given by $C_3 = \mu_{ns,np}\mu_{ns,(n-1)p}$ and $\sqrt{D_\varphi}$ contains the angular momentum part.

It is convenient to introduce the symmetrized and anti-symmetrized states given by $|\pm\rangle = (|np\,(n-1)p\rangle \pm |(n-1)p\, np\rangle)/\sqrt{2}$, since the anti-symmetric state $|-\rangle$ does not couple to $|ns\, ns\rangle$, such that the number of relevant states is reduced to two, $|ns\, ns\rangle$ and $|+\rangle$.

The diatomic Hamiltonian Eq. (2.6) in the basis $(|ns\, ns\rangle, |+\rangle)$ of the two pair states can be written as

$$\mathcal{H}_{\text{AB}} = \begin{pmatrix} 0 & \sqrt{2D_\varphi}C_3/R^3 \\ \sqrt{2D_\varphi}C_3/R^3 & \Delta E \end{pmatrix}, \tag{2.12}$$

where the energy defect ΔE (also called *Förster defect*) is defined as

$$\Delta E = E_{np} + E_{(n-1)p} - 2E_{ns}. \tag{2.13}$$

The eigenvalues of Eq. (2.12), which explicitly depend on the interatomic distance R, can be analytically obtained, yielding

$$E_\pm = \frac{1}{2}\left(\Delta E \pm \sqrt{\Delta E^2 + 8D_\varphi\frac{C_3^2}{R^6}}\right). \tag{2.14}$$

In the non-degenerate regime ($\Delta E \gg C_3/R^3$), the dipole-dipole interaction can be treated as a perturbation to the far off-resonant basis states. The resulting interaction-induced energy shift is of van der Waals type C_6/R^6,

$$E_- \simeq -\frac{\sqrt{2}D_\varphi C_3^2/\Delta E}{R^6}, \quad E_+ \simeq \Delta E + \frac{\sqrt{2}D_\varphi C_3^2/\Delta E}{R^6}. \tag{2.15}$$

Given that the dipole moments scale as n^2, and for adjacent levels ΔE scales as n^{-3} (cf. Tab. 2.1), we see that the van der Waals interaction scales as $n^4 \times n^4 \times n^3 = n^{11}$. Since R, C_3^2 and D_φ are positive, the sign of ΔE determines whether the van der Waals interaction is repulsive or attractive. For $\Delta E > 0$, the van der Waals interaction is repulsive while for $\Delta E < 0$ it is attractive.

So far, we neglected states other than $|+\rangle$ and $|ns\, ns\rangle$, and we restricted our attention to just two sets of quantum numbers, ignoring Zeeman degeneracy. In a quantitative treatment, a large number of basis states has to be taken into account for the diagonalization, particularly at low interatomic distances when new resonances arise due to the strong mixing of pair states by the dipole-dipole interaction [96]. Additionally, an accurate treatment needs to account for the full set of quantum numbers (n, ℓ, j, m_j).

Figure 2.2(b) shows the result of a full numerical diagonalization of the two-atom Hamiltonian (2.6) around the ^{87}Rb pair state $|43s_{1/2}\, 43s_{1/2}\rangle$. Since no directly-coupled states are energetically close-by, the state experiences an energy shift of van der Waals type, with a fitted C_6 coefficient of $C_6/2\pi \approx 2.4$ GHz μm^6, agreeing with the value listed in Ref. [151]. Note that around $R \sim 1$ μm, states from the $|40p_{3/2}\, 43f_{5/2,7/2}\rangle$ manifold weakly admix, leading to a deviation of the energy shift from a purely van der Waals C_6/R^6 behavior. Due to the inverse dependence of the van der Waals interaction on the energy difference of the respective pair states, it is essential to use reliable alkali state energies in either perturbation theory or numerical diagonalization, such as those given by Eq. (2.4), where the quantum defect is chosen to yield eigenenergies matching the experimentally measured values.

We note that for non-degenerate pair states, the interaction-induced energy shift of a certain pair state $|\psi_\mathrm{A}\,\psi_\mathrm{B}\rangle$ can be obtained via standard second-order non-degenerate perturbation theory [139, 149, 151], which includes summation over all possible intermediate pair basis states except $|\psi_\mathrm{A}\,\psi_\mathrm{B}\rangle$. For the toy example, where we are interested in the $|ns\,ns\rangle$ state and the states $|\pm\rangle$ are the only relevant pair states, perturbation theory yields the same energy shift as Eq. (2.15). Dispersion coefficients for $|ns\,ns\rangle$, $|np\,np\rangle$, and $|nd\,nd\rangle$ rubidium Rydberg states calculated via second-order perturbation theory can be found in Ref. [151]. (This reference defines $V(R) \simeq -C_6/R^6$ in contrast to our definition $V(R) \simeq C_6/R^6$, leading to a different sign of the dispersion coefficient C_6.) Note that the notion of dispersion coefficients relies on perturbation theory. At 'small' interatomic separations, the dipole-dipole interaction induces a strong mixing of pair states, creating the so-called "spaghetti region", in which standard perturbation theory no longer applies.

When the Förster energy defect ΔE is small compared to the dipole-dipole interaction, the interaction between the pair states is no longer of van der Waals type, but is rendered resonant; for $\Delta E \ll C_3/R^3$, the eigenvalues of Eq. (2.12) in our toy model read as

$$E_\pm \simeq \pm\frac{\sqrt{2}D_\varphi C_3}{R^3}. \tag{2.16}$$

In this case, when the dipole-dipole interaction is much larger than the *Förster* energy defect, one speaks of a *Förster resonance.* Förster resonances can be created artificially using electric [104, 152, 153] or microwave fields [154, 155] and allow for the tailoring of strength and angular dependence of the dipole-dipole interaction [156]. We will make use of a Förster resonance later to enhance the interaction between two states.

Note that this thesis is not concerned with the numerical calculation of dispersion coefficients for Rydberg-Rydberg interactions. For details on the calculation of the dipole matrix elements and the numerical diagonalization of the dipole-dipole interaction Hamiltonian with a specified basis we refer to Refs. [96, 140, 147–149] and the references therein. For a detailed account of the effects of an external electric field on Rydberg-Rydberg interactions, see Refs. [130, 140, 157–160].

Dipole blockade

Interactions between Rydberg atoms give rise to an effect called "dipole blockade" [69]. This denotes the inhibition of multiple Rydberg excitations within a spatially confined ensemble of atoms addressed by a narrowband laser on resonance with the single-atom ground-Rydberg ($|g\rangle$ to $|r\rangle$) transition. Due to interactions between the Rydberg $|r\rangle$ states, collective states with more than a single $|r\rangle$ excitation are shifted in energy. Hence, a laser that is tuned to resonance between the ground $|g\rangle$ and Rydberg $|r\rangle$ state is no longer resonant with collective states with multiple Rydberg excitations. Multiple Rydberg excitations are thus inhibited in such an interacting ensemble.

Figure 2.3 illustrates the dipole blockade for a simple diatomic system consisting of ground $|g\rangle$ and Rydberg $|r\rangle$ states. The two Rydberg states interact via the van der Waals interaction C_6/R^6. At large interatomic distances R, the energy of the doubly-excited Rydberg state $|rr\rangle$ is negligibly shifted. Accordingly, a laser that resonantly excites the ground state to the Rydberg state is also in resonance with the doubly excited state. As the interatomic distance decreases, the magnitude of the energy shift of the doubly excited state increases due to the van der Waals interaction, thus rendering the laser off-resonant with respect to the transition between singly-excited and doubly-excited Rydberg states [35, 71, 129].

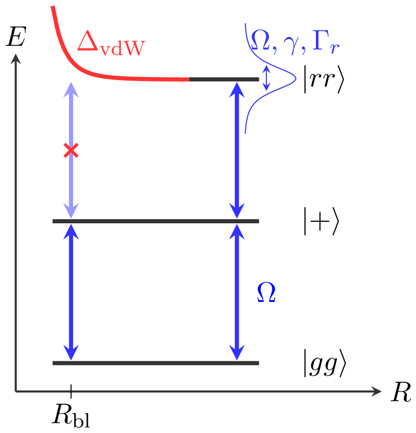

Figure 2.3: Illustration of the dipole blockade effect. The energy levels correspond to the pair states of two atoms consisting of ground $|g\rangle$ and Rydberg $|r\rangle$ states, with $|+\rangle \equiv (|rg\rangle + |gr\rangle)/\sqrt{2}$. Each atom is addressed by a laser (Rabi frequency Ω) resonantly driving the transition from the ground to the Rydberg state. At small interatomic distances, the interaction-induced energy shift Δ_{vdW} (assumed to be of van der Waals type) shifts the doubly-excited state $|rr\rangle$ out of laser resonance. Power broadening $\propto \Omega^2$ [161], decay Γ_r of the Rydberg level and also dephasing γ (e.g. due to the laser linewidth) [162] can lead to a broadening of the $|rr\rangle$ resonance, counteracting the dipole blockade. The figure is adapted from Ref. [163].

In a dipole-blockaded atomic ensemble, only a single Rydberg excitation is admitted. In the absence of decohering processes, the laser Hamiltonian is symmetric under exchange of particles [164], such that rather than a single localized excitation, the system exhibits a symmetric superposition of singly-excited states, such as $|+\rangle \equiv (|rg\rangle + |gr\rangle)/\sqrt{2}$ for the diatomic system depicted in Fig. 2.3. The Rabi frequency associated with the transition $|g\rangle \leftrightarrow |+\rangle$ is collectively enhanced by a factor of $\sqrt{2}$ for 2 atoms, and $\sqrt{N}$ for N atoms [97, 165–168].

The distance at which the doubly-excited state can no longer be populated is called the *blockade radius* and can be estimated by equating the interaction-induced energy shift $\Delta_{\mathrm{vdW}} = C_6/R^6$ with the collectively enhanced Rabi frequency $\sqrt{N}\Omega$, yielding [35]

$$R_{\mathrm{bl}} \simeq \left(\frac{C_6}{\sqrt{N}\Omega} \right)^{1/6} . \tag{2.17}$$

The blockade radius is a helpful concept, e.g. for estimating the number of Rydberg excitations that fit into a certain volume filled with ultracold atoms resonantly excited to the Rydberg state. It is not to be understood as a hard-core sphere inside which no multiple-Rydberg excitations are possible. Rather, the blockade is a gradual process with decreasing probability of finding another Rydberg excitation as we move closer to an existing Rydberg excitation.

Note, however, that if the Rydberg state $|r\rangle$ is excited via a resonant two-step excitation process and the Rydberg-Rydberg interactions are repulsive, multiphoton resonances can give rise to enhanced Rydberg state populations as compared to the non-interacting case [169], rendering the simple blockade picture questionable. Additionally, the blockade picture can be rendered invalid in the presence of nearly-resonant dipole-dipole interactions [136] or due to non-additivity of van der Waals potentials [137], for instance.

Although we do not make explicit use of the dipole blockade in the remainder of this chapter, the dipole-blockade concept will be helpful for the discussion of optical response properties of a Rydberg medium, which we address in Sec. 2.2.4.

2.2.3 Laser excitation and decay of Rydberg atoms

We now briefly discuss the interaction of a single three-level atom with two classical laser fields. More specifically, we address the optical excitation of a ground state atom to the Rydberg state via a two-step scheme, which we employ throughout this chapter. We then introduce the master equation, which allows us to take into account radiative decay.

The interaction between an electric field and a single atom is described by the interaction Hamiltonian[3]

$$\mathcal{H}_\mathrm{L} = -\boldsymbol{\mu} \cdot \boldsymbol{E}(\boldsymbol{R}_0, t) = -e\boldsymbol{r} \cdot \boldsymbol{E}(\boldsymbol{R}_0, t), \tag{2.18}$$

with $\boldsymbol{E}$ denoting the electric field, $\boldsymbol{\mu}$ the transition dipole moment of the atom, and $\boldsymbol{r}$ the location of the electron relative to the center of mass position $\boldsymbol{R}_0$ of the atom [161, 171]. In writing Eq. (2.18), we employed the *dipole approximation*, i.e., the assumption that the field associated with the laser is constant over the dimension of the atom [161]. For highly-excited Rydberg atoms with spatial extent of the electronic wave function on the order of μm [121], this approximation seems highly questionable. It turns out, however, that even though the dimension of the wave function of the Rydberg electron is no longer small compared to the wavelength of the laser used to induce a certain transition (for the systems we consider, on the order of 500 nm), the use of the dipole approximation is justified since the interaction with the laser light primarily occurs close to the core [175, 176]. In ^{87}Rb, for example, the transition matrix element between the state $|5p_{3/2}\rangle$ and a high-lying $|ns_{1/2}\rangle$ Rydberg state acquires its value in a region close to the core, since the spatial extent of the $|5p_{3/2}\rangle$ electron wave function is confined to a region close to the core. Remarkably, this reasoning even applies for the treatment of photoionization of Rydberg states [175, 176], for which the wave functions clearly extend far beyond the core region. Accordingly, we safely apply the dipole approximation in laser-addressed Rydberg atoms despite their huge size, which can be comparable to the laser wavelength.

Assuming a monochromatic laser field with frequency ω_L and amplitude $\boldsymbol{\mathcal{E}}$, the field at the center of mass of the atom is given by

$$\boldsymbol{E}(\boldsymbol{R}_0, t) = \boldsymbol{\mathcal{E}} \cos(\omega_\mathrm{L} t). \tag{2.19}$$

Deviations from a monochromatic laser source (such as a finite linewidth of the laser) are not considered here, but can be accounted for by adding a dephasing term in the master equation [147, 177].

In this work, we consider a two-step excitation scheme to the Rydberg state using two classical laser fields. If we want to populate the $|ns_{1/2}\rangle$ Rydberg states via laser driving, a single laser field is not sufficient due to the dipole selection rules, since the ground state of rubidium is also an $|s\rangle$ state. Furthermore, a three-level scheme will provide us with "richer physics", as we will see in the following section.

The two-step excitation of a rubidium Rydberg $|s\rangle$ state via an intermediate $|p\rangle$ state is sketched in Fig. 2.4. Here, a *probe* laser with field amplitude $\boldsymbol{\mathcal{E}}_p$ couples the ground state $|g\rangle = |5s_{1/2}\rangle$ with the intermediate state $|e\rangle = |5p_{3/2}\rangle$. A second laser with field amplitude $\boldsymbol{\mathcal{E}}_c$, called the *coupling* laser, then couples the intermediate state $|e\rangle$ to a Rydberg $|r\rangle = |ns_{1/2}\rangle$ state. We assume that the two lasers are almost resonant with the respective $|g\rangle \leftrightarrow |e\rangle$ and $|e\rangle \leftrightarrow |r\rangle$ transitions, but far detuned from any other electronic state, such that we accurately

---

[3] We note that using the Schrödinger equation rather than the Dirac or Pauli equation implies that we neglect spin magnetic moment and specific relativistic effects [170]. Besides, we neglect any modification of the incident radiation resulting from the interaction with the atom [171]. For further details on the derivation of the Hamiltonian describing the interaction between atom and electromagnetic field, and in particular the equivalence and caveats regarding different choices of gauge transformations, we refer to Refs. [161, 171–174].

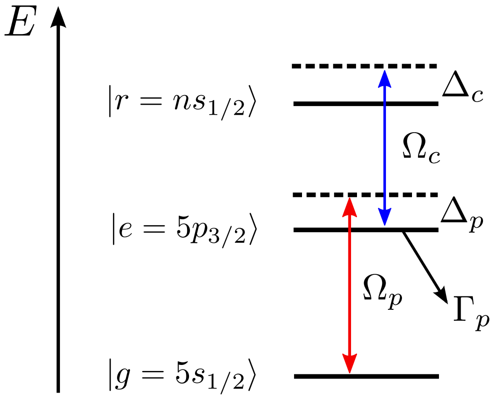

Figure 2.4: Level diagram of the laser excitation scheme considered in this chapter. The *probe* laser (Rabi frequency Ω_p, wavelength $\lambda_p = 780$ nm) couples the ground state of ^{87}Rb, $|g\rangle = |5s_{1/2}\rangle$, to the intermediate $|e\rangle = |5p_{3/2}\rangle$ state. The *coupling* laser (Rabi frequency Ω_c, wavelength $\lambda_c = 480$ nm) then couples the intermediate state to a Rydberg $|ns_{1/2}\rangle$ state. The laser detuning Δ_p (Δ_c) quantifies the frequency mismatch between the probe (coupling) laser frequency and the $|5s_{1/2}\rangle \to |5p_{3/2}\rangle$ ($|5p_{3/2}\rangle \to |ns_{1/2}\rangle$) transition frequency. Γ_p accounts for the radiative decay from the intermediate state $|e\rangle$ to the ground state $|g\rangle$.

describe the system by means of the three-state basis $\{|g\rangle, |e\rangle, |r\rangle\}$. Within the *rotating wave approximation (RWA)*, the corresponding atom-laser Hamiltonian $\mathcal{H}_{\text{laser}}$ resulting from Eq. (2.18) for the two applied laser fields is given by

$$\mathcal{H}_{\text{laser}} = \begin{pmatrix} 0 & \Omega_p/2 & 0 \\ \Omega_p/2 & -\Delta_p & \Omega_c/2 \\ 0 & \Omega_c/2 & -(\Delta_p + \Delta_c) \end{pmatrix}. \tag{2.20}$$

Here, $\Omega_{p,c}$ denote the (real) Rabi frequencies [178],

$$\Omega_p = -\langle g|e\boldsymbol{r} \cdot \boldsymbol{\mathcal{E}}_p|e\rangle, \quad \Omega_c = -\langle e|e\boldsymbol{r} \cdot \boldsymbol{\mathcal{E}}_c|r\rangle, \tag{2.21}$$

associated with the respective $|g\rangle \leftrightarrow |e\rangle$ and $|e\rangle \leftrightarrow |r\rangle$ transitions. The laser detunings $\Delta_{p,c}$ are defined as $\Delta_p = \omega_p - (E_e - E_g)$ and $\Delta_c = \omega_c - (E_r - E_e)$, for the laser frequencies $\omega_{p,c}$. The RWA approximation [171, 173, 178] amounts to performing a unitary transformation into a frame rotating with the laser frequencies and then neglecting rapidly oscillating phases [163, 177, 179]. For this approximation to be valid, we need $\Omega_p \ll (E_e - E_g)$ and $\Omega_c \ll (E_r - E_g)$ to hold [171]. With Rabi frequencies of ~ 10 MHz and transition energies of $\sim 10^8$ MHz, this approximation is well justified.

So far, we have assumed that the quantum systems we consider are isolated from any environment, such that the dynamics of the relevant states follows the Schrödinger equation. We now abandon this assumption to treat processes such as radiative decay, which arise from interaction with a continuum of electromagnetic modes [180]. One way of treating open quantum systems is to introduce a *master equation* of *Lindblad* form [3, 4, 181]. That is, instead of using the Schrödinger equation to calculate the time evolution of a pure state vector $|\psi\rangle$, we employ the von Neumann equation for the density matrix ρ,

$$\dot{\rho}(t) = -i[\mathcal{H}, \rho(t)] + \mathcal{L}_{L_j}[\rho(t)], \tag{2.22}$$

with the Lindblad superoperator $\mathcal{L}_{L_j}[\rho(t)]$ for the Lindblad operator L_j reading as

$$\mathcal{L}_{L_j}[\rho(t)] = \frac{1}{2}\left\{[L_j\rho(t), L_j^\dagger] + [L_j, \rho(t)L_j^\dagger]\right\}. \tag{2.23}$$

Here, the index j of the Lindblad operator indicates that several Lindblad operators may occur in the master equation, e.g. corresponding to different decay processes. For the radiative decay of the short-lived $|e\rangle$ state depicted in Fig. 2.4 to the ground state $|g\rangle$, the Lindblad operator takes the form

$$L = \sqrt{\Gamma_p}\,|g\rangle\langle e|\,. \tag{2.24}$$

The radiative decay rate $\Gamma_p = \tau_p^{-1}$ is given by the natural linewidth (FWHM) of the state $|e\rangle$. The Lindblad equation (2.23) with the operator (2.24) gives an appropriate description of spontaneous emission of an atom in vacuum [182].

We will depend on the master equation (2.22) in the following for the description of our system consisting of ultracold Rydberg atoms. Note that the Lindblad superoperator (2.23) is derived in the Born-Markov approximation, i.e., assuming weak coupling to the environment (Born approximation) and fast decay of the correlations in the bath on the timescales relevant for the system dynamics (Markov approximation). In addition, a secular (or rotating wave) approximation has been applied to arrive at the Lindblad form [3].

Instead of formulating the master equation Eq. (2.22) using density matrices, it can be convenient to employ a formulation in *Liouville space* [4, 183], in which the master equation for the density vector $|\rho\rangle$ reads as

$$|\dot{\rho}\rangle = \mathcal{L}^{\mathrm{lv}}\,|\rho\rangle\,. \tag{2.25}$$

Here, the density operator is vectorized using Choi's isomorphism $|\psi_i\rangle\langle\psi_j| \to |\psi_i\,\psi_j\rangle$ [184], which maps any operator ρ to a vector $|\rho\rangle$. Accordingly, the Liouvillian superoperator $\mathcal{L}^{\mathrm{lv}}$ for the master equation Eq. (2.22) is given by [183, 184]

$$\mathcal{L}^{\mathrm{lv}} = -i\left(\mathcal{H}\otimes I + I\otimes\mathcal{H}\right) + \sum_j \frac{1}{2}\left(2L_j\otimes L_j^* - L_j^\dagger L_j\otimes I - I\otimes L_j^T L_j^*\right), \tag{2.26}$$

with I denoting the identity operator, and the star denoting complex conjugation. A discussion of the advantages of the Liouvillian formulation can be found in Ref. [183]. For our part, we mention this alternative formulation as it proves convenient in the numerical implementation of the Lindblad terms in Sec. 2.4.1, given that $\mathcal{L}^{\mathrm{lv}}$ is typically sparse.

2.2.4 Optical response of a Rydberg medium

Having addressed the excitation of Rydberg atoms via laser fields, we have everything at hand to review the linear optical response properties of Rydberg atoms [147, 177, 185], which are crucial for the understanding of excitation transport imaging in Sec. 2.3, i.e., the optical discrimination between the two Rydberg states (s and p) involved in the excitation transport. We start by discussing the optical response properties of two-level atoms and then continue with those of three-level atoms, which feature effects unseen in two-level systems, such as electromagnetically induced transparency. Lastly, we briefly discuss how Rydberg-Rydberg interactions influence the optical response properties of Rydberg atoms.

Optical susceptibility and absorption

As light travels through a polarizable medium, it is both attenuated and diffracted, with the amount of absorption and diffraction determined by the complex refractive index n of the medium. The optical resonse of a medium can be quantified by means of the complex susceptibility χ, which is related to the refractive index n via $\mathrm{n} = \sqrt{1+\chi}$. For an illustration, consider a laser field with wave vector k propagating through a medium with associated refractive index n. The output electric field after a distance L is given by $\boldsymbol{E}(L) = e^{ik\mathrm{n}L}\boldsymbol{E}(0)$.

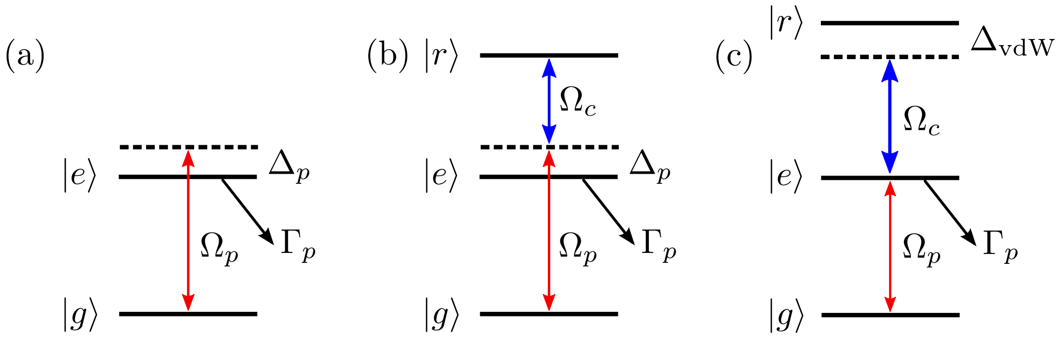

Figure 2.5: Level diagrams of two and three-level atoms in EIT configuration. (a) Two-level atom, coupled via a laser (probe laser, Rabi frequency Ω_p and detuning Δ_p) to the short-lived excited state $|e\rangle$. (b) Three-level atom with additional driving of a transition $|e\rangle \leftrightarrow |r\rangle$ with a second laser (coupling laser, Rabi frequency Ω_c) that is tuned to resonance with respect to the transition $|e\rangle \leftrightarrow |r\rangle$. (c) Three-level atom similar to (b), but with resonant probe laser ($\Delta_p = 0$) and interacting Rydberg level $|r\rangle$. The interaction-induced energy shift Δ_{vdW} moves the two-photon transition $|g\rangle \leftrightarrow |r\rangle$ out of resonance.

For $|\chi| \ll 1$, the refractive index can be expanded as $\mathrm{n} = \sqrt{1+\chi} \simeq 1 + (\mathrm{Re}[\chi] + i\,\mathrm{Im}[\chi])/2$, leading to an output intensity

$$I(L) = e^{-k\mathrm{Im}[\chi]L} I(0). \tag{2.27}$$

Hence, the imaginary part of the complex susceptibility, which can be calculated in theory as detailed below, describes the absorption of the medium, which can be measured in experiment.

In the following, we are interested in the optical response of an atomic medium to laser light, specifically to the laser light of the *probe* laser introduced in the previous section 2.2.3, which couples the two states $|g\rangle$ and $|e\rangle$. To evaluate this optical response, we first note that the electric polarization P of a dielectric medium is linked to the incident electric field E via the first-order complex susceptibility χ [173]

$$P = \varepsilon_0 \chi E. \tag{2.28}$$

The polarization P acts as a source term in Maxwell's equations and thus determines the electromagnetic field dynamics. Note that we restrict ourselves to the case of *linear optical response* here, i.e., the case where the polarization of the medium is directly proportional to the incident field.

In an atomic medium without a permanent dipole moment, the polarization P of the atomic medium is induced by the electric field, giving rise to a complex interplay between the electric field and the induced polarization in general [161]. It is thus instructive to consider the atomic medium in its steady state. In this case, the macroscopic polarization P of a resonantly-driven two-level medium [cf. Fig. 2.5(a)] is determined by the corresponding transition dipole of the individual atoms via

$$P = n_0 \langle \mu \rangle . \tag{2.29}$$

Here, n_0 is the atomic density, $\mu = \mu_{e,g}(|e\rangle\langle g| + \mathrm{H.c.})$ is the transition dipole moment of a single atom and $\langle \cdot \rangle = \mathrm{Tr}\{\cdot \tilde{\rho}\}$ denotes the expectation value with respect to the steady-state density matrix $\tilde{\rho}$ of the two-level system.

Combining the two relations (2.28) and (2.29) for the polarization P allows one to obtain an explicit expression for the steady-state complex optical susceptibility $\tilde{\chi}$ [147, 177, 185, 186],

$$\tilde{\chi} = -\frac{2n_0\mu_{e,g}^2}{\varepsilon_0 \Omega_p} \tilde{\rho}_{eg}, \tag{2.30}$$

where Ω_p denotes the Rabi frequency of the transition $|g\rangle \leftrightarrow |e\rangle$. Making use of the definition of the decay rate of a two-level system for the level $|e\rangle$ [180],

$$\Gamma_p = \frac{k_p^3 \mu_{e,g}^2}{3\pi\varepsilon_0}, \tag{2.31}$$

where k_p denotes the wave vector $k_p = 2\pi/\lambda_p$ of the transition $|g\rangle \leftrightarrow |e\rangle$, we can recast Eq. (2.30) into the form [187]

$$\tilde{\chi} = -\frac{6\pi n_0 \Gamma_p}{k_p^3 \Omega_p} \tilde{\rho}_{eg} \equiv -\chi_0 \frac{\Gamma_p}{\Omega_p} \tilde{\rho}_{eg}. \tag{2.32}$$

Here we defined the two-level resonant susceptibility $\chi_0 = 6\pi n_0/k_p^3 \equiv \sigma_0/k_p n_0$ where σ_0 is the absorption cross section of a single atom [80]. Employing the relation $\rho_{eg} = \rho_{ge}^*$, we can further write[4]

$$\mathrm{Im}[\tilde{\chi}]/\chi_0 = -\frac{\Gamma_p}{\Omega_p} \tilde{\rho}_{eg} = \frac{\Gamma_p}{\Omega_p} \tilde{\rho}_{ge}. \tag{2.33}$$

Equation (2.33) relates the optical absorption of an atomic medium to its quantum state. We will rely on this expression in Sec. 2.3.1 to determine the optical response of a background gas for Rydberg excitation imaging.

Electromagnetically induced transparency (EIT)

Electromagnetically induced transparency (EIT) is one among many effects that enters when moving from two-level to three-level atomic physics. As we have seen in the previous section, a resonantly-driven two-level atom absorbs light. If a third resonantly-driven level is added, the absorption vanishes. This effect is called EIT [80], and will be crucial for Rydberg excitation transport imaging, discussed in Sec. 2.3.

For an illustration of how EIT arises, consider the three-level system sketched in Fig. 2.5(b), which is driven on two-photon resonance $\Delta_p + \Delta_c = 0$. The corresponding laser Hamiltonian in the basis $\{|g\rangle, |e\rangle, |r\rangle\}$ reads as (cf. Eq. (2.20))

$$\mathcal{H}_{\mathrm{EIT}} = \begin{pmatrix} 0 & \Omega_p/2 & 0 \\ \Omega_p/2 & -\Delta_p & \Omega_c/2 \\ 0 & \Omega_c/2 & 0 \end{pmatrix}. \tag{2.34}$$

Evaluating the product $\mathcal{H}_{\mathrm{EIT}} |d\rangle$ with $|d\rangle$ defined by

$$|d\rangle = \frac{\Omega_c |g\rangle - \Omega_p |r\rangle}{\sqrt{\Omega_p^2 + \Omega_c^2}}, \tag{2.35}$$

we see that $|d\rangle$ is an energy-zero eigenstate, $\mathcal{H}_{\mathrm{EIT}} |d\rangle = 0$. This implies that $|d\rangle$ is a dark state, i.e., a state that does not interact with the electromagnetic field [161]. In particular, $|d\rangle$ does not have any contribution of the short-lived state $|e\rangle$, such that within our description it does not lose population nor scatter any light. The susceptibility $\chi \propto \rho_{ge}$ of a system in state $|d\rangle$ thus vanishes, rendering the three-level medium transparent to the probe beam.

To quantify EIT in the three-level ($|g\rangle, |e\rangle, |r\rangle$) case and to compare to the two-level ($|g\rangle, |e\rangle$) case, we evaluate the imaginary part of the steady-state complex susceptibility $\tilde{\chi}$, which is

---

[4] Note that the imaginary part of the steady-state coherence $\tilde{\rho}_{ge}$ and the steady-state population $\tilde{\rho}_{ee}$ are related via $\mathrm{Im}[\tilde{\rho}_{ge}] = \Gamma_p/\Omega_p \tilde{\rho}_{ee}$ [76], which allows one to simulate the optical response of an atomic gas via rate equations.

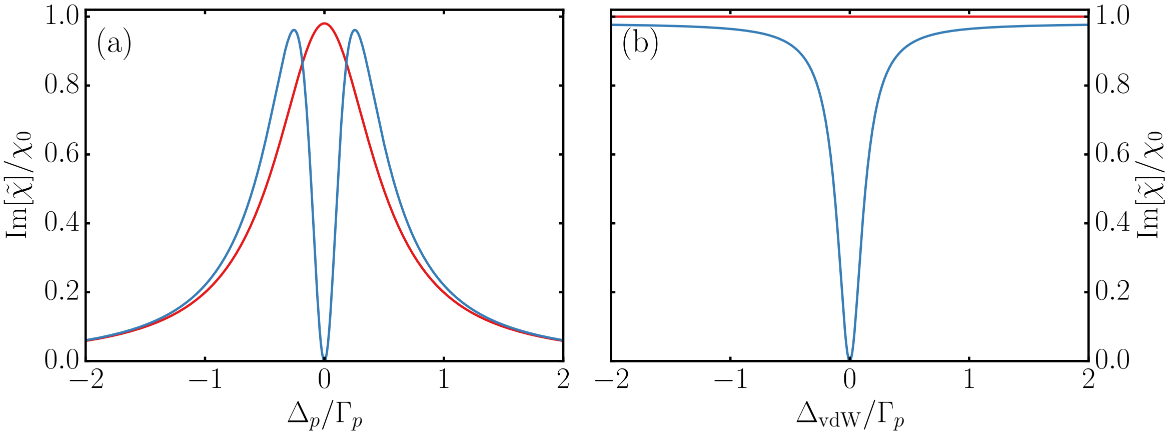

Figure 2.6: (a) Imaginary part of the scaled steady-state susceptibility $\tilde{\chi}/\chi_0$ as a function of the probe laser detuning Δ_p, for both the three-level (solid blue, $\Delta_c = 0$) and the two-level (solid red, obtained via $\Omega_c = 0$) case. (b) Imaginary part of the steady-state susceptibility as a function of the interaction-induced energy shift Δ_{vdW}, for both three-level (solid blue) and two-level (solid red, obtained via $\Omega_c = 0$) case. Parameters are $\Omega_p = 5\Omega_c = 10\Gamma_p$.

proportional to the density matrix $\tilde{\rho}_{ge}$, as shown in Eq. (2.33). The two and three-level atoms are driven-dissipative systems, which reach a unique *steady state* after a finite time [188], with the steady-state coherences $\tilde{\rho}_{ge}$ given by

$$\tilde{\rho}_{ge}^{(2\mathrm{lvl})}(\Delta_p) = \frac{\Omega_p(2\Delta_p + i\Gamma_p)}{4\Delta_p^2 + \Gamma_p^2 + 2\Omega_p^2}, \tag{2.36a}$$

$$\tilde{\rho}_{ge}^{(3\mathrm{lvl})}(\Delta_p) = \frac{2\Delta_p\Omega_p(4\Delta_p^2 + 2i\Delta_p\Gamma_p - \Omega_c^2)}{16\Delta_p^4 + 4\Delta_p^2(\Gamma_p^2 + 2\Omega_p^2 - 2\Omega_c^2) + (\Omega_p^2 + \Omega_c^2)^2} \tag{2.36b}$$

for $\Delta_c = 0$.

Figure 2.6(a) shows the imaginary part of the steady-state susceptibility $\tilde{\chi}$ divided by the two-level value χ_0 for an exemplary set of parameters, for both the two-level (solid red) and the three-level (solid blue) case [from Eqns. (2.33) and (2.36)]. The two-level atom absorbs maximally on resonance $\Delta_p = 0$ and exhibits a Lorentzian absorption line shape with a FWHM of Γ_p in the absence of power broadening $\propto \Omega_p^2$. In the three-level case, in contrast, the absorption drops to zero on resonance $\Delta_p = 0$ due to the EIT effect.

If the upper state $|r\rangle$ is a Rydberg state that interacts via van der Waals interaction, the Rydberg state will experience an interaction-induced energy shift Δ_{vdW} in the vicinity of an existing Rydberg excitation. The corresponding level scheme is depicted in Fig. 2.5(c). For large Δ_{vdW}, the Rydberg state will be shifted out of resonance with respect to the coupling laser, which alters the absorption properties of the atom. For a resonant probe beam, $\Delta_p = 0$, Fig. 2.6(b) shows the imaginary part of the scaled steady-state susceptibility $\tilde{\chi}/\chi_0$ using Eq. (2.33) with

$$\tilde{\rho}_{ge}^{(3\mathrm{lvl})}(\Delta_{\mathrm{vdW}}) = \frac{2\Delta_{\mathrm{vdW}}\Omega_p(2i\Gamma_p\Delta_{\mathrm{vdW}} - \Omega_c^2)}{4\Delta_{\mathrm{vdW}}^2(\Gamma_p^2 + 2\Omega_p^2) + (\Omega_p^2 + \Omega_c^2)^2}, \tag{2.37}$$

with the two-level case also shown as a reference. For large interaction-induced energy shifts Δ_{vdW}, the susceptibility essentially equals that for the two-level case since Δ_{vdW} shifts the Rydberg state $|r\rangle$ out of resonance with the coupling laser, rendering the system effectively two-level-like. For small Δ_{vdW}, in contrast, EIT is recovered and the atom becomes transparent to the probe beam.

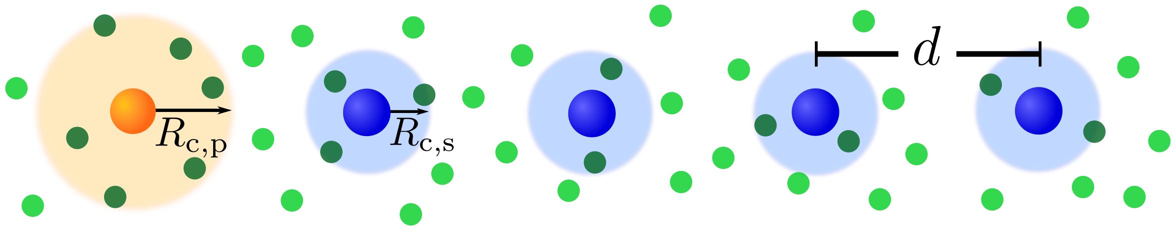

Figure 2.7: Sketch of an embedded Rydberg aggregate. An assembly of several Rydberg atoms in state $|s\rangle$ (large blue) and one in state $|p\rangle$ (large orange) is linearly arranged with spacing d in a background atomic gas (shades of green). When addressed in an EIT scheme, the laser-driven background gas atoms are rendered transparent only outside the critical radii $R_{\mathrm{c,p}}$ and $R_{\mathrm{c,s}}$, which are of different magnitude for the aggregate states $|p\rangle$ and $|s\rangle$.

To obtain an estimate for when the three-level system transitions from transparency to absorption with respect to the probe beam, we define the *EIT width* γ_{EIT} via the critical interaction Δ_{crit} at which $\mathrm{Im}[\tilde{\chi}]/\chi_0$ equals half its value at full absorption $\Delta_{\mathrm{vdW}} \to \infty$, which corresponds to the condition

$$\tilde{\rho}_{ge}(\Delta_{\mathrm{crit}}) = \tilde{\rho}_{ge}(\Delta_{\mathrm{vdW}} \to \infty)/2. \tag{2.38}$$

For low probe fields, i.e., evaluating the steady-state coherence $\tilde{\rho}_{ge}$ only up to first order in Ω_p, we obtain

$$\Delta_{\mathrm{crit}} = \frac{\Omega_c^2}{2\Gamma_p}. \tag{2.39}$$

The EIT width is then given by $\gamma_{\mathrm{EIT}} = 2\Delta_{\mathrm{crit}}$. In the case that the interaction-induced energy shift can be described by a simple power law, such as $\Delta_{\mathrm{vdW}} = C_6/R^6$ for the van der Waals interaction, one can express the condition for breakdown of EIT in terms of a *critical radius*

$$R_{\mathrm{c}} = \left(\frac{2\Gamma_p C_6}{\Omega_c^2}\right)^{1/6}. \tag{2.40}$$

This formulation will prove useful in the context of excitation transport imaging in Sec. 2.3.

2.2.5 The embedded Rydberg aggregate

We are now in a position to introduce the setup that we study throughout this chapter, sketched in Fig. 2.7. We consider a laser-driven gas of ultracold ^{87}Rb atoms, the positions of which could be random (Secs. 2.3 and 2.4) or arranged in a regular fashion (Secs. 2.5 and 2.6). Within this *background gas* (green circles in Fig. 2.7), we excite N Rydberg atoms, which form the *aggregate*, our system of interest. For what follows, we consider a particular geometry of this aggregate, namely a chain of N Rydberg atoms ($N = 5$ in Fig. 2.7) with spacing d. Such an equidistant arrangement of Rydberg atoms can be created by exciting Rydberg states from a trapped ultracold atomic gas using tightly focused laser beams [53–55, 110]. In principle, pulsed or chirped excitation in the dipole blockade regime also gives rise to spatially correlated Rydberg excitation patterns [111, 189–197]; however, this technique might not provide a large degree of control over the distance distributions.

By using an ultracold gas for our proposal, we ensure that thermal motional effects are negligible, and do not have to be accounted for in our theoretical description. This is the *frozen gas* regime. In current experiments, the temperatures of the atomic gas ranges from the nK [196] to the μK [168, 198, 199] regime, for which the thermal velocity is of order nm/μs.

Forces due to interactions might, however, invalidate this assumption; some estimates in this regard can be found in Sec. 2.3.1.

While the *aggregate* comprises our *system*, the *background gas* constitutes a versatile and controllable *environment* for the system. In the following subsections, we detail the modeling of the aggregate, the background gas, and their mutual interactions.

System: The aggregate

The Rydberg aggregate consists of N Rydberg atoms in a certain arrangement. For simplicity, we use a linear arrangement of Rydberg atoms with equidistant spacing d; in principle, arbitrary arrangements are possible. Of these N atoms, $N-1$ atoms are initially prepared in the state $|s\rangle = |43s\rangle$ with angular momentum $\ell = 0$, while a single atom is excited to the state $|p\rangle = |43p\rangle$ with angular momentum $\ell = 1$. Such a configuration can be achieved in experiment similar to Ref. [52] by first preparing the $|p\rangle$ state via a microwave pulse starting from an initial $|s\rangle$ state, or, alternatively, via a direct excitation from the ground state [200]. The $|s\rangle$ states can be excited subsequently via a two-photon transition [81].

The $|p\rangle$ excitation can migrate through the aggregate via resonant dipole-dipole exchange interactions [34, 47], with a dynamical evolution depending on the interaction with the environment. Dipole-dipole interactions thus induce *excitation transport* in the aggregate, in the same way as they do in other physical setups, including photosynthesis [201, 202], quantum-dot arrays [203], and molecular aggregates [204, 205]. This turns our Rydberg aggregate into a model system for excitation transport, or *exciton transport*. The term exciton here originates from the analogy between Rydberg and molecular aggregates [46, 206]. In molecular aggregates, the so-called Frenkel exciton model [73] describes excitation transport where the moving excitation energy is an intramolecular excitation (i.e., no charge transfer between different molecules occurs) [5]. Note that we use *energy transport* synonymous with excitation or exciton transport, as the $|p\rangle$ state is higher in energy than the $|s\rangle$ state.

Since we only consider a single Rydberg $|p\rangle$ excitation, we can restrict our discussion to the "single-excitation" manifold, with the term "excitation" again referring to the $|p\rangle$ excitation. This manifold is spanned by basis states in which the $|p\rangle$ excitation is localized on different atoms, or sites. Specifically, the state $|\pi_1\rangle = |pss\cdots\rangle$ denotes the state with the $|p\rangle$ excitation localized on site one, $|\pi_2\rangle = |spss\cdots\rangle$ etc. Setting the constant energy offset to zero, the aggregate Hamiltonian in this basis reads as[5]

$$\mathcal{H}_{\text{agg}} = \sum_{n\neq m} W_{nm}\, |\pi_n\rangle\langle\pi_m|\,, \tag{2.41}$$

where $W_{nm} = C_3/|\boldsymbol{R}_n - \boldsymbol{R}_m|^3 = C_3/(|n-m|d)^3$ denotes the resonant dipole-dipole interaction and C_3 is given by $C_3/(2\pi) = 1619\ \text{MHz}\,\mu\text{m}^3$ [64]. Note that Roman indices such as n, m always refer to aggregate atoms in this chapter. For simplicity, we ignore van der Waals interactions between aggregate atoms in Eq. (2.41) [146], which is valid for the large interatomic separations between the aggregate atoms that we predominantly employ in this chapter. In addition, we ignore the finite lifetime of the Rydberg $|s\rangle$ and $|p\rangle$ excitations. This implies that we cannot consider arbitrarily large aggregate sizes in our study of excitation transport without heavily relying on post-selection, as will be detailed in Sec. 2.3.1.

Besides inducing excitation transport within the aggregate, resonant dipole-dipole interactions also modify the eigenenergy structure of the aggregate. That is, for nonzero interaction W_{nm}, the eigenstates of the aggregate Hamiltonian (2.41) are no longer given by the localized

---

[5] See Ref. [143] for more details on how to obtain a convenient form of the resonant dipole-dipole interaction in one-dimensional geometries via suitable choice of the quantization axis.

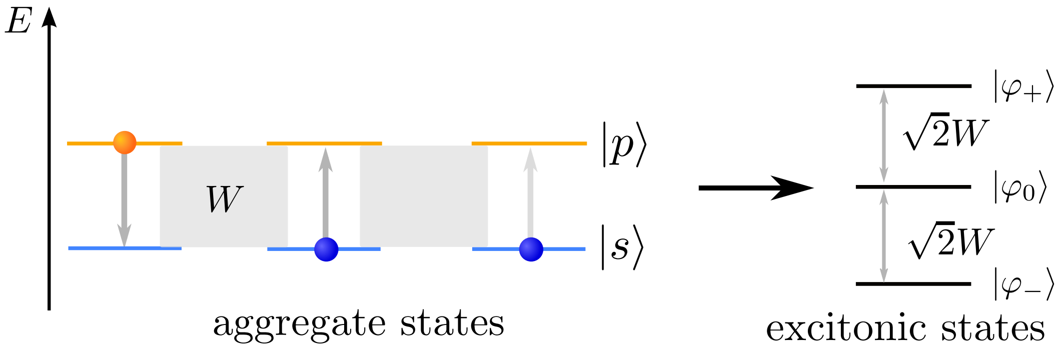

Figure 2.8: Sketch of the level structure of a Rydberg aggregate in the $|\pi_1\rangle$ state, i.e., with the first aggregate atom excited to the Rydberg state $|p\rangle$ (orange) and the remaining atoms excited to the Rydberg state $|s\rangle$ (blue). The $|p\rangle$ and $|s\rangle$ states are coupled by resonant dipole-dipole interactions with magnitude W. Within the singly-excited manifold and nearest-neighbor coupling, the energies of the eigenstates split into an exciton band with energy splitting $\sqrt{2}W$ of adjacent levels.

states $|\pi_n\rangle$, but rather by a superpositions of localized states. To illustrate this, let us consider a chain of three Rydberg aggregates, sketched in Fig. 2.8. For an equidistant chain of atoms ($W = C_3/d^3$ with spacing d) and assuming only nearest-neighbor coupling, the Hamiltonian for the aggregate is

$$\mathcal{H}_{\text{agg}}^{(3\times3)} = \begin{pmatrix} 0 & W & 0 \\ W & 0 & W \\ 0 & W & 0 \end{pmatrix} . \tag{2.42}$$

The eigenstates are superpositions of the localized excitations,

$$|\varphi_+\rangle = \tfrac{1}{2}(|\pi_1\rangle + \sqrt{2}\,|\pi_2\rangle + |\pi_3\rangle), \tag{2.43a}$$

$$|\varphi_-\rangle = \tfrac{1}{2}\,|\pi_1\rangle - \sqrt{2}\,|\pi_2\rangle + |\pi_3\rangle), \tag{2.43b}$$

$$|\varphi_0\rangle = \tfrac{1}{\sqrt{2}}(|\pi_1\rangle - |\pi_3\rangle), \tag{2.43c}$$

with the corresponding energies $E_\pm = \pm\sqrt{2}W$ and $E_0 = 0$. Following Refs. [5, 46, 201, 206], we call also the eigenstates of the aggregate Hamiltonian excitons.

Although localized excitations are easier to measure experimentally than delocalized exciton states, the eigenstate basis is often more appropriate to assess physical properties of the aggregate, such as temperature. We will come back to this in more detail in Section 2.6, in which we discuss how thermal mixtures of exciton states can be dissipatively prepared.

Environment: The background gas

The background gas that constitutes a controllable environment for our aggregate is laser driven (cf. Sec. 2.2.3). A laser with Rabi frequency Ω_p and detuning Δ_p couples the ground state $|g\rangle$ to an intermediate, short-lived state $|e\rangle$. A second laser with Rabi frequency Ω_c and photon detuning Δ_c couples the intermediate state $|e\rangle$ to a Rydberg state $|r\rangle$ or $|r'\rangle$, with $|r\rangle\,(|r'\rangle) \neq |s\rangle\,, |p\rangle$. Tuning of laser frequencies and intensities enables the control over the background atoms. In the rotating wave approximation, the laser-driven background gas is described by the Hamiltonian

$$\mathcal{H}_{\text{bg}} = \sum_\alpha \left[\frac{\Omega_p}{2}\,[|e\rangle\langle g|]_\alpha + \frac{\Omega_c}{2}\,[|r\rangle\langle e|]_\alpha + \text{H.c.} \right] - \Delta_p\,[|e\rangle\langle e|]_\alpha - (\Delta_p + \Delta_c)\,[|r\rangle\langle r|]_\alpha\,, \tag{2.44}$$

where $[|a\rangle\langle b|]_\alpha$ is an operator $|a\rangle\langle b|$ acting only in subspace α. Note that Greek indices always refer to background atoms in the following. For the atomic states we choose $|g\rangle = |5s_{1/2}\rangle$, $|e\rangle = |5p_{3/2}\rangle$, and $|r\rangle$ either $|r\rangle = |38s_{1/2}\rangle$ or $|r'\rangle = |17s_{1/2}\rangle$ in our setup.

In writing the many-body laser Hamiltonian (2.44) as a sum of single-atom laser Hamiltonians (2.20), we assume that the lasers address each background atom alike. This assumption ignores propagation effects such as non-linear beam attenuation due to multiple Rydberg excitations in the propagation direction of the laser beams; an assumption that is is valid for quasi two-dimensional background atom geometries, for instance. A more detailed discussion of this assumption can be found in Sec. 2.3.1. Note that spatially varying constant phases of the Rabi frequencies $\propto e^{i\boldsymbol{k}\cdot\boldsymbol{R}_\alpha}$ with $\boldsymbol{k}$ denoting the wave vector of probe respectively coupling beam and $\boldsymbol{R}_\alpha$ the position of background atom α can be transformed away via local unitary transformations [163, 177].

The radiative decay from the intermediate state $|e\rangle$ is accounted for via the Lindblad operator $L_\alpha = \sqrt{\Gamma_p}\,[|g\rangle\langle e|]_\alpha$ (cf. Sec. 2.2.3) with $\Gamma_p/(2\pi) = 6.1$ MHz [64, 199]. The many-body Lindblad superoperator is given by the sum of the individual Lindblad superoperators (2.23),

$$\mathcal{L}[\rho(t)] = \sum_\alpha \mathcal{L}_{L_\alpha}[\rho(t)]. \tag{2.45}$$

Here we assume the absence of of coherent processes such as superradiance and related processes such as non-linear propagation and diffraction [180]. In fact, the parameter $C = n_0\lambda_p^3/(4\pi^2)$ [207] associated with cooperative effects is well below one for the atomic densities used in this thesis. We also ignore the decay from the Rydberg state $|r\rangle$ since the corresponding decay rate $\Gamma_r/(2\pi) \approx 3$ kHz for $|r\rangle = |38s_{1/2}\rangle$ [72] is much smaller compared to Γ_p, which sets the relevant timescale for the driven-dissipative background gas dynamics.

The Rydberg states $|r\rangle$ of the background atoms interact among themselves via van der Waals interaction,

$$\mathcal{H}_{\text{bg,int}} = \sum_{\alpha<\beta} V_{\alpha\beta}^{(rr)}\,[|r\rangle\langle r|]_\beta\,[|r\rangle\langle r|]_\alpha\,, \tag{2.46}$$

with $V_{\alpha\beta}^{(rr)} = C_{6,rr}/|\boldsymbol{R}_\alpha - \boldsymbol{R}_\beta|^6$. For $|r\rangle = |38s_{1/2}\rangle$, the van der Waals dispersion coefficient is given by $C_{6,rr}/(2\pi) = 530$ MHz μm^6; for $|r'\rangle = |17s_{1/2}\rangle$, we have $C_{6,r'r'}/(2\pi) \approx 7$ kHz μm^6 [208].

System-environment interaction

The system (i.e., the aggregate) and the environment (i.e., the background gas) interact via state-dependent Rydberg-Rydberg interactions, namely interactions that depend on the states ($|p\rangle$ vs. $|s\rangle$) of the aggregate atoms. For simplicity, we assume isotropic interactions, meaning that the interaction between the state $|p\rangle$ and another Rydberg state $|s\rangle$, $|r\rangle$, $|r'\rangle$ only depends on the separation between the two excitations and not on their orientation with respect to a given quantization axis. Accordingly, the Hamiltonian describing the interactions between aggregate and background gas atoms reads as

$$\begin{aligned}\mathcal{H}_{\text{agg-bg}} &= \sum_{\alpha,n} V_{n\alpha}^{(pr)}\,|\pi_n\rangle\langle\pi_n|\,[|r\rangle\langle r|]_\alpha + \sum_{\alpha,n,m\neq n} V_{m\alpha}^{(sr)}\,[|r\rangle\langle r|]_\alpha\,|\pi_n\rangle\langle\pi_n| &\text{(2.47a)}\\ &= \sum_{\alpha,n} \bar{V}_{n\alpha}\,|\pi_n\rangle\langle\pi_n|\,[|r\rangle\langle r|]_\alpha, &\text{(2.47b)}\end{aligned}$$

where we introduced $\bar{V}_{n\alpha} = V_{n\alpha}^{(pr)} + \sum_{m\neq n} V_{m\alpha}^{(sr)}$, which denotes the overall interaction of the specific background atom α with the entire aggregate if the latter is in the state $|\pi_n\rangle$.

The interaction between $|r\rangle$ and $|s\rangle$ is of van der Waals type, $V_{n\alpha}^{(sr)} = C_{6,rs}/|\boldsymbol{R}_n - \boldsymbol{R}_\alpha|^6$ with $C_{6,rs}/(2\pi) = -87\ \mathrm{MHz}\,\mu\mathrm{m}^6$, while the interaction between $|r\rangle$ and $|p\rangle$ is parameterized via an effective R^{-4} scaling[6], reading $V_{n\alpha}^{(pr)} = C_{4,rp}/|\boldsymbol{R}_n - \boldsymbol{R}_\alpha|^4$ with $C_{4,rp}/(2\pi) = -1032\ \mathrm{MHz}\,\mu\mathrm{m}^4$ [64]. Note that in principle, van-der-Waals forces are not additive [137, 209]. In our case, however, for which $n = n'$ for the van der Waals interaction between the background atom states $|r\rangle$ or $|n - n'| > 2$ for the interaction between $|s\rangle$ and $|r\rangle$, Ref. [137] suggests that we may assume additivity, which we do indeed.

Using $|r\rangle$ as the Rydberg state of the background atoms allows us to have much stronger interactions $|V^{(pr)}| \gg |V^{(sr)}|$ between $|p\rangle$ and $|r\rangle$ as compared to $|s\rangle$ and $|r\rangle$ at interatomic separations of a few μm. This difference in interaction strengths in particular leads to different sizes of the critical radii depicted in Fig. 2.7,

$$R_{\mathrm{c,p}} = \left(\frac{2\Gamma_p |C_{4,rp}|}{\Omega_c^2}\right)^{1/4} \simeq 1.93\ \mu\mathrm{m}, \tag{2.48a}$$

$$R_{\mathrm{c,s}} = \left(\frac{2\Gamma_p |C_{6,rs}|}{\Omega_c^2}\right)^{1/6} \simeq 1.03\ \mu\mathrm{m}, \tag{2.48b}$$

where the numerical values are obtained for $\Omega_c/(2\pi) = 30$ MHz. In Sec. 2.3, in which we address the imaging of excitation transport within the aggregate, these critical radii will play a crucial role, since they will allow us to distinguish a $|p\rangle$ from an $|s\rangle$ excitation.

Using the state $|r'\rangle$ as Rydberg state of the background gas, we obtain significantly smaller interactions, which are of van der Waals type, $V_{n\alpha}^{(r's)} = C_{6,r's}/|\boldsymbol{R}_n - \boldsymbol{R}_\alpha|^6$ with $C_{6,r's}/(2\pi) = -0.1\ \mathrm{MHz}\,\mu\mathrm{m}^6$ and $V_{n\alpha}^{(pr)} = C_{6,r'p}/|\boldsymbol{R}_n - \boldsymbol{R}_\alpha|^6$ with $C_{6,rp}/(2\pi) = -0.4\ \mathrm{MHz}\,\mu\mathrm{m}^6$ [64]. Here, the interactions between $|r\rangle$ and $|p\rangle$ respectively $|r\rangle$ and $|s\rangle$ are very similar.

In addition to varying the Rydberg state ($|r\rangle$ vs. $|r'\rangle$) of the background atoms to control the interactions between aggregate atoms and background gas we also vary the density n_0 of the background gas. Combining the control over background atom Rydberg states and background gas densities allows us to manipulate excitation transport even with a disordered background gas, as detailed in Secs. 2.4.2 and 2.4.3.

Putting everything together

Assembling the Hamiltonians of aggregate (Eq. (2.41)), background gas (Eqs. (2.44) and (2.46)), and their mutual interaction (Eq. (2.47)), as well as the Lindblad superoperators of the background atoms (Eq. (2.45)), we arrive at the many-body master equation

$$\dot{\rho}(t) = -i[\mathcal{H}_{\mathrm{agg}} + \mathcal{H}_{\mathrm{agg\text{-}bg}} + \mathcal{H}_{\mathrm{bg}} + \mathcal{H}_{\mathrm{bg,int}}, \rho(t)] + \mathcal{L}[\rho(t)]. \tag{2.49}$$

The master equation (2.49) constitutes the basis for calculations in this chapter.

We stress that while the numerical calculations performed in the following depend (via the dispersion coefficients of the Rydberg interactions) on the state choices we made, the concepts underlying our proposal do not. Similar results to the ones presented in this thesis may be obtained using state or parameter choices different to the ones employed here. On that account we list the conditions that need to be met by any viable state or parameter choice in the subsequent sections. The main focus of these sections, though, lies on substantiating our proposal by showing its feasibility with experimentally accessible parameters.

---

[6] Due to nearly resonant process $|43p\rangle + |38s\rangle \leftrightarrow |41d\rangle + |38p\rangle$ resulting in a small Förster defect, $V^{(pr)}$ has several significant dispersion coefficients. The R^{-4} form has been chosen to reproduce the same critical radius $R_{\mathrm{c,p}}$ as the full interaction for our parameters [64].

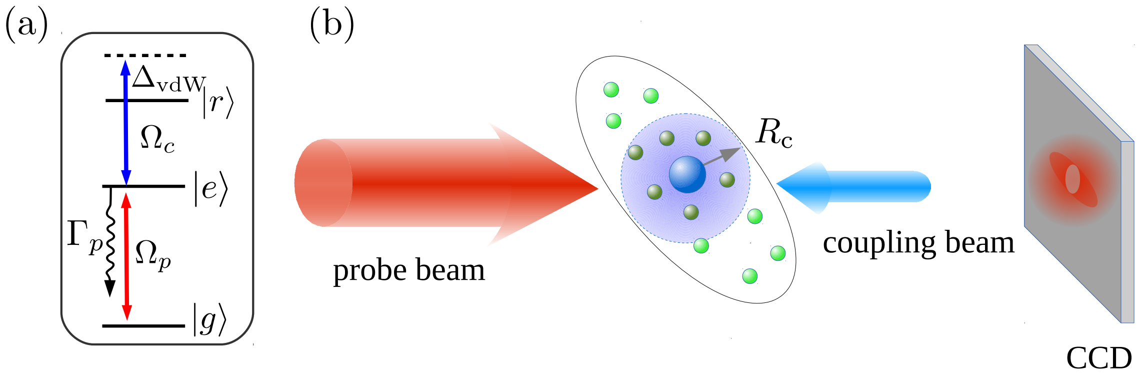

Figure 2.9: Sketch of the imaging setup we have in mind. (a) Level scheme of the background gas atoms. The interaction-induced energy shift Δ_{vdW} shifts the Rydberg level $|r\rangle$ out of resonance. (b) An ultracold atomic cloud is illuminated by a probe and a coupling laser beam, which are counter-aligned. Background atoms with a distance smaller than the critical radius R_{c} to the Rydberg excitation absorb the probe beam light while atoms with larger distances are transparent to the probe beam. A CCD camera detects the difference in probe beam absorption.

2.3 Imaging excitation transport

In this section we show that excitation transport within the aggregate can be imaged using the optical response of the background gas. Our setup thus provides an intrinsic means to obtain information on the aggregate state. This is important since we are only interested in the aggregate dynamics in this chapter.

The idea relies on the proposal of Ref. [77] (see also Ref. [82]), which has been recently employed in Ref. [81] to observe diffusive dipole-mediated energy transport in an ultracold Rydberg gas. With the help of Fig. 2.9, this imaging scheme can be summarized as follows: Consider a single Rydberg excitation that is embedded in a background gas, visualized in Fig. 2.9(b). The background gas is in an EIT configuration shown in Fig. 2.9(a), with the $|r\rangle$ state being a Rydberg state. Due to the interaction with the existing Rydberg excitation, the Rydberg states of the background gas atoms are shifted out of resonance within a sphere with radius R_{c}, rendering the background gas absorbing to the probe beam. Atoms outside the blockade sphere are transparent to the probe beam (EIT effect). If the probe beam intensity after propagation through the atomic cloud is measured by a CCD camera, an intensity drop of the transmitted probe beam light (absorption shadow) can be measured around the existing Rydberg excitation. This allows one to obtain information about the position of the existing Rydberg excitation. We note that such a setup can also be used to measure the initial Rydberg population in an atomic cloud [210] or even to reconstruct the full density matrix of the background gas atoms [187].

There are, of course, other ways than imaging to experimentally access the aggregate state, such as spatially-resolved field ionization [211] or fluorescence imaging [52, 196, 212, 213]. The reason we suggest using EIT-imaging of the aggregate dynamics nonetheless is to stress the versatility of the setup: by the same means, excitation transport can be measured *and* manipulated. This is the appeal of our setup. For the proposals of Secs. 2.5 and 2.6, where we use only a small number of background atoms, other means than imaging are in fact better suited to extract information on the aggregate state.

To be able to monitor excitation transport in our aggregate, the timescales associated with aggregate dynamics, image acquisition and aggregate lifetime have to be compatible. This leads to constraints regarding laser parameters, aggregate spacing, and background gas density.

Table 2.2: Parameter set for optical aggregate monitoring.

Variable	Symbol	Numerical value
Number of aggregate atoms	N_{agg}	11
Aggregate spacing	d	19 μm
Probe Rabi frequency	Ω_p	$2\pi \times 1.3$ MHz
Probe laser detuning	Δ_p	0 MHz
Coupling Rabi frequency	Ω_c	$2\pi \times 30$ MHz
Coupling laser detuning	Δ_c	0 MHz
Radiative decay rate	Γ_p	$2\pi \times 6.1$ MHz
Lifetime of state $\lvert s\rangle^a$	$\tau_{\lvert s\rangle}$	87 μs
Lifetime of state $\lvert p\rangle^a$	$\tau_{\lvert p\rangle}$	159 μs
Background gas density	n_0	3.8×10^{18} m^{-3}
Background gas Rydberg state	$\lvert r\rangle$	—
Number of photons per image	N_{phot}	100

[a] The lifetimes are calculated according to Ref. [72] for zero temperature $T = 0$, not taking black-body radiation-induced depopulation of the Rydberg level into account.

We address these constraints in Sec. 2.3.1 and detail parameters for which we expect imaging to be feasible. Exemplary numerical results also shown in this section support the feasibility of imaging in our setup. It turns out that the imaging process does not leave the aggregate dynamics unaffected. In fact, the measurement on the aggregate state performed via imaging induces decoherence in the aggregate dynamics. This measurement-induced decoherence is the topic of Sec. 2.3.2.

2.3.1 Using the environment as a probe

Parameter constraints

For our proposal to be experimentally accessible, we need a realistic set of parameters for which imaging can be achieved. This set of parameters has to comply with several constraints. The first set of constraints are imposed by the feasibility of imaging, viz. the feasibility of extracting meaningful information about the excitation distribution in the aggregate. The second set of constraints concerns the validity of our modeling. In this regard, we have to revisit several assumptions (such as the neglect of atomic motion) made during the derivation of the equations (2.33) and (2.49) and assess whether they still hold for the chosen parameters.

Our discussion is based on a chosen set of parameters, listed in Tab. 2.2. We show that this parameter set indeed fulfills the given constraints. We do so by deriving the quantities, on which the imaging constraints are imposed, from our chosen set of parameters and verify that they comply with the given constraints. A summary of these derived quantities is listed in Tab. 2.3. By fleshing out the dependence on the derived quantities on the various parameters we also discuss the possibility of alternative parameter choices.

Feasibility of imaging

In order for the aggregate dynamics to be imageable, the timescales relating to background atom dynamics, aggregate dynamics, and imaging have to be compatible. Introducing the measurement time τ_{imag}, the time required to take an image, and the aggregate lifetime τ_{agg}, we first of all need $\tau_{\text{imag}} < \tau_{\text{agg}}$. An even tighter bound on τ_{imag} is given by the condition that τ_{imag} has to be smaller than the hopping time τ_{hop}, which denotes the timescale on which a single Rydberg excitation significantly moves through the aggregate. Lastly, the background

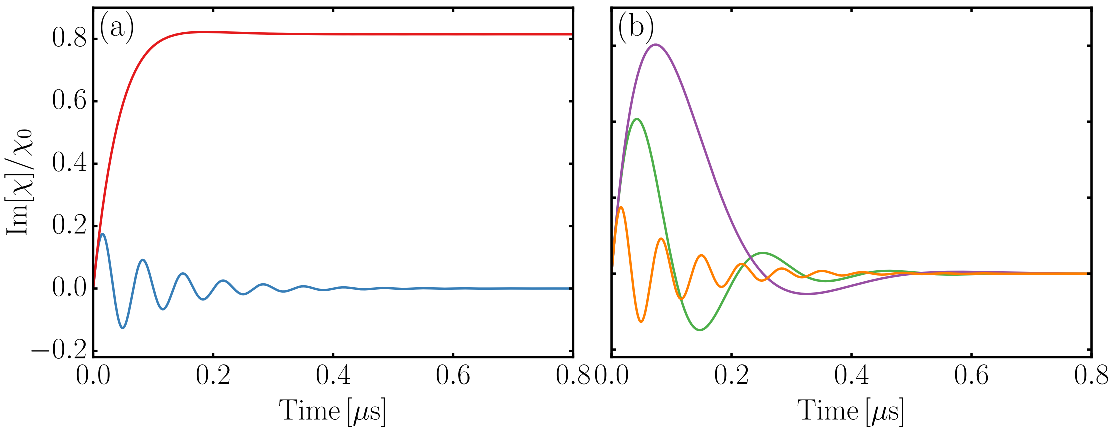

Figure 2.10: Time dependence of Im[χ], normalized to the two-level resonant susceptibility χ_0, for different parameters sets. (a) Effect of interaction-induced detuning on the EIT dynamics, comparing resonant (solid blue) and off-resonant ($\Delta_c/(2\pi) = 200$ MHz, solid red) dynamics, both using $\Omega_p/(2\pi) = 1.3$ MHz, $\Omega_c/(2\pi) = 30$ MHz, and $\Gamma_p/(2\pi) = 6.1$ MHz. (b) Effect of the coupling Rabi frequency on resonant EIT dynamics. The three curves correspond to the sets ($\Omega_c/(2\pi) = 30$ MHz, orange), ($\Omega_c/(2\pi) = 10$ MHz, green), and ($\Omega_c/(2\pi) = 5$ MHz, purple), all using $\Omega_p/(2\pi) = 0.2$ MHz and $\Gamma_p/(2\pi) = 6.1$ MHz.

gas atoms need to adiabatically follow the aggregate dynamics. In particular, the timescale on which the background atoms reach their steady state after the probe and coupling lasers have been turned on — the EIT equilibration time τ_{EIT} — has to be small compared to the imaging time τ_{imag}. This condition is required for consistency, since a direct connection (i.e., without solving the Maxwell-Bloch equations) between the absorption of the probe laser and the susceptibility of the background atomic medium is only given in the steady state of the atomic medium (see Sec. 2.2.4 and Ref. [161]).[7] Consequently, any set of parameters has to ensure that

$$\tau_{\mathrm{EIT}} < \tau_{\mathrm{imag}} < \tau_{\mathrm{hop}} < \tau_{\mathrm{agg}}. \tag{2.50}$$

We first consider the shortest timescale, the EIT equilibration time τ_{EIT}. This is the timescale on which the background atoms adapt their optical response to a given interaction-induced energy shift of the Rydberg level once probe and coupling have been turned on. To assess τ_{EIT}, we evaluate the atomic susceptibility for two different values of the coupling laser detuning Δ_c, namely $\Delta_c = 0$ MHz and $\Delta_c/(2\pi) = 200$ MHz. Here, zero detuning corresponds to resonant excitation with negligible interaction-induced energy shift of the Rydberg level; large detuning corresponds to an interaction-induced energy shift larger than the EIT width γ_{EIT} (cf. Sec. 2.2.4). From the equilibration dynamics of the atomic susceptibility we then estimate the EIT equilibration time τ_{EIT}. Note that, for a given state choice, this timescale only depends on the laser parameters Ω_p and Ω_c.

In Fig. 2.10(a) we show the time dependence of Im[χ]/χ_0 of a single background atom using the laser parameters listed in Tab. 2.2, for $\Delta_c = 0$ MHz (blue curve) and $\Delta_c/(2\pi) = 200$ MHz (red curve). The envelope of the blue curve can be fitted by a monoexponential, yielding $\tau_{\mathrm{EIT}} \approx 0.1$ μs. Albeit the optical response reaches its steady state only after $t \gtrsim 0.5$ μs, a measurement performed at earlier times with a finite measurement time $\Delta t > 0.1\ \mu$s will carry only a small error due to the oscillating nature of $\mathrm{Im}[\chi]/\chi_0$. For a large detuning $\Delta_c/(2\pi) = 200$ MHz of the Rydberg state, the optical response reaches its steady state at $t \gtrsim 0.13\ \mu$s, but with a small $\approx 5\%$ error at $0.1\ \mu$s. We thus estimate the EIT equilibration time as $\tau_{\mathrm{EIT}} \approx 0.1\ \mu$s for the laser parameters listed in Tab. 2.2.

---

[7] This condition can be relaxed for continuous measurement, i.e., if probe and coupling lasers are not switched off after the measurement time τ_{imag}. In this case, as long as the susceptibility of the background atomic medium adiabatically follows the excitation transport in the aggregate, imaging is feasible. Since the timescale of the adiabatic motion is set by τ_{hop} rather than τ_{imag}, the requirement for imaging is weaker here. Note, however, that as we show in Sec. 2.3.2, continuous measurement has certain disadvantages compared to “stroboscopic” measurement, in which the lasers are turned off after the measurement.

Figure 2.10(b) illustrates the dependence of τ_{EIT} on the coupling Rabi frequency Ω_c, for fixed $\Omega_p/(2\pi) = 0.2$ MHz and $\Gamma_p/(2\pi) = 6.1$ MHz. While decreasing the probe Rabi frequency does not strongly affect τ_{EIT} (cf. the blue curve in panel (a) with the orange curve in panel (b)), decreasing the coupling Rabi frequency results in a decreased frequency of the oscillations in $\mathrm{Im}[\chi]/\chi_0$ and a larger amplitude of this oscillation. Choosing smaller values for the coupling Rabi frequency is hence possible, provided that τ_{EIT} still fulfills $\tau_{\mathrm{EIT}} < \tau_{\mathrm{imag}}$. Choosing a larger coupling Rabi frequency is, by contrast, not desirable, since this leads to smaller differences in the critical radii $R_{\mathrm{c,p}}$ and $R_{\mathrm{c,s}}$ (cf. Eqs. (2.48)), which in turn impairs the imaging time τ_{imag}, as detailed below.

To estimate the imaging time τ_{imag}, we need to elaborate more about the experimental procedure we have in mind. Since the aggregate states are given by the two Rydberg states $|p\rangle$ and $|s\rangle$, which both induce absorption around their respective positions, the discrimination between the two states has to be achieved by employing the different sizes of the absorption shadows associated with the critical radii $R_{\mathrm{c,p}}$ and $R_{\mathrm{c,s}}$. Accordingly, determining the image differential between two images taken at the same time after preparation of the aggregate but (i) without a $|p\rangle$ excitation and (ii) with a $|p\rangle$ excitation present in the aggregate provides a means for discriminating between $|p\rangle$ and $|s\rangle$ excitation. Information about the excitation location, i.e., the location of the state $|p\rangle$, is hence only provided through the photons scattered by the background gas atoms that are situated in the spherical shell defined by $R_{\mathrm{c,s}} < R < R_{\mathrm{c,p}}$. In order to be experimentally accessible, the number of photons scattered by those atoms has to be large enough. Here we assume that $N_{\mathrm{phot}} = 100$ (proportional to CCD counts, assuming a detection efficiency of ≈ 1) is a sufficient number of scattered information-carrying photons for a single-shot image (i.e., during the imaging time τ_{imag}).

The scattering rate γ_{phot} of an absorbing background atom is given by the radiative decay rate Γ_p, weighted with the population in state $|e\rangle$, $\gamma_{\mathrm{phot}} = \Gamma_p \rho_{ee}$. Defining Δ as the interaction-induced detuning of the Rydberg state $|r\rangle$, the steady-state value $\tilde{\rho}_{ee}$ of the density matrix element ρ_{ee} reads as

$$\tilde{\rho}_{ee}(\Delta) = \frac{4\Delta^2\Omega_p^2}{4\Delta^2(\Gamma_p^2 + 2\Omega_p^2) + (\Omega_p^2 + \Omega_c^2)^2}. \tag{2.51}$$

For large detunings, $\Delta \to \infty$, Eq. (2.51) simplifies to

$$\tilde{\rho}_{ee}(\Delta \to \infty) = \frac{\Omega_p^2}{\Gamma_p^2 + 2\Omega_p^2} \simeq \frac{\Omega_p^2}{\Gamma_p^2}, \tag{2.52}$$

where the second simplification corresponds to the weak-probe assumption, namely keeping only terms up to second order in Ω_p. Denoting the number of background gas atoms within a sphere with radius $R_{\mathrm{c,s}}$ ($R_{\mathrm{c,p}}$) by $N_{\mathrm{bg,s}}$ ($N_{\mathrm{bg,p}}$), the imaging time τ_{imag} can be estimated via

$$\tau_{\mathrm{imag}} = \frac{N_{\mathrm{phot}}}{\gamma_{\mathrm{phot}}(N_{\mathrm{bg,p}} - N_{\mathrm{bg,s}})}. \tag{2.53}$$

Using the parameters listed in Tab. 2.3 (which have been derived from the chosen parameter set, Tab. 2.2), we obtain $\tau_{\mathrm{imag}} \approx 0.59\ \mu$s. Note that the imaging time depends on the Rabi frequencies Ω_p and Ω_c as well as the background gas density n_0. Short imaging times can be achieved for large background densities, large probe Rabi frequencies, and small coupling

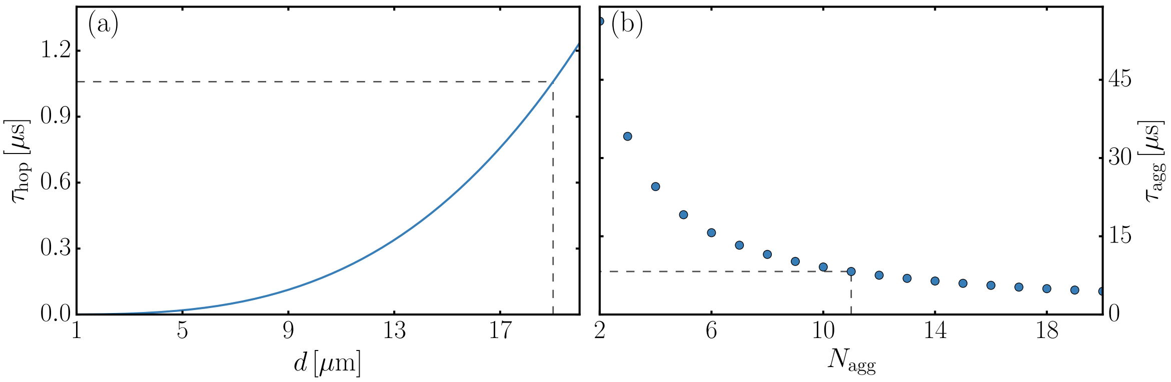

Figure 2.11: (a) Hopping time τ_{hop} as a function of the aggregate spacing d. (b) Aggregate lifetime τ_{agg} as a function of the number of aggregate atoms N_{agg}. The parameters chosen for the imaging proposal as well as the corresponding timescales are indicated with dashed, gray lines.

Rabi frequencies. Large values for both background density and probe Rabi frequency are restricted, however, by conditions regarding the validity of our modeling assumptions (see below). Our parameter choice therefore balances both requirements.

The timescale of significant redistribution of excitation in the aggregate we estimate via the hopping time τ_{hop}, i.e., the time it takes for the transition $|\pi_1\rangle \to |\pi_2\rangle$ in a diatomic aggregate (dimer). For a dimer, the dipole-dipole Hamiltonian coincides with the resonantly-driven two-level laser Hamiltonian, such that τ_{hop} can be estimated via the Rabi flopping time,

$$\tau_{\mathrm{hop}} = \frac{\pi}{2W}. \tag{2.54}$$

For the parameters of Tab. 2.2, Eq. (2.54) yields $\tau_{\mathrm{hop}} \approx 1.06\ \mu$s. Note that this is a rough estimate since the timescale for excitation transport in the aggregate actually depends on the interaction with the background gas atoms (see Sec. 2.4.2).

The hopping time only depends on the aggregate spacing d. This dependence is displayed in Fig. 2.11(a), with dashed, gray lines indicating our parameter choice. Significantly smaller aggregate spacings than the chosen one are restrained by the condition $\tau_{\mathrm{imag}} < \tau_{\mathrm{hop}}$.

The aggregate lifetime τ_{agg} can be calculated from the individual lifetimes of the $|p\rangle$ and $|s\rangle$ state listed in Tab. 2.2,

$$\tau_{\mathrm{agg}} = \left(\frac{N_{\mathrm{agg}} - 1}{\tau_{|s\rangle}} + \frac{1}{\tau_{|p\rangle}} \right)^{-1}. \tag{2.55}$$

In Figure 2.11(b) we illustrate this dependence of the aggregate lifetime on the number of aggregate atoms. With increasing aggregate size N_{agg}, the aggregate lifetime τ_{agg} decreases. Here we choose $N_{\mathrm{agg}} = 11$, for which $\tau_{\mathrm{agg}} \approx 8.2\ \mu$s. If no further post-selection is applied, only the short-time dynamics of the excitation transport can be experimentally probed for large aggregates. Post-selection implies that only those experimental measurements are included in the final analysis in which no aggregate atom has decayed during the experimental procedure. This allows one to experimentally access excitation dynamics of larger aggregate sizes at the cost of a increased number of experimental realizations.

Plugging in the timescales derived above and listed in Tab. 2.3 in Eq. (2.50), we find that the parameters of Tab. 2.2 are compatible with the constraints required by a feasible imaging procedure. We note that the comparison of time-scale constraints performed provides only a first, rough estimate of the feasibility of imaging. In a given experimental setup, the estimate needs to be refined, additionally considering the signal-to-noise ratio (cf. Refs. [77, 214]) as well as the optical resolution that can be achieved. We believe though that the proposed imaging procedure is within experimental reach.

Model validity

We continue by addressing the validity of our model assumptions, namely the neglect of (i) mutual Rydberg-Rydberg interactions in the background gas, (ii) motion of background Rydberg atoms due to attractive van der Waals forces, and (iii) aggregate lifetime-reducing effects pertaining to the high background-atom density.

(i) *Mutual Rydberg-Rydberg interactions in the background gas.* In our explanation of the imaging mechanism, and likewise in the derivation of the timescale estimates, we have not accounted for the interaction of background Rydberg atoms among themselves. We have done so assuming that the fraction of Rydberg excitations in the background gas is low, such that the absorption in the background gas is exclusively due to the interaction with the aggregate atoms, and not due to interactions with Rydberg-excited background gas atoms. To verify this assumption, we estimate the number of Rydberg excitations within the spherical shell defined by $R_{\mathrm{c,s}} < R < R_{\mathrm{c,p}}$. If the probability for a background-atom Rydberg excitation in this region is low, we can neglect the effect of background Rydberg excitations on the imaging procedure.

With this in mind we consider the steady-state value of the Rydberg state with interaction-induced detuning Δ,

$$\tilde{\rho}_{rr}(\Delta) = \frac{\Omega_p^2(\Omega_p^2 + \Omega_c^2)}{4\Gamma_p^2\Delta^2 + 8\Delta^2\Omega_p^2 + (\Omega_p^2 + \Omega_c^2)^2}. \tag{2.56}$$

In the absence of interaction ($\Delta = 0$), the Rydberg population reaches its maximum

$$p_r \equiv \tilde{\rho}_{rr}(\Delta = 0) = \frac{\Omega_p^2}{\Omega_p^2 + \Omega_c^2} \simeq \frac{\Omega_p^2}{\Omega_c^2}, \tag{2.57}$$

where the last relation follows in the weak-probe approximation, i.e., to second order in Ω_p. This allows us to define the blockade fraction f_{bl}, the number of Rydberg excitations within the spherical shell defined by $R_{\mathrm{c,s}} < R < R_{\mathrm{c,p}}$,

$$f_{\mathrm{bl}} = p_r n_0 \left(\mathrm{Vol}(R_{\mathrm{c,p}}) - \mathrm{Vol}(R_{\mathrm{c,s}})\right) \approx 0.18, \tag{2.58}$$

for the parameters of Tab. 2.2. Since f_{bl} is not well below one, there might be a small contribution of background Rydberg-Rydberg interactions to the measured background gas absorption, which require post-selection in experiment. To reduce f_{bl}, smaller probe Rabi frequencies can be employed, at the expense of a larger imaging time.

(ii) *Motion of background Rydberg atoms.* In contrast to $|ns, ns\rangle$ van der Waals interactions, which are repulsive over a wide range of principal quantum numbers ($n \lesssim 235$ for rubidium [151]), in our setup, the interaction between aggregate and background gas Rydberg states is attractive. Since the background gas atoms are not trapped in general, a Rydberg-excited atom created in the background gas can accelerate towards the aggregate, inducing unwanted effects such as the loss of an aggregate excitation due to atom-atom collision. Hence, the imaging time τ_{imag} has to be smaller than the collision time τ_{coll}, i.e., the time it takes until two Rydberg-excited atoms with initial separation $\bar{R}_0$ in an attractive pair-potential $V(R) = -|C_k|/R^k$ collide. For the following exemplary calculation, we assume van der Waals interaction $\propto R^{-6}$. The bare collision time τ'_{coll}, which is ignorant of the fact that background atoms are Rydberg-excited only with a small probability, can be estimated by using energy conservation [215, 216],

$$V(\bar{R}_0) = V(R) + \frac{m_{\mathrm{red}}}{2}\left(\frac{\mathrm{d}R}{\mathrm{d}t}\right)^2, \tag{2.59}$$

where $m_{\mathrm{red}} = m_{\mathrm{Rb}}/2$ is the reduced mass of rubidium. Separating variables in Eq. (2.59) and specifying van der Waals interaction $V(R) = -|C_6|/R^6$ allows us to evaluate

$$\tau'_{\mathrm{coll,s}} = \int_0^{\bar{R}_0} \frac{\mathrm{d}R}{\sqrt{2m_{\mathrm{Rb}}^{-1}(V(\bar{R}_0) - V(R))}} = \frac{\sqrt{\pi}\,\Gamma(2/3)}{2\,\Gamma(1/6)}\bar{R}_0^4\sqrt{\frac{m_{\mathrm{Rb}}}{|C_6|}} \approx 0.2156\bar{R}_0^4\sqrt{\frac{m_{\mathrm{Rb}}}{|C_6|}}. \tag{2.60}$$

Similarly, the collision time can be evaluated for the $\propto R^{-4}$ interaction of the $|p\rangle$ state, yielding $\tau'_{\mathrm{coll,p}} \approx 0.2995\bar{R}_0^3\sqrt{m_{\mathrm{Rb}}/|C_4|}$. As initial distance $\bar{R}_0$ between the Rydberg excitations we take the critical radius $R_{\mathrm{c,s}}$ for the $|s\rangle$ state and $R_{\mathrm{c,p}}$ for the $|p\rangle$ state. Note that the mean nearest-neighbor distance [217]

$$R_0 = \frac{1}{3}\left(\frac{3}{4\pi n_0}\right)^{1/3}\Gamma\left(\frac{1}{3}\right) \approx 0.35~\mu\mathrm{m} \tag{2.61}$$

is much smaller than both critical radii. The choice of the critical radius for the initial distance hence relies on the fact that background gas atoms with smaller separation from the aggregate than the critical radius experience a strong interaction-induced energy shift of the Rydberg level, which inhibits population of the Rydberg state.

Due to the small fraction of Rydberg excitations in the background gas, the quantity that we have to compare with the imaging time is the *dressed* collision time τ_{coll} rather than the bare collision time τ'_{coll}. The dressed collision time denotes the collision time with the C-dispersion coefficient multiplied by the probability to be in the Rydberg state [87, 93], utilizing the analogy with Rydberg dressing (see also Refs. [88, 90–92]). This can be seen by evaluating the expectation value of the aggregate-background interaction $\bar{V}_{n\alpha}\,|\pi_n\rangle\langle\pi_n|\,[|r\rangle\langle r|]_\alpha$ (cf. Eq. (2.47)) in the steady state of the background gas:

$$\mathrm{Tr}\{\bar{V}_{n\alpha}\,|\pi_n\rangle\langle\pi_n|\,[|r\rangle\langle r|]_\alpha\,\rho\} = p_r\bar{V}_{n\alpha}\,\mathrm{Tr}_{\mathrm{agg}}\{|\pi_n\rangle\langle\pi_n|\,\rho^{\mathrm{agg}}\}. \tag{2.62}$$

Here, $\mathrm{Tr}_{\mathrm{agg}}$ denotes the partial trace over the aggregate subspace, ρ^{agg} the aggregate density matrix, and p_r the population of the Rydberg state, defined in Eq. (2.57).

On account of the smaller critical radius $R_{\mathrm{c,s}}$ and the steeper potential slope, the collision time $\tau_{\mathrm{coll,s}}$ associated with the $|s\rangle$ state sets the relevant timescale (cf. Tab. 2.3). Calculating $\tau_{\mathrm{coll,s}}$ for our chosen parameter set, we find $\tau_{\mathrm{coll,s}} \approx 8.8~\mu$s, which is slightly larger than the aggregate lifetime. Since $\tau_{\mathrm{coll,s}}$ is the collision time for a single $|s\rangle$ excitation, the total lifetime of the aggregate will be further reduced. This necessitates post-selection or, alternatively, trapping of Rydberg atoms (cf. Ref. [218]).

(iii) *Reduction of Rydberg aggregate lifetime due to high background density.* If a Rydberg excitation with high principal quantum number is embedded in a high-density gas (or condensate) such that many ground state background gas atoms lie within a radius corresponding to the extent of the Rydberg electron wave function, scattering between the Rydberg electron and the ground state gas can lead to a reduction of the Rydberg state lifetime [121, 219]. To ensure that this effect is negligible in our setup, we calculate the number of background gas atoms in the spherical volume with radius given by the expectation value of the radial coordinate of the electron in state $|s\rangle$ and $|p\rangle$, respectively.

We find that for our parameters at most $N_{\mathrm{orb}} \approx 0.03$ atoms are enclosed in the Rydberg orbit. Hence we do not expect lifetime-reducing effects due to Rydberg electron scattering (in Ref. [121], significant lifetime reduction was observed for $N_{\mathrm{orb}} > 10^3$).

In addition, the high background gas densities pose questions concerning the validity of using dispersion coefficients for parameterizing Rydberg-Rydberg interactions[8]. As to this regard, we note that for the discrimination between $|p\rangle$ and $|s\rangle$ excitation via the background gas we need our modeling to be reliable *in the region between the critical radii*, since it is this region which facilitates imaging of the aggregate dynamics. This region is on the order of a μm (cf. Eq. (2.48)), and hence larger than the distances at which our modeling might be invalidated.

We further note that due to the high background atom density, the condition $|\chi| \ll 1$ is not generally fulfilled in our setup, i.e., not for arbitrary laser parameters. (This condition is required for the first-order Taylor expansion of the refractive index to be valid, i.e., for the imaginary part of the optical susceptibility to be proportional to the optical absorption of the laser beam, cf. Sec. 2.2.4.) For the laser parameters that we have chosen, however, aborting the Taylor expansion of the refractive index after the first term gives still a good approximation.

For an accurate modeling of an experimental imaging procedure for a three-dimensional background gas, also effects pertaining to beam propagation have to be accounted for in principle. For simplicity, we have not considered these effects, which depend on the specific experimental setup. For a quasi-two-dimensional background gas surrounding the Rydberg aggregate, for instance, such effects do not play a role.

Table 2.3 completes our discussion of parameter constraints for imaging, summarizing the quantities employed to estimate the feasibility of an experimental realization of excitation transport imaging. We conclude that the parameters listed in Tab. 2.2 fulfill the constraints developed above.

Note that an measurement scheme for excitation dynamics in the Rydberg aggregate is not restricted to the proposed imaging setup. In particular, other atomic states can be used for the imaging, given that the constraints detailed above are fulfilled. (For example, states with repulsive interactions between aggregate and background atoms are not subject to the restrictions related to attractive interactions between aggregate and background atoms.) In addition, one could imagine to place the background atoms on a lattice, at a distance R fulfilling $R_{\mathrm{c,s}} < R < R_{\mathrm{c,p}}$. In such a way, imaging efficiency could be improved.

Exemplary numerical results

To illustrate the imaging of excitation transport via the background gas, we now consider an exemplary numerical solution of the full master equation (2.49) for $N = 3$ aggregate atoms and four background gas atoms in a one-dimensional geometry. The aggregate atoms are placed on a linear chain with equidistant spacing $d = 19$ μm, in accordance with the parameter set listed in Tab. 2.2.

To mimic the high background density $n_0 = 3.8 \times 10^{18}$ m^{-3}, one would need to account for a large number of background atoms in principle. This is intractable numerically, owing to the exponential scaling of the Hilbert space associated with the background gas atoms. To include

---

[8] For an atom in the ^{87}Rb $|43s_{1/2}\rangle$ state and another in the $|38s_{1/2}\rangle$ state, the LeRoy radius above which exchange effects can be neglected is $R_{\mathrm{LR}} \approx 0.33$ μm, for two atoms in the $|38s_{1/2}\rangle$ state, $R_{\mathrm{LR}} \approx 0.29$ μm. Moreover, for small interatomic distances ($< \mu$m for the states considered), states get strongly mixed such that perturbation theory, on which the notion of dispersion coefficients relies [151], can no longer be applied.

Table 2.3: Summary of the quantities employed to estimate the feasibility of an experimental realization of excitation transport imaging using the parameters of Tab. 2.2.

Variable	Symbol	Expression	Numerical value
Hopping time	τ_{hop}	$\pi/2 \times 1/W$	1.1 μs
Aggregate lifetime	τ_{agg}	$((N_{\text{agg}}-1)/\tau_{\|s\rangle} + 1/\tau_{\|p\rangle})^{-1}$	8.2 μs
EIT width[a]	γ_{EIT}	$\simeq \Omega_c^2/\Gamma_p$	$2\pi \times 142$ MHz
Critical radius for $\|p\rangle$	$R_{\text{c,p}}$	$(2\|C_{4,rp}\|\Gamma_p/\Omega_c^2)^{1/4}$	1.93 μm
Critical radius for $\|s\rangle$	$R_{\text{c,s}}$	$(2\|C_{6,rs}\|\Gamma_p/\Omega_c^2)^{1/6}$	1.03 μm
Blockade volume	$\text{Vol}(R)$	$4\pi R^3/3$	
Blocked atoms around $\|p\rangle$	$N_{\text{bg,p}}$	$n_0\text{Vol}(R_{\text{c,p}})$	17
Blocked atoms around $\|s\rangle$	$N_{\text{bg,s}}$	$n_0\text{Vol}(R_{\text{c,s}})$	115
Photon scattering rate[a]	γ_{phot}	$\simeq \Omega_p^2/\Gamma_p$	$2\pi \times 0.25$ MHz
Imaging time[b]	τ_{imag}	$N_{\text{phot}}(\gamma_{\text{phot}}(N_{\text{bg,p}} - N_{\text{bg,s}}))^{-1}$	0.6 μs
EIT equilibration time	τ_{EIT}	Fitted	≈ 0.1 μs
Bg. Rydberg fraction[a]	p_r	$\simeq \Omega_p^2/\Omega_c^2$	0.002
Bg. blockade fraction	f_{bl}	$p_r n_0(\text{Vol}(R_{\text{c,p}}) - \text{Vol}(R_{\text{c,s}}))$	0.18
Mean NN distance	R_0	$\frac{1}{3}\left(\frac{3}{4\pi n_0}\right)^{1/3}\Gamma(1/3)$	0.35 μm
Min. dist. between $\|r\rangle$, $\|s\rangle$	$\bar{R}_{0,s}$	$\max[R_0, R_{\text{c,s}}]$	1.03 μm
Bare $\|s\rangle$ collision time	$\tau'_{\text{coll,s}}$	$0.2156\bar{R}_{0,s}^4\sqrt{m_{\text{Rb}}/\|C_{6,rs}\|}$	0.4 μs
Bg. $\|s\rangle$ collision time	$\tau_{\text{coll,s}}$	$0.2156\bar{R}_{0,s}^4\sqrt{m_{\text{Rb}}/(\|C_{6,rs}\|p_r)}$	8.8 μs
Min. dist. between $\|r\rangle$, $\|p\rangle$	$\bar{R}_{0,p}$	$\max[R_0, R_{\text{c,p}}]$	1.93 μm
Bare $\|p\rangle$ collision time	$\tau'_{\text{coll,p}}$	$0.2995\bar{R}_{0,p}^3\sqrt{m_{\text{Rb}}/\|C_{4,rp}\|}$	1.0 μs
Bg. $\|p\rangle$ collision time	$\tau_{\text{coll,p}}$	$0.2995\bar{R}_{0,p}^3\sqrt{m_{\text{Rb}}/(\|C_{4,rp}\|p_r)}$	23 μs
Aggregate Rydberg orbit	$\langle r\rangle_{\text{agg}}$	$\max[\langle r\rangle_{\|43p\rangle}, \langle r\rangle_{\|43s\rangle}]$	0.13 μm
Bg. atoms in orbit	N_{orb}	$\text{Vol}(\langle r\rangle_{\text{agg}})n_0$	0.03

[a] Numerical values calculated using the exact expressions. The expressions in the table are derived in weak-probe approximation up to second order in Ω_p.

[b] Here we assume that all scattered photons can be detected. For a more precise estimate, this needs to be further weighted by the solid angle covered by the detector.

effects pertaining to small interatomic distances between the background gas atoms that would occur in a high-density gas nevertheless, we distribute the four background gas atoms in pairs of two with interatomic separation $\Delta R \approx 0.3$ μm. Such an interatomic separation corresponds approximately to the mean nearest-neighbor distance in the dense gas (cf. Tab. 2.3). Specifically, we randomly distribute two background atoms with uniform distribution in an interval extending $d/2$ to the left (right) of the first (third) aggregate atom. The remaining two background atoms are placed at a distance ΔR from the distributed background atoms each. Distributing the background gas atoms in pairs allows us to include the effect of significant interactions between background atoms on the imaging. (The Rydberg-Rydberg interactions between two background gas atoms with interatomic separation $\Delta R \approx 0.3$ μm yields $V^{(rr)}(\Delta R)/(2\pi) \approx 730$ GHz.)

We solve the master equation (2.49) via a stochastic unraveling, namely via the Monte-Carlo wave function method (also called quantum jump method) [163, 220–223]. In general, a stochastic unraveling of the master equation allows to access larger Hilbert spaces than the density matrix formalism, since the density matrix is an object of size $\bar{n}^2$ where $\bar{n}$ is the dimension of the underlying Hilbert space. In our case, the Hilbert space is $\bar{n} = 3^4 \times 3 = 243$ dimensional. Furthermore, a stochastic approach is easily implemented on a parallel architecture because different stochastic realizations (viz., trajectories) of the dynamics are independent.[9]

From the stochastic trajectories, the exact master equation result is obtained by averaging over a large ensemble of stochastic realizations. In the numerical implementation employed in this section, we use a fixed numerical time step of $\delta t = 5 \times 10^{-4}$ μs and calculate 150 stochastic realizations for each of the $\sim 10^4$ random distributions of background gas atoms. The average optical susceptibility of the background gas $\chi(x,t)$ we approximate by spatial binning of the individual susceptibilities $\chi_\alpha(t)$ of the background atoms,

$$\chi_\alpha(t) = \frac{\Gamma_p}{\Omega_p}\,\mathrm{Tr}\{[|g\rangle\langle e|]_\alpha\,\rho\}, \tag{2.63}$$

according to

$$\chi(x,t) = \left(\sum_{\alpha,\aleph} \delta_{x,x_\alpha^{(\aleph)}}\,\mathrm{Tr}\left\{\frac{\Gamma_p}{\Omega_p}\,[|g\rangle\langle e|]_\alpha\,\rho^{(\aleph)}(t)\right\}\right) \Big/ \sum_\alpha \delta_{x,x_\alpha^{(\aleph)}}. \tag{2.64}$$

Here, $\delta_{x,x_\alpha^{(\aleph)}}$ is 1 only if atom α in stochastic realization $\aleph$ is positioned in the interval $[x - \Delta x/2, x + \Delta x/2)$ with bin size Δx.

To monitor the excitation transport in the aggregate, we follow the procedure typically employed in experiments in which single Rydberg excitations are imaged [77, 81, 187]. There, to account for residual absorption and spatial inhomogeneity of the laser beams, besides the image with a Rydberg excitation present, a reference image without Rydberg excitation is taken, and the location of the Rydberg excitation is determined from the image differential. Similarly, we here infer the location of the $|p\rangle$ state by subtracting a reference signal $\chi_{\mathrm{ref}}(x,t)$ corresponding to the absorption of an empty aggregate (chain of only $|s\rangle$ states) from $\chi(x,t)$. The susceptibility $\chi_{\mathrm{ref}}(x,t)$ we calculate from an initial state in which all aggregate (background) atoms are in the $|s\rangle$ ($|g\rangle$) state; the susceptibility $\chi(x,t)$ we determine from an initial state in which the aggregate is prepared in state $|\pi_1\rangle$ and all background atoms are in their ground state $|g\rangle$.

Figure 2.12 shows the resulting signal $\mathrm{Im}[\chi(x,t) - \chi_{\mathrm{ref}}(x,t)]/\chi_{\mathrm{2lvl}}$. The green lines indicate the positions x_n of the three aggregate atoms and their thickness the corresponding $|p\rangle$ populations $p_n(t)$. Starting from an excitation localized at the leftmost aggregate atom ($|\pi_1\rangle$ state), the $|p\rangle$ excitation travels through the aggregate, with almost perfect excitation transfer to the rightmost atom ($|\pi_3\rangle$ state) at $t \approx 1.5$ μs and recovery of the initial $|\pi_1\rangle$ state at $t \approx 3$ μs. The resulting spatially-resolved absorption signal is shown in color coding. After a short transient at $t \lesssim 0.2$ μs on which EIT establishes — visible via fringes in the color-coded signal shown in Fig. 2.12 —, the absorption signal adiabatically follows the excitation dynamics. This implies that the absorption signal is directly linked to the probability distribution $p_n(t) = \mathrm{Tr}\{\rho\,|\pi_n\rangle\langle\pi_n|\}$ of the excitation. Consequently, background-background interactions $V_{\alpha\beta}^{(rr)}$ are relatively benign for the chosen states and densities.

---

[9] For reasons of numerical efficiency, we cut off state energies at $E_{\mathrm{cutoff}} = 600$ MHz. This still amounts to a full Rydberg blockade, but allows us to avoid using an infinitesimal numerical time step in the propagation. That is, for our numerical implementation to be valid, the non-Hermitian Hamiltonian (more precisely, the modulus of the largest eigenvalue of the Hamiltonian) multiplied with the numerical time step δt has to be small compared to one [163, 222]. Since we use a fixed time step for the propagation, this implies that for large interaction-induced state energies the numerical time step has to be infinitesimal small, rendering the numerical procedure intractable. We hence employ an energy cutoff at E_{cutoff}.

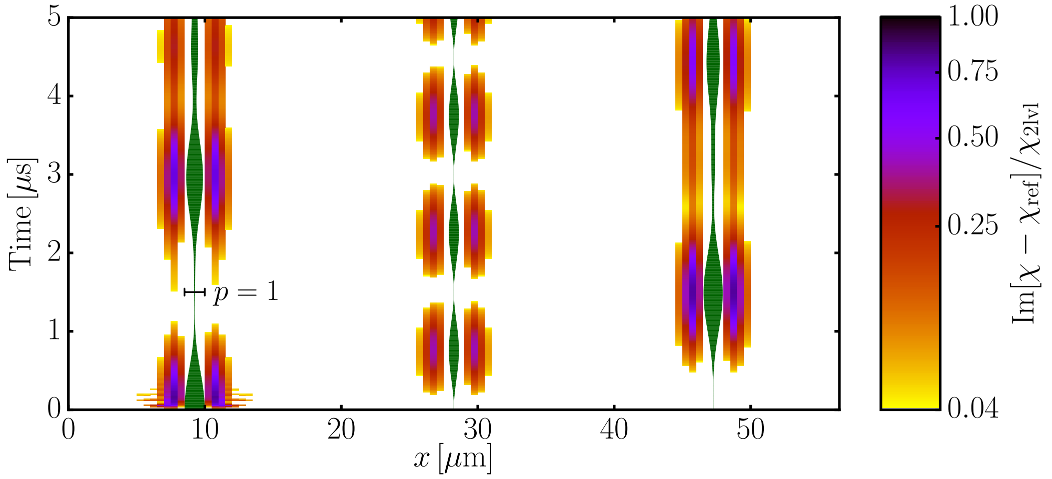

Figure 2.12: Difference in optical response between dynamic and empty aggregate $\mathrm{Im}[\chi(x,t) - \chi_{\mathrm{ref}}(x,t)]$ during transport, normalized by the two-level response $\chi_{2\mathrm{lvl}}$ (cf. main text). Green lines indicate the locations x_n of the aggregate atoms and their thickness the populations $p_n(t)$. The spatial bin size is $\Delta x = 0.5$ μm. Apart from $\Omega_p/(2\pi) = 0.2$ MHz, the parameters are as listed in Tab. 2.2.

We note that the difference in susceptibilities $\mathrm{Im}[\chi(x,t) - \chi_{\mathrm{ref}}(x,t)]$ in Fig. 2.12 is not normalized by χ_0 but rather by $\chi_{2\mathrm{lvl}}$,

$$\chi_{2\mathrm{lvl}} = \chi_0 \frac{\Gamma_p}{\Omega_p} \mathrm{Im}[\tilde{\rho}_{ge}] = \chi_0 \frac{\Gamma_p^2}{\Gamma_p^2 + \Omega_p^2}. \tag{2.65}$$

This expression is more general than χ_0, since it is not only valid in the weak-probe limit, in which $\Gamma_p \gg \Omega_p$. In the simulation shown in Fig. 2.12, however, $\chi_{2\mathrm{lvl}}$ and χ_0 are essentially identical since $\Omega_p/(2\pi) = 0.2$ MHz is sufficiently small, yielding $\chi_{2\mathrm{lvl}} \approx 0.999\chi_0$.

In the case of a background gas that adiabatically follows the aggregate dynamics, the susceptibilities of the individual background gas atoms can be directly related to the population dynamics in the aggregate. Introducing the steady-state susceptibility $\tilde{\chi}(\Delta)$ of a single background atom with detuning Δ of the Rydberg state,

$$\tilde{\chi}(\Delta) = \frac{\Gamma_p}{\Omega_p} \mathrm{Im}[\tilde{\rho}_{ge}(\Delta)], \tag{2.66}$$

the time-dependent absorption signal such as shown in Fig. 2.12 can be described by $\chi_\alpha(t) = \sum_n \tilde{\chi}(\bar{V}_{n\alpha}) p_n(t)$. Here, the detuning Δ accounts for the interaction $\bar{V}_{n\alpha}$ (defined below Eqs. (2.47)) between a background atom α and an aggregate atom in state $|\pi_n\rangle$. The steady-state value of the density matrix element $\tilde{\rho}_{ge}$ in Eq. (2.66) can be straightforwardly evaluated for a given set of laser parameters, yielding

$$\tilde{\rho}_{ge}(\Delta) = \frac{2\Delta\Omega_p(\Omega_c^2 - 2i\Gamma_p\Delta)}{4\Gamma_p^2\Delta^2 + 8\Delta^2\Omega_p^2 + (\Omega_p^2 + \Omega_c^2)^2}. \tag{2.67}$$

We conclude this section by noting that the proposed imaging scheme does not rely on the specific states chosen for the numerical simulation, particularly the R^{-4} interaction of the $|p\rangle$ state. The crucial property on which the scheme relies is the different sizes of the critical radii $R_{\mathrm{c,s}}$ and $R_{\mathrm{c,p}}$, which yield an experimentally resolvable difference in the absorption images, thus allowing for excitation transport imaging. Other state choices with different dispersion coefficients can be employed, as long as the chosen states feature distinguishable sizes of critical radii. For example, higher-lying Rydberg states with larger critical radii may be more advantageous for imaging applications.

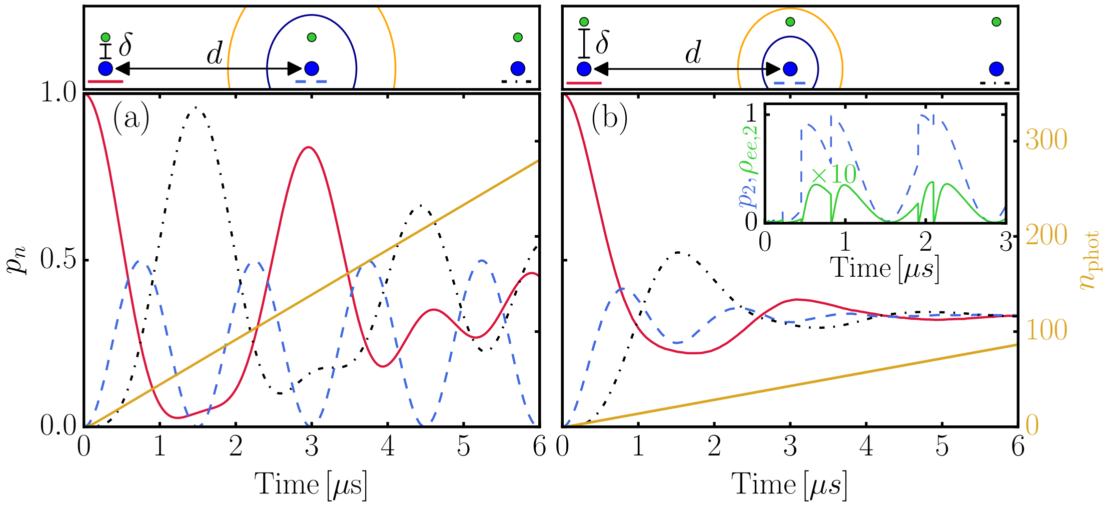

Figure 2.13: Exciton transport in a continuously monitored embedded Rydberg aggregate. Geometries are shown in the top panels, with the blue and orange circle indicating the critical radius $R_{\rm c,s}$ and $R_{\rm c,p}$, respectively. (a) Site occupations $p_n(t)$ for $n = 1, 2, 3$ (solid red, dashed blue, dot-dashed black) in a non-decohering case where $\delta = 0.55$ μm; other parameters are as listed in Tab. 2.2. The orange line counts the number of scattered photons $n_{\rm phot}(t)$. (b) The same for a strongly decohering case with $\delta = 1.5$ μm, other parameters as in (a). The inset shows aggregate and excited state $|e\rangle$ population at site 2 for a single stochastic (quantum jump) trajectory.

2.3.2 Measurement-induced dephasing

In the previous section, we have focused on the impact of the aggregate dynamics on the dynamics of the background gas atoms. In particular, we have shown that excitation transport in the aggregate can be measured using the intimate connection between the optical response of the background atoms in the vicinity of the aggregate and the state of the aggregate. In this section, we shift our focus to the back-action that measuring the aggregate state via the background gas has on the aggregate dynamics.

Measuring the aggregate state via the background gas induces dephasing of the aggregate dynamics. This effect could not be seen in Fig. 2.12, where we have chosen a small value for the probe Rabi frequency, $\Omega_p/(2\pi) = 0.2$ MHz. Such a small probe Rabi frequency does not comply with the parameter constraints required for experimentally accessible imaging, as detailed in Sec. 2.3.1. Hence, the aggregate is only "weakly" measured in this case. This indicates that the strength of the dephasing of the aggregate dynamics depends on the "strength" of the measurement, i.e., the amount of information on the aggregate state that is accessible via the optical response of the background gas atoms.

In fact, since a given background atom only provides significant information on the excitation location if it is located in a ring *between* the two critical radii $R_{\rm c,s} < R < R_{\rm c,p}$, we expect dephasing of the aggregate dynamics to strongly depend on the position of the background atoms. To demonstrate that this is indeed the case, we consider again a linear chain of $N = 3$ aggregate atoms (an experimental realization of which can be found in Ref. [52]), with a single background atom placed at a distance δ from each site, as shown in the top panels of Fig. 2.13. According to the previous reasoning, dephasing should occur only if the background atoms provide information on the excitation location. We thus examine two background atom configurations, in which, (a) the background atoms do not provide information on the aggregate state, and (b) the background atoms do provide information on the aggregate state.

(a) The background atoms are placed within the inner critical radius, $\delta < R_{\rm c,s} < R_{\rm c,p}$. Since the interaction between the Rydberg $|r\rangle$ state of the background atoms and both $|p\rangle$ and $|s\rangle$ states of the aggregate is large in this configuration, the background atoms scatter photons irrespective of the state of the aggregate. Although the number of scattered photons,

$$n_{\text{phot}}(t) = \Gamma_p \int \mathrm{d}t \sum_{\alpha} \mathrm{Tr}\left\{\rho(t)\left[|e\rangle\langle e|\right]_\alpha\right\}, \tag{2.68}$$

is large (cf. orange line in Fig. 2.13(a)), no information is provided by those photons. The aggregate dynamics in this case, also shown in Fig. 2.13(a), is the same as the one obtained without background atoms present. The population oscillations proceed coherently, which is best illustrated by the population p_2 of the $|\pi_2\rangle$ state, which exhibits undamped oscillations over the full time interval $[0, 6]$ μs.

(b) The background atoms are placed between the inner and the outer critical radius, $R_{\text{c,s}} < \delta < R_{\text{c,p}}$. Here, background atoms only scatter photons if the adjacent aggregate atom is in state $|p\rangle$; the scattered photons thus provide information on the aggregate state. Despite a smaller total number of scattered photons ($n_{\text{phot}}(6\ \mu\text{s}) \lesssim 90$ in this case as compared to $n_{\text{phot}}(6\ \mu\text{s}) \sim 280$ in case (a)), the dephasing of the aggregate dynamics is strong, as can be seen in Fig. 2.13(b). Already after $t = 6\ \mu$s, the $|p\rangle$ excitation is fully delocalized over the aggregate, with $p_1 = p_2 = p_3 = 1/3$.

The connection between information provided by the scattered photons and aggregate decoherence can be clearly seen in the quantum-jump unraveling of the full master equation. The inset of Fig. 2.13(b) shows for a single stochastic realization both the population p_2 of the second aggregate atom (dashed blue) and the $|e\rangle$ state population $\rho_{ee,2}$ of the second, adjacent background atom (solid green). The trajectory of the population $\rho_{ee,2}$ of the second background atom shows segments of continuous dynamics disrupted by discontinuous jumps, which correspond to the emission of a photon. Whenever a jump occurs in the background atom dynamics, the population p_2 of the aggregate also displays discontinuous behavior. Hence, photon emission directly affects the aggregate dynamics. Repeated measurement of the aggregate population induces dephasing, in the same way as the Lindblad operator describing dephasing of a certain state population is a projector onto this state [224]. (See Sec. 2.4.1 for details on the form of the Lindblad operator in the aggregate subspace that corresponds to the dephasing induced by a single background atom.) In literature, the link between measurement and measurement-induced decoherence is called *measurement-induced dephasing* [225].

We emphasize that this link between photon emission and discontinuous jumps in the aggregate state does not occur for the background atoms configuration shown in in panel (a). There, single trajectories (not plotted) show no effect of quantum jumps on the aggregate population.

Lastly, we comment on the implications of measurement-induced dephasing on aggregate dynamics imaging. Since measurement induces dephasing of the aggregate dynamics, a continuous measurement scheme is not well suited to study excitation transport within the aggregate, as the observed dynamics is partly induced by the measurement process itself. To obtain information on the aggregate state without strongly perturbing the aggregate dynamics, it is thus preferable to abandon continuous measurement and employ a "stroboscopic" measurement scheme instead. In a "stroboscopic" measurement scheme, a measurement would only be performed during the image acquisition stage of duration τ_{imag} (see Sec. 2.3.1). The time-resolution of the imaging would then arise from changing the waiting time between preparation of the initial aggregate state and image acquisition, in this way allowing for the monitoring of the aggregate dynamics with (discrete) spatial and temporal resolution. The imaging sequence would then be given by

1. Initialization of the aggregate (state preparation).
2. Free or background-controlled (cf. Secs. 2.4.2 and 2.4.3) aggregate evolution.
3. Image acquisition with duration τ_{imag}.

2.4 Simulating energy transport

Having shown the viability of excitation transport imaging, we now proceed with harnessing the flipside of the information on the aggregate state obtainable through the background gas, i.e., the decoherence introduced to the aggregate dynamics. The motivation behind this is to provide a model system for studying the transition from coherent to incoherent energy transport. In naturally occurring systems such as light harvesting complexes, energy transport always proceeds under the interplay between the fundamentally coherent transport and the coupling to the environment (cf. Refs. [44, 226–234]). To study the transition from coherent to incoherent exciton transport, Haken, Strobl, and Reinecker (HSR) introduced a theoretical model [235–239] that allows one to assess the impact of the different degrees of decoherence on the transport.

In this section, we show that our setup allows for an almost ideal realization of the HSR model. In particular, we show that energetic disorder and dephasing introduced by the interaction with the background gas atoms can be controlled by the parameters of the lasers driving the background atoms. Accordingly, the setup we propose allows not only to image quantum energy transport, but also to experimentally study the transition from coherent to incoherent energy transport. This will benefit the study of excitation transport in open systems [40, 239, 240], be it semi-conductors or light harvesting complexes. Note that for light harvesting complexes, extensions to exciton-vibrational coupling and non-Markovian environments may be required [11, 41, 43, 46, 226, 241]; we thus address the route towards non-Markovian aggregate dynamics in Sec. 2.5.

In Sec. 2.4.1 we derive an effective master equation for the aggregate alone, which furnishes a HSR-type model for excitation transport. This is essential, since the background gas used for providing decoherence to our aggregate consists of a large number of atoms, which impedes a numerical study of decoherence effects on excitation transport by means of the full master equation (2.49). We then show how the disorder and dephasing distributions, which introduce decoherence to the aggregate dynamics and modify the excitation transport, can be controlled via the background gas. Specifically, in Sec. 2.4.2 we discuss how Gaussian disorder and dephasing can lead to diffusive excitation transport whereas non-Gaussian disorder, which can cause transport of sub-diffusive kind, is studied in in Sec. 2.4.3.

2.4.1 Effective model for excitation transport

Even though excitation transport occurs only in the aggregate, in our current theoretical description we have to solve the full master equation for both aggregate and background gas if we want to theoretically study energy transport within the aggregate. For a background gas consisting of a large number of background atoms, this is infeasible due to the exponential size of the corresponding Hilbert space. For the theoretical study of excitation transport, we are therefore interested in an *effective* model for the aggregate alone, in which the properties of the background atoms enter only effectively, e.g., via energy shifts of the aggregate atoms or additional dephasing terms. Besides, such an effective model might provide physical insight into the aggregate dynamics that is concealed in the full description.

The derivation of reduced, effective descriptions of open quantum systems has been a long-standing problem, to which different routes have been developed. One prime route involves the use of Feshbach-Zwanzig projectors [242, 243], which separate the degrees of interest from the remaining degrees of freedom, which are treated as a bath. This allows for the derivation of the Nakajima-Zwanzig equation [3–5, 244], a generalized master equation in which approximations can be introduced in a systematic way. Other schemes employed to reduce the complexity of the theoretical description rely on adiabatic elimination [245–247]. Here, initially not occupied states that couple only weakly and non-resonantly to initially populated states are removed from the theoretical description of the initially populated states, leading to additional energy shifts and couplings of those states [245]. The formalism developed in Ref. [247] that we apply below relies on both techniques (Feshbach-Zwanzig projector formalism and adiabatic elimination).

In order to derive an effective master equation for the aggregate alone, we regard the ground state $|g\rangle$ of the background atoms as the state of interest for our theoretical description, with the excited $|e\rangle$ and Rydberg $|r\rangle$ states introducing merely perturbative corrections to the ground state dynamics. For the following reasons this point of view seems justified in the *regime of electromagnetically induced transparency*, which we delimit via the conditions for the laser parameters reading $\Delta_p = \Delta_c = 0$, $\Omega_p \ll \Omega_c$, and $\Omega_p \ll \Gamma_p$: (i) The steady state is reached on a timescale much shorter than the aggregate dynamics, warranting a background gas dynamics that adiabatically follows the aggregate dynamics. Using the quantities from Tab. 2.3, defined in Sec. 2.3.1, this is fulfilled via $\tau_{\text{EIT}} \ll \tau_{\text{hop}}$. (ii) The populations of Rydberg and excited state are generally small, both for no interaction-induced energy shift (cf. Eqs. (2.51) and (2.57) for $\Delta = 0$), as well as large interaction-induced energy shift of the Rydberg level (cf. Eqs. (2.52) and (2.56) for $\Delta \to \infty$). Here, the numerical values for the parameters of Tab. 2.2 and zero (infinite) interaction-induced detuning of the Rydberg state read $\tilde{\rho}_{ee}(\Delta = 0) = 0$ ($\tilde{\rho}_{ee}(\Delta \to \infty) \approx 0.04$) and $\tilde{\rho}_{rr}(\Delta = 0) \approx 0.002$ ($\tilde{\rho}_{rr}(\Delta \to \infty) = 0$).

Hence, we can derive an effective model for the aggregate in the EIT regime, assuming further that Rydberg-Rydberg interactions among the background atoms can be neglected (cf. the discussion in Sec. 2.3.1). The derivation is detailed in Appendix A.2. We find that the evolution of the *reduced* aggregate density matrix $\rho^{(\text{agg})} = \sum_{nm} \rho_{nm} |\pi_n\rangle\langle\pi_m|$ obeys

$$\dot{\rho}^{(\text{agg})} = -i[\mathcal{H}_{\text{agg}} + \mathcal{H}_{\text{eff}}, \rho^{(\text{agg})}] + \sum_\alpha \mathcal{L}_{L_{\text{eff}}^{(\alpha)}}[\rho^{(\text{agg})}], \tag{2.69}$$

with the respective effective operators in the case $\Delta_p = \Delta_c = 0$ and to second order in Ω_p reading as

$$\mathcal{H}_{\text{eff}} = \sum_n \left[\sum_\alpha \frac{\Omega_p^2}{\Omega_c^2} \frac{\bar{V}_{n\alpha}}{1 + (\bar{V}_{n\alpha}/V_c)^2} \right] |\pi_n\rangle\langle\pi_n| \,, \tag{2.70a}$$

$$L_{\text{eff}}^{(\alpha)} = \sum_n \left[\frac{\Omega_p}{\sqrt{\Gamma_p}} \frac{1}{i + V_c/\bar{V}_{n\alpha}} \right] |\pi_n\rangle\langle\pi_n| \,. \tag{2.70b}$$

The competing energy scales here are $\bar{V}_{n\alpha}$ as defined in Eq. (2.47), the overall interaction of the background atom α with the entire aggregate if the latter is in the state $|\pi_n\rangle$, and V_c, the critical interaction-induced Rydberg state detuning marking the transition from EIT transparency to absorption. In terms of the EIT width, V_c is defined as $V_c = \gamma_{\text{EIT}}/2 \approx \Omega_c^2/(2\Gamma_p)$.

In addition to the original aggregate Hamiltonian, the effective equation (2.69) for the reduced aggregate density matrix $\rho^{(\text{agg})}$ contains two new terms. One is the effective Hamiltonian (2.70a), which describes an energy shift of aggregate site n due to the interaction with the level $|r\rangle$ of the background atoms, weighted by the steady-state occupation of state $|r\rangle$

[cf. Eq. (2.57)]. Consequently, the states $|\pi_n\rangle$ where the $|p\rangle$ excitation is localized at different sites n experience different energy shifts, leading to site-energy *disorder* in the aggregate. The interpretation of Eq. (2.70a) in terms of energy shifts will be substantiated in more detail in Sec. 2.4.2.

The other term (2.70b) is a Lindblad term, whose real part accounts for the *dephasing* caused by background atom α. The dephasing strength is set by the two-level atom photon scattering rate $\gamma_{\text{phot}} \approx \Omega_p^2/\Gamma_p$ within the critical radius of an aggregate atom [cf. the discussion preceding Eq. (2.52)]. The imaginary part of the Lindblad term (2.70b) can be interpreted as contributing to the energy shift of the aggregate states, as will be discussed in Sec. 2.4.2. Note that the Lindblad term (2.70b) captures the dependence of the dephasing strength caused by a background gas atom on its location, which we discussed in Sec. 2.3.2. That is, a background atom positioned such that photons scattered from it do not provide information on the excitation location in the aggregate, viz. the aggregate state $|\pi_n\rangle$, does not contribute to aggregate decoherence. This can be seen by noting that if a background atom α is located within the inner critical radius such that $V_c \ll \bar{V}_{n\alpha}$ regardless of the excitation location n, the Lindblad term $L_{\text{eff}}^{(\alpha)}$ becomes proportional to a unit matrix and hence does not cause any decoherence (since $\mathcal{O}$ in the superoperator $\mathcal{L}_{\mathcal{O}}[\rho]$ commutes with ρ).

The effective equations (2.70) derived for the parameter regime of EIT are of particularly simple form, which enabled us to identify the contributions to disorder and dephasing caused by a single background atom α. The assumptions, however, under which the effective model was derived may also hold for parameters outside the EIT regime. Extending the effective model to allow for laser detunings, Eqs. (2.70) become Eqs. (A.25),

$$\mathcal{H}_{\text{eff}} = \sum_n \left[\sum_\alpha \frac{\Omega_p^2 \tilde{V}_{n\alpha}(\Omega_c^2 + 4\tilde{V}_{n\alpha}\Delta_p)}{\Omega_c^4 + 8\tilde{V}_{n\alpha}\Delta_p\Omega_c^2 + 4\tilde{V}_{n\alpha}^2(\Gamma_p^2 + 4\Delta_p^2)} \right] |\pi_n\rangle\langle\pi_n| \,, \tag{2.71a}$$

$$L_{\text{eff}}^{(\alpha)} = \sum_n \left[\frac{2i\tilde{V}_{n\alpha}\sqrt{\Gamma_p}\Omega_p}{2\tilde{V}_{n\alpha}(\Gamma_p - 2i\Delta_p) - i\Omega_c^2} \right] |\pi_n\rangle\langle\pi_n| \,, \tag{2.71b}$$

where we denote the total energy shift of the Rydberg level of background gas atom α induced by the aggregate in state $|\pi_n\rangle$ by $\tilde{V}_{n\alpha} = \bar{V}_{n\alpha} - \Delta_p - \Delta_c$. For details on the derivation of Eqs. (2.71), see Appendix A.2.

The relative contributions of disorder and dephasing terms can be controlled through the EIT laser parameters, as well as by choosing Rydberg states with different interactions. Note that the effective equation (2.69) furnishes a Haken-Strobl-Reineker type model [239] for excitation transport. All scenarios from dominant dephasing to dominant disorder can be realized by varying the intermediate state detuning Δ_p while keeping the two-photon detuning fixed: $\Delta_p + \Delta_c \approx 0$. In particular, for large intermediate state detunings Δ_p, the contribution of dephasing can be significantly reduced, as we will see in Sec. 2.4.3.

Validation of the effective equation

We now comment on the validity and the limitations of the effective equation (2.69), on which we rely in further calculations. For this purpose we again consider the setup we used for the illustration of measurement-induced dephasing in Sec. 2.3.2, namely a linear chain of $N = 3$ aggregate atoms with a single background atom placed at a distance δ from each site, as shown in the top panel of Fig. 2.14.

In Fig. 2.14(a) and (b) we show the same excitation transport dynamics as plotted in Fig. 2.13, but this time including the effective model results, which are indicated by color-matched diamonds. We see that both the case of strong dephasing, Fig. 2.14(b), as well as the case of no dephasing, Fig. 2.14(a), is well reproduced by the effective model (see panels

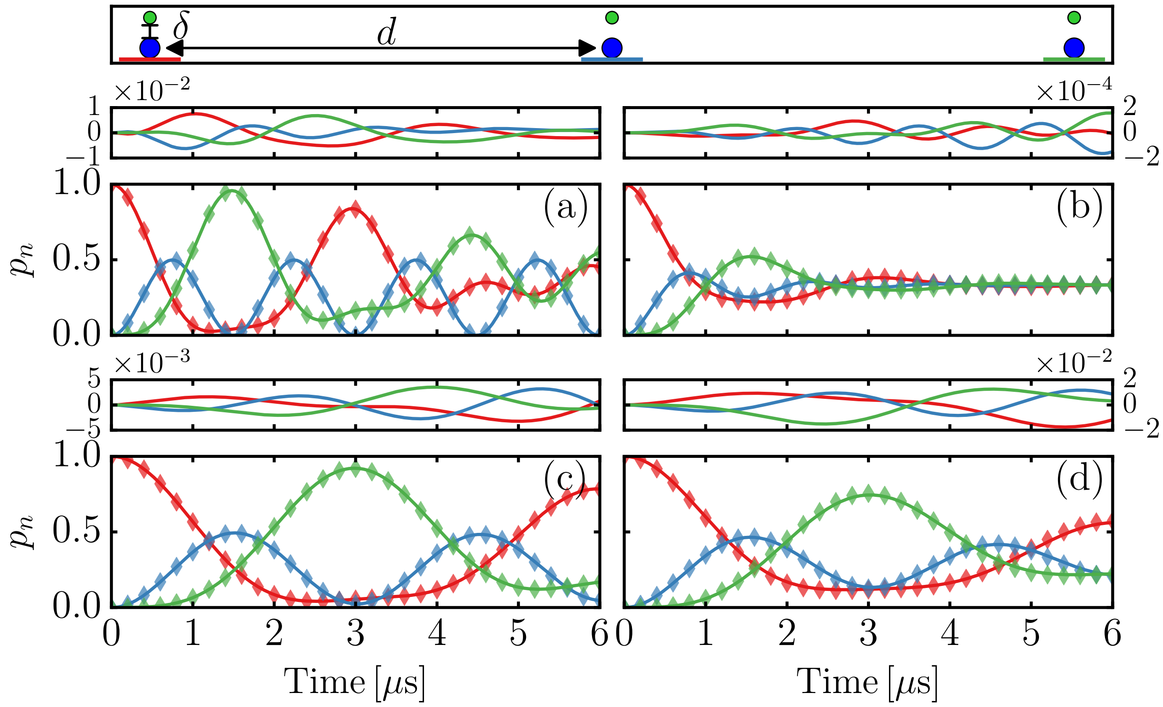

Figure 2.14: Comparison of site populations p_n plotted in red, blue, green for the populations of sites $n = 1, 2, 3$ obtained by the full master equation (2.49) [solid lines in (a)-(d)] and the effective model, Eqs. (2.69) and (2.71) [diamonds in (a)-(d)]. The geometry is shown in the top panel, the small panel above each labeled plot details the deviations $p_n - p_{n,\text{eff}}$ between full and effective equation. The first row (a)-(b) shows the cases previously depicted in Fig. 2.13 with parameters taken from Tab. 2.2, using $\delta = 0.55$ μm in (a) and $\delta = 1.5$ μm in (b). The plots shown in the second row (c)-(d) are obtained in the presence of an intermediate-state detuning $\Delta_p/(2\pi) = -20$ MHz with $\Omega_p/(2\pi) = 12$ MHz, $\Omega_c/(2\pi) = 90$ MHz, $\Gamma_p/(2\pi) = 6.1$ MHz, $d = 24$ μm and $\Delta_c/(2\pi) = 22$ MHz, $\delta = 0.53$ μm in (c) whereas $\Delta_c/(2\pi) = 20$ MHz, $\delta = 0.3$ μm in (d). Note that the Rydberg state of the background atoms is $|r'\rangle$ in panels (c) and (d), which has much smaller dispersion coefficients than the state $|r\rangle$ used in panels (a) and (b).

above (a) and (b), in which the deviations between effective model and full master equation are shown). This is in accordance with the conclusions drawn from the analytic form of Eq. (2.70b), i.e., that a background atom with large $\bar{V}_{n\alpha}$ does not introduce dephasing to the aggregate. Although excitation dynamics is shown only for two specific values of δ, also intermediate values yield good (albeit in some cases slightly worse) agreement with the full master equation, thus confirming the validity of the effective model for the parameter regime of Tab. 2.2.

In Fig. 2.14(c) and (d) we show excitation dynamics in a different regime that will become important later, namely the *two-photon excitation regime*, which we delimit via the following conditions on the laser parameters: $\Delta_p + \Delta_c \approx 0$, $\Omega_p < \Delta_p$, and $\Omega_p < \Omega_c$. These conditions are fulfilled by the parameters used in the figure, $(\Delta_p + \Delta_c)/(2\pi) = 2$ MHz, $\Delta_p/(2\pi) = -20$ MHz, $\Omega_p/(2\pi) = 12$ MHz and $\Omega_c/(2\pi) = 90$ MHz. Besides, instead of the state $|r\rangle$, the state $|r'\rangle$ is used as Rydberg state of the background atoms, leading to smaller interactions $V^{(pr)}(\delta) \approx -113$ MHz, $V^{(sr)}(\delta) \approx -28$ MHz in panel (c). The resulting dynamics, which is well reproduced by the effective model, is almost coherent. Figure 2.14(d) depicts excitation dynamics for larger interactions corresponding to smaller distances δ, for which stronger dephasing arises. Apart from small deviations around $t \simeq 6$ μs, the dynamics is again well

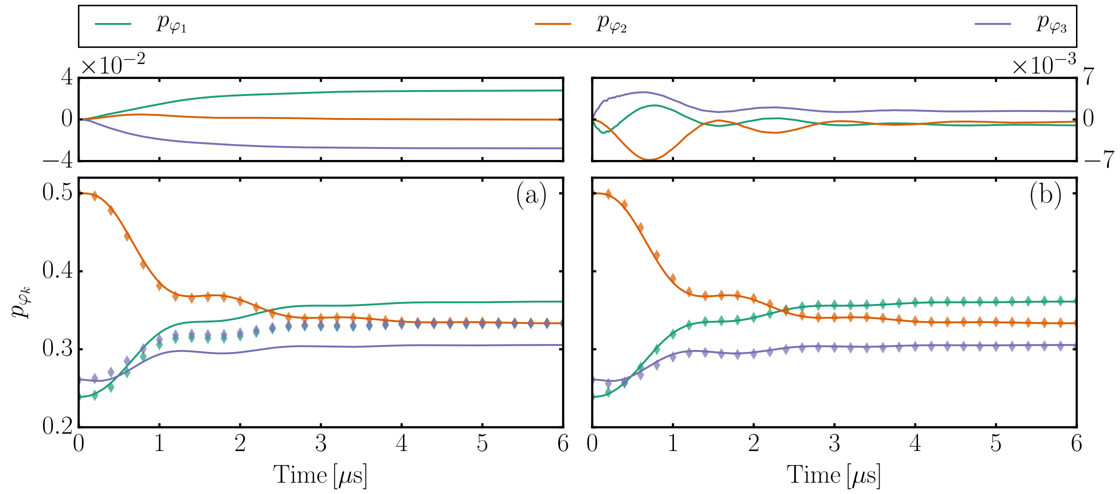

Figure 2.15: Populations p_{φ_k} of the aggregate eigenstates $|\varphi_k\rangle$ (with $E_{k-1} < E_k$) for the parameters of Fig. 2.14(b). Solid lines indicate solutions obtained by solving the full master equation (2.49). Color-matched diamonds show the results of the effective model (2.70) [panel (a)], as well as the extended model (2.73) [panel (b)]. The small panel above each labeled plot details the deviations $p_k - p_{k,\text{eff}}$ between full and effective (a) respectively extended effective (b) equation.

captured by the effective model.[10] We thus conclude that the effective model indeed reproduces the full master equation in the parameter regimes of both EIT and two-photon excitation.

To assess the limitations of the effective model, it is instructive to evaluate not only aggregate populations, but also coherences. We will do so by looking at the populations of the aggregate eigenstates. This allows us to determine to which degree coherences within the aggregate are captured by the effective model.

The aggregate eigenstates $|\varphi_k\rangle$ of the aggregate Hamiltonian are superpositions of the $|\pi_n\rangle$ states,

$$|\varphi_k\rangle = \sum_n c_{nk}\, |\pi_n\rangle\,. \tag{2.72}$$

For the $N = 3$ aggregate, on which we focus here in our comparison between effective equation and full master equation, the eigenenergies in case $d = 19\ \mu$m read as $E_1 \approx -2$ MHz, $E_2 \approx -0.19$ MHz, and $E_3 \approx 2.2$ MHz. Note that since we include next-nearest-neighbor interaction in the aggregate Hamiltonian $\mathcal{H}_{\text{agg}}^{(3\times 3)}$, the eigenergies are not equispaced, as opposed to the aggregate Hamiltonian (2.42).

Evaluating the populations of the eigenstates $|\varphi_k\rangle$ for the parameters of Fig. 2.14(b), we obtain Fig. 2.15(a), in which the full master equation results (effective equation results) are represented by solid lines (color-matched diamonds). In stark contrast to the faithful reproduction of the aggregate populations $|\pi_n\rangle$ in Fig. 2.14(b), the effective model fails in capturing the eigenstate dynamics. In particular, the effective equation predicts equal populations of the aggregate eigenstates in the steady state as opposed to the full master equation, which predicts larger occupations of states with lower eigenenergies. This can be understood from the form of the Lindblad operators (2.70b), which are essentially projectors on the localized aggregate states $|\pi_n\rangle$. The dephasing introduced by such Lindblad operators introduces fluctuations to the energies of the localized states and so destroys the coherences between the aggregate states $|\pi_n\rangle$, thereby producing a totally mixed aggregate state [224].[11] Note that this behavior is actually a shortcoming of the original Haken-Strobl-Reinecker model, which yields an equal distribution of aggregate eigenstates corresponding to infinite temperature in the case considered here (i.e., equivalent sites) [248]. Hence, our HSR-type model fails to produce thermal distributions of aggregate eigenstates, which would be highly desirable for the simulation of an aggregate at finite temperature. Harnessing the tunability of the environment provided by the background atoms, we show in Sec. 2.6 that in our setup, thermal distributions of aggregate eigenstates can indeed be prepared using reservoir engineering, thus extending the scope of our setup and opening new avenues for simulating non-equilibrium dynamics with ultracold atoms.

---

[10] The reason that the effective model, which relies on treating the ground-state coupling to the “excited” state manifold spanned by $|e\rangle$ and $|r\rangle$ as a perturbation, is still valid for a relatively strong probe Rabi frequency $\Omega_p/(2\pi) = 12$ MHz is that the detuning Δ_p effectively reduces the coupling, inhibiting significant excitation of the intermediate state $|e\rangle$.

The limitations of the effective model Eq. (2.71) can be partially overcome by taking into account the interaction between the aggregate atoms in the derivation of the effective model. Taking accordingly the aggregate eigenstates as the starting point of the perturbative expansion (as outlined in Appendix A.2), we attain an extended effective model (A.28),

$$\begin{aligned}\mathcal{H}_{\text{eff}} = \sum_{n,m} \Bigg(\sum_{\alpha,k} \frac{\kappa_k^{nm}\Omega_p^2}{2} \Bigg[& \frac{(\tilde{V}_{n\alpha} - E_k)}{2(\tilde{V}_{n\alpha} - E_k)(2E_k + 2\Delta_p + i\Gamma_p) + \Omega_c^2} \\ & + \frac{(\tilde{V}_{m\alpha} - E_k)}{2(\tilde{V}_{m\alpha} - E_k)(2E_k + 2\Delta_p - i\Gamma_p) + \Omega_c^2} \Bigg] \Bigg) |\pi_n\rangle \langle \pi_m| , \end{aligned} \tag{2.73a}$$

$$L_{\text{eff}}^{(\alpha)} = \sum_{n,m} \left(\sum_k \frac{-2\Omega_p \sqrt{\Gamma_p} (\tilde{V}_{n\alpha} - E_k) \kappa_k^{nm}}{2(\tilde{V}_{n\alpha} - E_k)(2E_k + 2\Delta_p + i\Gamma_p) + \Omega_c^2} \right) |\pi_n\rangle \langle \pi_m| , \tag{2.73b}$$

where we defined $\kappa_k^{nm} = c_{nk} c_{mk}^*$.

Figure 2.15(b) shows the results obtained using this model for the parameters of Fig. 2.15(a). The extended version of the effective model reproduces the occupations of the aggregate eigenstates. This can be understood by considering the effective Lindblad operator L_{eff} of the extended effective model. Since L_{eff} has not been derived starting from the localized aggregate states $|\pi_n\rangle$ but rather from the aggregate eigenstates, the dephasing terms introduce fluctuations to the eigenstate energies rather than the energies of the localized states. Coherences between localized states are thus allowed for in the steady state.

We note that the extended effective model (2.73) still relies on a perturbative description of the "excited" states $|e\rangle$ and $|r\rangle$, which sets a strong constraint on the range of validity of the model. In fact, numerical evidence indicates that the extended effective model yields worse agreement with the full master equation than the effective model considering the populations of localized aggregate states in the two-photon excitation regime, for example, using relatively large probe Rabi frequencies such as $\Omega_p/(2\pi) = 12$ MHz. The benefit of the extended model is rather to be seen in its success in describing aggregate coherences. In the following two sections, Sec. 2.4.2 and Sec. 2.4.3, we will be interested in the aggregate populations only and will make use of the relatively simple structure of Eqs. (2.71), such that we resort again to the initial effective model.

2.4.2 Gaussian disorder and dephasing

In this section we show that the effective Hamiltonian as well as the effective Lindblad terms arising in the effective model can indeed be understood as introducing site-energy disorder and site-specific dephasing to the aggregate. In particular, we show that the disorder and dephasing distributions are approximately given by Gaussian distributions for the background gas parameters employed for excitation dynamics imaging in Sec. 2.3.1, which gives rise to diffusive excitation transport in the aggregate.

---

[11] A totally mixed state is totally mixed in any basis since the corresponding density matrix is proportional to the unit matrix.

To analyze the disorder and dephasing introduced by the background gas and to assess its influence on the aggregate dynamics, we evaluate the action of Eqs. (2.69) on the density matrix elements. For a Lindblad operator L consisting of sums of projectors with complex rates γ such as in Eq. (2.70b), $L = \sum_n \gamma_n |\pi_n\rangle\langle\pi_n|$, the action of L on the density matrix can be cast into the form

$$\mathcal{L}_L[\rho]_{nm} = -\frac{1}{2}\left(|\gamma_n|^2 + |\gamma_m|^2 - 2\gamma_n\gamma_m^*\right)\rho_{nm}. \tag{2.74}$$

Defining further a resonant dipole-dipole interaction matrix W with $W_{nn} = 0$ to capture the dynamics induced by the aggregate Hamiltonian (2.41), we arrive at a more explicit form of the HSR-type master equation (2.69),

$$\dot\rho_{nm}^{(\mathrm{agg})} = \sum_k i(W_{km}\rho_{nk}^{(\mathrm{agg})} - W_{nk}\rho_{km}^{(\mathrm{agg})}) + i(E_m - E_n + \epsilon_{nm})\rho_{nm}^{(\mathrm{agg})} - \frac{\gamma_{nm}}{2}\rho_{nm}^{(\mathrm{agg})}, \tag{2.75}$$

with the different contributions reading as

$$E_n = \sum_\alpha \mathcal{H}_{\mathrm{eff}}^{(n\alpha)}, \tag{2.76a}$$

$$\gamma_{nm} = \sum_\alpha (|L_{\mathrm{eff}}^{(n\alpha)}|^2 + |L_{\mathrm{eff}}^{(m\alpha)}|^2 - 2\mathrm{Re}[L_{\mathrm{eff}}^{(n\alpha)}L_{\mathrm{eff}}^{(m\alpha)*}]), \tag{2.76b}$$

$$\epsilon_{nm} = \sum_\alpha \mathrm{Im}[L_{\mathrm{eff}}^{(n\alpha)}L_{\mathrm{eff}}^{(m\alpha)*}]. \tag{2.76c}$$

Writing out the HSR-type model (2.69) in the density matrix components, as done in Eq. (2.75), allows us to interpret the contributions of the effective Hamiltonian and Lindblad operators, respectively. In particular, the structure of E_n and γ_{nm} in Eq. (2.75) suggests the interpretation of E_n as diagonal disorder [249] and γ_{nm} as dephasing. The interpretation of ϵ_{nm} is less clear since it depends on two indices n, m. Numerical evaluation shows, however, that for the EIT parameters listed in Tab. 2.2, ϵ_{nm} can be approximated by

$$\epsilon_{nm} \sim 2\sum_\alpha \left(\mathcal{H}_{\mathrm{eff}}^{(n\alpha)} - \mathcal{H}_{\mathrm{eff}}^{(m\alpha)}\right)\Big|_{C_{4,rp}=0}. \tag{2.77}$$

Thus, ϵ_{nm} can be approximated by sums of contributions arising from single aggregate sites[12], and consequently the term $i(E_m - E_n + \epsilon_{nm})\rho_{nm}$ in Eq. (2.75) can be cast into the form $i(E'_m - E'_n)\rho_{nm}$, with $E'_k = E_k - 2\sum_\alpha \mathcal{H}_{\mathrm{eff}}^{(k\alpha)}|_{C_{4,rp}=0}$. This is the reason we refer to ϵ_{nm} as to a correction to the diagonal disorder.

To study the effect of the background gas atoms on the aggregate dynamics, we now analyze the disorder and dephasing distributions that arise from many realizations of a disordered background gas. To this end, we define the distributions $P_E(E_n - \langle E_n\rangle)$, $P_\epsilon(\epsilon_{nm} - \langle\epsilon_{nm}\rangle)$, and $P_\gamma(\gamma_{nm})$. Here, the site energies E_n (their correction ϵ_{nm}) have been adjusted by the site-energy mean (site-energy correction mean), which is different for each realization. More

---

[12] The Gaussian distribution P_ϵ in Fig. 2.16(a)(ii) is reproduced by this expression with a standard deviation overestimating the correct one by $\sim 10\%$. Note that this does not hold true for all sets of parameters, specifically not for those of Tab. 2.4 corresponding to non-Gaussion disorder. For these parameters, however, ϵ_{nm} is negligible.

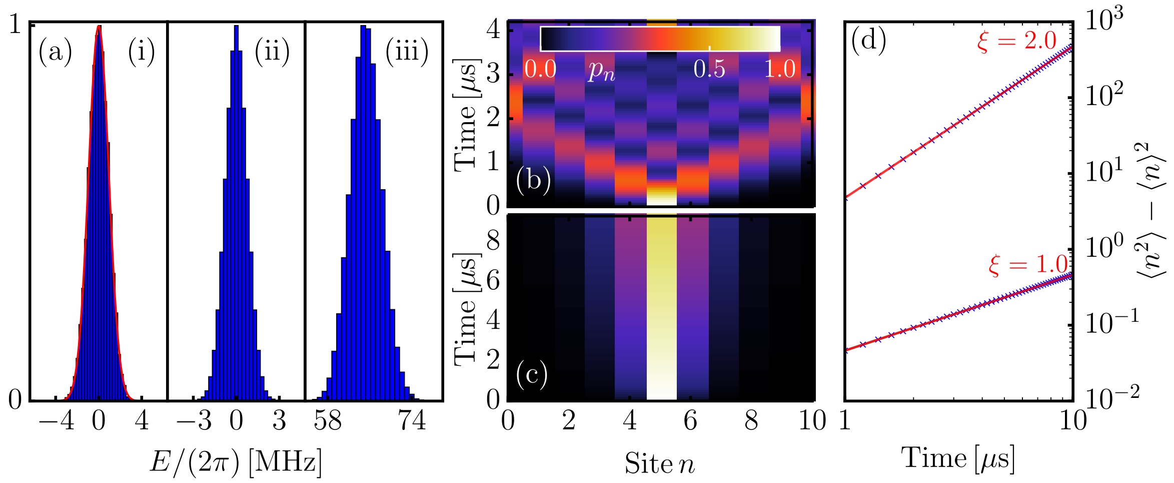

Figure 2.16: (a) Histograms of disorder and dephasing distributions (i) P_E, (ii) P_ϵ, (iii) P_γ, using the parameters listed in Tab. 2.2. The red line in (i) indicates a Gaussian fit with mean 0 and variance $\approx 2\pi \times 0.95$ MHz. (b) Excitation transport in the absence of disorder and dephasing, with parameters as in (a) but $\Omega_p = 0$. (c) Effect of disorder and dephasing on the excitation transport, arising from the disorder and dephasing distributions shown in (a). Note the different scales of the y axes and the square-root scaling of the color map. (d) Variance of the excitation location (crosses), fitted by $\sigma_n^2(t) = St^\xi$. From top to bottom, the parameters are as in (b) and (c), but with $N = 31$ instead of $N = 11$ for the $\xi = 2$ case. The distributions in (a) leading to the diffusive excitation transport (d) are calculated from an ensemble of $N_\aleph = 2 \times 10^3$ realizations of background gas positions.

precisely, the ensemble arising from many different realizations $\aleph$ of background atom positions that underlies the distribution of site energies $P_E(E_n - \langle E_n \rangle)$ reads as

$$\sum_{n,\aleph} \left(E_n^{(\aleph)} - \frac{1}{N} \sum_{m=1}^{N} E_m^{(\aleph)} \right) . \tag{2.78}$$

A similar relation applies for the site-energy correction ϵ_{nm}. The distributions P_E, P_ϵ, and P_γ quantify the probabilities with which an individual background atom α contributes to disorder and dephasing in an ensemble average over background atom positions. Note that we focus here on the effects expected from a background gas of homogeneous density. By placing background atoms deterministically, the dynamics of the aggregate can be tailored more accurately via the control over background atom positions, as well as laser parameters. Shaping environments for the aggregate using deterministically placed background atoms is discussed in Sec. 2.5 and Sec. 2.6.

As an example, we consider a linear chain of $N = 11$ aggregate atoms with spacing $d = 19$ μm, embedded in a background gas confined to a box with dimensions $209 \times 8 \times 8$ μm (in $x \times y \times z$ direction), with background gas atoms extending 4 μm beyond the aggregate positions in the y and z direction while 9.5 μm in the x direction. Taking into account 5×10^4 background atoms corresponding to a density of $n_0 = 3.8 \times 10^{18}$ m^{-3} and the laser parameters of excitation transport imaging, listed in Tab. 2.2, we obtain the site energy disorder and dephasing distributions shown in Fig. 2.16(a)(i)-(iii). For the sake of presentation, the maximum of the distributions P_E, P_ϵ, and P_γ has been set to one. This implies that the distributions as shown are not normalized according to a probability distribution.

The disorder and dephasing distributions (i)-(iii) show that we find Gaussian distributions [cf. the Gaussian fit in Fig. 2.16(a)(i)] in the case of resonant EIT excitation. Gaussian distributions for the site energies are often employed as convenient choices to study the effect of an ambient environment on exciton transport [250]. Our setup thus provides a link to exciton transport simulations using simple Gaussian site-energy disorder models. The dominant energy scale of the dephasing distribution indicated in Fig. 2.16(a)(iii) we expect to lead to strongly-damped aggregate dynamics. Note that disorder and dephasing strength can be controlled via the laser parameters in principle, as discussed previously in Sec. 2.4.1.

Figure 2.16(b) and (c) show examples of excitation transport within the aggregate, visualizing the effect of strong disorder and dephasing on the energy transport. In the presence of the strong disorder and dephasing depicted in (a), the coherent excitation transport shown in Fig. 2.16(b) gets significantly slowed down [cf. panel (c)].

To quantify this effect, we examine the spatial width of the excitation distribution over aggregate sites $\sigma_n^2 = \langle n^2 \rangle - \langle n \rangle^2$, with the expectation values indicating an ensemble average over many realizations. The spatial width $\sigma_n^2(t)$ carries the transport signatures, as demonstrated in Fig. 2.16(d). Parametrizing $\sigma_n^2(t) = St^{\xi}$, we find $\xi = 2$ for $\Omega_p = 0$, which signifies ballistic transport. In contrast, for the disorder and dephasing distributions of Fig. 2.16(a) we obtain $\xi = 1$, which is what we expect for diffusive transport. Dominant dephasing of the aggregate dynamics through measurement thus leads to diffusive excitation transport, similarly to what was observed experimentally in Ref. [81]. (See also Ref. [251] for a theoretical investigation of coherent and diffusive excitation transport in a chain of Rydberg atoms.) We verified that the results of Fig. 2.16(a) and (d) are not artifacts of box size or ensemble size $N_{\aleph}$.

Before discussing how more exotic forms of disorder could be realized, let us remark that it is a great advantage of the effective model that it allows us to cast its action on the density matrix components into the form (2.75). This is not possible with the extended model, whose action on the density matrix elements (considering only the Lindblad terms) reads as

$$\dot{\rho}^{(\text{agg})}_{nm} = \sum_{\alpha,k,l} \left[-\frac{1}{2} \left(L^{(kn\alpha)*}_{\text{eff}} L^{(kl\alpha)}_{\text{eff}} \rho^{(\text{agg})}_{lm} + L^{(kl\alpha)*}_{\text{eff}} L^{(km\alpha)}_{\text{eff}} \rho^{(\text{agg})}_{nl} \right) + L^{(mk\alpha)*}_{\text{eff}} L^{(nl\alpha)}_{\text{eff}} \rho^{(\text{agg})}_{lk} \right], \tag{2.79}$$

where $L^{(km\alpha)}_{\text{eff}} = (L^{(\alpha)}_{\text{eff}})_{km}$. It follows that no attribution of the resulting terms similar to Eq. (2.75) is possible.

2.4.3 Non-Gaussian disorder

In the previous section we have seen that the parameter regime used for excitation transport imaging via EIT induces dominant dephasing that gives rise to diffusive transport, and that the corresponding disorder and dephasing distributions are Gaussian-shaped. A Gaussian distribution for the site energies is, however, not always the appropriate model for the effect of a surrounding environment on the aggregate. For instance, single-molecule studies on chlomophores embedded in a glassy host have shown indications of non-Gaussian disorder distributions such as Lévy stable distributions [252–254]. Excitation transport can be crucially modified in the presence of such heavy-tailed disorder [255]. It is therefore of interest to extend the range of possible disorder distributions that can be simulated with our setup.

To assess the flexibility of the proposed setup regarding more exotic disorder distributions and excitation transport regimes, we now abandon the EIT imaging parameters listed in Tab. 2.2 and turn to a different setting with (i) weaker and more similar Rydberg-Rydberg interactions between background atom state $|r'\rangle$ and aggregate states $|s\rangle$ and $|p\rangle$, (ii) lower background gas density, and (iii) appreciable laser detuning of the intermediate state $|e\rangle$ of the background atoms (two-photon excitation regime). We will see that this modified setting allows for the realization of non-Gaussian site-energy disorder distributions and negligible dephasing. The reasons are detailed below, and can be summarized as follows: Due to (i)

Table 2.4: Parameter set for generating non-Gaussian disorder. Only the parameters are listed that are modified with respect to the imaging parameters listed in Tab. 2.2.

Variable	Symbol	Numerical value
Aggregate spacing	d	24 μm
Probe Rabi frequency	Ω_p	$2\pi \times 12$ MHz
Probe laser detuning	Δ_p	$2\pi \times (-20)$ MHz
Coupling Rabi frequency	Ω_c	$2\pi \times 90$ MHz
Coupling laser detuning	Δ_c	$2\pi \times 22$ MHz
Background gas density	n_0	9.5×10^{17} m^{-3}
Background gas Rydberg state	$\lvert r'\rangle$	—

and (ii), only outliers in the background gas contribute to the site-energy disorder, and (iii) guarantees that dephasing is reduced compared to the site-energy disorder introduced by the background atoms.

Parameter constraints

Turning away from the parameter set specified for excitation transport imaging, listed in Tab. 2.2, to the one listed in Tab. 2.4, we again have to verify that the assumptions of our modeling, here the assumptions under which the effective equation (2.69) has been derived, are still fulfilled by the new set of parameters. This we do by revisiting the triad of Sec. 2.3.1, addressing the neglect of (i) mutual Rydberg-Rydberg interactions in the background gas, (ii) motion of background Rydberg atoms due to attractive van der Waals forces, and (iii) aggregate lifetime reducing effects pertaining to the background atom density. Subsequently, we comment on timescale constraints required for the validity of approximating the aggregate dynamics by the effective equation (2.69), and show that these are met by our parameter choice listed in Tab. 2.4.

(i) *Mutual Rydberg-Rydberg interactions in the background gas.* Our effective model has been derived under the assumption that mutual Rydberg-Rydberg interactions among background gas atoms are negligible. Hence, we have to verify that this assumption is still valid for the parameters of Tab. 2.4. In the case of nonzero detuning Δ_p and Δ_c, the Rydberg fraction of the background atoms in the steady state can be calculated via

$$\tilde{\rho}_{rr}(\Delta_p, \Delta_c) = \frac{\Omega_p^2(\Omega_p^2 + \Omega_c^2)}{4\Gamma_p^2\Delta_{p+c}^2 + (\Omega_c^2 - 4\Delta_p\Delta_{p+c})^2 + 2\Omega_p^2(4\Delta_{p+c}^2 + \Omega_c^2) + \Omega_p^4}, \tag{2.80}$$

where we denoted the sum of probe and coupling laser detuning, $\Delta_p + \Delta_c$, as Δ_{p+c}. For the parameters of Tab. 2.4, we obtain $p_{r'} = \tilde{\rho}_{r'r'}(\Delta_p, \Delta_c) \approx 0.02$.

Figure 2.17(a) shows the Rydberg population $p_{r'}$ as a function of the coupling laser detuning Δ_c. For off-resonant excitation, the Rydberg population $p_{r'}$ is no longer a Lorentzian centered at $\Delta_c = 0$. Accordingly, $p_{r'}$ can increase in the presence of an interaction-induced energy shift of the Rydberg $\lvert r'\rangle$ level. The notion of Rydberg blockade has thus lapsed; repulsive van der Waals interactions between $\lvert r'\rangle$ states with $C_{6,r'r'}/(2\pi) \approx 7$ kHz μm$^6 > 0$ can compensate for the two-photon detuning $-(\Delta_p + \Delta_c)$ and thereby enhance Rydberg excitation of the $\lvert r'\rangle$ state (cf. Refs. [195, 223]).

In Fig. 2.17(b) we show $p_{r'}$ as a function of the interatomic distance between a ground-state and a Rydberg-excited background atom using $\Delta_c \to \Delta_c - C_{r'r'}/R^6$. (Here, the

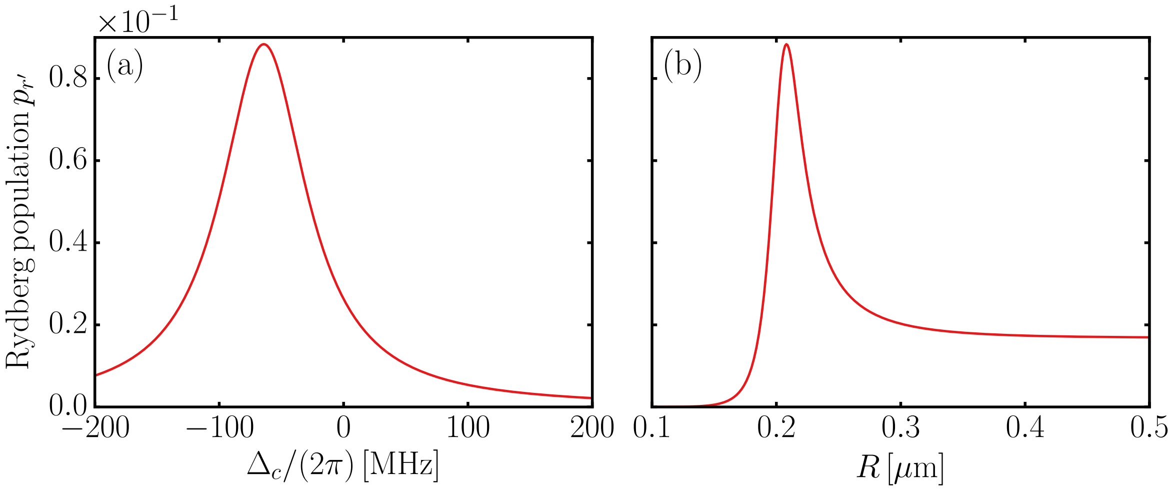

Figure 2.17: Rydberg population $p_{r'}$ of a background atom (a) as a function of the coupling laser detuning Δ_c and (b) as a function of the interatomic distance from an existing background-gas Rydberg excitation, using $\Delta_c' = \Delta_c - C_{r'r'}/R^6$.

repulsive van der Waals interaction enters with a minus sign since Δ_c enters with a minus sign in the Hamiltonian (2.44).) We see that the repulisve background-atom Rydberg-Rydberg interaction favors the creation of another Rydberg excitation at a distance $\Delta R \approx 0.21$ μm from an existing one, with $p_{r'}(\Delta R) \approx 0.09$. Due to the low background gas density n_0, however, the probability to find a background gas atom in a suitable distance is well below 10%. Taking further into account the small probability $p_{r'} \approx 0.02$ to off-resonantly excite a background gas Rydberg excitation in the first place, the probability for background gas excitations further drops. For this reason we do not expect Rydberg-Rydberg interactions within the background gas to have an effect on our effective modeling of excitation transport.

(ii) *Motion of background Rydberg atoms.* Evaluating the estimates introduced in Sec. 2.3.1 with the parameters of Tab. 2.4, we find that the dressed collision times $\tau_{\text{coll,s}}$ and $\tau_{\text{coll,p}}$ are given by $\tau_{\text{coll,s}} \approx 8.1$ μs and $\tau_{\text{coll,p}} \approx 4.4$ μs, respectively (see Tab. 2.5). Note that we have used the mean nearest-neighbor distance $R_0 \approx 0.56$ μm here as the initial distance of the two Rydberg excitations to evaluate $\tau_{\text{coll,s}}$ and $\tau_{\text{coll,p}}$, since for off-resonant excitation we cannot rely on the standard concept of a blockade radius [cf. reasoning in (i)]. In addition, we have taken into account the interaction-induced energy shift at R_0 for the calculation of $p_{r'}$, $p_{r'} = \tilde{\rho}_{r'r'}(\Delta_p, \Delta_c - C_{r'a}/R_0^6)$ with $a \in \{s, p\}$.

Both collision times $\tau_{\text{coll,s}}$ and $\tau_{\text{coll,p}}$ are shorter than the aggregate lifetime τ_{agg} (cf. Tab. 2.3). This implies that in the case of off-resonant excitation, the interaction-induced lifetime-reduction of the aggregate comprises a challenge to an experimental realization of energy transport studies. We believe though that this challenge can be tackled by post-selection, trapping of Rydberg atoms, or parameter optimization.

(iii) *Aggregate lifetime reducing effects due to high background density.* Aggregate lifetime reduction due to Rydberg electron scattering is even lower for the parameters of Tab. 2.4 as compared to the EIT parameters listed in Tab. 2.2. Specifically, using the parameters of Tab. 2.4 we obtain $N_{\text{orb}} \approx 0.01$; thus we do not expect lifetime-reducing effects due to Rydberg-electron scattering.

We now comment shortly on the applicability of the effective equation (2.69) for the

Table 2.5: Summary of the quantities employed to estimate the feasibility of an experimental realization of non-Gaussian site-energy disorder, using the parameters of Tab. 2.4.

Variable	Symbol	Expression	Numerical value
Hopping time	τ_{hop}	$\pi/2 \times 1/W$	2.1 μs
Bg. equilibration time	τ_{SS}	Fitted	≈ 0.1 μs
Bg. Rydberg fraction	$p_{r'}$	$\tilde{\rho}_{r'r'}(\Delta_p, \Delta_c)$	0.02
Mean NN distance	R_0	$\frac{1}{3}\left(\frac{3}{4\pi n_0}\right)^{1/3}\Gamma(1/3)$	0.56 μm
Bare $\lvert s\rangle$ collision time	$\tau'_{\text{coll,s}}$	$0.2156 R_0^4 \sqrt{m_{\text{Rb}}/\lvert C_{6,r's}\rvert}$	1.0 μs
Bg. $\lvert s\rangle$ collision time	$\tau_{\text{coll,s}}$	$0.2156 R_0^4 \sqrt{m_{\text{Rb}}/(\lvert C_{6,r's}\rvert p_{r'})}$	8.1 μs
Bare $\lvert p\rangle$ collision time	$\tau'_{\text{coll,p}}$	$0.2156 R_0^4 \sqrt{m_{\text{Rb}}/\lvert C_{6,r'p}\rvert}$	0.51 μs
Bg. $\lvert p\rangle$ collision time	$\tau_{\text{coll,p}}$	$0.2156 R_0^4 \sqrt{m_{\text{Rb}}/(\lvert C_{6,r'p}\rvert p_{r'})}$	4.4 μs
Aggregate Rydberg orbit	$\langle r\rangle_{\text{agg}}$	$\max[\langle r\rangle_{\lvert 43p\rangle}, \langle r\rangle_{\lvert 43s\rangle}]$	0.13 μm
Bg. atoms in orbit	N_{orb}	$\text{Vol}(\langle r\rangle_{\text{agg}})n_0$	0.01

parameters of Tab. 2.4. In particular, for the effective equation to be valid, we need the timescale of the background atom dynamics, i.e., the timescale on which ground, intermediate, and Rydberg state reach their steady state, to be short compared to the aggregate dynamics. Fitting a monoexponential to the Rydberg state population of a single background atom for the parameters of Tab. 2.4, we find $\tau_{\text{SS}} \approx 0.1$ μs. In the presence of an interaction-induced energy shift of $\Delta_{\text{int}}/(2\pi) = -100$ MHz arising from background-aggregate interactions at an interatomic distance smaller than the mean nearest-neighbor distance R_0, we find $\tau_{\text{SS}} \approx 0.4$ μs. The timescale of the aggregate dynamics we estimate via the hopping time $\tau_{\text{hop}} \sim \pi/(2W)$, which is ≈ 2.1 μs for the parameters listed in Tab. 2.4. Thus we have indeed $\tau_{\text{SS}} < \tau_{\text{hop}}$.

Besides, we need that the populations of both intermediate $|e\rangle$ and Rydberg $|r'\rangle$ state are small; else, adiabatic elimination of these states is not appropriate. Due to the large detuning of the intermediate state, we find $\tilde{\rho}_{ee} \approx 3 \times 10^{-5}$ for the parameters of Tab. 2.4, and $p_{r'} \approx 0.02$. Note that in contrast to background-atom Rydberg-Rydberg interactions, which are repulsive, the interactions between background and aggregate atoms are attractive, such that neither Rydberg nor intermediate state population can be enhanced by the interaction between background and aggregate atoms.

The reasoning from the previous two paragraphs indicate that our assumption of an adiabatic background gas is justified and hence the use of the effective model, which we have already verified in Fig. 2.14, where we compared the effective model results with results obtained by the full master equation. The quantities employed to estimate the feasibility of an experimental realization of non-Gaussian site-energy disorder in our setup are summarized in Table 2.5.

Lastly, we discuss the parameter choice listed in Tab. 2.5. To that end, we consider the infinite-interaction limit $\tilde{V}_{n\alpha} \to -\infty$ of the components of the effective Hamiltonian $\mathcal{H}_{\text{eff}}^{n\alpha}$ and Lindblad term $L_{\text{eff}}^{n\alpha}$ [cf. Eqs. (2.71)],

$$\lim_{\tilde{V}_{n\alpha}\to-\infty} \mathcal{H}_{\text{eff}}^{(n\alpha)} \equiv \mathcal{H}_{\text{eff}\uparrow}^{(n\alpha)} = \frac{\Delta_p\Omega_p^2}{\Gamma_p^2 + 4\Delta_p^2}, \tag{2.81a}$$

$$\lim_{\tilde{V}_{n\alpha}\to-\infty} L_{\text{eff}}^{(n\alpha)} \equiv L_{\text{eff}\uparrow}^{(n\alpha)} = -\frac{2\sqrt{\Gamma_p}\Delta_p\Omega_p}{\Gamma_p^2 + 4\Delta_p^2}. \tag{2.81b}$$

In the two-photon excitation regime, both $\mathcal{H}_{\text{eff}}^{(n\alpha)}$ and $L_{\text{eff}}^{(n\alpha)}$ are extremal for $\tilde{V}_{n\alpha} \to -\infty$. Thus,

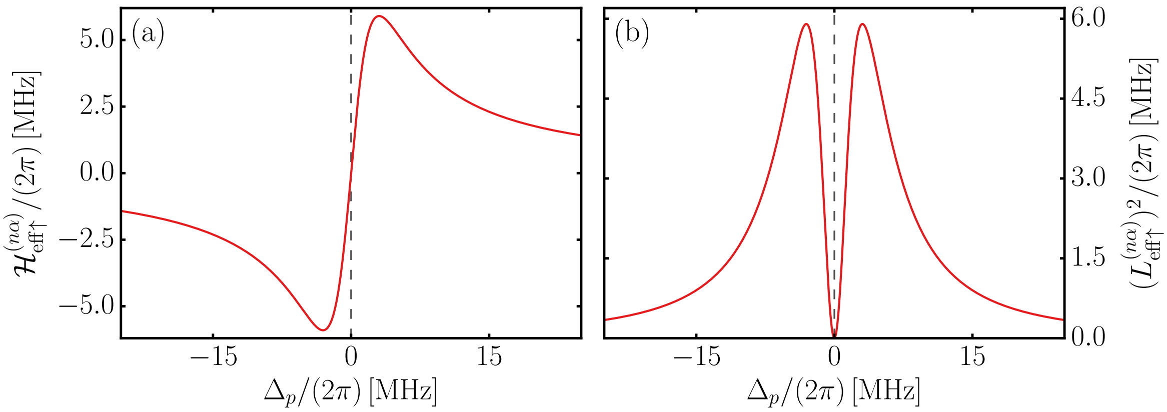

Figure 2.18: (a) Effective Hamiltonian components $\mathcal{H}^{(n\alpha)}_{\mathrm{eff}\uparrow}$ and (b) effective dephasing rates $(L^{(n\alpha)}_{\mathrm{eff}\uparrow})^2$ in the infinite-interaction limit $\tilde{V}_{n\alpha} \to -\infty$ as a function of the background intermediate state detuning Δ_p, with parameters of Tab. 2.4. The dashed lines indicate $\Delta_p = 0$.

considering the parameter dependencies of Eqs. (2.81) allows us to estimate the parameter dependencies of the energy scales associated with energy disorder and dephasing.

Figure 2.18 shows the numerical values of $\mathcal{H}^{(n\alpha)}_{\mathrm{eff}\uparrow}$ and $(L^{(n\alpha)}_{\mathrm{eff}\uparrow})^2$ as a function of the intermediate state detuning Δ_p, with other parameters taken from Tab. 2.4. The reason for displaying $(L^{(n\alpha)}_{\mathrm{eff}\uparrow})^2$ instead of $L^{(n\alpha)}_{\mathrm{eff}\uparrow}$ is that the dephasing rates in the effective model are related to the square of the Lindblad operator components, see Eq. (2.76b). To achieve dominant disorder, the dephasing rates have to be small compared to the disorder scale, which is set by the components of $\mathcal{H}^{(n\alpha)}_{\mathrm{eff}}$ [see Eq. (2.76a)]. Contrasting panel (a) with panel (b) in Fig. 2.18, we find that both dephasing and disorder scale decreases with increasing intermediate state detuning Δ_p. Since the dephasing scale decreases faster, however, Δ_p can be chosen to meet the requirements of both large disorder scale and small dephasing scale. We did so by choosing $\Delta_p/(2\pi) = 20$ MHz.

The probe Rabi frequency Ω_p in Tab. 2.4 has been chosen to balance the requirement of large disorder scale [cf. Eqs. (2.81)] and applicability of the effective model, i.e., the condition that $p_{r'}$ is small. Similarly, large coupling Rabi frequencies lead to small values of $p_{r'}$, which is required for our modeling approximations (neglect of background Rydberg interactions in the derivation of the effective model and adiabatic elimination) to be valid. The two-photon resonance condition $\Delta_p + \Delta_c \approx 0$ in turn guarantees that the disorder scale vanishes for negligible background-aggregate interaction $\tilde{V}_{n\alpha} = \bar{V}_{n\alpha} - (\Delta_p + \Delta_c) \to 0$. This ensures that disorder arises from outliers in the background atom distribution, as will be discussed below.

Note that the scale relevant for the aggregate dynamics is not the absolute disorder scale, but rather the disorder scale compared to the dipole-dipole interaction. To increase the visibility of the effect pertaining to disorder in the aggregate dynamics, the aggregate spacing d has been reduced in Tab. 2.4 in comparison with the aggregate spacing specified for excitation transport imaging in Tab. 2.2.

Numerical results

To assess excitation transport properties and disorder and dephasing distributions for the parameters listed in Tab. 2.4, we again consider a linear chain of $N = 11$ aggregate atoms with spacing $d = 24$ μm, embedded in a background gas confined to a box with dimensions $264 \times 5 \times 5$ μm $(x \times y \times z)$, with background gas atoms extending 2.5 μm beyond the aggregate

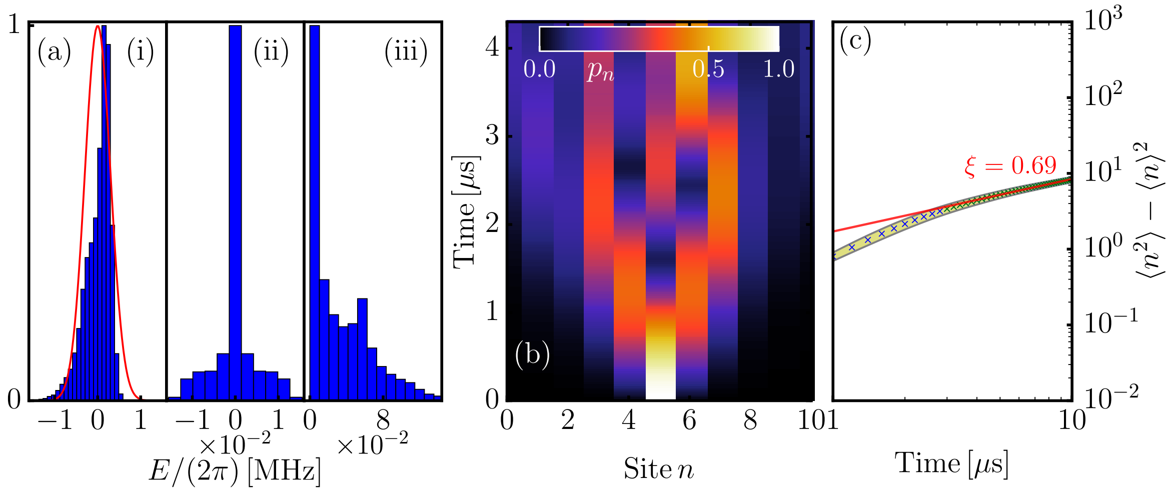

Figure 2.19: (a) Histograms of disorder and dephasing distributions (i) P_E, (ii) P_ϵ, (iii) P_γ, using the parameters of Tab. 2.4. The red line in (i) indicates for comparison a Gaussian fit with mean 0 and variance $\approx 2\pi \times 0.3$ MHz. (b) Effect of site-energy disorder on a single excitation-transport realization, with parameters as in (a). Note the square-root scaling of the color map. (c) Variance of the excitation location (crosses), fitted by $\sigma_n^2(t) = St^\xi$, using parameters as in (a) but with $N = 31$ instead of $N = 11$. The standard deviation of $\sigma_n^2(t)$ obtained by Gaussian error propagation of the standard error of the mean (SEM) is indicated in yellow shading. Both (a) and (c) have been calculated from an ensemble of $N_\aleph = 5 \times 10^3$ realizations of background gas positions.

positions in the y and z direction while 12 μm in the x direction. Distributing 6270 background atoms corresponding to a density of $n_0 = 9.5 \times 10^{17}$ m^{-3} and using the laser parameters of Tab. 2.4, we obtain the site energy and disorder distributions shown in Fig. 2.19(a)(i)-(iii). For the sake of presentation, the maximum of the distributions P_E, P_ϵ, and P_γ has again been set to one.

Here, the dephasing rates are small compared to the variations in the site energies. This has been achieved via the detuning from the intermediate level, which reduces the influence of spontaneous emission and makes dephasing weaker than disorder. Remarkably, for the low background density and weak interactions employed, we find significant outliers in the atomic distance distribution that cause a non-Gaussian, and in particular "heavy-tailed" disorder distribution P_E. The large and rare site energy fluctuations leads to strongly-varying excitation transport in single realizations. Figure 2.19(b) shows an exemplary single realization of transport in the presence of the non-Gaussian disorder distribution shown in panel (a). The asymmetric excitation transport indicates that different aggregate sites have different energies. The effect of the different single excitation-transport realizations on the excitation transport in an ensemble average is displayed in panel (c). Fitting the spatial width of the transport arising from the distributions (a) by $\sigma_n^2 = St^\xi$, we find sub-diffusive transport with $\xi = 0.69$. (Note that the precise value of ξ depends on the fit range, which is $[3, 10]$ μs in Fig. 2.19(c).)

To study the various excitation transport regimes that can be realized in our setup quantitatively, one would need to vary the disorder distribution P_E. We do not aim here to give a detailed account of the dependence of ξ on shape and energy range of P_E (always relating the latter to the energy scale given by the nearest-neighbor dipole-dipole interaction), as well as box size and ensemble size $N_\aleph$. Rather, the calculation performed in Fig. 2.19 serves as an illustration of how site energy disorder and dephasing in the aggregate can be tuned in our setup and demonstrates that this gives rise to excitation transport which is no longer of ballistic or diffusive kind. To experimentally realize a specific disorder distribution, more

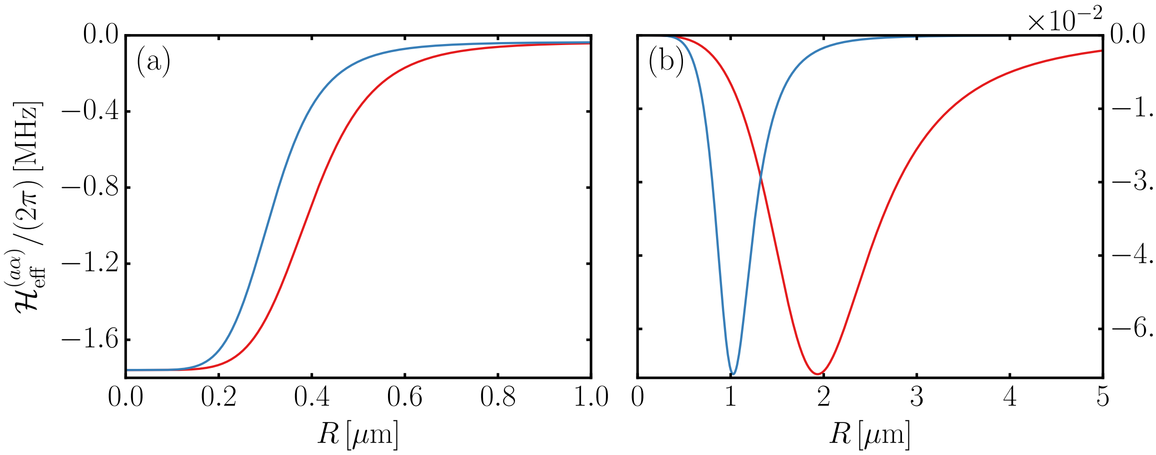

Figure 2.20: Dependence of the effective potentials $\mathcal{H}_{\text{eff}}^{(a\alpha)}$ on the interatomic separation between a single aggregate atom in state $a \in \{s,p\}$ and background atom α. The case $a = p$ is indicated in solid red, the case $a = s$ in solid blue. The potential shapes obtained for the parameters of Tab. 2.4 are depicted in (a), the shapes resulting from the imaging parameters listed in Tab. 2.2 in (b).

detailed calculations are required; in particular, it may turn out that controlled placement of individual background atoms using microstructured optical traps may be more advantageous than using a random background gas.

To understand the difference between the non-Gaussian disorder distributions presented in Fig. 2.19 and the Gaussian disorder distributions presented in Fig. 2.16, it is instructive to consider the Pearson correlation coefficient between the site energies for different realizations, which is defined as

$$\text{corr}(E_n, E_m) = \frac{E[(E_n - \mu_{E_n})(E_m - \mu_{E_m})]}{\sigma_{E_n}\sigma_{E_m}}. \tag{2.82}$$

Here, $E_{n(m)}$ is the site energy of site n (m), $\mu_{E_{n(m)}}$ denotes the expectation value of site energy $E_{n(m)}$ with respect to the ensemble given by different realizations of background atom positions, and $\sigma_{E_{n(m)}}$ denotes the standard deviation of the site energy of site n (m). For the site energies underlying Fig. 2.19(a)(i), which exhibit non-Gaussian energy disorder, the correlation coefficient (2.82) of the bare site energies (not adjusted by the site-energy mean) indicates large correlations, $\text{corr}(E_n, E_m) \sim 0.97$ for $n \neq m$. This implies that the effective interaction $\tilde{V}_{n\alpha} = \bar{V}_{n\alpha} - \Delta_p - \Delta_c$ between an aggregate site and a background gas atom α is, for small densities and weak, similar interactions, mainly given by the sum of the detunings $-(\Delta_p + \Delta_c)$ plus rare outliers. More precisely, since the interactions $V_{n\alpha}^{(pr')}$ and $V_{n\alpha}^{(sr')}$ are similar, also the site-energy shifts caused by $\tilde{V}_{n\alpha}$ are similar, apart from rare realizations of background-atom positions that lead to stronger site-energy shifts.

The asymmetric, non-Gaussian shape of Fig. 2.19(a)(i) emerges from the shape of the components $\mathcal{H}_{\text{eff}}^{(a\alpha)}$ of the effective Hamiltonian $\mathcal{H}_{\text{eff}}$. Figure 2.20(a) shows the effective potentials arising from the interactions $V_{n\alpha}^{(pr')}$ (solid red) and $V_{n\alpha}^{(sr')}$ (solid blue) as a function of the background-aggregate distance. We have chosen the background gas density n_0 such that the mean nearest-neighbor distance $R_0 \approx 0.56$ μm (cf. Tab. 2.5) falls in the tail of $\mathcal{H}_{\text{eff}}^{(a\alpha)}$; therefore, only outliers in the atomic distance distribution give rise to appreciable site energy shifts. This explains the "heavy-tailed" disorder distribution P_E in Fig. 2.19(a)(i).

The strong correlations between the bare site energies, which we interpret as indicators for a site-energy statistics that is dominated by outliers, is only present for the parameters of non-Gaussian disorder, listed in Tab. 2.4. In particular, for the imaging parameters listed in Tab. 2.2, which lead to Gaussian disorder [see Fig. 2.16(a)(i)], the site-energy correlations between different realizations of background-atom positions are significantly decreased, $\mathrm{corr}(E_n, E_m) \sim 0.46$ for $n \neq m$. This can be understood by considering again the components $\mathcal{H}_{\mathrm{eff}}^{(a\alpha)}$ of the effective Hamiltonian. Figure Fig. 2.20(b) shows $\mathcal{H}_{\mathrm{eff}}^{(a\alpha)}$ as a function of aggregate-background distance for the two interactions $V_{n\alpha}^{(pr)}$ and $V_{n\alpha}^{(sr)}$. Since here $\mathcal{H}_{\mathrm{eff}}^{(a\alpha)}$ features distinct distance-dependencies, the site-energy shifts caused by the interaction with the background gas are intrinsically more distinct, leading to smaller correlations among the site energies in a single realization of background-atom positions.

Note that the correlation coefficient (2.82) is reduced to $\mathrm{corr}(E_n, E_m) \sim 0.1$ for $n \neq m$ for the site energies of both Fig. 2.16(a) and Fig. 2.19(a) if they are adjusted by the site-energy mean as in Eq. (2.78). This indicates that the energy fluctuations between different realizations of background-atom positions are indeed captured by the ensemble (2.78).

In summary, we have shown that the background gas can serve as a controlled environment for the aggregate, modifying the excitation transport through the aggregate. Parameters can be found for which the background gas realizes an environment providing dominant dephasing and dominant site-energy disorder, respectively, to the aggregate. Site-energy disorder distributions can be further tuned to be of non-Gaussian shape. Given that the dynamics involving other states than the ground state of the background atoms can be treated as a perturbation to the ground-state dynamics, an effective model for the energy transport within the aggregate can be derived, which is described by a master equation of HSR type. The effect of disorder and dephasing on energy transport within the aggregate can thus be experimentally studied, which shows that our setup implements a flexible quantum simulator. This quantum simulator could be further extended by including the analogue of internal molecular vibrations engineered as in Ref. [84]; disorder distributions could be controlled even further using an additional class of background atoms [256]. The aggregate dynamics can be extracted using either EIT detection discussed earlier or by different means [51]. All these features would extend the HSR-type model proposed here to quantum simulations of light-harvesting processes in a similar spirit but with complementary technology to the proposals of Refs. [11, 257, 258].

2.5 Tuning non-Markovianity of aggregate dynamics

In the previous section we have seen that the setup proposed in Sec. 2.2.5 can serve as a quantum simulator for excitation transport with a controlled environment, and have derived an effective equation for the aggregate alone. In this effective equation, the effect of the environment was incorporated via a correction to the aggregate Hamiltonian and additional, time-independent Lindblad terms. The dynamics described by such a Lindblad equation is Markovian, which implies in particular that information flows unidirectional to the environment but never flows back. In this section, we show that our environment can also exhibit memory [65]: information that flows into our environment can flow back. The the back-action of the environment onto our system thus depends on previous system dynamics, which renders the system dynamics non-Markovian.

The interest in a non-Markovian quantum simulator is twofold. Firstly, in many physical systems, the environment consists of a large number of degrees of freedom at finite temperature. Such an environment often exhibits a back-action onto the system that depends on previous system dynamics. Secondly, from a practical point of view, a memoryless (Markovian) environment enables one to derive simple equations of motion for the system alone, such as the Lindblad equation [259], which allows for efficient numerical solution. For strongly-coupled environments or environments with memory, typically sophisticated and numerically expensive

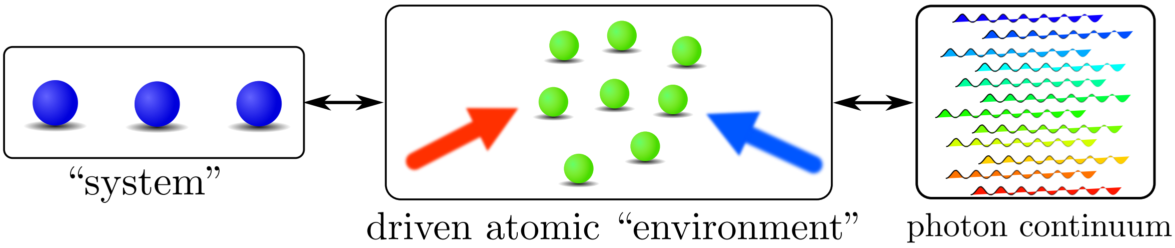

Figure 2.21: Conceptual sketch of our setup. A "system" of Rydberg atoms, the Rydberg aggregate, is coupled to a laser-driven atomic "environment", which is dissipative through its coupling to the electromagnetic continuum.

methods such as path integral approaches [260] and hierarchical equations of motion [261–263] are required. From this point of view, it would be advantageous to possess a quantum simulator that can capture the non-Markovian dynamics of a system not accessible to numerical approaches on present-day conventional computers.

Accordingly, non-Markovian quantum simulators [264–266] have been proposed to study energy transport [11, 12, 239, 257, 267] such as arising in the initial stage of photosynthesis. There, the electronic degrees of freedom are coupled to a structured vibrational environment, posing severe challenges to the efficient numerical simulation of excitation transport on classical computers. Here, the environment of our model system we use to study non-Markovian excitation transport consists of a single background atom. As we will show, this allows us to control the degree of Markovianity in our setup, thus paving the way towards a non-Markovian quantum simulator harnessing ultracold Rydberg atoms.

The exploitation of a single background atom as an "environment" may seem unusual, given the more typical situation where the environment is characterized by a particularly large number of quantum states. One should not forget, though, that the modeling of the background atom includes spontaneous emission from the intermediate state $|e\rangle$ via a Lindblad term. This Lindblad term embodies the coupling of the background atom to an electromagnetic radiation field, which acts as a bath to the background atom. Hence, the three-level background atom is only part of a nested environment (cf. Refs. [60–62, 66, 268–272]), which is driven-dissipative. This is illustrated in Fig. 2.21, in which our setup is depicted from a conceptual point of view. The tunability of the environment arises through its composition of a finite part, the laser-driven three-level atoms, and an infinite part, the photon bath. By tuning the parameters of the lasers addressing the environment atoms, the timescale of the dynamics within the finite part can be controlled. Besides, the coupling strength between Rydberg system and atomic environment can be controlled via the positions of the atoms constituting the environment, as well as via the laser parameters.

We emphasize that the calculations performed in this section, which show that the degree of Markovianity can be controlled in our setup, are meant to demonstrate the flexibility and versatility of our environment consisting of laser-driven background atoms. Tailoring an atomic environments that is able to emulate the environment of a certain molecular aggregate is a formidable task, which remains to be done.

The system we consider is sketched in Fig. 2.22(a). For simplicity, we do not consider an extended aggregate here, but a Rydberg dimer, i.e., a Rydberg aggregate consisting of $N = 2$ atoms with interatomic distance d. The environment consist of a single laser-driven background atom, which is placed at a distance δ from the first aggregate atom, at a right angle to the connecting line between the aggregate atoms and in such a way that the atoms are arranged in a planar geometry. Calculations with larger aggregates and background atom

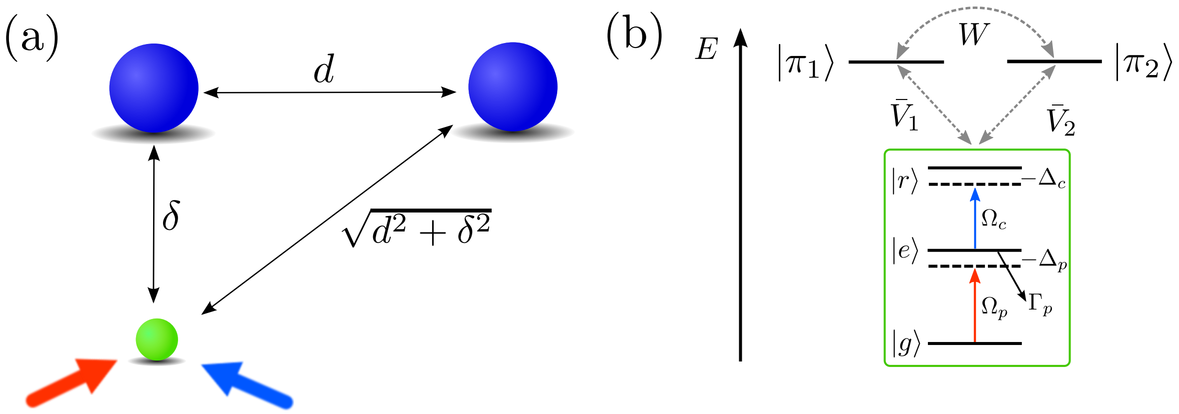

Figure 2.22: Sketch of the setup. (a) Two aggregate atoms form a Rydberg dimer with interatomic separation d. The environment is given by a laser-driven background atom placed at a distance δ from the first aggregate atom, such that the vectors along d and δ respectively enclose a right angle. (b) Level sketch of the setup. The dimer states $|\pi_1\rangle$ and $|\pi_2\rangle$ are coupled to each other via resonant dipole-dipole interaction with strength W and interact with the Rydberg level $|r\rangle$ of the background atom via the effective interactions $\bar{V}_1$ and $\bar{V}_2$. The level scheme of the background atom is the same as in Fig. 2.9(a).

numbers are presented in Sec. 2.6.

The level diagram including the interactions between Rydberg dimer and background atom is depicted in Fig. 2.22(b). The localized dimer states $|\pi_{1(2)}\rangle$ (corresponding to the configurations with the $|p\rangle$ excitation at site 1(2)) are coupled via resonant dipole-dipole interaction W. Their effective interaction with the background atom is denoted by $\bar{V}_n = \bar{V}_{n\alpha}$, with index $\alpha = 1$ dropped since we have only a single background atom ($\bar{V}_{n\alpha} = V_{n\alpha}^{(pr)} + \sum_{m\neq n} V_{m\alpha}^{(sr)}$). The interaction $\bar{V}_n$ between aggregate and background atom conserves the population of the Rydberg dimer. The background atom is addressed by two lasers, a probe laser with Rabi frequency Ω_p and detuning Δ_p coupling the ground $|g\rangle$ and the intermediate state $|e\rangle$, and a coupling laser with Rabi frequency Ω_c and detuning Δ_c coupling intermediate state $|e\rangle$ to the Rydberg state $|r\rangle$. The intermediate state $|e\rangle$ decays via spontaneous emission with rate Γ_p to the ground state. We ignore the decay of the Rydberg state $|r\rangle$, which has a much longer lifetime than the state $|e\rangle$ (cf. Sec. 2.2.5). Note that the findings of this section do not rely on the specific Rydberg states chosen, but on the state-dependence of interactions between dimer and background atom, which, in principle, can also be achieved with different choices.

2.5.1 A measure for non-Markovianity

To quantify the degree of non-Markovianity in our Rydberg dimer, we need to employ an appropriate non-Markovianity measure. Over the last few years, a suitable measure to quantify non-Markovianity in an open quantum system has been actively pursued and debated (see e.g. Refs. [270, 273–291]), as well as used to gain insight into the dynamics of physical systems [264, 271, 292, 293]. In what follows, we adopt a measure related to the information flow from the environment to the system, introduced in Ref. [273]. By this definition, the dynamics is non-Markovian whenever the trace distance quantifying the distinguishability between two initial density operators of the system increases at some point during their time propagation.

The trace distance between two density matrices ρ_1 and ρ_2 is defined as

$$D(\rho_1, \rho_2) = \frac{1}{2}\,\mathrm{Tr}\left\{|\rho_1 - \rho_2|\right\}, \tag{2.83}$$

with $|\rho| = \sqrt{\rho^\dagger \rho}$. The rate of change of the trace distance for some initial states $\rho_1(0)$ and $\rho_2(0)$ reads as

$$\sigma(\rho_1(t), \rho_2(t)) = \frac{\mathrm{d}}{\mathrm{d}t} D(\rho_1(t), \rho_2(t)), \tag{2.84}$$

where $\rho_{1(2)}(t)$ denotes the time-evolved density matrix with initial state $\rho_{1(2)}(0)$. Whenever $\sigma > 0$, the dynamics is said to be non-Markovian, as the distinguishability between two initial states increases, which can be interpreted as information flowing back from the environment to the system [273]. Markovian dynamics conversely is characterized by a unidirectional information flow towards the environment, which can be described using quantum dynamical semigroups [3, 273]. To quantify the strength of non-Markovianity, given the initial states $\rho_1(0)$ and $\rho_2(0)$, the rate $\sigma(\rho_1(t), \rho_2(t))$ has to be integrated over all time intervals in which it takes a positive value:

$$\mathcal{N}_{\rho_1,\rho_2} = \int_{\sigma>0} \mathrm{d}t\, \sigma(\rho_1(t), \rho_2(t)). \tag{2.85}$$

Note that in order for $\mathcal{N}_{\rho_1,\rho_2}$ to fulfill the properties of an actual measure, maximization over all pairs $(\rho_1(0), \rho_2(0))$ has to be performed in Eq. (2.85) [273, 277].

In the following, we take as initial states $\rho_1^{(\mathrm{tot})}(0) = |\pi_1\rangle\langle\pi_1| \otimes |g\rangle\langle g|$ and $\rho_2^{(\mathrm{tot})}(0) = |\pi_2\rangle\langle\pi_2| \otimes |g\rangle\langle g|$, which can be easily prepared (and probed) experimentally and have numerically shown to yield large values $\mathcal{N}_{\rho_1,\rho_2}$ [294]. Note that we have dropped the superscript (agg) here to indicate the reduced density matrix of the aggregate, but use the superscript (tot) instead to indicate the full density operator of aggregate plus environment atom.

The aggregate states $\rho_n(0) = \mathrm{Tr}_{\mathrm{bg}}\{\rho_n^{(\mathrm{tot})}(0)\}$ with the subscript bg indicating the partial trace over the background atom states, have maximal initial trace distance, $D(\rho_1(0), \rho_2(0)) = 1$. Upon calculating the full dynamics of both Rydberg dimer and background atom, we evaluate the trace distance $D(\rho_1, \rho_2)$ and the corresponding rate of change $\sigma(\rho_1, \rho_2)$ in the subsystem of interest (dimer) by tracing out the environment first and subsequently applying the definitions Eqs. (2.83) and (2.84).

The above method allows us to quantify non-Markovianity without having to deal with the specifics of the environment. This stands in contrast to definitions of non-Markovianity that explicitly depend on properties of the environment, such as a delta-correlated bath correlation function [4, 272], which is typically employed as a definition of Markovianity for environments consisting of harmonic oscillators [5]. A drawback of a measure that only requires knowledge about system degrees of freedom is, however, that the full system dynamics has to be evaluated before the non-Markovianity of the dynamics can be quantified. Besides, not all instances of non-Markovianity can be witnessed by the trace-distance based approach (2.85) [283, 284].

2.5.2 Model system results

Having established a way to quantify the degree of non-Markovianity in our Rydberg dimer dynamics, we now show illustrative calculations, which demonstrate that, despite its simplicity, the environment provided by the background atom is highly tunable, and in particular that the time evolution of the dimer can be tuned from Markovian dynamics to various degrees of non-Markovian dynamics.

We start by demonstrating the tunability of the dimer dynamics via the environment constituted by the background atom by means of a single laser parameter, namely the probe Rabi frequency Ω_p. In Fig. 2.23(a) we show different dimer dynamics arising for different Rabi frequencies Ω_p of the probe field driving the background atom, indicating that both dephasing strength and steady-state value of the dimer dynamics can be easily controlled via the parameters of lasers acting on the background atom.

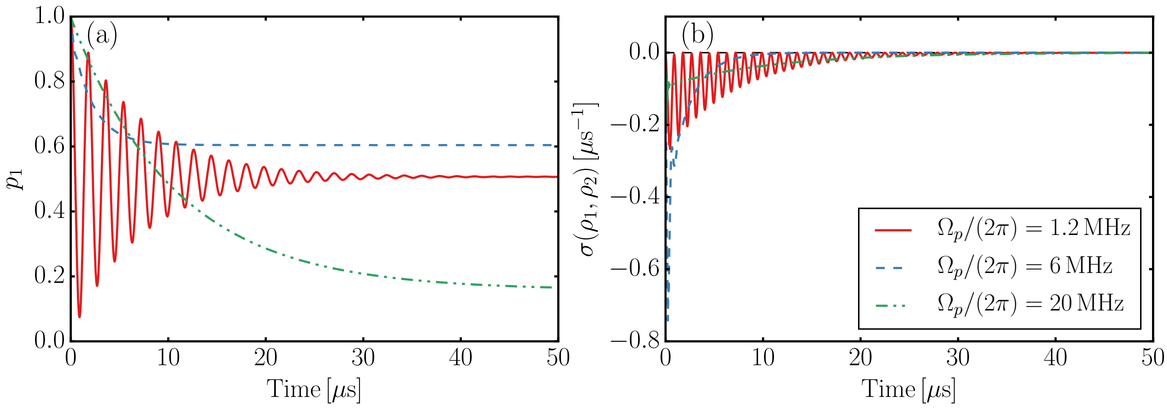

Figure 2.23: Dimer dynamics for three different values of the Rabi frequency Ω_p. Panel (a) shows the population p_1 of state $|\pi_1\rangle$ for the initial state $\rho_1^{(\mathrm{tot})}(0)$, and panel (b) the trace distance change rate $\sigma(\rho_1, \rho_2)$ between $\rho_1(t)$ and $\rho_2(t)$, which correspond to initial preparation in $\rho_1^{(\mathrm{tot})}(0)$ and $\rho_2^{(\mathrm{tot})}(0)$, respectively. The parameters are $\Gamma_p/(2\pi) = 6.1$ MHz, $W/(2\pi) = 0.28$ MHz, $\Omega_c/(2\pi) = 20$ MHz, $\bar{V}_1/(2\pi) = -26.4$ MHz and $\bar{V}_2/(2\pi) = -0.37$ MHz, corresponding to the interatomic distances $d = 18$ μm and $\delta = 2.5$ μm. The detunings Δ_p and Δ_c are set to zero. The Rabi frequencies are $\Omega_p/(2\pi) = 1.2$ MHz (red solid curve), $\Omega_p/(2\pi) = 6$ MHz (blue dashed curve) and $\Omega_p/(2\pi) = 20$ MHz (green dashed-dotted curve). As evident from the time evolution of $\sigma(\rho_1, \rho_2)$, the three sets correspond to completely Markovian system dynamics according to Eq. (2.85), even though the population dynamics in the system shows very different equilibration timescales as well as steady-state values. Note that $\mathcal{N}_{\rho_1,\rho_2}$ has been calculated using data up to $t = 100$ μs.

The different strengths of dephasing can be understood on grounds of the strong difference in the interactions $\bar{V}_1 \gg \bar{V}_2$. In this way, the environment can distinguish whether the system is in state $|\pi_1\rangle$ or $|\pi_2\rangle$ and acts as a measurement device, causing dephasing and decoherence in the system. The underlying reasoning can be summarized as follows (cf. Sec. 2.3.2): Consider the case when the laser fields are applied resonantly, $\Delta_p = \Delta_c = 0$. The background atom is then tuned to conditions of EIT, in which it evolves into a so-called dark state, which has no contribution from state $|e\rangle$ (cf. Sec. 2.2.4). If the dimer is in the state $|\pi_2\rangle$, the background atom remains in the dark state since the interaction $\bar{V}_2$ is negligible by design of the setup. However, if the dimer is in the state $|\pi_1\rangle$, the strong interaction $\bar{V}_1$ shifts the Rydberg level $|r\rangle$ of the background atom out of resonance, disturbing EIT and yielding a non-zero population of the state $|e\rangle$. This state then decays with rate Γ_p, and the emitted photons provide a potential observer with information about the state of the dimer. The stronger the driving Ω_p, the more photons will be scattered by the background atom, allowing one to infer the state of the dimer more quickly, and thereby dephasing the dimer dynamics more quickly.

As depicted in Fig. 2.23(b), however, various dimer dynamics with vastly different dephasing timescales and steady-state values can still be purely Markovian according to Eq. (2.85). That is, since $\sigma(\rho_1, \rho_2)$ is always negative for the parameters of Fig. 2.23(a), the integrated quantity $\mathcal{N}_{\rho_1,\rho_2}$ is zero, which indicates purely Markovian dimer dynamics. Accordingly, it can be misleading to estimate the Markovianity of the dynamics via properties of the population dynamics such as stead-state values or dephasing timescales.

We now demonstrate the control of the degree of non-Markovianity via the laser parameters in our setup. In Fig. 2.24 we show an example of a specific geometrical arrangement for which the dimer dynamics can be switched from Markovian to non-Markovian (cf. Ref. [266]) by modifying the laser parameters of both probe and coupling laser. While small, asymmetric driving $\Omega_p < \Omega_c$ and small laser detunings result in Markovian dimer dynamics with regular

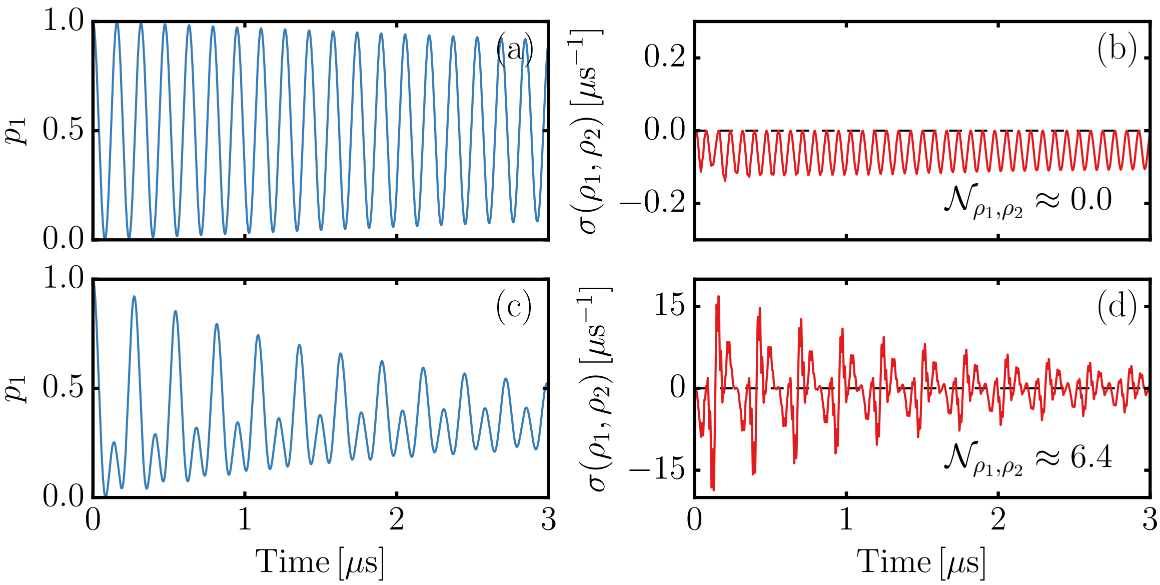

Figure 2.24: Dimer dynamics tuned from Markovian to non-Markovian via change of laser parameters. (a) Population p_1 of state $|\pi_1\rangle$. The damped oscillations correspond to Markovian dynamics, as can be seen from the time evolution of $\sigma(\rho_1, \rho_2)$ shown in panel (b). Laser parameters are $\Omega_p/(2\pi) = 0.5$ MHz, $\Delta_p/(2\pi) = 5.4$ MHz, $\Omega_c/(2\pi) = 25.2$ MHz, and $\Delta_c/(2\pi) = 5.4$ MHz. (c) Same as (a), but for a different set of laser parameters, $\Omega_p/(2\pi) = 27.6$ MHz, $\Delta_p/(2\pi) = -69.9$ MHz, $\Omega_c/(2\pi) = 20.4$ MHz, and $\Delta_c/(2\pi) = 69.5$ MHz. The population dynamics of state $|\pi_1\rangle$ exhibits alternating oscillations of different amplitude, suggesting non-Markovian dynamics. This is is verified in (d) where we find $\mathcal{N}_{\rho_1,\rho_2} \approx 6.4$. For both cases, $W/(2\pi) = 3.2$ MHz, $\bar{V}_1/(2\pi) = -64.5$ MHz, and $\bar{V}_2/(2\pi) = -1.6$ MHz, corresponding to the interatomic distances $d = 8$ μm and $\delta = 2$ μm. Note that $\mathcal{N}_{\rho_1,\rho_2}$ has been calculated using data up to $t = 100$ μs.

damped oscillations, we find non-Markovian dimer dynamics with oscillations of alternating amplitude for large Rabi frequencies $\Omega_p \sim \Omega_c$ and large laser detunings obeying $\Delta_p + \Delta_c \sim 0$. Note that although $\sigma(\rho_1, \rho_2)$ is only shown up to $t = 3$ μs, the data underlying $\mathcal{N}_{\rho_1,\rho_2}$ extends to longer times ($t = 100$ μs), guaranteeing that $\mathcal{N}_{\rho_1,\rho_2}$ has converged. In experiment, dimer dynamics cannot be studied for arbitrarily long times due to the finite dimer lifetime ($\tau_{\text{agg}} \approx 56$ μs, cf. Fig. 2.11(b)).

The difference in the population oscillations in panel (a) of Figure 2.24 compared to panel (c) suggests that non-Markovian dynamics manifests itself in temporal structures of the population dynamics, such as revivals. This is not always the case. We stress that visible non-Markovian features in the population dynamics are not necessarily present even if the system dynamics is non-Markovian. Indeed, in Fig. 2.25 we show two examples of non-Markovian system dynamics with clearly positive contributions $\sigma(\rho_1, \rho_2) > 0$ but distinct dynamics. The population dynamics of $|\pi_1\rangle$ displayed in panel (a) with $\mathcal{N}_{\rho_1,\rho_2} \approx 3.3$ as shown in panel (b) does not exhibit noticeable revivals or other features often associated with non-Markovian dynamics. Panel (c), in contrast, shows oscillations of irregular amplitude of the population of state $|\pi_1\rangle$ and large-amplitude oscillations in $\sigma(\rho_1, \rho_2)$, yielding $\mathcal{N}_{\rho_1,\rho_2} \approx 7.8$. It should be noted that this cannot be explained by the larger value of the quantity $\mathcal{N}_{\rho_1,\rho_2}$ in (a) as compared to (c). Even dynamics with smaller values of $\mathcal{N}_{\rho_1,\rho_2}$ than 3.3 can display non-Markovian features [65]. Hence, the population dynamics does not represent a good indicator for non-Markovianity.

What is more, the features found in the oscillations of p_1 shown in panels (c) of Figs. 2.24 and 2.25 cannot be explained by the use of a single background atom in the simulations, but have to be attributed to the specific dynamics within the environment. We have verified

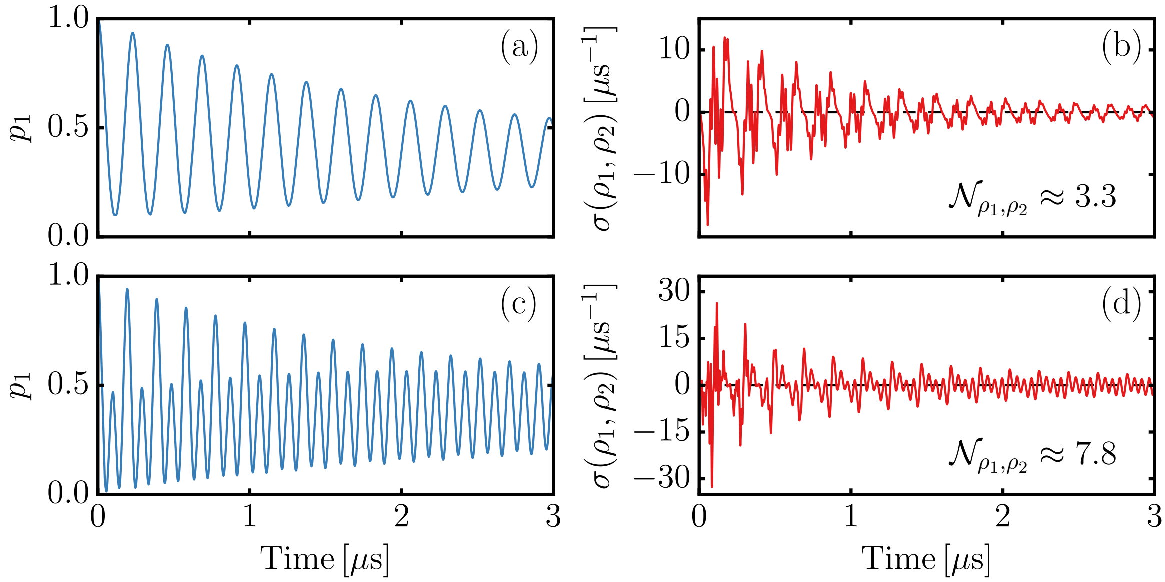

Figure 2.25: Aggregate dynamics for two different degrees of non-Markovianity. Panel (a) shows non-Markovian aggregate dynamics with $\mathcal{N}_{\rho_1,\rho_2} \approx 3.3$, for which the population dynamics of state $|\pi_1\rangle$ does not exhibit noticeable irregularities. The time evolution of $\sigma(\rho_1, \rho_2)$ is displayed in panel (b). Both (a) and (b) have been obtained using the parameters $\Omega_p/(2\pi) = 29.7$ MHz, $\Delta_p/(2\pi) = -53.2$ MHz, $\Omega_c/(2\pi) = 27.2$ MHz, $\Delta_c/(2\pi) = 56$ MHz, $W/(2\pi) = 2.4$ MHz, $\bar{V}_1/(2\pi) = -44.1$ MHz, and $\bar{V}_2/(2\pi) = -0.9$ MHz, corresponding to the interatomic distances $d = 8.8$ μm and $\delta = 2.2$ μm. Panel (c) shows non-Markovian aggregate dynamics with $\mathcal{N}_{\rho_1,\rho_2} \approx 7.8$, also reflected in the irregular population oscillations of state $|\pi_1\rangle$. The corresponding time evolution of $\sigma(\rho_1, \rho_2)$ is depicted in panel (d). The parameters used here are $\Omega_p/(2\pi) = 29$ MHz, $\Delta_p/(2\pi) = 77.5$ MHz, $\Omega_c/(2\pi) = 24$ MHz, $\Delta_c/(2\pi) = -80$ MHz, $W/(2\pi) = 4.7$ MHz, $\bar{V}_1/(2\pi) = -64.5$ MHz, and $\bar{V}_2/(2\pi) = -1.7$ MHz, corresponding to the interatomic distances $d = 7$ μm and $\delta = 2$ μm.

this by introducing a second background atom with separation δ (d) from the second dimer atom (first background atom), which yields a population dynamics of the aggregate states that also exhibits "irregular" features. Effects pertaining to the asymmetric setup (two aggregate atoms, one background atom) are thus not responsible for non-Markovian dynamics or even steady-state values with unequal population $p_1 \neq p_2$. The control over the degree of Markovianity of the system dynamics is enabled by the possibility to influence the timescale of the background dynamics via the laser parameters.

The results discussed above show that by modifying the interatomic distances as well as the laser parameters, we can switch the dimer dynamics from Markovian to non-Markovian and can tune the degree non-Markovianity. This allows one to study Markovian and non-Markovian dynamics in a controlled fashion. We have found that the following ingredients are required to observe non-Markovianity in the system dynamics:

(i) "Long" intrinsic timescale of the background dynamics, in particular of the Rydberg population, to provide environment memory. A long intrinsic timescale can be achieved by, e.g., reducing the radiative decay rate Γ_p (which is, however, experimentally impractical) or by introducing a large detuning Δ_p of the intermediate state while at the same time keeping the two-photon resonance condition $\Delta_p + \Delta_c \sim 0$. The timescale to which the intrinsic timescale (or equilibration timescale) compares to is the dipole-dipole interaction strength W.

(ii) Comparability of timescales of aggregate and background atom dynamics. Comparable timescales between aggregate and background atom dynamics are important since coupling between two systems with significantly different time (or energy) scales is inhibited. A similar timescale of the dynamics can be most easily attained by tuning the aggregate coupling W, as the background atom timescale results from a complex interplay of laser parameters, radiative decay and interactions.

(iii) Correlation between aggregate dynamics and photon emission from the background atom, i.e., ability to deduce the state of the aggregate by measuring the photons emitted by the background atom. Though this condition is not fully separable from the previous one (ii), it can be met by ensuring a strong interaction $\bar{V}_1$ between the aggregate in state $|\pi_1\rangle$ and the background atom, and a strong difference $\bar{V}_1 \gg \bar{V}_2$ between the interactions $\bar{V}_1$ and $\bar{V}_2$ of the two aggregate states with the background atom.

In the above list, the first condition (i) guarantees the presence of environment memory, and conditions (ii) and (iii) guarantee the visibility of the environment dynamics in the system dynamics. This can be seen in Fig. 2.25: To reduce the degree of non-Markovianity in Fig. 2.25(a) as compared to Fig. 2.25(c), we reduced the detuning $|\Delta_p|$, the interaction $\bar{V}_1$, and the aggregate coupling W. Reducing the detuning $|\Delta_p|$ decreases the equilibration time of the background dynamics, decreasing the interaction $\bar{V}_1$ reduces the correlation between aggregate and background atom, and reducing the aggregate coupling W decreases the visibility of the back-action induced by the background dynamics. In Fig. 2.24, where we keep the aggregate coupling W as well as the interactions $\bar{V}_{1,2}$ fixed, non-Markovian dynamics is introduced via intermediate state detuning Δ_p and increased Rabi frequencies of both probe and coupling laser. This illustrates that the three conditions (i)-(iii) listed above are intertwined since all conditions depend on the laser parameters, which strongly influence the background atom dynamics. Still, condition (iii) is reflected in the difficulty to find parameters for Markovian dynamics for larger Rabi frequencies Ω_p, and correspondingly larger dephasing rates of the aggregate.[13]

The seeming contradiction between conditions (i) and (ii) is due to the difficulty to classify the large parameter space in which non-Markovian dynamics can be achieved. Clearly, for slow aggregate dynamics, the timescale on which the intrinsic dynamics of the background atom proceeds can be much longer than for fast aggregate dynamics. In fact, if the aggregate spacing d in Fig. 2.23 is reduced to 5 μm, non-Markovian dynamics arises also in this case. If the timescale of the aggregate dynamics is reduced further, however, the degree of non-Markovianity decreases again since the timescales of aggregate and background atom become incompatible [condition (ii)]. This is illustrated in Fig. 2.26, which shows $\mathcal{N}_{\rho_1,\rho_2}$ as a function of the aggregate spacing d [panel (a)], as well as the corresponding resonant dipole-dipole interaction strength W [panel (b)]. One finds that there exists an aggregate spacing ($d \approx 3.7$ μm, corresponding to $W \approx 201$ MHz) that maximizes the non-Markovian quantifier (2.85), which supports our reasoning from above. We note that for numerical reasons, only dynamics until $t = 10$ μs has been taken into account for the calculation of $\mathcal{N}_{\rho_1,\rho_2}$ in Fig. 2.26. More precisely, since the sampling time step has to be adjusted for each aggregate spacing due to the change in oscillation frequency over orders of magnitudes during the scan over aggregate spacings, long propagation times are numerically expensive. In addition, the steady state is reached only after long times ($t \gg 10$ μs), which implies that calculations are significantly slowed down, and numerical errors can accumulate during the

---

[13] Numerical optimization using the method detailed in Sec. 2.6.1 with $\mathcal{N}_{\rho_1,\rho_2}$ being the objective function to be minimized with respect to the constraints $\Omega_p/(2\pi) \in [1, 30]$ MHz, $\Omega_c/(2\pi) \in [1, 90]$ MHz, and $\Delta_p/(2\pi)$ as well as $\Delta_c/(2\pi) \in [-70, 70]$ MHz did not yield parameter sets with large Rabi frequencies, if a result was obtained at all.

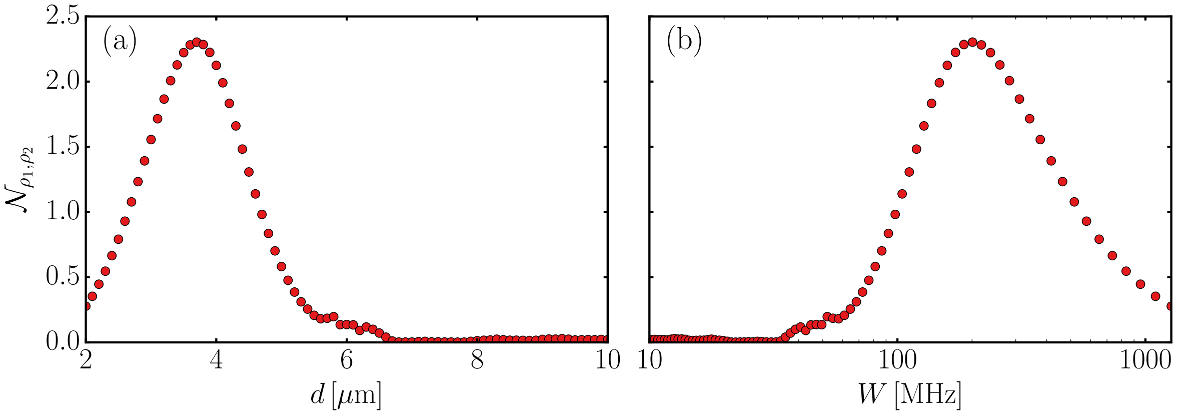

Figure 2.26: Non-Markovianity quantifier $\mathcal{N}_{\rho_1,\rho_2}$ as a function of the aggregate spacing d (a) respectively the corresponding resonant dipole-dipole interaction strength W (b), using the parameters of Fig. 2.23 with $\Omega_p/(2\pi) = 6$ MHz. For the evaluation of $\mathcal{N}_{\rho_1,\rho_2}$, the time evolution of $\rho_1(t)$ and $\rho_2(t)$ has been calculated until $t = 10$ μs.

evolution. By evaluating the same observable $\mathcal{N}_{\rho_1,\rho_2}$ for a fixed number of oscillations instead of a fixed final time, we have verified that the shape of Fig. 2.26 is not an artifact of the propagation time.

In summary, the presented setup provides a test bench to study non-Markovianity in open quantum systems. We have shown that both Markovian as well as non-Markovian system dynamics can be achieved by the driven-dissipative environment provided by the background atom. Control over laser parameters driving the background atom enable manipulation of the background atom dynamics, thereby also providing control over the degree of Markovianity of the system dynamics. Besides, our analysis reveals that (non-)Markovianity of the system (dimer) dynamics cannot be easily inferred from population dynamics alone; a measure relying on the information provided by the full density matrix of the system has to be employed. Having shown the variety of Markovian and non-Markovian dynamics as well as dephasing timescales and steady-state values of the system in the case of a simple setup employing a single background atom, we expect even richer tunability of the dynamics in the case of many background atoms. This might open up new prospects for using Rydberg aggregates as quantum simulators with a controlled environment.

2.6 Engineering aggregate states

In the previous sections we have seen that various dynamical effects such as decoherence and non-Markovianity can be induced in the aggregate using the control over the atomic environment, viz., the background atoms. Now we address the question of how the environment provided by the background atoms can be used to prepare particular aggregate states. For a quantum simulator designed to solve the dynamics of open quantum systems, this question is of crucial importance. Firstly, quantum simulation of certain processes require the system to be initially prepared in a specific state, such as a thermal state or an entangled state. Secondly, in an open quantum system, the interaction with the environment typically brings the system into a steady state, which depends on specifics of the environment such as environment temperature, for example. A quantum simulator, whose task is to reproduce the dynamics generated by the environment-couplings of the target system, must capture the evolution towards such steady states. What is more, its is desirable to realize a broad range of environments with specific

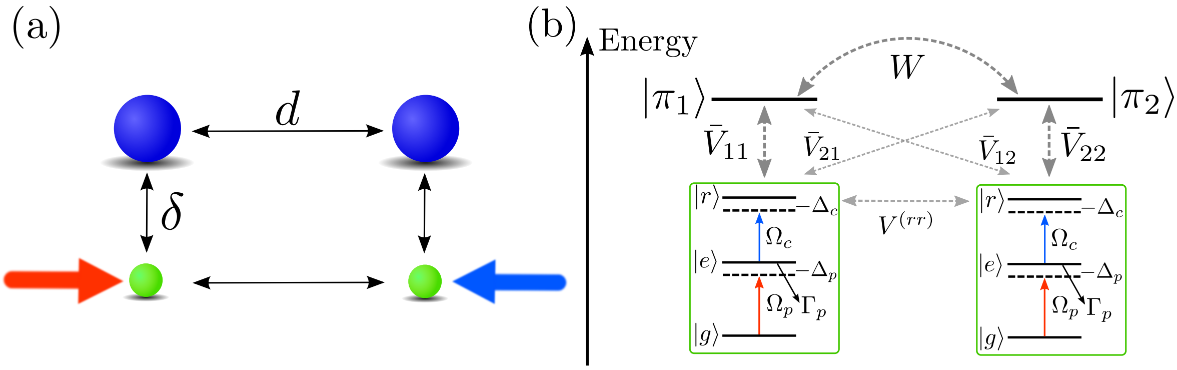

Figure 2.27: Sketch of the setup. (a) Laser-driven environment atoms are placed at a distance δ from each of the system atoms, which have interatomic separation d. (b) Level sketch. The dimer states $|\pi_1\rangle$ and $|\pi_2\rangle$ are coupled to each other via resonant dipole-dipole interaction with strength W and interact with the Rydberg states $|r\rangle$ of the background atoms via the interactions $\bar{V}_{n\alpha}$. The background atoms are laser-driven, realizing the level scheme depicted in the green boxes.

properties using the same quantum simulation setup.

Coherent [295, 296] and incoherent approaches [297] have been developed for this reservoir engineering problem, for particular environments or degrees of freedom in the system. Reservoir engineering, which involves the design of the environment or its coupling to the system, guarantees that the dynamics generated by the environment-couplings of the target system is reproduced in the simulator [8, 298], even though the quantum simulator is a physical system totally different from the target system.

In this section, we consider reservoir engineering of thermal environments [66], i.e., environments that induce thermal populations of aggregate eigenstates. Specifically, using optical control, we transform a typically non-thermal environment into a thermal environment with controllable temperature. Access to an arbitrary-temperature thermal environment provides two-fold benefits. Firstly, a system with a fixed-temperature environment can simulate more general non-equilibrium dynamics. In our case, the temperature of the Rydberg aggregate can be significantly higher than the ambient, ultralow temperature. Secondly, thermal state preparation allows the study of interacting systems initially at equilibrium, which has motivated the design of digital algorithms [299–302]. In addition to thermal states, we also give examples for the preparation of the Rydberg aggregate in a single (entangled) eigenstate. This provides a convenient means to prepare the initial state required, e.g., for entanglement transport in a flexible Rydberg chain [303].

The state preparation technique we employ harnesses the driven-dissipative environment constituted by the background atoms and visualized before in Fig. 2.21. Due to the dissipation, system and environment evolve towards a unique steady state [188], which is independent of the initial condition. Accordingly, information on the initial state is lost during the dissipative preparation. This is an unwanted effect in quantum computing, where the final state after a gate operation is intimately linked to the initial state, but a wanted one in state preparation, where one wants to obtain the desired final state irrespective of the initial state. Using this dissipative approach, we prepare system eigenstates and thermal states (i) on a timescale shorter than the system decay timescale and (ii) in a long time limit. While (i) demonstrates dissipative state preparation of entangled and thermal states, (ii) can be used to mimic a thermal environment for a quantum simulator. We highlight that the effective temperature scale of the Boltzmann distribution of eigenstates is determined by the system interaction strength rather than the 'ambient' temperature of the ultracold environment.

We now exemplify the relevant properties of our setup for a Rydberg dimer, i.e., two Rydberg atoms with interatomic separation d as shown in Fig. 2.27(a). The environment for the Rydberg system is provided by laser-driven atoms. For simplicity, we place each at a distance δ from a given system-atom, such that the vectors along d and δ respectively enclose a right angle. For the larger system sizes discussed later, this arrangement is straightforwardly extended, keeping the interatomic separation between adjacent system atoms (system and environment atoms) at d (δ). The environment atoms are addressed by two laser beams. The first laser, with Rabi frequency Ω_p and detuning Δ_p, couples the ground state $|g\rangle$ of an environment atom to a short-lived intermediate state $|e\rangle$ with radiative decay rate Γ_p. The second laser, with Rabi frequency Ω_c and detuning Δ_c, couples the intermediate state $|e\rangle$ to a Rydberg state $|r\rangle \neq |p\rangle, |s\rangle$. Again we ignore the decay of the Rydberg state $|r\rangle$, which has a much longer lifetime than the state $|e\rangle$ (cf. Sec. 2.2.5). For simplicity, we also do not include the finite lifetime of the system in our calculations; this is approximately 56 μs for the dimer states we consider [72]. Effects of these decay channels are discussed in Sec. 2.6.3.

The resulting level diagram including the interactions between Rydberg dimer and background atoms is depicted in Fig. 2.27(b). The dimer states $|\pi_{1(2)}\rangle$ (corresponding to the configurations with the $|p\rangle$ excitation localized at site 1(2)) are coupled via resonant dipole-dipole interaction W. In the dimer case, this leads to the eigenvalues $E_\pm = \pm W$ of the dimer Hamiltonian, and the corresponding eigenstates are the Bell states $|\Psi^\pm\rangle = (|\pi_1\rangle \pm |\pi_2\rangle)/\sqrt{2}$. The effective interactions of the dimer states with the background atoms are denoted by $\bar{V}_{n\alpha} = V_{n\alpha}^{(pr)} + \sum_{m\neq n} V_{m\alpha}^{(sr)}$. Due to their distance-dependence, the interactions $V_{n\alpha}^{(pr)}$ and $V_{n\alpha}^{(sr)}$ are strongest for $\alpha = n$, i.e. adjacent environment and system atoms. Since furthermore $|V_{nn}^{(pr)}| \gg |V_{nn}^{(sr)}|$, the interactions $\bar{V}_{nn}$ are much stronger than the interactions $\bar{V}_{n\neq m}$, as indicated by the thickness of the arrows in Fig. 2.27(b). Lastly, the van der Waals interaction between the environment atoms is given by $V^{(rr)}$. Note that the findings of this section do not rely on the specific Rydberg states chosen, but on the state-dependence of interactions between Rydberg aggregate and background atoms.

Control over the environment dynamics is achieved by tuning the laser parameters addressing the environment atoms. The numerical optimization procedure by which we obtain an appropriate set of laser parameters, as well as measures which allow one to quantify the quality of the numerical optimization result are discussed in Sec. 2.6.1. Section 2.6.2 shows that the Rydberg dimer can be dissipatively prepared in the Bell eigenstates $|\Psi^\pm\rangle$ of the system Hamiltonian, and briefly discusses the responsible mechanism. In Sec. 2.6.3, we extend the dissipative preparation to thermal states and give a detailed account of the robustness of our preparation scheme with respect to laser parameter variations, distance variations, and aggregate size.

2.6.1 Numerical optimization and distance measures

To obtain a suitable set of laser parameters $(\Omega_p, \Delta_p, \Omega_c, \Delta_c)$ for dissipative preparation of aggregate states we employ numerical optimization using a fixed, experimentally accessible [98, 213] environment-atom geometry with $d = 5$ μm and $\delta = 2$ μm. The aggregate spacing of $d = 5$ μm implies a clear separation of aggregate eigenstates in energy, $2W/(2\pi) = 26$ MHz, which allows one to energetically resolve either aggregate eigenstate on a short (microsecond) timescale. Moreover, for the chosen aggregate-environment distance $\delta = 2$ μm, the aggregate-environment interactions are strongly state-dependent, $|V_{nn}^{(pr)}|/|V_{nn}^{(sr)}| \sim 50$ with $|V_{nn}^{(sr)}|$ being smaller than the power-broadening resulting from typical coupling Rabi frequencies Ω_c, which gives rise to distinct aggregate-state-dependent dynamics in the adjacent environment atom. In terms of the critical EIT radius, an environment atom in EIT configuration placed at a distance $\delta = 2\ \mu$m from an aggregate atom lies within the region that allows one to distinguish between $|p\rangle$ and $|s\rangle$ state for a large range of Rabi frequencies Ω_c. Our choice of distances allows therefore for grand tunability of the aggregate dynamics via the laser parameters addressing the environment atoms. Note that the optimized laser parameters are independent of the initial state of system or environment. We thus use an initial system (environment) state that is easy to access experimentally in our numerical simulations, given by $|\pi_1\rangle$ ($|gg\rangle$).

To perform the numerical optimization, we use the bound-constrained "Controlled Random Search (CRS) with local mutation (`GN_CRS2_LM`)"-alorithm provided by the `nlopt` package in python; the numerical simulations are done with `QuTiP` [304]. This algorithm has been chosen owing to its good performance, even compared to local optimization algorithms with random initial parameter guesses. In fact, bound-constrained local optimization (Nelder-Mead or COBYLA) starting from the optimization result obtained via `GN_CRS2_LM` yielded an improved result only in a few cases.

The optimization algorithm `GN_CRS2_LM` iteratively tries to find the global parameter optimum (depending on the specification, either maximum or minimum) with respect to the objective function. It requires an objective function (or cost function) that depends on the laser parameters $(\Omega_p, \Delta_p, \Omega_c, \Delta_c)$, an initial guess for the optimal parameter set, and parameter constraints. We choose the parameter constraints as follows: $\Omega_p/(2\pi) \in [0.1, 35]$ MHz, $\Omega_c/(2\pi) \in [0.1, 100]$ MHz, and $\Delta_p/(2\pi)$ as well as $\Delta_c/(2\pi) \in [-100, 100]$ MHz. These constraints restrict our parameters to currently-achievable experimental parameters [93, 218]; the detunings are small enough to guarantee that no resonance other than the intended transition is hit.

Although we use a global optimization algorithm, we found that the optimization results do depend on the initial parameter choices, since specified tolerances determine the stopping criteria of the algorithm. In our simulation, we use a relative stopping criterion, i.e., the algorithm stops in case of a relative change of less than 10^{-3} in either the objective function or the parameter values in two subsequent iterations of the algorithm. To obtain a good optimization result, numerical optimization starting from different (randomly determined) initial parameter guesses can thus be advisable. For optimization problems which seemed to have difficulties finding a global optimum, we looped over different random initial conditions and used the optimization result only if it met a criterion specified beforehand in terms of an objective function value.

To assess the difference between the target density matrix and the density matrix obtained after numerical propagation, we employ two often-adopted distance measures (cf. Refs. [305, 306]). The first measure is the *fidelity* $F(\rho_1, \rho_2)$. The fidelity between two density matrices ρ_1 and ρ_2 is defined as [305]

$$F(\rho_1, \rho_2) = \mathrm{Tr}\left\{\sqrt{\sqrt{\rho_1}\rho_2\sqrt{\rho_1}}\right\}, \tag{2.86}$$

and can be interpreted a generalized measure of the overlap between two quantum states [306]. The second measure is related to the *trace distance* via

$$F_D(\rho_1, \rho_2) = 1 - D(\rho_1, \rho_2). \tag{2.87}$$

The trace distance $D(\rho_1, \rho_2)$, which can be interpreted as a measure of state distinguishability [273], has been defined previously in Eq. (2.83). From the relation $1 - F(\rho_1, \rho_2) \leq D(\rho_1, \rho_2)$ [305] it follows that $F_D(\rho_1, \rho_2) \leq F(\rho_1, \rho_2)$, which implies that $F_D(\rho_1, \rho_2)$ is a more conservative measure.

To illustrate the different timescales on which steady-state preparation is feasible, we evaluate the two distance measures F and F_D at $t = 1\ \mu$s and $t \to \infty$ respectively, denoting the $t \to \infty$ case by $\tilde{F}$ and $\tilde{F}_D$. Note that a summary of all values $(F, F_D, \tilde{F}, \tilde{F}_D)$ for the state

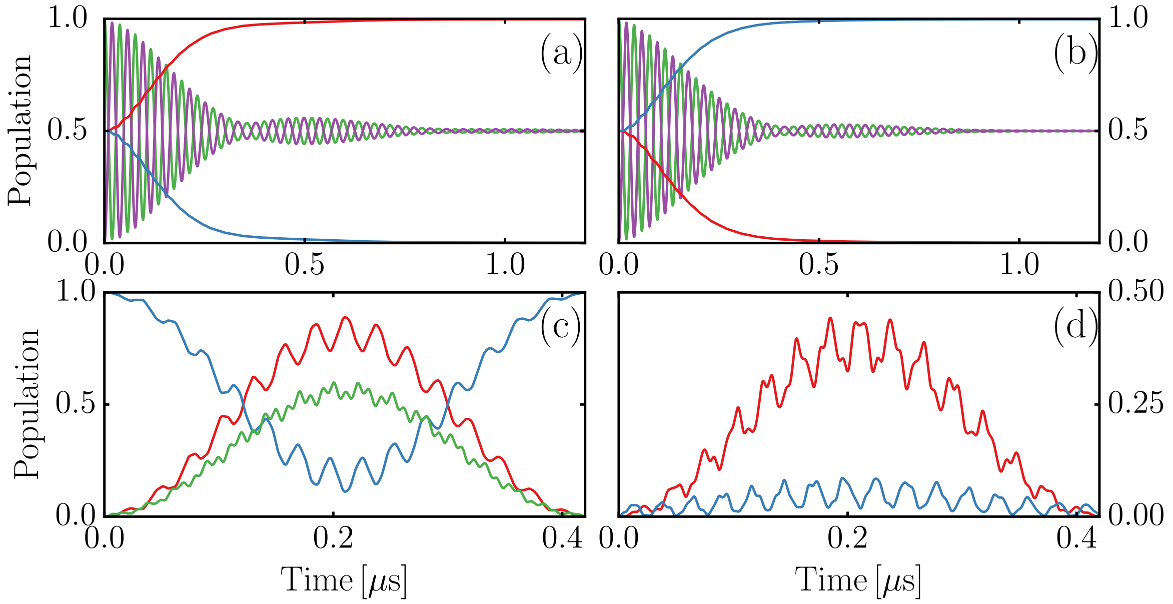

Figure 2.28: Bell state preparation in a Rydberg dimer. (a,b) Population dynamics of anti-symmetric (a) and symmetric (b) Bell state. Red (blue) lines indicate the population of the anti-symmetric (symmetric) Bell state and green (purple) lines indicate the populations of the states $|\pi_1\rangle$ ($|\pi_2\rangle$). Laser parameters are listed in Tab. 2.6. (c,d) Coherent evolution (neglecting dissipation) with parameters as in panel (a). Note the different timescale from the upper plots. In (c), the green (red/blue) line denotes the population dynamics of $P_{r(-/+)}$ after initial preparation in state $|\Psi^+\rangle\,|gg\rangle$ (cf. main text). (d) The red (blue) line denotes $P_{-(+)}$ as in (c), but additionally projected on the state $|e\rangle$ of the environment.

preparations shown in this chapter together with the corresponding laser parameters and states is given in Tab. 2.6 below. To obtain these exemplary parameter values we used F (F_D) as an objective function in our simulations for aggregate sizes with $N < 3$ ($N \geq 3$).

2.6.2 Bell-state preparation

We start our discussion of numerical results with the preparation of a single aggregate eigenstate, which is a Bell state in case of a Rydberg dimer. In Fig. 2.28 we illustrate the preparation of the anti-symmetric $|\Psi^-\rangle$ [panel (a)] as well as the symmetric $|\Psi^+\rangle$ Bell state [panel (b)]. The marked revival feature in the population dynamics [green and purple lines in panels (a) and (b)] is absent in the dynamics of the eigenstate populations [red and blue lines in panels (a) and (b)], indicating that the eigenstates can indeed be selectively addressed by the dissipative environment. Using the laser parameters listed in Tab. 2.6, the preparation of the anti-symmetric (symmetric) Bell state is performed with fidelity $F = 0.999$ ($F = 0.999$) respectively $F_D = 0.992$ ($F_D = 0.997$) after 1 μs. In the steady state, F stays constant while F_D improves for both states to $\tilde{F}_D = 0.998$ (cf. Tab. 2.6). Hence, high-fidelity preparation of single aggregate eigenstates is possible on a timescale short compared to the aggregate lifetime of $t = 56$ μs.

To gain insight into the dissipative state preparation mechanism, we now examine the underlying coherent evolution for the system and atomic environment. In particular, we consider the preparation of the $|\Psi^-\rangle$ state as in Fig. 2.28(a); the same mechanism (with $|\Psi^+\rangle \leftrightarrow |\Psi^-\rangle$) describes preparation of the $|\Psi^+\rangle$ state. We accordingly focus on the dynamics of the Bell eigenstates of the system, which are separable from environment states containing no Rydberg excitations. That is, since the Rydberg-Rydberg interactions between system and environment (i.e., background atoms) are state-dependent, correlations exist between environment and system in the presence of environment Rydberg-excitations, whereas in their absence no correlations exist.

In Fig. 2.28(c) we plot the coherent population dynamics (with no dissipative decay from $|e\rangle$) of both system eigenstates $|\Psi^{\pm}\rangle$ and environment Rydberg state $|r\rangle$ after initial preparation in state $|\Psi^{+}\rangle\,|gg\rangle$; i.e., the system (environment) is initially in the symmetric Bell state (ground state). The population in a particular Bell state is evaluated by taking the expectation value of the projection operators $P_{+(-)}$ on the coupled system-environment dynamics in the subspace of the aggregate (and unity in the environment subspace), given by

$$P_{+(-)} = |\Psi^{+(-)}\rangle\langle\Psi^{+(-)}|\,. \tag{2.88}$$

The environment atom Rydberg population we evaluate using the projection operator in the environment subspace (and unity in the aggregate subspace),

$$P_r = I \otimes |r\rangle\langle r| + |r\rangle\langle r| \otimes I. \tag{2.89}$$

As can be seen in Fig. 2.28(c), the $|\Psi^{+}\rangle$ and $|\Psi^{-}\rangle$ system states are coherently coupled. Since the system eigenstates are decoupled in the absence of the environment atoms, this coupling proceeds via the environment. In fact, the $|\Psi^{-}\rangle$ state becomes accessible through Rydberg-Rydberg interactions between system and environment atoms, as illustrated by the correlation between the dynamics of the anti-symmetric Bell state (red line) and the Rydberg population (green line) in Fig. 2.28(c). When we subsequently project the populations of the Bell eigenstates on the environment state $|e\rangle$, shown in Fig. 2.28(d), we observe a strong correlation between occupation of $|e\rangle$ and the target $|\Psi^{-}\rangle$ system-state. This implies that when decay from $|e\rangle$ is introduced, population is dissipatively pumped into the $|\Psi^{-}\rangle\,|gg\rangle$ state, which is effectively dark to both driving and dissipation. Thus, the state-selective Rydberg-Rydberg interaction between system and environment allows us to couple only a single system eigenstate to the dissipative channel of our environment, thereby engineering a particular system steady state.

2.6.3 Thermal-state preparation

In addition to the preparation of a single system eigenstate, we can also prepare mixtures of eigenstates. To illustrate this, we consider thermal states [307]

$$\rho_T^{\mathrm{th}} = \frac{1}{Z}\sum_n e^{-\mathcal{H}_{\mathrm{agg}}/(kT)}\,|\varphi_n\rangle\langle\varphi_n|, \tag{2.90}$$

where $Z = \mathrm{Tr}\{e^{-\mathcal{H}_{\mathrm{agg}}/(kT)}\,|\varphi_n\rangle\langle\varphi_n|\}$, $|\varphi_n\rangle$ denotes the eigenstates of $\mathcal{H}_{\mathrm{agg}}$, k the Boltzmann constant and T the temperature of the system. The target populations indicated with black dashed lines in the subsequent figures are calculated according to this formula. Note that the relevant energy scale providing the temperature scale here is the resonant dipole-dipole interaction W. For a dimer, the two system eigenstates are separated in energy by $2W$, such that $\rho_T^{\mathrm{th}} \propto (|\varphi_1\rangle\langle\varphi_1| + e^{-2W/(kT)}\,|\varphi_2\rangle\langle\varphi_2|)$. We emphasize that T is not the ambient temperature of the environment atoms, which is typically $\sim \mu$K.

To illustrate the versatility of the scheme we demonstrate low and high temperature mixtures, given by $kT_L = 1.2\ W$ and $kT_H = 12.3\ W$ respectively. The numerical values are chosen such that T_L yields strong asymmetries in the eigenstate populations while T_H yields similar occupations of the eigenstates.

For a Rydberg dimer, the preparation of thermal states with temperature T_L (a) and T_H (b) is shown in Fig. 2.29, using exemplary laser parameter sets (see Tab. 2.6). Both states can

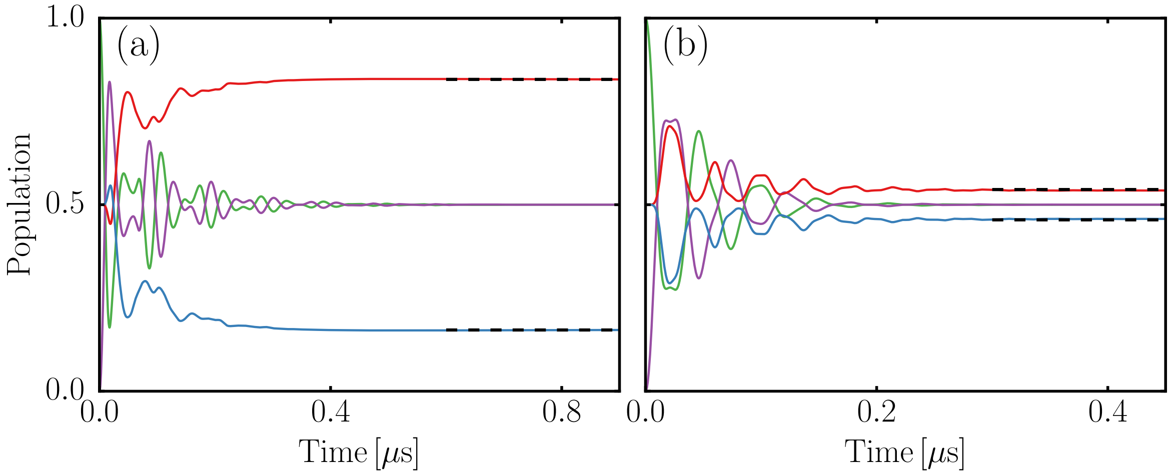

Figure 2.29: Population dynamics of thermal state preparation in a Rydberg dimer with temperatures T_L (a) and T_H (b). Solid red (blue) lines denote the population of the lower (higher) energy eigenstate $\left|\Psi^{-(+)}\right\rangle$ while green (purple) lines indicate localized state $|\pi_1\rangle$ ($|\pi_2\rangle$) populations. The target populations are shown with black dashed lines. Laser parameters are listed in Tab. 2.6. Note the different scaling of the time axes.

be prepared with high fidelity ($F_D \geq 0.997$ after 1 μs, with no further improvement in the steady state). In contrast to the Bell state preparation illustrated in Fig. 2.28, the oscillatory features in the aggregate population in Fig. 2.29 (green and purple lines) are reflected in the eigenstate dynamics (red and blue lines). This indicates that the mechanism responsible for the state preparation can no longer be understood as a single aggregate eigenstate coupled to a dissipative channel.

The thermal state is sustained through competition between the dissipative decay and coherent dynamics. This is in contrast to Bell state preparation, which involves laser parameters such that the target system eigenstate (and ground environment state) is minimally affected by either coherent or incoherent dynamics. This complicates a clear understanding of the preparation mechanism such as outlined above. Considering the large landscape of possible laser parameter values which yield high preparation fidelity (see discussion below), we cannot give a simple explanation of the state-preparation mechanism that covers all possible parameter combinations in this case.

As a side note, the dimer-state preparations discussed so far involve non-Markovian system evolution according to Eq. (2.85). The degree of non-Markovianity does not correlate with the preparation fidelity, nor is there a clear correlation between the degree of non-Markoviantiy and thermal-state temperature. This is consistent with our conclusion in Sec. 2.5, namely that non-Markovian dynamics does not necessarily exhibit distinct features.

Robustness of the preparation scheme

We now assess the robustness of the preparation scheme. That is, for the target state to be experimentally accessible, it is important that small variations in the laser parameters or distances do not lead to a strong reduction of the fidelity. We thus study the dependence of the state-preparation quality for thermal-state preparation, quantified by F_D, for both laser parameters and distances in the following.

In Fig. 2.30 we show the dependence of F_D for thermal dimer-state preparation with temperature T_L on all possible combinations of laser-parameter tuples involving the laser

Table 2.6: Summary of measures F and F_D as well as the laser parameters $\Omega_p, \Delta_p, \Omega_c, \Delta_c$. The two measures F and F_D are evaluated at $t = 1$ μs (F, F_D) and in the steady state $(\tilde{F}, \tilde{F}_D)$.

N	Target state	$(F, \tilde{F})$	$(F_D, \tilde{F}_D)$	$\Omega_p/(2\pi)$ (MHz)	$\Omega_c/(2\pi)$ (MHz)	$\Delta_p/(2\pi)$ (MHz)	$\Delta_c/(2\pi)$ (MHz)
2	$\vert\Psi^-\rangle\langle\Psi^-\vert$	(0.999, 0.999)	(0.992, 0.998)	7.6	95.3	-75.8	-44.9
2	$\vert\Psi^+\rangle\langle\Psi^+\vert$	(0.999, 0.999)	(0.997, 0.998)	8.0	89.8	65.3	-7.7
2	$\rho^{\text{th}}_{T_L}$	(>0.999, >0.999)	(>0.999, 0.999)	19.7	35.6	-18.1	-4.6
2	$\rho^{\text{th}}_{T_H}$	(>0.999, >0.999)	(0.997, 0.997)	30.0	48.9	-7.3	-70.4
3	$\rho^{\text{th}}_{T_L}$	(>0.999, >0.999)	(0.994, 0.992)	9.5	34.5	-7.5	-71.0
3	$\rho^{\text{th}}_{T_H}$	(>0.999, >0.999)	(0.999, 0.999)	27.8	66.9	-18.3	-33.7
4	$\rho^{\text{th}}_{T_L}$	(0.996, >0.999)	(0.931, 0.990)	34.6	34.9	-34.5	-70.6
4	$\rho^{\text{th}}_{T_H}$	(>0.999, >0.999)	(0.994, 0.994)	35.0	43.3	-1.3	-45.8

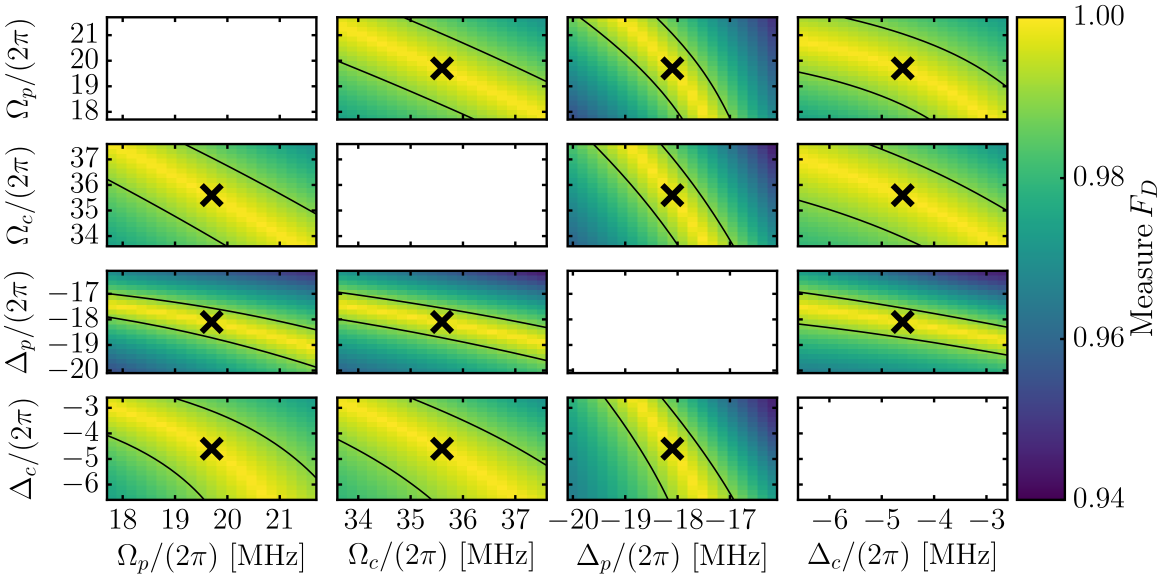

Figure 2.30: Measure F_D of the thermal-state preparation quality in a Rydberg dimer with temperature T_L as a function of the various laser parameters Ω_p, Ω_c, Δ_p, and Δ_c. Crosses mark the values of the laser parameters used for the thermal-state preparation shown in Fig. 2.29; the laser parameters that are not indicated in the axes are set to their respective values listed in Tab. 2.6. The solid black lines mark the contour defined by $F_D = 0.99$. Note that for the sake of presentation, the unit MHz has been omitted in the y-axes labels.

parameters Ω_p, Ω_c, Δ_p, and Δ_c. The laser parameters are centered around their 'optimal' values (corresponding to the values used in Fig. 2.29 and listed in Tab. 2.6), which are indicated by black crosses. Solid black lines mark the contour defined by $F_D = 0.99$. As can be seen from the figure, for any parameter tuple there is a direction in parameter space in which F_D does not decrease significantly. The range of possible parameter variations for which $F_D \geq 0.99$ depends on the parameters which are varied. This implies that (i) the laser parameter values required to obtain high target-state fidelities are non-unique, (ii) thermal state-preparation is robust with respect to small ($\lesssim 0.5 \times 2\pi$ MHz) fluctuations in the laser parameters and (iii) even large fluctuations of laser parameters in parameter space can still yield high-fidelity thermal-state preparation, if the fluctuations are along certain directions in parameter space. We note that the F_D-landscape depends on the desired target state, which is the thermal state with temperature T_L for the scenarios shown in Fig. 2.30.

The points (i–iii) become clearer when considering Fig. 2.31, which shows F_D for a thermal-state preparation of a Rydberg dimer with temperature T_H (left panel: F_D evaluated after $t = 1$ μs, right panel: steady-state value $\tilde{F_D}$) as a function of the laser detunings Δ_p and Δ_c, while keeping the Rabi frequencies fixed at their respective 'optimal' value listed in Tab. 2.6. The laser detuning values span the whole range in which numerical optimization is performed. The region enclosed by the solid black lines in the left (right) panel corresponds to thermal-state preparation with $F_D > 0.99$ ($\tilde{F_D} > 0.99$). Several, not connected islands exist in parameter space for which high-fidelity thermal-state preparation is possible. These islands extend for larger times, reflecting the general observation that steady-state preparation fidelities are typically more robust with respect to parameter variations than the fidelities obtained at $t = 1$ μs. Since the optimal regions are extended along some direction in parameter space, joint variations of laser parameters are possible without significant loss of preparation fidelity.

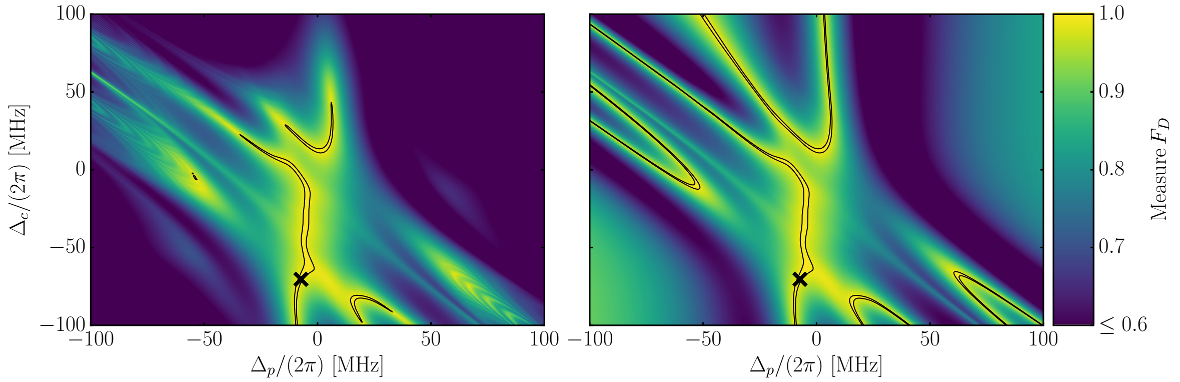

Figure 2.31: Thermal-state preparation in a Rydberg dimer with temperature T_H as a function of the laser detunings Δ_p and Δ_c. The left panel shows F_D evaluated after $t = 1$ μs while the right one the respective steady-state value $\tilde{F}_D$. Crosses mark the values used in the thermal-state preparation shown in Fig. 2.29. The solid black lines mark the contour defined by $F_D = 0.99$. The values of the Rabi frequencies used in the simulation are listed in Tab. 2.6.

Besides, Fig. 2.31 illustrates the challenges a numerical optimization procedure faces when trying to find the optimum of the objective function: several — interconnected or disconnected — islands of high preparation fidelity can exist in parameter space. Accordingly, optimization results may not always correspond to the global optimum, as noted before. In fact, the maximal value of F_D in Fig. 2.31(a), $F_D > 0.999$, is larger than the value $F_D = 0.997$ at the position of cross (cf. Tab. 2.6), and is obtained for $\Delta_p/(2\pi) = -6.6$ MHz and $\Delta_c/(2\pi) = -67.8$ MHz. For this reason we refer to the parameter sets listed in Tab. 2.6 as "exemplary" parameter sets; larger preparation fidelities may be achieved with "better" parameter sets.

We stress that the high-fidelity landscape crucially depends on the target state. Together with an assessment of the robustness with respect to distance variations, this is illustrated in Fig. 2.32. Here, panels (a) and (b) show F_D as a function of the dimer separation d and the dimer-environment atom distance δ for the temperatures T_L and T_H, respectively; laser parameters are set to the values given in Tab. 2.6. Contour lines corresponding to $F_D = 0.99$ ($F_D = 0.95$) are displayed using black solid (dashed) lines. The crosses mark the distances $d = 5$ μm and $\delta = 2$ μm used for the numerical optimization in this section, and the gray boxes indicate a ±5% uncertainty in the distances, which is a realistic experimental uncertainty [52]. It can be seen that the landscape of high F_D differs strongly between thermal state preparation with high (T_H) respectively low (T_L) temperature; in particular the preparation-scheme robustness with respect to distance variations is different. For high-temperature (T_H) preparation, only one island of high fidelity exists; for low-temperature (T_L) thermal-state preparation, we find three islands. The value of largest F_D, $F_D > 0.999$, is located at $d = 4.7$ μm and $\delta = 1.85$ μm in (a) and $d = 4.95$ μm and $\delta = 2$ μm in (b). This demonstrates (i) that state-preparation fidelity can be improved by optimizing the interatomic distances, and (ii) small changes in atomic distances can lead to decreased preparation fidelity for particular laser parameter sets. Still, small variations in the distances do not lead to a large ($\gg 0.05$) drop in the preparation quality F_D in both cases.

Panels (c) and (d) of Fig. 2.32 show the dependence of F_D on the individual distances $\delta_{1(2)}$ between aggregate atom 1 (2) and environment atom 1 (2), again for the temperatures T_L and T_H, respectively. Since due to the symmetry of the setup, F_D is symmetric with respect to exchange $\delta_1 \leftrightarrow \delta_2$, the plots are mirror-symmetric around the diagonal, which is indicated by a gray, dash-dotted line. The island with high-fidelity preparation is again extended, showing that small fluctuations in the distances still allow for high-fidelity preparation after

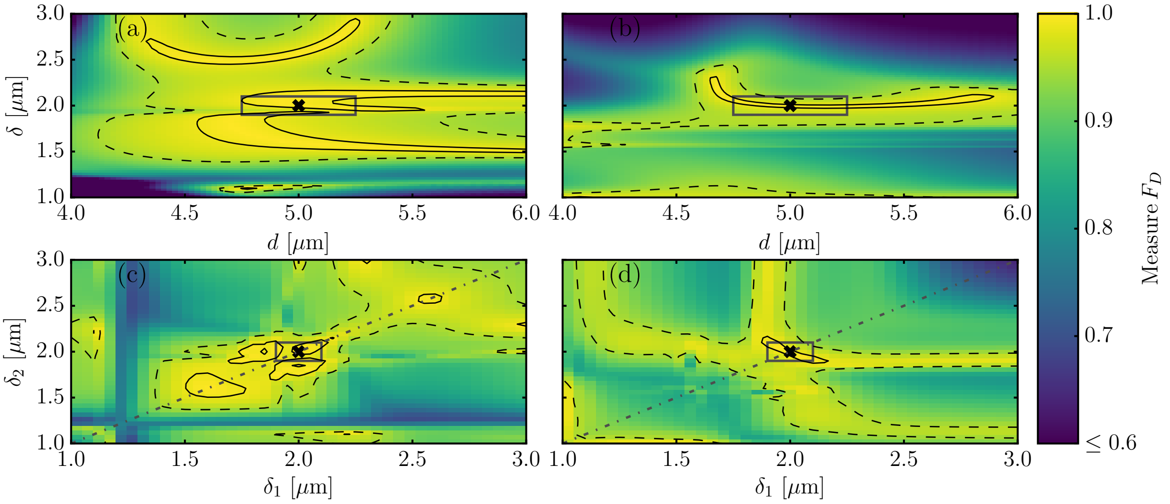

Figure 2.32: Measure F_D of the thermal-state preparation in a Rydberg dimer with temperature T_L (a,c) respectively T_H (b,d). Panels (a) and (b) show F_D as a function of the dimer separation d and the dimer-environment atom distance δ. Panels (c) and (d) display F_D as a function of the two dimer-environment atom distances δ_1 and δ_2; the dash-dotted line indicates the symmetry axis of the plot, which corresponds to a symmetric configuration $\delta_1 = \delta_2$. Crosses mark the values of the thermal-state preparation shown in Fig. 2.29. The solid (dashed) black lines mark the contours defined by $F_D = 0.99$ ($F_D = 0.95$). The gray boxes indicate a ±5% uncertainty in the distances. Laser parameters are listed in Tab. 2.6.

a preparation time of $t = 1$ μs. The increased number of high-fidelity ($F_D > 0.99$) islands for the low-temperature (T_L) parameter set already found in (a) carries over to the fidelity variation with respect to the individual system-environment distances $\delta_{1,2}$; likewise, there is only a single high-fidelity island in (d), as is in (b).

In principle, one could harness the different fidelity landscapes to meet the needs of an actual experiment. That is, one could think of implementing an adjusted objective function, in which constraints shaped by the primary experimental error sources are included. Laser parameters (or interatomic distances) which distinguish themselves by an exceptional robustness as to the dominating experimental errors could thereby be favored, and an experimental realization of state-preparation can be made more reliable.

Note that the inclusion of spontaneous emission from the Rydberg state $|r\rangle$ (rate $\Gamma_r/(2\pi) \approx$ 3 kHz with corresponding Lindblad operator $L = \sqrt{\Gamma_r}\, |e\rangle\langle r|$ for $|r\rangle = |38s_{1/2}\rangle$ [72]) does not cause a drop in the target-state fidelities of thermal-state preparation in a Rydberg dimer. This supports our expectation of high-fidelity thermal-state preparation being feasible under realistic experimental conditions.

Results for larger system sizes

Dissipative state-preparation is not limited to a Rydberg dimer. In Fig. 2.33 we demonstrate the preparation of thermal states with temperatures T_L (a) and T_H (b) for a Rydberg trimer ($N = 3$ system atoms, I) as well as a quadromer ($N = 4$ system atoms, II) using exemplary laser parameter sets. In both cases, the thermal states can be prepared with good fidelity ($F_D \geq 0.99$ in the steady state, cf. Tab. 2.6). Note, however, that these values might not correspond to the global maximum, since for larger system sizes it becomes numerically more challenging to explore the whole parameter space. Optimization results are clearly initial-state dependent, reflecting a ragged optimization landscape, and the location of the global optimum

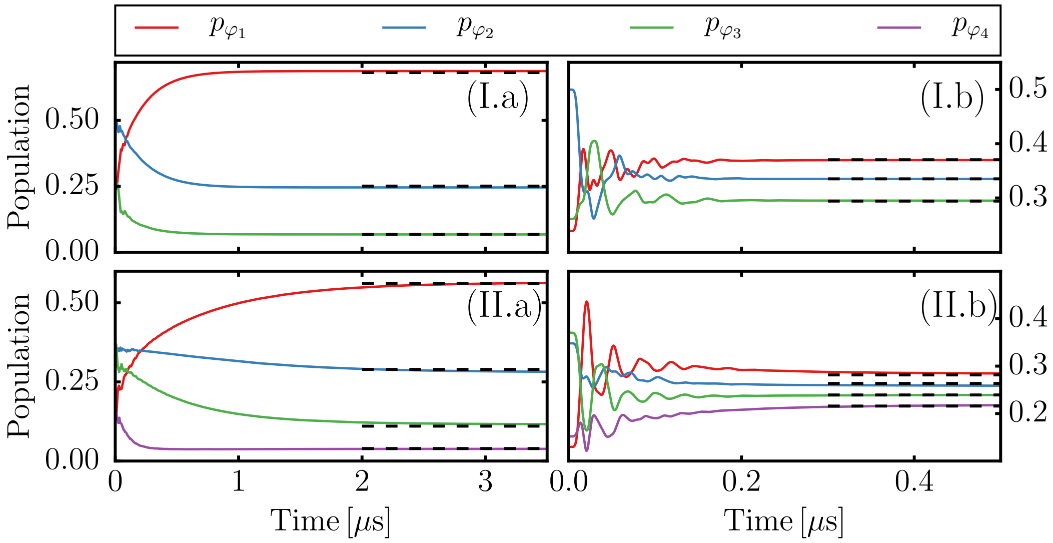

Figure 2.33: Thermal state preparation in a trimer (I) and quadromer (II) with temperatures T_L (a) and T_H (b). Solid colored lines show the populations p_{φ_k} of the system eigenstates $|\varphi_k\rangle$, and the target populations are indicated with dashed black lines. Laser parameters are listed in Tab. 2.6. Note the different axes scales between the panels.

is not easily assessable. The result is nonetheless remarkable: An environment consisting of only a few atoms can induce non-trivial thermal states with tunable temperature in a quadromer.

State preparation at short timescales becomes more difficult for larger system sizes, which can be seen, e.g., by the low value $F_D = 0.931$ for thermal-state preparation of a quadromer with temperature T_L, which rises to $F_D = 0.990$ in the steady state. In particular, for constant atom spacing, the energy differences between the system eigenenergies decrease with increasing system size. Larger timescales are thus required for distinctive dynamics for individual eigenstates to emerge. Accordingly, state preparation on a timescale of a few microseconds might be challenging to achieve in larger aggregates if the interatomic separation d between adjacent aggregate atoms is kept constant.

We note that scalability of the Rydberg system to larger sizes is limited by the radiative lifetimes of the Rydberg $|p\rangle$ and $|s\rangle$ states. This is illustrated in Fig. 2.34, which shows as before the thermal-state preparation in a Rydberg trimer (I) and quadromer (II) with temperatures T_L (a) and T_H (b), respectively, including additionally decay from the Rydberg aggregate states $|\pi_n\rangle$ with rate $1/\tau_{\text{agg}}$ [cf. Eq. (2.55)]. The resulting fidelities are listed in Tab. 2.7. Only the values obtained after $t = 1$ μs are shown since the aggregate is decayed in the steady state, and thus $\tilde{F} = \tilde{F}_D = 0$. Taking the decay from the aggregate states into account, the state-preparation fidelity drops below $F_D = 0.91$ for a quadromer with temperature T_L, using the laser parameters of Tab. 2.6. To maintain high-fidelity preparation with large aggregate sizes, an experimental realization would require conditioning on a non-decayed system. In this way, fidelity loss due to aggregate decay could be eliminated at the cost of an increased number of experimental realizations. Additionally, the demands on the experiment could be diminished by using higher-lying Rydberg states with longer lifetimes. States with interactions fulfilling e.g. $|V_{nn}^{(pr)}| \gg |V_{nn}^{(sr)}|$ have to be found again in this case.

In summary, we have shown that just a few laser-driven atoms, with global addressing, already realize a tunable environment enabling tailored dissipative state preparation in a Rydberg system. In particular, thermal states with temperatures vastly different from the

Table 2.7: Summary of measures F and F_D for the thermal-state preparation displayed in Fig. 2.34. The measures F and F_D are evaluated at $t = 1$ μs (F, F_D).

N	Target state	F	F_D
2	$\rho^{\mathrm{th}}_{T_L}$	0.991	0.982
2	$\rho^{\mathrm{th}}_{T_H}$	0.991	0.982
3	$\rho^{\mathrm{th}}_{T_L}$	0.985	0.970
3	$\rho^{\mathrm{th}}_{T_H}$	0.985	0.970
4	$\rho^{\mathrm{th}}_{T_L}$	0.977	0.909
4	$\rho^{\mathrm{th}}_{T_H}$	0.980	0.960

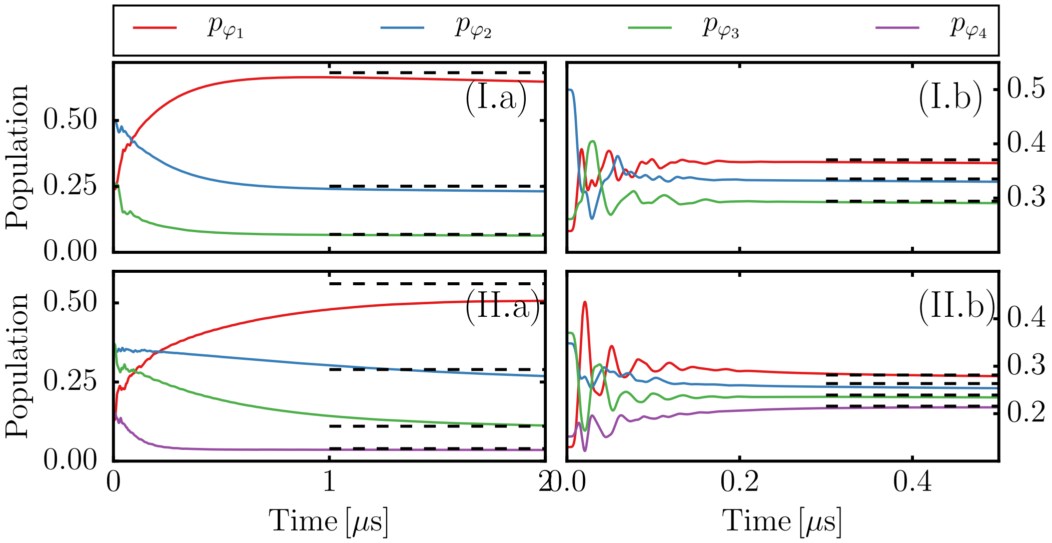

Figure 2.34: Thermal state preparation in a trime (I) and quadromer (II) with temperatures T_L (a) and T_H (b), in the presence of aggregate decay with rate $1/\tau_{\mathrm{agg}}$. Solid colored lines show the populations p_{φ_k} of the system eigenstates $|\varphi_k\rangle$, and the target populations are indicated with dashed black lines. Laser parameters are listed in Tab. 2.6. Note the different axes scales between the panels.

temperature of the ultracold atomic environment can be prepared with high fidelity, using only the laser frequencies and intensities driving the environment atoms as control parameters. We highlight the flexibility provided by an intermediate, controllable environment for engineering target system-environment interactions; this flexible reservoir engineering is highly desirable for quantum simulation schemes.

Chapter 3

Tuning displacement in non-Hermitian optomechanical resonators

Abstract — Optomechanical systems operate at the interface of light and matter and have intriguing prospects as sensors, transducers, and quantum memories. Introducing optical gain to optomechanical resonators was recently shown to give rise to a giant enhancement of the optomechanical coupling strength, which is quantified via the mechanical mode displacement [*Jing et al.*, Phys. Rev. Lett. 113, 053604 (2014)]. It was suggested that parity-time ($\mathcal{PT}$) symmetry, which corresponds to balanced gain and loss of the optical resonators, was an important ingredient to obtain large enhancement values. By considering the same optically-driven optomechanical system consisting of two coupled optical resonators, one of which supports a vibrational mechanical mode, we show that this is not the case: with off-resonant optical driving, larger enhancement values can be obtained outside the $\mathcal{PT}$ symmetric region. We furthermore assess the stability properties of the steady-state enhancement values and find that the previously-found large enhancement values correspond to unstable steady states, which we ascribe to the unbounded optical gain used in the modeling. By introducing gain saturation, we show that, depending on the optical design and driving parameters, a new regime of nonlinear dynamics, marked by sustained oscillations, emerges.

The work described in this chapter is based on the following publication [308]:

Optomechanical interactions in non-Hermitian photonic molecules
D. W. Schönleber, A. Eisfeld, and R. El-Ganainy
New J. Phys. **18**, 045014 (2016)

3.1 Introduction

Cavity optomechanics, which studies the interaction between light and mechanical systems, has attracted considerable attention on both theoretical and experimental fronts during the past decade [58, 309–311]. At the heart of cavity optomechanics lie the radiation-pressure forces arising from momentum transfer between photon and interacting object. Similarly to laser cooling of atomic gases [312], radiation pressure forces have been demonstrated to allow for cooling of micromechanical oscillators [313–315]. This opened up a rapidly developing field studying optomechanical coupling at the intersection of nanophysics and quantum optics. Nowadays, optomechanical interactions are being utilized in various applications such as gravitational wave detectors [314, 316], quantum memories [317], and acceleration sensors [318], just to mention a few. Furthermore, optical cooling of macroscopic mechanical oscillators [319] provides a unique opportunity to study the classical-quantum correspondence.

A different notion that has gained a lot of attention recently is parity-time ($\mathcal{PT}$) symmetry. There, the interest was aroused by the demonstration that certain $\mathcal{PT}$ symmetric Hamiltonians can posses real eigenspectra [320]. Enabled by the mathematical equivalence between the Schrödinger equation for a free particle in two spatial dimensions and the paraxial wave equation in optics, the concept of $\mathcal{PT}$ symmetry was then extended to optics [321–324], where its experimental manifestations were observed in optical systems with engineered gain and loss profiles [325], as well as other fields (see Ref. [326], for instance). Noteworthy, most of the striking features of $\mathcal{PT}$ symmetric structures also persist for the wider class of non-Hermitian materials that do not necessarily respect $\mathcal{PT}$ symmetry. For example, the existence of the spectral singularities known as exceptional points, at which at least two eigenvalues of the Hamiltonian describing the system coalesce, do not require $\mathcal{PT}$ symmetry and can occur in a general non-Hermitian systems [327–329]. The ability to manipulate light in photonic systems by controlling these singularities has opened the door for new device applications such as single-mode microring lasers [56, 57] and light sources based on non-Hermitian phase matching [330].

Recently, the marriage between the two themes of optomechanics and $\mathcal{PT}$ symmetry has been proposed in Ref. [59]. In particular, this work has investigated the optomechanical coupling in phonon laser (or saser) structures similar to those studied in Ref. [331], but with the additional ingredient of $\mathcal{PT}$ symmetry. Including optical gain to allow for the realization of $\mathcal{PT}$ symmetry was shown to give rise to a giant enhancement of the optomechanical coupling strength around the exceptional points when compared to a gain-less structure. We will use the results of Ref. [59] as the starting point of our subsequent investigation.

In the context of a different physical setup, the theme of Chapter 2, namely reservoir engineering with a nested environment structure, reappears here in the question as to how one can influence the properties of a certain system (here: the mechanical degree of freedom) by changing properties of the environment (here: the parameters pertaining to the optical degrees of freedom). The connection between the atomic system studied in Chap. 2 and the optomechanical system studied in this chapter becomes apparent when comparing the conceptual sketch of the atomic system (cf. Fig. 2.21) with the one of the optomechanical system, displayed in Fig. 3.1: A system of interest is coupled to a small controllable intermediate system, which in turn is coupled to a further macroscopic environment. In both cases we are interested in properties of the system as a result of controlled changes in the nested environment. Whereas in the atomic system the control parameters are the atomic distances, translating into Rydberg interaction strengths, as well as laser frequencies and intensities, we have here additionally control over the ratio between gain and loss rates, provided via the fabrication process.

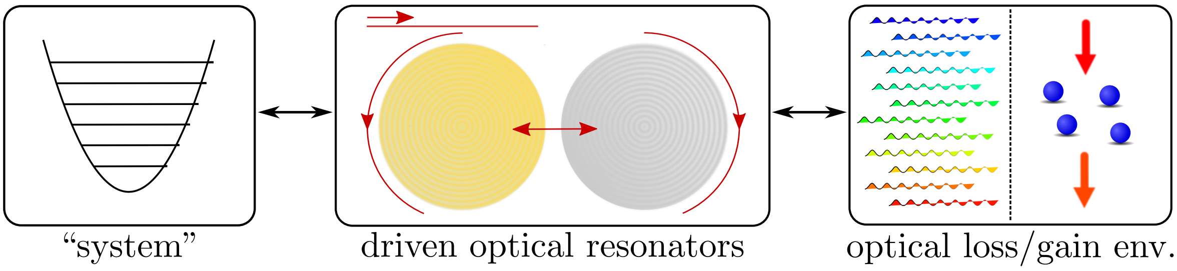

Figure 3.1: Conceptual sketch of the optomechanical setup. A "system" mechanical degree of freedom is optomechanically coupled to a laser-driven "environment", which consists of two optical resonators (photonic molecules) that experience photon loss/gain as a result of their material properties. The loss/gain rates can be controlled through fabrication, and can be interpreted as a coupling to loss/gain-providing reservoirs (or environments, env.). While optical loss arises from photon leakage out of the cavity (here depicted by a continuum of electromagnetic modes), optical gain can be provided to the cavity through doping with optically-pumped Er^{3+} ions, for example, as depicted here (see Refs. [59, 332] and main text for more details).

The structure of this chapter is as follows: In Sec. 3.2 we introduce the optomechanical system of interest. To assess the tunability of the mechanical degree of freedom via "environment" properties, we perform a comprehensive analytical and numerical investigation of the optomechanical enhancement of the mechanical displacement in Sec. 3.3. Specifically, we characterize the nonlinear steady-state solutions and the stability properties in terms of the optical and acoustic (i.e., mechanical) design parameters as well as the optical pumping power levels and frequencies. In Sec. 3.4 we study the dynamical evolution of the system and show that different regimes of operation can be identified based on the design parameters, excitation power levels and frequency detunings.

Our study reveals several important results: (1) The maximum achievable optomechanical interaction enhancement for stable steady-state solutions does not occur in the neighborhood of the $\mathcal{PT}$ phase transition point, and (2) Depending on the design parameters, pump properties and gain saturation effects, different regimes of nonlinear dynamics such as fixed points and sustained oscillations are possible.

3.2 System and model

We consider a "photonic molecule" that supports two photonic supermodes and one acoustic mode as shown schematically in Fig. 3.2. Such as system can be realized using whispering-gallery-mode microtoroid resonators (WGMRs) [59, 311, 315, 333].

WGMRs, which are typically fabricated of silica with radii of several tens of micrometers [331, 333], feature ultra-high quality factors. (The quality factor is proportional to the confinement time of light in the cavity in units of the optical period [333, 334]). The light is trapped in WGMRs as a result of total internal reflection, which leads to a localization of the optical mode along the rim of the circular resonator. Coupling between two WGMRs is facilitated via the evanescent field outside the cavities, which drops exponentially, resulting in a coupling that exponentially depends on the separation between the resonators [331, 335]. This coupling produces a frequency splitting of the normal modes (or supermodes) of the optical cavities. Due to the similarity between the optical modes in WGMR structures and the electronic states of diatomic molecules, such WGMR structures are also called "photonic molecules" [336].

In addition to optical modes, WGMRs exhibit a large number of mechanical normal modes of vibration [58, 311]. Radiation pressure can couple an isolated optical mode to a co-localized

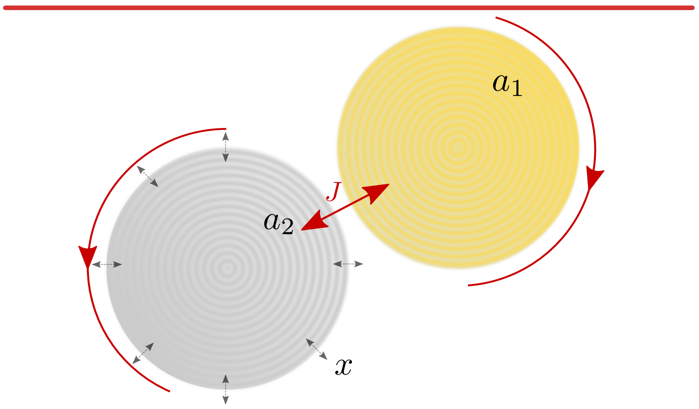

Figure 3.2: Schematic of the optomechanical system under consideration. Two optical resonators a_1 and a_2 are coupled to each other via evanescent coupling of strength J. Both optical resonators have a finite quality factor and experience optical gain or loss due to optical or electrical pumping (not shown here). The gain/loss profile across the cavities is in general asymmetric as indicated by their different colors. Resonator a_2 supports a vibrational mechanical mode x at frequency ω_m. Optical excitation of the system takes place via the evanescent coupling between resonator a_1 and an external waveguide (thick red line).

mechanical mode since mechanical distortions modify the path length of the optical resonator and thereby its resonance frequency, which results in optomechanical coupling. Similar to Refs. [59, 331, 337–341], we here assume that the acoustic mode is localized in one of these cavities. The acoustic mode is characterized by a resonance frequency ω_m, damping coefficient Γ and an effective mass m, while the optomechanical coupling is characterized by the coupling constant g. The uncoupled photonic states of the two resonators we take to have identical resonance frequencies ω_0 and quality factors (not necessarily the same) quantified by the inverse of the radiation loss coefficients α_1 and α_2, respectively. The optical coupling coefficient between the two resonators is given by J. Optical excitation of the cavities is achieved through a waveguide coupled to the cavity a_1 with a coupling constant μ.

Additional gain or loss factors $\tilde{\gamma}_{1,2}$ can be engineered by an appropriate design of the material system, for instance by doping the resonator with gain/loss material and applying different optical pumping conditions [59, 332] [1]. As a result, the total net gain/loss in each resonator is described by the coefficients $\gamma_1 = \tilde{\gamma}_1 - \alpha_1 - \mu$ and $\gamma_2 = \tilde{\gamma}_2 - \alpha_2$. These values can be either positive or negative depending on whether the net effect is optical amplification or decay. In our study, we do not discuss in detail how these gain or loss parameters can be controlled (see Ref. [59] for more details on that subject) but rather focus on how their values affect the dynamics.

In the semiclassical limit, i.e., neglecting quantum correlations and fluctuations, the corresponding equations of motion for the (complex) classical optical field amplitudes $a_{1,2}$ in the two resonators and the (real) acoustic oscillator displacement x respect the following nonlinear

---

[1] By doping the optically active resonator (i.e., the resonator experiencing optical gain) with Er^{3+} ions which emit at the resonance frequency ω_0 of the cavity, optical pumping with light at a specific, higher frequency provides optical gain to the cavity.

Parameter	Value
ω_m	$23.4 \times 2\pi$ MHz
ω_0	$193 \times 2\pi$ THz (corresponds to $\lambda_0 = 1.55$ μm)
g	5.61 GHz/nm
m	5×10^{-11} kg
Γ	0.24 MHz
J	6.45 MHz
γ_0	6.45 MHz
μ	3.14 MHz

Table 3.1: List of the design parameters that we use throughout this chapter (cf. Refs. [59, 331, 332, 339]) for the numerical calculations.

system of differential equations [58, 59, 332, 339, 342, 343]:

$$\dot{a}_1 = (-i\Delta + \gamma_1)a_1 - iJa_2 + \sqrt{2\mu} f_0, \tag{3.1a}$$
$$\dot{a}_2 = (-i\Delta + \gamma_2)a_2 - iJa_1 - iga_2 x, \tag{3.1b}$$
$$\ddot{x} = -\Gamma\dot{x} - \omega_m^2 x + \frac{\hbar g}{m}|a_2|^2. \tag{3.1c}$$

Here, Δ denotes the laser detuning $\Delta = \omega_0 - \omega_L$, and μ is the coupling rate between the waveguide and the resonator a_1. The numerical implementation of Eqs. (3.1) is done in atomic units; the scaling procedure is outlined in Appendix B.1.

We note that the above equations (3.1) are written in the rotating frame of reference of the optical excitation signal $f_{\text{in}}(t) = f_0 \exp(-i\omega_L t)$, where f_0 is the amplitude of the external excitation laser and ω_L is its frequency. The power P_{in} of the excitation laser transmitted to the resonator a_1 can be obtained from f_0 via $P_{\text{in}} = \hbar\omega_L|f_0|^2$ [339]. The non-Hermitian structure of Eqs. (3.1) originates from the imaginary part of the refractive index of the optical cavity medium that confines the electric field, which we denote by the gain respectively loss terms γ_1 and γ_2 [321, 325].

In the absence of any non-Hermiticity, the above system was reported to operate as a saser (acoustic laser) device where the frequency splitting between the photonic supermodes of the photonic molecule can be treated as a two-level system that can provide acoustic gain for the mechanical mode [331]. In what follows we do not emphasize the saser action picture presented in Refs. [59, 331] but rather treat the system from the dynamical point of view. To link our analysis to recent experiments [331, 332], we use the parameters summarized in Tab. 3.1.

The notion of $\mathcal{PT}$ symmetry in Eqs. (3.1) arises in the optical degrees of freedom in the absence of driving, $f_0 = 0$. That is, ignoring the mechanical degree of freedom, Eqs. (3.1) can be cast into the form $\partial_t\psi = -i\mathcal{H}\psi$ with $\psi = (a_1, a_2)^T$, where the superscript T denotes the matrix transpose, and $\mathcal{H}$ the non-Hermitian "Hamiltonian"

$$\mathcal{H} = \begin{pmatrix} \Delta + i\gamma_1 & J \\ J & \Delta + i\gamma_2 \end{pmatrix}. \tag{3.2}$$

For balanced gain and loss, $\gamma_2 = -\gamma_1$, this "Hamiltonian" is invariant under combined parity ($\mathcal{P}$) and time-reversal ($\mathcal{T}$) transformation, whose effects are $\mathcal{P} : (a_1, a_2)^T \to (a_2, a_1)^T$ and $\mathcal{T} : i \to -i$ [344], and hence the "Hamiltonian" (3.2) is $\mathcal{PT}$ symmetric. Its eigenvalues in this case read as $\pm\sqrt{J^2-\gamma_1^2}$, exhibiting an interesting feature: with increasing γ_1 the eigenvalues turn from purely real ($\gamma_1 < J$) to purely imaginary ($\gamma_1 > J$). Since also the corresponding eigenvectors change from respecting $\mathcal{PT}$ symmetry ($\gamma_1 < J$) to not respecting (or breaking) $\mathcal{PT}$ symmetry ($\gamma_1 > J$), one speaks of a $\mathcal{PT}$ phase transition which occurs at the exceptional point $\gamma_2 = -\gamma_1 = -J < 0$, at which the eigenvalues of $\mathcal{H}$ coalesce [344, 345].

3.3 Steady-state solutions and their stability properties

To develop an understanding for the dependence of the mechanical degree of freedom on the parameters pertaining to the optical degrees of freedom, it is instructive to start with the investigation of the steady-state solutions of the classical amplitudes of Eqs. (3.1). Being an indicator of the advantage a non-Hermitian WGM structure with gain might have over a gain-less structure, our special focus in this analysis lies on the "optomechanical enhancement", a figure of merit introduced in Ref. [59]. In Sec. 3.3.1 we both analytically and numerically study the dependence of the optomechanical enhancement on the laser power and frequency, as well as WGM design parameters. The stability properties of the steady-state solutions, which are essential to assess whether they are also dynamically reachable, are then examined in Sec. 3.3.2.

3.3.1 Steady-state analysis

We start our analysis by investigating the steady-state solutions associated with the non-Hermitian optomechanical system depicted in Fig. 3.2. We do so by setting the time derivatives of $a_{1,2}$ and x to zero and solving Eqs. (3.1) for the steady state x_s of the mechanical oscillator. This yields an algebraic cubic polynomial equation that can have up to three different real solutions, corresponding to oscillator displacements which are invariant under the dynamics of Eqs. (3.1).

In the following analysis, we concentrate on a figure of merit called "optomechanical enhancement". It quantifies the enhancement of the mechanical displacement obtained in a WGM structure with optical gain as compared to the one obtained in a gain-less WGM structure. To evaluate this figure of merit, we consider a reference system in which both optical resonators have identical losses, i.e., $\gamma_1 = \gamma_2 < 0$. The resulting mechanical steady-state amplitude $x_\mathrm{s,p}$ serves as a reference to estimate the enhancement η,

$$\eta = \frac{x_\mathrm{s}}{x_\mathrm{s,p}}. \tag{3.3}$$

Here, the subscript p denotes the passive case, i.e., the case where both resonators have losses. Accordingly, the optomechanical enhancement is an indicator of what advantage introducing gain in one of the optical cavities has over gain-less cavities when aiming at achieving large mechanical displacements. It has been shown in Ref. [59] that the optomechanical enhancement can feature a gain-facilitated nonlinearity with respect to the pump power, i.e., η can increase with decreasing pump power. Better understanding of such gain-facilitated nonlinearity can be useful for engineering phononic systems, which is the reason we concentrate in the subsequent analysis on the optomechanical enhancement η.

It is worth noting that in the work by Jing *et al.* [59], a strong enhancement η of two orders of magnitude has been found at the $\mathcal{PT}$ symmetric point when $\gamma_2 = -\gamma_1$ and under resonant excitation conditions, i.e. $\Delta = 0$. Here we also explore the case of off-resonant $\Delta \neq 0$ driving. Besides, we note that that in Ref. [59] a different scaling of the optical amplitude f_0 has been used, i.e. $\sqrt{2\gamma_1}$ instead of $\sqrt{2\mu}$. Therefore, the enhancement values found in [59] are scaled with respect to the ones obtained in this work.

Analytical considerations

In order to gain an insight into the behavior of the system beyond the full numerical solution of Eqs. (3.1), we first consider the optical modes only and ignore the driving term while accounting for the nonlinear interaction between the mechanical oscillator and optical amplitude a_2 through a non-linearly induced frequency shift. In other words, we treat the steady-state displacement of the mechanical oscillator x_s as a parameter that effectively introduces an additional detuning $\Delta_x \equiv g x_\mathrm{s}$ to the second cavity. Note that this detuning in reality depends on the strength of the laser driving; a feature that is absent in this simplified analysis. Within this picture, the optical amplitudes are modeled by the following linear equations:

$$\partial_t \begin{pmatrix} a_1 \\ a_2 \end{pmatrix} = -i \begin{pmatrix} i\gamma_1 & J \\ J & \Delta_x + i\gamma_2 \end{pmatrix} \begin{pmatrix} a_1 \\ a_2 \end{pmatrix}. \tag{3.4}$$

By diagonalizing Eqs. (3.4), we obtain the eigenfrequencies of the two supermodes as well as the associated linewidths as given by the real and imaginary parts, respectively, of the complex frequencies

$$\omega_\pm = \frac{1}{2}\left(\Delta_x + i(\gamma_1+\gamma_2) \pm \sqrt{4J^2 + (\Delta_x - i(\gamma_1-\gamma_2))^2}\right). \tag{3.5}$$

Hence, by scanning the frequency of the pump laser [represented by Δ in Eqs. (3.1)] to match the real part of either $\omega_\pm$, resonant interaction is expected to take place. From Equation (3.5), the following features can be observed:

(i) For antisymmetric gain/loss profile ($\gamma_2 = -\gamma_1 < 0$) and low laser power ($\Delta_x \ll J, \gamma_1$), we expect the system to exhibit two sharp resonances at $\pm\sqrt{J^2 - \gamma_1^2}$ for $J > \gamma_1$, while for $J < \gamma_1$ we expect a single broad resonance at zero.

(ii) For smaller values of the gain coefficient, $0 < \gamma_1 < |\gamma_2|$ with $\gamma_2 < 0$ and nonzero Δ_x, the square root in Eq. (3.5) has both real and an imaginary parts, which we denote by Re and Im, respectively. In this regime, the resonance frequencies of the supermodes and their associated linewidths are given by $\Delta_x/2 \pm \mathrm{Re}/2$ and $(\gamma_1+\gamma_2)/2 \pm \mathrm{Im}/2$, and correspondingly we expect an asymmetric spectrum for positive and negative laser detuning.

Our discussion so far has focused on the eigenfrequencies of the optical supermodes of the photonic molecule in the absence of pumping. In order to gain more insight into the system's behavior, we now consider the effect of the driving field in our simple picture, i.e., we add $(\sqrt{2\mu} f_0, 0)^T$ to the right hand side of Eqs. (3.4). Under these conditions and by assuming a constant detuning Δ_x, we find that Eqs. (3.4) admit a non-trivial steady-state solution for the field amplitudes $a_{1,2}$. By noting that $x_\mathrm{s} \propto |a_2|^2$ under steady-state conditions [cf. Eq. (3.1c)], we find that the enhancement η is given by $\eta = |a_2|^2/|a_{2,\mathrm{p}}|^2$ with p again indicating the passive case with $\gamma_1 = \gamma_2 < 0$. By evaluating the quantity $|a_2|^2/|a_{2,\mathrm{p}}|^2$ exactly at the onset of the linear $\mathcal{PT}$ phase transition point, we obtain (see Appendix B.2 for the general case):

$$\eta = 1 + \frac{4\gamma_2^2}{\Delta_x^2} \qquad (\gamma_2 = -\gamma_1 = -J < 0). \tag{3.6}$$

Equation (3.6) indicates that a larger nonlinearly-induced detuning Δ_x will decrease the enhancement factor η. Since the mechanical amplitude x_s is proportional to the detuning Δ_x and increases with laser power, we expect the enhancement η to drop as the driving power

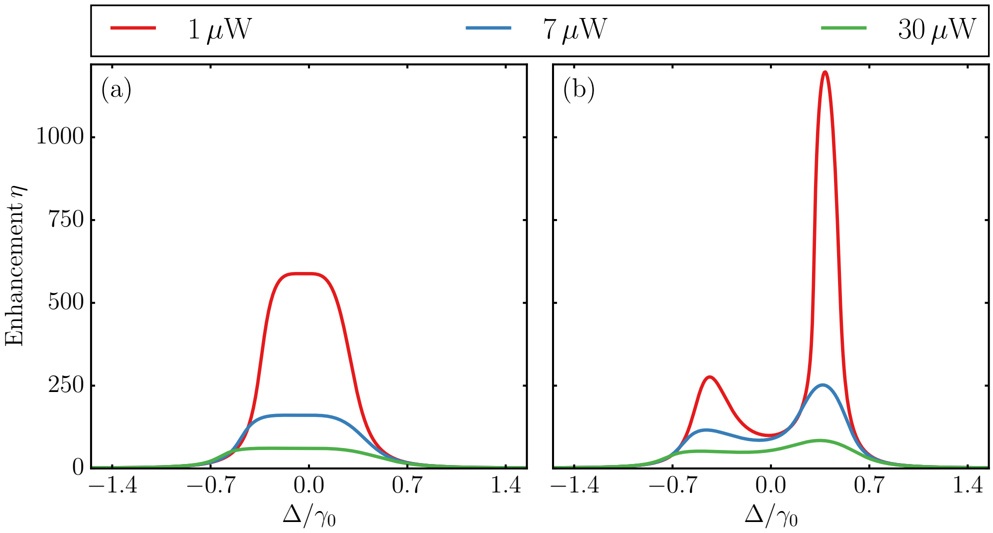

Figure 3.3: Enhancement η as a function of the detuning Δ for various laser powers P_{in}. In (a), $\gamma_1 = \gamma_0$ and $\gamma_2 = -\gamma_0$ whereas in (b) $\gamma_1 = 0.8\gamma_0$ and $\gamma_2 = -\gamma_0$. The red, blue, and green lines (from top to bottom) correspond to laser powers of $P_{\mathrm{in}} = 1\mu\mathrm{W}$, $7\mu\mathrm{W}$, and $30\mu\mathrm{W}$, respectively. Other parameters as in Tab. 3.1.

increases. The reason we explicitly consider the $\mathcal{PT}$ point is that at this point the ratio $|a_2|^2/|a_{2,\mathrm{p}}|^2$ becomes particularly simple; for more details we refer to Appendix B.2.

Having gained some qualitative insight into the problem by using this simplified linearized analysis, we turn to the discussion of the numerical steady-state results of the full nonlinear system of Eqs. (3.1).

Numerical evaluation of the steady-state solutions

We now consider the full numerical evaluation of the steady-state solutions of Eqs. (3.1) under general conditions. Figure 3.3(a) shows the enhancement factor η as a function of Δ/γ_0 in the $\mathcal{PT}$ symmetric case where $\gamma_1 = -\gamma_2 = \gamma_0$. In this scenario, the enhancement curve displays a plateau with no sharp peaks and its maximal value is found to occur at zero detuning $\Delta = 0$, in accordance with what was observed in Ref. [59]. Note that the point of maximal enhancement ($\Delta = 0$ and $J = \gamma_1 = -\gamma_2$) coincides with the exceptional point, at which the eigenfrequencies of the supermodes of the linear system coalesce.

In Fig. 3.3(b), the case of unbalanced gain/loss profile, $\gamma_1 < \gamma_0$ and $\gamma_2 = -\gamma_0$, is shown. In this case, two peaks of different heights that correspond to two different laser detunings can be observed in the enhancement curve. Notably, at the location of the positive detuning peak, the enhancement value even exceeds the one found for the $\mathcal{PT}$ symmetric case on resonance. Our analysis thus uncovers the important result that $\mathcal{PT}$ symmetry is not necessarily the optimum choice for obtaining stronger optomechanical interactions as compared to a passive system. These results clearly show that the enhancement of the optomechanical coupling coefficient is not simply an outcome of increasing the optical gain in resonator a_1, but rather a result of a complex interplay between the non-Hermitian parameters of the system (optical gain and loss), detuning between the pump laser, the resonance frequency of the optical cavities, and the properties of the acoustic mode. The asymmetry observed for the broken $\mathcal{PT}$ symmetry case with $\gamma_1 \neq -\gamma_2$ [Fig. 3.3(b)] can be understood in the light of our simplified picture of the previous section where the effective detuning introduced to the second cavity a_2 due to optomechanical interaction was shown to introduce an asymmetry to the supermode

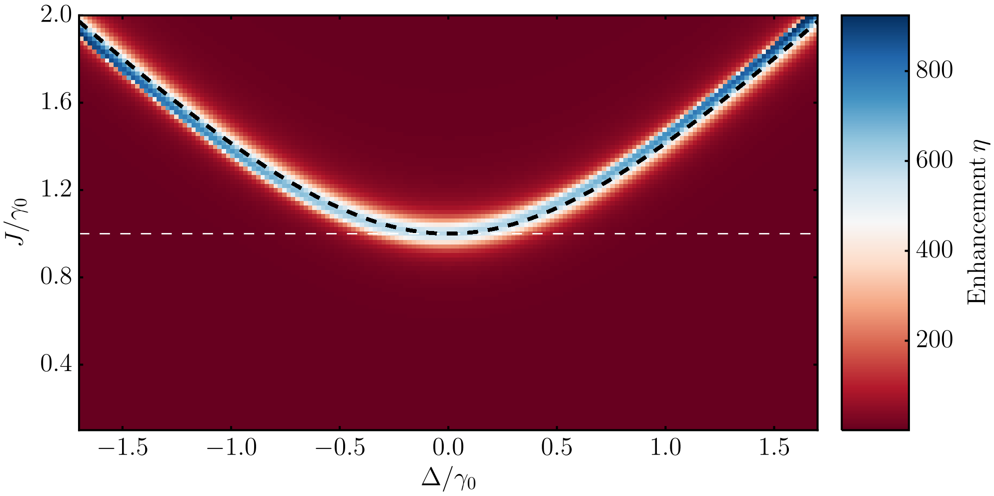

Figure 3.4: Enhancement η as a function of the detuning Δ and the optical inter-cavity coupling J at a driving power of $P_{\text{in}} = 1\ \mu$W and $\gamma_1 = -\gamma_2 = \gamma_0$. The horizontal white dashed line is a cross section corresponding to the parameters of Fig. 3.3(a). The dashed black line shows the $\sqrt{J^2 - \gamma_0^2}$ dependence of the eigenfrequencies found from the simplified picture in the previous section [Eq. (3.5)]. Other parameters as in Tab. 3.1.

frequencies and linewidths.

Surprisingly, as the driving laser power is increased, the enhancement values drop, indicating that the difference in the mechanical steady-state displacement between the active-passive (gain/loss) and passive-passive (loss/loss) system vanishes. Conversely, the enhancement increases nonlinearly with decreasing pump power. This feature is consistent with our simplified picture introduced in the previous section where the enhancement factor was shown to degrade with increasing nonlinearly-induced detuning Δ_x [see Eq. (3.6)].

The resonant behavior of the enhancement curve [the appearance of two sharp peaks in Fig. 3.3(b)] at nonzero detuning can occur not only when the optical gain in one cavity is unequal to the loss in the other, but also in the case of equal gain and loss, provided that the inter-cavity coupling exceeds the gain and loss values. This behavior is illustrated in Fig. 3.4, where the optical inter-cavity coupling J is varied while maintaining balanced gain and loss, $\gamma_1 = -\gamma_2 = \gamma_0$. For $J > \gamma_0$, the maximal enhancement is no longer found at the excitation resonance $\Delta = 0$ but rather shifts to $\Delta \neq 0$, in good agreement with our earlier discussion as outlined in (i) in the previous section (black dashed line in Fig. 3.4). That is, the sizable enhancement value at the exceptional point (found on the dashed white line for $\Delta = 0$) is outperformed by the enhancement obtained for $J > \gamma_0$ at the position of the supermode frequencies.

Finally, we consider the special case of zero-loss and zero-gain, i.e., $\gamma_1 = \gamma_2 = 0$, shown in Figure 3.5. Under this condition, two different regimes for the steady-state solutions of x_{s} can be identified depending the excitation detuning Δ. In particular, within the range $0 < \Delta < \Delta_{\text{B}}$, with $\Delta_{\text{B}}/J \sim 0.92/0.85/0.75$ for laser drivings of $1/7/30\,\mu$W, three real solutions exist for x_{s}. (Δ_{B} denotes the branching detuning value, i.e., the detuning at which the single real solution for x_{s} branches into three real solutions.) Note that two of these solutions diverge as $\Delta \to 0$. Conversely, when $x_{\text{s}} > \Delta_{\text{B}}$, only one real solution exists. This is illustrated in Fig. 3.5(a) where the diverging branches of the real solutions for x_{s} are indicated by dotted lines whereas the finite ones are plotted with solid lines. Figure 3.5(b) shows the enhancement corresponding to the steady-state values of the finite branch in (a), evaluated as before with

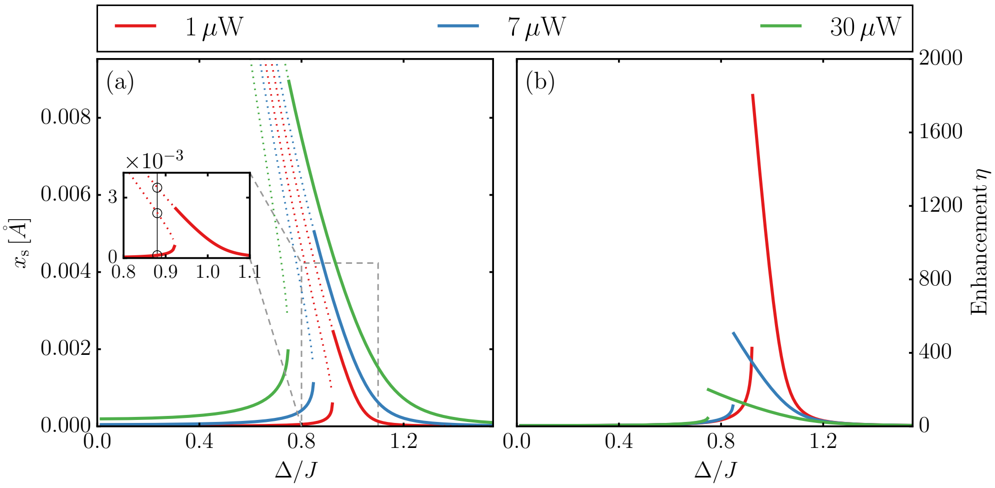

Figure 3.5: Steady-state amplitude x_s (a) as well as enhancement factor η (b) as a function of the detuning Δ for various laser powers P_{in} and $\gamma_1 = \gamma_2 = 0$. The red, blue, and green lines (top to bottom in the right panel, bottom to top in the left panel) correspond to laser powers of $P_{\text{in}} = 1\mu$W, 7μW, and 30μW, respectively. Dotted lines indicate real solutions that diverge as $\Delta \to 0$. The inset in (a) shows an enlarged part of the steady-state amplitude for $P_{\text{in}} = 1\mu$W, indicating the presence of three real solutions for $\Delta/J \lesssim 0.92$, of which two are diverging as $\Delta \to 0$. All other parameters are listed in Tab. 3.1.

respect to a reference state with $\gamma_1 = \gamma_2 = -\gamma_0 = -J$.

Considering Figs. 3.3(b) and 3.5(b), we see that the enhancement η of the mechanical steady-state amplitude obtained in a loss-gain balanced system as compared to a system with both cavities experiencing equal loss can be outperformed by introducing nonzero detuning. In addition, even in the $\mathcal{PT}$ symmetric case a larger enhancement η can be obtained when increasing the inter-cavity coupling J and tuning the laser frequency to the supermode resonance frequency (cf. Fig. 3.4). This demonstrates that combining control over design parameters (gain/loss rates and inter-cavity coupling strength) with laser control gives a significant improvement in the range of tunability of the mechanical mode.

3.3.2 Stability analysis of the steady-state solutions

We have so far investigated only steady-state solutions. An important feature of these solutions is their stability. In fact, any steady-state solution is dynamically meaningless unless it is stable. We thus carry out the linear stability analysis of the fixed points of Eqs. (3.1) in this section by linearizing Eqs. (3.1) around the steady-state values [346]. We do so by rewriting the second-order differential equation Eq. (3.1c) as two first-order differential equations,

$$\begin{aligned} \dot{x} &= v, \\ \dot{v} &= -\Gamma v - \omega_m^2 x + \frac{\hbar g}{m}|a_2|^2. \end{aligned}$$

By introducing a perturbation vector $\delta\vec{q} = (\delta a_{1r}, \delta a_{1i}, \delta a_{2r}, \delta a_{2i}, \delta x, \delta v)^T$ (cf. also Ref. [339]) over any particular steady-state solution, substituting back in Eqs. (3.1) and neglecting higher

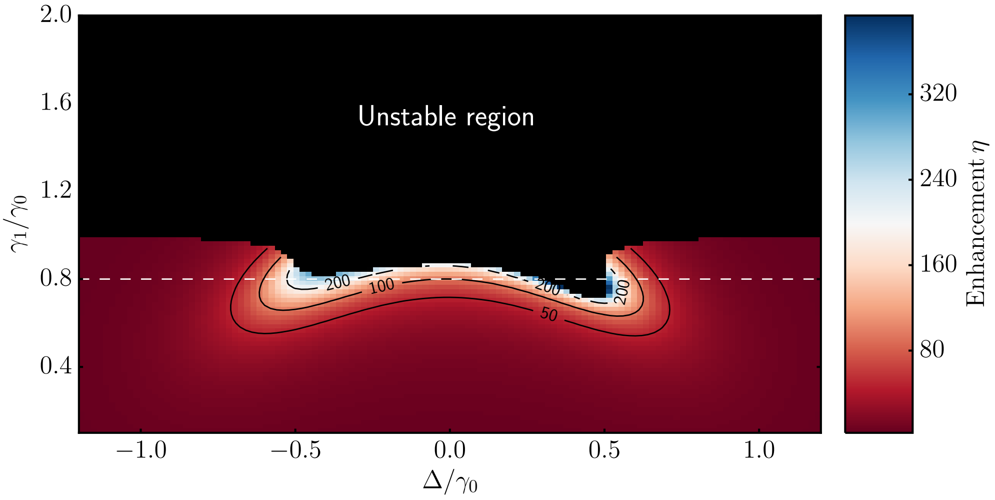

Figure 3.6: Enhancement η as a function of the detuning Δ and the gain-to-loss ratio $\gamma_1/\gamma_2 \equiv \gamma_1/\gamma_0$ at a driving power of $P_{\text{in}} = 1\ \mu$W. All other parameters are listed in Tab. 3.1. The black region indicates the parameter regime where steady-state solutions are not stable according to linear stability analysis. Contours of equal enhancement η are also shown. The horizontal white dashed line corresponds to the parameters of Fig. 3.3(b).

order terms, we find $\delta\dot{\vec{q}} = \boldsymbol{M}\delta\vec{q}$, where the matrix $\boldsymbol{M}$ is given by

$$\boldsymbol{M} = \begin{pmatrix} \gamma_1 & \Delta & 0 & J & 0 & 0 \\ -\Delta & \gamma_1 & -J & 0 & 0 & 0 \\ 0 & J & \gamma_2 & gx_{\text{s}} + \Delta & ga_{2i,\text{s}} & 0 \\ -J & 0 & -gx_s - \Delta & \gamma_2 & -ga_{2r,\text{s}} & 0 \\ 0 & 0 & 0 & 0 & 0 & 1 \\ 0 & 0 & 2\hbar ga_{2r,\text{s}}/m & 2\hbar ga_{2i,\text{s}}/m & -\omega_m^2 & -\Gamma \end{pmatrix}. \tag{3.8}$$

The matrix $\boldsymbol{M}$ is the Jacobian matrix associated with perturbations of the steady state of the nonlinear system of Eqs. (3.1); the subscript s denotes the steady state and r, i denote real and imaginary parts, respectively, of the amplitudes $a_{1,2}$. Note that $\boldsymbol{M}$ is a function of the steady-state solutions and varies from one to another.

The stability of steady-state solutions for any set of given design/excitation parameters depend on the eigenvalues of $\boldsymbol{M}$. In particular, a given steady-state solution is *stable* if all eigenvalues of $\boldsymbol{M}$ have negative real parts. In this case, the steady-state solution is represented by a fixed point surrounded by an attracting region in phase space, meaning that all trajectories in the vicinity of this fixed point will converge into it. Otherwise, if some of the eigenvalues have positive real parts, the steady state becomes *unstable* and might exhibit limiting cycles or display chaotic behavior [339, 346].

By constructing a linear stability map for the fixed points of Eqs. (3.1) as a function of the gain $\gamma_1 > 0$ and detuning Δ parameters (see Fig. 3.6), we uncover the following remarkable result: Steady-state solutions that correspond to the $\mathcal{PT}$ symmetric case $\gamma_1 = -\gamma_2 = \gamma_0$ are not stable. In other words, $\mathcal{PT}$ symmetry is not necessarily the optimal choice for enhancing optomechanical interactions in the steady state. Instead, Fig. 3.6 shows that stable steady-state solutions that exhibit significant enhancement (up to 200 fold) can be still achieved for nonzero pump detuning and broken $\mathcal{PT}$ symmetry. Specifically, the gain values must satisfy $\gamma_1/\gamma_0 \lesssim 0.7$ in order to guarantee stability over the full range of the considered detuning. Hence, the peak enhancement in the case of Fig. 3.3(b), indicated by the white dashed line in Fig. 3.6, as well as that reported in Ref. [59] is indeed misleading since it does not correspond

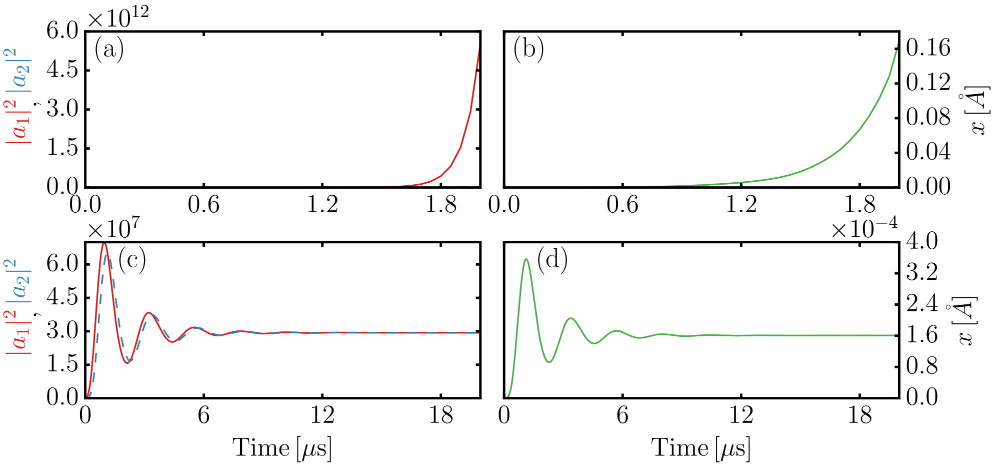

Figure 3.7: Dynamics of the populations $|a_1(t)|^2$ (left column, solid red), $|a_2(t)|^2$ (left column, dashed blue) and the mechanical oscillator amplitude $x(t)$ (right column, solid green). In (a) and (b), $\gamma_1 = -\gamma_2 = \gamma_0$ whereas in (c) and (d) $\gamma_2 = -\gamma_0$ and $\gamma_1 = 0.8\gamma_0$. The laser power is $P_{\text{in}} = 1\mu$W and $\Delta = 0$ MHz; all other parameters are as listed in Tab. 3.1. Note the different scaling of the x and y axes.

to stable steady-state solutions. As we will show later, including gain saturation effects can result in stable steady-state solutions even in the $\mathcal{PT}$ symmetric case.

We conclude this section by noting that while linear stability analysis suffices to question the validity of claims made on the basis of steady-state analysis alone, it does not provide information regarding the dynamical behavior of the system, i.e., whether it converges to a limit cycle or even becomes chaotic. In order to explore the full behavior of the system, we now numerically integrate the temporal dynamics associated with Eqs. (3.1).

3.4 Nonlinear dynamics

In the previous section, we studied the stability properties of steady-state solutions associated with optomechanical photonic molecules having optical gain and loss profiles (see Fig. 3.2). We have shown that in the case of $\mathcal{PT}$ symmetry (equal gain and loss) the phase-space fixed points are unstable. We also revealed that steady-state solutions that exhibit significant enhancement in optomechanical interactions can be attained by tailoring the pump detuning and the gain/loss profile (with unbalanced distribution). This analysis, however, leaves several important questions unanswered: What are the dynamics when the steady-state solutions are unstable? And further: What is the effect of gain saturation?

In this section we investigate the above posed questions. We begin by studying the temporal evolution of the dynamical quantities $|a_1(t)|^2, |a_2(t)|^2$ and $x(t)$ for the two different cases depicted in Figure 3.3 ($\mathcal{PT}$ symmetry and unbalanced gain and loss) when the detuning is zero and for an input laser power of $P_{\text{in}} = 1\mu$W. By integrating Eqs. (3.1) numerically, we find that, in the first case of $\mathcal{PT}$ symmetric gain and loss distribution where $\gamma_1 = -\gamma_2 = \gamma_0$, the optical intensities and mechanical displacement grow exponentially as shown in Figs. 3.7(a) and (b). (Note that we do not study long-time dynamics subsequent to the exponential growth, which might exhibit chaotic features [339].) In contrast, Figs. 3.7(c) and (d) show that for unbalanced gain and loss, $\gamma_1 = 0.8\gamma_0$ and $\gamma_2 = -\gamma_0$, the steady state is reached on a timescale of $\sim 10\mu$s.

While these results are consistent with stability analysis, it is important to note that the

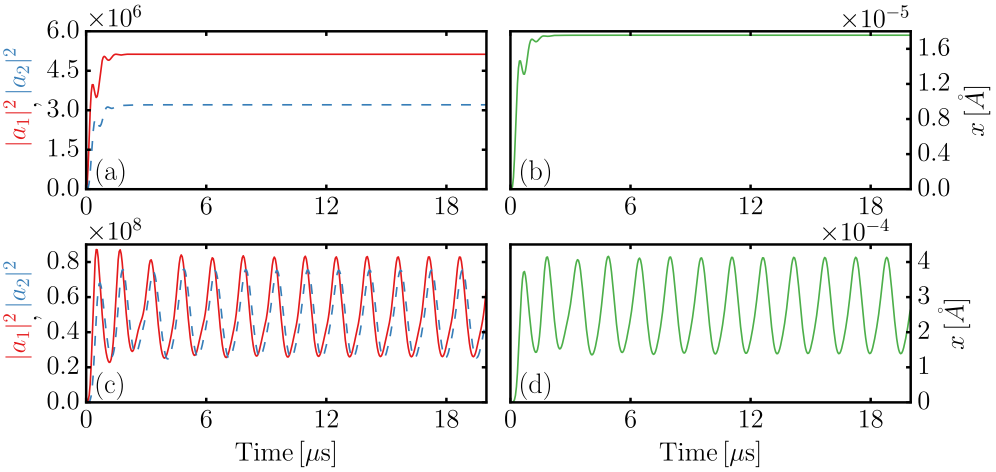

Figure 3.8: Dynamics of the populations $|a_1|^2$ (left column, solid red), $|a_2|^2$ (left column, dashed blue) and the mechanical oscillator amplitude $x(t)$ (right column, solid green). In (a) and (b), the saturation parameter $a_s = 10^3$ whereas in (c) and (d) $a_s = 10^4$. In both plots, $\gamma_2 = -\gamma_0$, $\gamma_1 = 1.5\gamma_0$, $\Delta = -5$ MHz and $P_{\rm in} = 1\mu$W; all other parameters as in Tab. 3.1. Note the different scaling of the y axes.

unbounded exponential growth in the first case cannot continue indefinitely in general. In fact, gain saturation mechanisms [344] are expected to regulate these divergence of the optical and mechanical amplitudes.

Consequently, a full model should include a gain coefficient of the form $\gamma_1/(1 + |a_1|^2/a_s^2)$ with a_s being the gain saturation threshold, rather than just γ_1 [344, 347]. By taking this effect into account, which introduces an additional — gain saturation-induced — nonlinearity, we find that the divergent mechanical oscillation amplitude behavior in Fig. 3.7(b) indeed reaches a steady-state value. In contrast to our previous finding in the case of unsaturated gain, for appropriate gain saturation threshold we now obtain steady-state solutions even in the $\mathcal{PT}$ symmetric case ($\gamma_2 = -\gamma_1$ and $\Delta = 0$), with enhancement factors ranging from $\eta \sim 8$ for $a_s = 10^3$ to $\eta \sim 340$ for $a_s = 3 \times 10^4$, when using $\gamma_1 = J = \gamma_0$ and $P_{\rm in} = 1\mu$W. Note that we use different values for a_s in our simulations as the gain saturation threshold depends on the details of the experiment.

Moreover, when we choose the design and pumping parameters such that $\gamma_2 = -\gamma_0$, $\gamma_1 = 1.5\gamma_0$, $\Delta = -5$MHz and $P_{\rm in} = 1\mu$W, we find two different dynamical regimes depending on the value of the gain saturation. In particular, as shown in Fig. 3.8, whereas the system reaches a steady state for $a_s = 10^3$, the dynamics converges to a sustained oscillation reminiscent of an oscillator limit cycle for $a_s = 10^4$. This feature illustrates the potential importance of accounting for effects such as gain saturation in order to understand reported mechanical oscillatory dynamics [331]. Hence, taking into account gain saturation does not only regulate the divergences previously observed in the mechanical displacement, but introduces a new dynamical behavior: sustained oscillations.

Finally, in order to gain more insight into the dynamics of the mechanical degree of freedom in the presence of an effective gain, we evaluate the mean values as well as oscillation amplitudes as a function of gain and detuning. Figure 3.9 shows an exemplary dynamical landscape obtained by using gain saturation with $a_s = 10^4$. Interestingly, near resonant pumping $\Delta = 0$, the mechanical oscillator always relaxes towards a steady state. On the other hand, oscillatory behavior can occur for off-resonant driving, highlighting the rich dynamics associated with our optomechanical system under different conditions. For appropriate design parameters, the

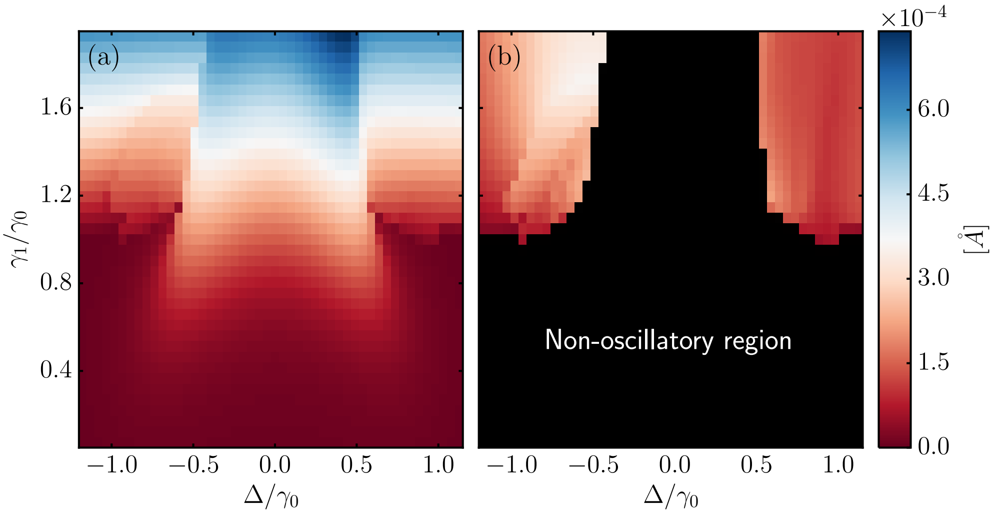

Figure 3.9: Analysis of the dynamics of the mechanical amplitude in the presence of gain saturation, $a_s = 10^4$. In (a), the mean of the oscillation amplitude $\langle x \rangle$ is shown whereas (b) shows the amplitude of the oscillation (maximal amplitude minus minimal amplitude). Back shading in (b) indicates parameter regimes where a steady state rather than an oscillatory motion is reached. The laser power $P_{\text{in}} = 1\mu$W; all other parameters are listed in Tab. 3.1.

dynamics of the mechanical degree of freedom can thus be tuned by changing the frequency of the pumping laser. Accordingly, laser control combined with material design provides a powerful tool to change dynamical as well as steady-state properties of the mechanical mode in the considered optomechanical system.

In summary, we have carried out a comprehensive study of the static and dynamic behavior of optomechanical interaction in non-Hermitian photonic molecules that support an acoustic mode. Our steady-state analysis demonstrates that the strength of the interaction between the photonic supermodes and the mechanical oscillators of an active (gain/loss) system as compared to a passive (loss/loss) system can be significantly enhanced under different conditions for design and pump parameters. Interestingly, we found that $\mathcal{PT}$ symmetry is not necessarily the optimal choice for achieving maximum enhancement. Instead, we have shown that pump frequency detuning can lead to higher enhancement values.

Furthermore, we have studied the linear stability properties of these systems and have shown that the enhancement factors reported in the $\mathcal{PT}$ symmetric case near the exceptional point correspond to unstable solutions. In this regard, we have identified regions in parameter space that correspond to unbalanced optical gain/loss distribution and laser detuning, where much stronger interactions (two orders stronger than the passive cavities) can be still achieved for linearly stable solutions. In addition, we have investigated the dynamical evolution of the system by numerically integrating the nonlinear equations. Our analysis revealed that gain saturation effects play an important role in regulating the behavior of the otherwise exponentially growing oscillations that correspond to unstable fixed points. Moreover, gain saturation allows for two distinct dynamical behaviors, depending on the material design and optical pump parameters: stable fixed points and sustained oscillations.

Chapter 4

Shifting individual modes between system and environment

Abstract — Harmonic oscillator environments are a common means to model complex open quantum system environments. In many cases of interest, these environments are structured, which means that the coupling strength of the environmental modes to the system degrees of freedom is peaked around certain frequencies. These peaks can be decomposed into a number of “pseudomodes”, damped modes that are strongly-coupled to the system degrees of freedom. Shifting these modes from the environment to the system part (or vice versa) can significantly ease numerical simulation. For thermal environments, however, this procedure raises an issue: temperature is incorporated via the initial environment state, and this state is affected by the shift of modes between system and environment. Here we show how the bath correlation function, which quantifies the effect of the environment on the system, depends on different system-environment partitionings. The environment we consider exhibits a particular, nested structure: a single mode coupled to a harmonic bath. We find that the differences in the bath correlation function due to different system-environment partitionings can give rise to pronounced differences in the dynamics of the system. Our results demonstrate that when temperature is incorporated as a property of the environment, the initial environment state has to be chosen with care when modes are shifted between system and environment, and system-environment correlations may have to be accounted for.

The work described in this chapter is based on the following publication [272]:

Pseudomodes and the corresponding transformation of the temperature-dependent bath correlation function
D. W. Schönleber, A. Croy, and A. Eisfeld
Phys. Rev. A **91**, 052108 (2015)

4.1 Introduction

In a widely-adopted approach to open quantum systems, the microscopic model underlying the environment consists of an infinite number of harmonic oscillators linearly coupled to the system degrees of freedom [4, 5, 348]. The popularity of this particular model is owed to its flexibility in simulating the intricate ambient environments of atomic or molecular systems. In particular, both spectrum and frequency-dependent coupling of the environmental modes can be adjusted to reproduce features observed in experiments; for instance, to describe the effect of polar solvents on dyes [5, 348, 349] or to treat vibrational modes of molecules [5, 60]. Harmonic environment models have thus become an indispensable tool for the treatment of open quantum systems.

The properties of a given harmonic environment are typically specified in terms of the spectral density (SD). The SD expresses the coupling strength of the environment modes as a function of their frequency, and hence encodes the information on the environment that is provided by the open quantum system Hamiltonian. In many cases of interest, the SD is structured, that is, the coupling strength of the environmental modes is peaked around certain frequencies, which renders the environment furthermore non-Markovian [42, 43]. Remarkably, such a structured SD has an equivalent formulation in terms of what are called "pseudomodes" [268, 350, 351]: damped, harmonic modes which are characterized by a frequency and a linewidth accounting for the damping. In this way, structured environments can be decomposed into a number of pseudomodes that couple strongly to the system degrees of freedom. As an example, consider a group of molecules. There, one might be interested in the dynamics of the electronic degrees of freedom and thus define those as the relevant system. The remaining degrees of freedom, in particular the internal vibrational modes of the molecule whose damping can be described via a coupling to another harmonic environment, are accordingly defined as the environment. The resulting system-environment partitioning is illustrated in Fig. 4.1(I). (For simplicity, we assume here that the relevant system degrees of freedom are strongly coupled to a single vibrational mode, or pseudomode, which in turn is coupled to an unstructured harmonic bath. See Ref. [60] for a detailed discussion of the relation between an internal vibrational mode and a pseudomode.) Alternatively, one might explicitly include the strongly-coupled (important) vibrational mode in the system part and treat the remaining unstructured (Markovian) part as the environment. This partitioning is illustrated in Fig. 4.1(II). Note that the very same considerations apply in the case of some electronic degrees of freedom being coupled to an imperfect (lossy) cavity [269, 271, 351].

Since in open quantum system theory only the system part is treated explicitly, different system-environment partitionings have immediate consequences for simulation approaches. That is, the environment in partitioning (I) is unstructured and hence Markovian, which may be convenient for some approaches. The rapid growth of the system Hilbert space associated with the explicitly-treated pseudomodes may render partitioning (II) the favorable one for other approaches. To adapt the system-environment partitioning according to the preferred (numerical) treatment, it is thus convenient to switch between different partitionings.

The discussion of switching between different system-environment partitionings has so far focused on the spectral density (SD) [37–39, 41, 60–63]. It has been shown, for example, how the coupling strength of the remaining environment modes transform when certain (pseudo)modes are shifted from the environment part to the system part; a procedure that allows one, for instance, to render a non-Markovian environment Markovian [60, 62, 63]. In transformations of the SD, however, an important environment property is not accounted for: temperature. This additional information on the environment is contained in the bath correlation function.

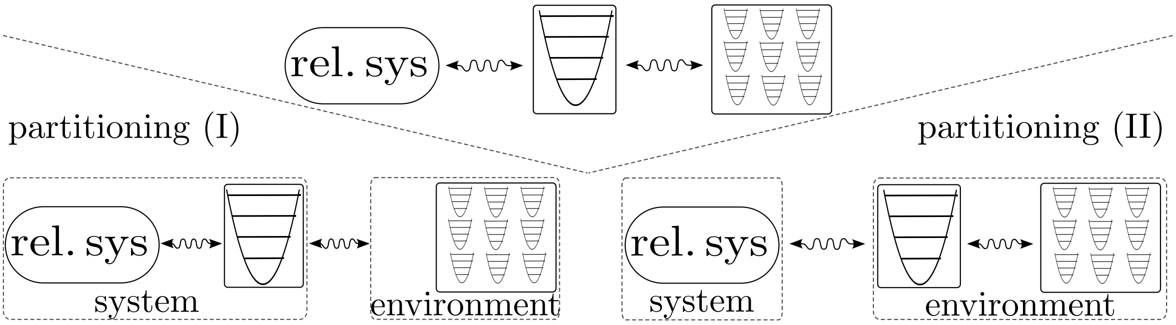

Figure 4.1: Illustration of two different ways to partition a nested open quantum system structure (top panel) into system and environment. The structure consists of relevant system degrees of freedom (rel. sys) strongly coupled to a pseudomode (see main text for details), which in turn is coupled to a harmonic bath. In partitioning (I), both rel. sys and pseudomode are defined as system. In partitioning (II), in contrast, only the rel. sys are defined as system, which results in a structured environment consisting of both pseudomode and harmonic bath.

The bath correlation function (BCF) [4, 5, 42, 263, 352] quantifies temporal correlations of environmental degrees of freedom and eventually determines the influence of the environment on the system. It also depends on the coupling strengths of the environmental modes and their frequencies, but additionally incorporates temperature via the initial environment state. That is, the environmental modes are taken to be initially in thermal equilibrium at a specified temperature. Since system and environment are typically assumed to be uncorrelated in open quantum system theory, shifting individual modes from the environment part to the system part raises the question of how the initial environment state should be chosen and what consequences different choices have.

In this chapter, we study the dependence of the BCF on different system-environment partitionings. In particular, we examine the effect of two different initial environment states, a factorizing and a correlated one, on the BCF. We consider an exemplary model (cf. Fig. 4.1) consisting of a harmonic bath coupled to a single pseudomode (PM). This PM we then couple to another harmonic oscillator that acts as a system, thus allowing us to study the influence of the different BCFs on a system dynamics. The structure of this nested environment is again the same as the one employed in Chaps. 2 and 3: the system is directly coupled to a finite environment part, which in turn is coupled to a macroscopic environment part. Whereas in the previous chapters, we were concerned with manipulating system properties using a nested, controllable environment, we now address the question of whether or not the environment structure is arbitrary, i.e., whether or not changing the system-environment partitioning can change a system's dynamics.

The chapter is structured as follows: In Sec. 4.2, we introduce the microscopic model on which our discussion is based. We outline the procedure according to which BCFs transform and state analytic formulas for the case of a single PM coupled to a harmonic bath. In Sec. 4.3, we evaluate the transformed BCFs numerically and discuss some examples, highlighting the regimes in which notable differences are induced by different initial states. Our analysis shows that environment transformations come with a caveat: thermal environment properties are encoded in the initial environment state, and different initial-state choices can give rise to different system dynamics. Accordingly, care has to be taken in choosing appropriate initial states after environment transformations.

4.2 Model system and analytic transformations

In this section, we detail model Hamiltonian and framework necessary to perform the analytic transformation of the BCF presented at the end of the section. In Sec. 4.2.1 we review the standard model of a system linearly coupled to an environment of independent oscillators and introduce the model Hamiltonian we consider in this chapter in Sec. 4.2.2. Subsequently, in Sec. 4.2.3, we discuss two particular ways to partition this Hamiltonian into a system and an environment part and explain then in Sec. 4.2.4 how the transformed BCF can be calculated. Lastly, we specify two initial environment states and present the corresponding transformed BCFs in Sec. 4.2.5.

4.2.1 Standard model for harmonic environments

We start our discussion by reviewing the standard model of a system linearly coupled to an environment of independent harmonic oscillators, which will allow us later on to point out differences in the transformed BCFs more clearly.

In the standard model, the total Hamiltonian is partitioned into three parts,

$$\mathcal{H}_{\text{tot}} = \mathcal{H}_{\text{S}} + \mathcal{H}_{\text{S-E}} + \mathcal{H}_{\text{E}}, \tag{4.1}$$

where $\mathcal{H}_{\text{S}}$ denotes the Hamiltonian of the system, containing the degrees of freedom in which one is interested in, and

$$\mathcal{H}_{\text{E}} = \sum_{\mu} \tilde{\omega}_{\mu} c_{\mu}^{\dagger} c_{\mu} \tag{4.2}$$

the Hamiltonian of the environment. Here, c_{μ} is the annihilation operator of an environment mode with frequency $\tilde{\omega}_{\mu}$; the frequencies $\tilde{\omega}_{\mu}$ define the spectrum of the harmonic environment. Since the oscillators in $\mathcal{H}_{\text{E}}$ are uncoupled, we call the environment $\mathcal{H}_{\text{E}}$ *diagonal*.

For linear coupling between system and environment, the Hamiltonian accounting for the interactions between system and environment reads as

$$\mathcal{H}_{\text{S-E}} = L_{\text{S}} \left(\sum_{\mu} k_{\mu} c_{\mu}^{\dagger} + \text{H.c.} \right). \tag{4.3}$$

The coupling Hamiltonian $\mathcal{H}_{\text{S-E}}$ couples the environment modes c_{μ} via the system coupling operator L_{S} linearly to the system, with strength k_{μ}. For convenience, one now encodes this frequency-dependent coupling in the SD, defined as ($\omega > 0$)

$$J(\omega) = \sum_{\mu} |k_{\mu}|^2 \delta(\omega - \tilde{\omega}_{\mu}). \tag{4.4}$$

The SD allows one to easily assess the frequencies at which environment modes couple strongly to the system. Note that we set $\hbar = k_{\text{B}} = 1$ throughout this chapter.

The relevant quantity typically entering open quantum system approaches such as Redfield [4, 5], Caldeira-Leggett [3, 4] and non-Markovian quantum state diffusion [352, 353] is the BCF. Microscopically, the BCF is the (two-time) correlation function of the environment operators in the system-environment coupling Hamiltonian and thus quantifies the temporal correlations of environmental degrees of freedom. Since the fluctuations induced by a linearly-coupled harmonic environment are strictly Gaussian [4], and Gaussian statistics is completely defined by its second-order statistics (assuming zero mean), the BCF fully characterizes the influence of the environment on the system. For Hermitian L_{S}, the BCF is given by

$$\alpha(t, t') = \text{Tr}_{\text{E}} \left\{ \left(C(t) + C^{\dagger}(t) \right) \left(C(t') + C^{\dagger}(t') \right) \rho_{\text{E}}(0) \right\}, \tag{4.5}$$

with $C(t)$ denoting the time-dependent environment coupling operator, defined as

$$C(t) = e^{i\mathcal{H}_{\mathrm{E}}t} \sum_{\mu} \left(k_{\mu}^{*} c_{\mu} \right) e^{-i\mathcal{H}_{\mathrm{E}}t} \equiv \sum_{\mu} k_{\mu}^{*} c_{\mu}(t). \tag{4.6}$$

To obtain Eq. (4.5) in the given form, the total initial state of system and environment is taken to be separable,

$$\rho_{\mathrm{tot}}(0) = \rho_{\mathrm{S}}(0) \otimes \rho_{\mathrm{E}}(0). \tag{4.7}$$

This implies that no correlations between system and environment exist before the interaction between system and environment is 'turned on'. As we will see later, this assumption, which is typically introduced by virtue of the ease of computation, establishes the significance of system-environment partitioning.

For a non-Hermitian system coupling operator L_{S}, the BCF is no longer given by Eq. (4.5). Rather, two correlation functions are required [354], reading as

$$\alpha_1(t, t') = \mathrm{Tr}_{\mathrm{E}} \left\{ C(t) C^{\dagger}(t') \rho_{\mathrm{E}}(0) \right\} \text{ and} \tag{4.8a}$$

$$\alpha_2(t, t') = \mathrm{Tr}_{\mathrm{E}} \left\{ C^{\dagger}(t) C(t') \rho_{\mathrm{E}}(0) \right\}. \tag{4.8b}$$

If the BCF is *stationary*, i.e., if $\alpha(t, t')$ is a function of the time difference only, $\alpha(t, t') = \alpha(t - t', 0)$, it is convenient to write $\alpha(\tau) \equiv \alpha(\tau, 0)$, with $\tau = t - t'$. Note that the stationarity of the BCF depends on the initial state of the environment in general.

If the initial state of the diagonal environment $\rho_{\mathrm{E}}(0)$, which enters Eq. (4.5), is a thermal state (and if L_{S} is Hermitian), the BCF of the environment is of the 'standard' form

$$\alpha(\tau) = \int_0^{\infty} d\omega J(\omega) \left(\coth\left(\frac{\omega}{2T} \right) \cos(\omega\tau) - i \sin(\omega\tau) \right), \tag{4.9}$$

with $\tau = t - t'$. In Eq. (4.9), T denotes the temperature of the environment and $J(\omega)$ the SD. For a detailed review of SD and BCF in the standard case we refer to Appendix C.1.

4.2.2 Model Hamiltonian with PM

We now introduce the total Hamiltonian on which we focus here, which is of the form

$$\mathcal{H}_{\mathrm{tot}} = \mathcal{H}_{\mathrm{rel}} + \mathcal{H}_{\text{rel-PM}} + \mathcal{H}_{\mathrm{PM}} + \mathcal{H}_{\text{PM-B}} + \mathcal{H}_{\mathrm{B}}. \tag{4.10}$$

In Eq. (4.10), $\mathcal{H}_{\mathrm{rel}}$ contains the relevant degrees of freedom we are interested in. This relevant part is via the Hamiltonian

$$\mathcal{H}_{\text{rel-PM}} = \left(g^{*} b L^{\dagger} + \text{H.c.} \right), \tag{4.11}$$

linearly coupled to the PM, whose Hamiltonian reads as

$$\mathcal{H}_{\mathrm{PM}} = \Omega b^{\dagger} b. \tag{4.12}$$

Here, L is some operator in the Hilbert space of the relevant Hamiltonian $\mathcal{H}_{\mathrm{rel}}$, g a coupling constant quantifying the strength of the coupling, and Ω the frequency of the PM with annihilation operator b. In addition, the PM is coupled to a diagonal bath

$$\mathcal{H}_{\mathrm{B}} = \sum_{\lambda} \omega_{\lambda} a_{\lambda}^{\dagger} a_{\lambda}, \tag{4.13}$$

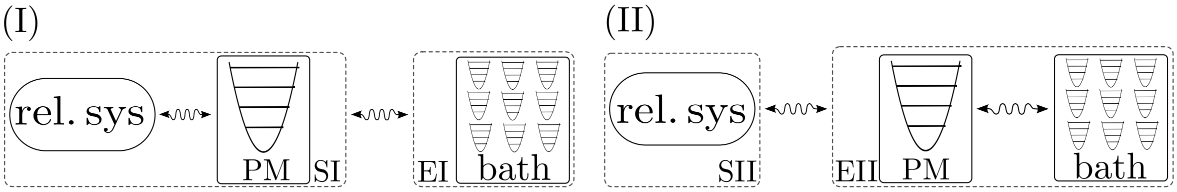

Figure 4.2: Illustration of two different ways of performing a system-environment partitioning in the presence of a PM linearly coupled to both system and bath. In (I), the system part SI consists of the relevant system degrees of freedom linearly coupled to the PM, which in turn is coupled to an (unstructured) environment EI whereas in (II) the system SII directly couples to a (structured) environment EII including the PM.

where ω_λ are the frequencies belonging to the bath modes λ with annihilation operators a_λ. The coupling Hamiltonian $\mathcal{H}_{\text{PM-B}}$ is taken to be bilinear,

$$\mathcal{H}_{\text{PM-B}} = \sum_\lambda \left(\kappa_\lambda^* a_\lambda b^\dagger + \text{H.c.} \right), \tag{4.14}$$

with κ_λ being the coupling constants quantifying the coupling between PM and bath modes. The generalization of our discussion to several PMs is straightforward in many cases of interest (e.g., for single linear chains of PMs [37, 38] and multiple linear chains [39, 41]), and will be addressed at the end of this section.

4.2.3 System-environment partitioning

We now consider two particular examples of assigning the PM to the different parts of the total Hamiltonian, illustrated in Fig. 4.2. This leads to different choices of the system Hamiltonian $\mathcal{H}_\text{S}$, the environment Hamiltonian $\mathcal{H}_\text{E}$, and the coupling between them. We denote the two different ways of partitioning by SI and SII for the system and EI and EII for the environment, respectively.

PM in the system

The first partitioning [(I) in Fig. 4.2] is to take the PM as part of the system, which amounts to setting

$$\mathcal{H}_{\text{SI}} = \mathcal{H}_{\text{rel}} + \mathcal{H}_{\text{rel-PM}} + \mathcal{H}_{\text{PM}}, \tag{4.15}$$

$$\mathcal{H}_{\text{EI}} = \mathcal{H}_{\text{B}}, \tag{4.16}$$

and

$$\mathcal{H}_{\text{SI-EI}} = \mathcal{H}_{\text{PM-B}}. \tag{4.17}$$

Note that the system now contains besides the relevant degrees of freedom also the PM, and that the environment is in the standard form (4.2).

PM in the environment

The second partitioning is illustrated in panel (II) in Fig. 4.2. Here, the system is given by

$$\mathcal{H}_{\text{SII}} = \mathcal{H}_{\text{rel}}, \tag{4.18}$$

while the environment EII contains both PM and bath,

$$\mathcal{H}_{\text{EII}} = \mathcal{H}_{\text{PM}} + \mathcal{H}_{\text{PM-B}} + \mathcal{H}_{\text{B}}. \tag{4.19}$$

Accordingly, the coupling between system and environment is given by

$$\mathcal{H}_{\text{SII-EII}} = \mathcal{H}_{\text{S-PM}}. \tag{4.20}$$

Note that the environment Hamiltonian $\mathcal{H}_{\text{EII}}$ is *not* in the standard form (4.2), since the environment is not diagonal. It can, however, be diagonalized by a simple transformation, as detailed in Appendix C.2.

4.2.4 Calculation of the BCF

In terms of the SD, it is known how to transform between different ways of system-environment partitioning [42, 60, 61, 63, 350]. For this procedure, it is sufficient to know the total Hamiltonian, since the SD is fully encoded in $\mathcal{H}_{\text{tot}}$.

The BCF, however, depends on the initial environment state, denoted by $\rho_{\text{EI}}(0)$ and $\rho_{\text{EII}}(0)$, respectively, for the two settings depicted in (I) and (II) in Fig. 4.2. Note that to obtain an uncorrelated total initial state of form (4.7), we need $\rho_{\text{tot}}(0) = \rho_{\text{SI}}(0) \otimes \rho_{\text{EI}}(0)$ in setting (I) whereas $\rho_{\text{tot}}(0) = \rho_{\text{SII}}(0) \otimes \rho_{\text{EII}}(0)$ in setting (II). In setting (I), the environment is diagonal and we can therefore directly use Eq. (4.5) to calculate the BCF. In setting (II), in contrast, the environment EII is not diagonal. Nonetheless, we can similarly to Eq. (4.6) write down the time evolution of the environment coupling operator,

$$B(t) = g^* \, e^{i\mathcal{H}_{\text{EII}}t} \, b \, e^{-i\mathcal{H}_{\text{EII}}t} \equiv g^* \, b(t), \tag{4.21}$$

whose time dependence arises via transformation into the interaction picture with respect to the environment Hamiltonian $\mathcal{H}_{\text{EII}}$.

For a Hermitian system operator $L = L^\dagger$, $\mathcal{H}_{\text{S-PM}}$ can be written as $\mathcal{H}_{\text{S-PM}} = L(g^* b + g b^\dagger)$, which has a Hermitian environment coupling operator. In this case, the BCF is given by

$$\begin{aligned} \alpha(t,t') &= \mathrm{Tr}_{\text{EII}} \left\{ \left(B(t) + B^\dagger(t)\right) \left(B(t') + B^\dagger(t')\right) \rho_{\text{EII}}(0) \right\} \\ &\equiv \left\langle \left(B(t) + B^\dagger(t)\right) \left(B(t') + B^\dagger(t')\right) \right\rangle_{\text{EII}}, \end{aligned} \tag{4.22}$$

where $\rho_{\text{EII}}(0)$ denotes the initial density operator of the environment and the subscript EII of the trace indicates that the trace is taken over the environmental degrees of freedom.

To evaluate the BCF (4.22), it is convenient to take advantage of the existence of a linear transformation between the PM operator b and the operators in which the Hamiltonian $\mathcal{H}_{\text{EII}}$ and the initial state, respectively, are diagonal (cf. Appendix C.2). Specifically, we first transform the PM operator into the basis in which the environment Hamiltonian $\mathcal{H}_{\text{EII}}$ is diagonal, $b(t) = [S\bar{c}(t)]_0$, by means of the transformation matrix S. The time evolution of the annihilation operators c_μ of the diagonal Hamiltonian $\mathcal{H}_{\text{EII}}$, however, is simply given by $c_\mu(t) = e^{-i\tilde{\omega}_\mu t} c_\mu$, where $\tilde{\omega}_\mu$ denote the eigenenergies of $\mathcal{H}_{\text{EII}}$. Subsequently, the operators c_μ are transformed into the basis in which the initial state is diagonal, if necessary, and the BCF is evaluated.

4.2.5 Choice of initial environment states

As discussed in the previous section, the total initial state in case (I) is typically taken to be $\rho_{\text{tot}}(0) = \rho_{\text{SI}}(0) \otimes \rho_{\text{EI}}(0)$. When moving the PM from the system part to the environment part, i.e., going from (I) to (II), one could thus reason that the initial state of the environment EII should be given by $\rho_{\text{EII}}(0) = \rho_{\text{PM}}(0) \otimes \rho_{\text{EI}}(0)$. Conversely, if one considers the PM to be part of the environment EII from the very beginning on, there is no reason why the PM should be uncorrelated with EI. From this point of view, a correlated initial state between

PM and EI seems to be more ‘natural’. To clarify the implications of the two aforementioned choices, we employ these initial states when evaluating the BCF in setting (II) in the following. We note that these two initial states are indeed of interest, since they arise in the calculation of absorption and emission spectra, where the factorized state corresponds to the initial state relevant for absorption spectra calculations while the correlated initial state to the one relevant for emission spectra calculations [355, 356].

Factorizing initial state between PM and EI

The first initial state we consider is the one typically associated with *factorizing* initial conditions between PM and bath EI,

$$\rho_{\mathrm{EII}}^{\mathfrak{F}}(0) = \frac{1}{Z} e^{-\beta\left(\Omega b^\dagger b + \sum_\lambda \omega_\lambda a_\lambda^\dagger a_\lambda\right)}, \tag{4.23}$$

where $\beta = 1/T$ is the inverse temperature and the partition function Z is defined such that $\mathrm{Tr}_{\mathrm{EII}}\{\rho_{\mathrm{EII}}^{\mathfrak{F}}(0)\} = 1$; the superscript $\mathfrak{F}$ here denotes the factorized initial PM-bath state. This particular initial state is widely used, owing to its convenient properties in analytic calculations. The physical assumption implied is that during thermal equilibration with an ambient heat bath no correlations are built up between PM and bath EI; a reasoning that only holds in the limit of vanishing coupling between PM and bath since only in this limit independent thermal equilibration (i.e., equilibration to the respective canonical states) of two coupled systems exists [357–360] (cf. also Refs. [361, 362]).

Evaluating the BCF (4.22) with factorizing initial state, we find (see Appendix C.2 for details)

$$\begin{aligned}\alpha(t,t') = |g|^2 \sum_{\mu,\nu,\eta} \Big[& S_{0\mu}^* S_{0\nu} S_{\eta\mu} S_{\eta\nu}^* e^{i(\tilde{\omega}_\mu t - \tilde{\omega}_\nu t')} n(\omega_\eta) \\ & + S_{0\mu} S_{0\nu}^* S_{\eta\mu}^* S_{\eta\nu} e^{-i(\tilde{\omega}_\mu t - \tilde{\omega}_\nu t')} \left(n(\omega_\eta) + 1\right) \Big] .\end{aligned} \tag{4.24}$$

Here, $n(\omega)$ is the mean occupation number of an environment oscillator with frequency ω,

$$n(\omega) = \frac{1}{(e^{\beta\omega} - 1)}. \tag{4.25}$$

Note that Eq. (4.24) is not in the form of Eq. (4.9); in fact, we cannot even write $\alpha(t,t') = \alpha(t-t',0)$.

Thermal (correlated) state of PM and EI

The second initial state we consider we call *diagonal* initial state; we thereby denote the canonical state of the environment EII. This state we obtain for increased coupling between PM and bath EI, since with increasing coupling the equilibrium state of PM and bath will be given by the thermal state of the joint PM-bath environment, which no longer factorizes into a PM and a bath part. Introducing the creation (annihilation) operators of the eigenmodes of the joint PM-bath system $c_\mu^\dagger$ (c_μ), the global thermal state reads as

$$\rho_{\mathrm{EII}}^{\mathfrak{D}}(0) = \frac{1}{Z} e^{-\beta \sum_\mu \tilde{\omega}_\mu c_\mu^\dagger c_\mu}. \tag{4.26}$$

Here, the superscript $\mathfrak{D}$ denotes the diagonal initial PM-bath state, implying that at $t = 0$ PM and bath have jointly evolved towards a thermal state whose occupation depends on the eigenenergies $\tilde{\omega}_\mu$ of the composite system. As before, Z is defined such that $\mathrm{Tr}_{\mathrm{EII}}\{\rho_{\mathrm{EII}}^{\mathfrak{D}}(0)\} = 1$.

For the diagonal initial state, the BCF reads as ($\tau = t - t'$)

$$\alpha(\tau) = |g|^2 \sum_{\mu} |S_{0\mu}|^2 \left[e^{i\tilde{\omega}_\mu \tau} n(\tilde{\omega}_\mu) + e^{-i\tilde{\omega}_\mu \tau} \left(n(\tilde{\omega}_\mu) + 1 \right) \right]. \tag{4.27}$$

Note that Eq. (4.27) is of the same form as in the standard case [cf. Eq. (C.5)] and can hence be written in the standard form (4.9), using a transformed SD.

Discussion

Equations (4.24) and (4.27) allow for several observations. Firstly, the BCF comprises of the time evolution of the eigenmodes of the PM-bath environment weighted by the populations of the eigenmodes in the initial state. Secondly, we explicitly see that for factorizing initial conditions the BCF is non-stationary (for small times) whereas in the case of a diagonal initial state we obtain a stationary BCF. This is to be expected, since for a PM-bath environment in thermal equilibrium, the expectation value of any number operator (e.g. $b^\dagger b$) should not depend on time — which is exactly what we observe if we set $\tau = 0$ in Eq. (4.27). (As $\alpha(t, t') \propto \langle b^\dagger(t) b(t') + b(t) b^\dagger(t') \rangle_{\mathrm{EII}}$, the stationarity of $\langle b^\dagger(t) b(t) \rangle_{\mathrm{EII}}$ can be directly read off from the BCF.) Conversely, for factorizing initial state, the environment is not in its equilibrium in the beginning, which renders the BCF non-stationary.

The procedure outlined above can be generalized straightforwardly to, e.g., linearly-coupled chains of PMs of which the last PM is possibly coupled to a diagonal harmonic bath [38, 63], directly-coupled PMs with independent baths [363], or a combination of both [39, 41]. As the BCF of the system is determined by the correlation function of the PM operator directly coupled to the system, we simply need to adjust $\mathcal{H}_{\mathrm{EII}}$ in the above treatment; the calculation of the BCF then proceeds in the exact same manner as detailed above.

Since the neglect of initial correlations can lead to noticeable differences in the dynamics [358, 364, 365], depending on the parameters of the underlying Hamiltonian, we now turn to the discussion of numerical examples.

4.3 Numerical examples

4.3.1 Evaluation of the transformed BCFs

In our numerical examples, we take as spectral density for EI an Ohmic SD with exponential cutoff ($\omega > 0$),

$$J_{\mathrm{EI}}(\omega) = \eta \omega e^{-\omega/\Lambda}, \tag{4.28}$$

where Λ is the cutoff frequency and η a scaling for the overall coupling strength. For numerical purposes, we sample $J_{\mathrm{EI}}(\omega)$ at discrete frequencies ω_λ. The couplings κ_λ of Eq. (4.14) we obtain by evaluating the quadrature [60]

$$\kappa_\lambda = \sqrt{J(\omega_\lambda) \Delta\omega_\lambda}, \tag{4.29}$$

with $\Delta\omega_\lambda = (\omega_{\lambda+1} - \omega_{\lambda-1})/2$ for $\lambda = 2, \ldots, N-1$; $\Delta\omega_1 = \omega_2 - \omega_1$ and $\Delta\omega_N = \omega_N - \omega_{N-1}$.

The sampling range is chosen such that the full SD is covered. For the particular cases shown, we use $N = 4000$ bath oscillators for the numerical discretization, with equidistantly-spaced frequencies, starting from $0.002\,\Lambda$. For the sake of clarity of presentation, we choose the PM frequency close to the maximum of the Ohmic SD, setting $\Omega = 1.5\,\Lambda$. This choice renders the coupling between PM and bath strongly dependent on the overall scaling of the SD, which is quantified by η.

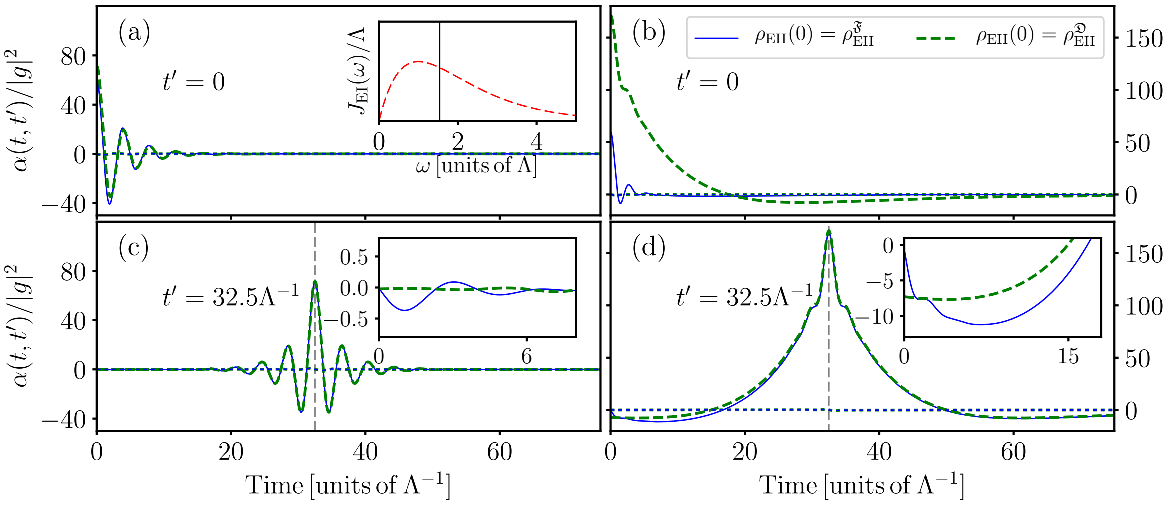

Figure 4.3: Bath correlation functions $\alpha(t,t')/|g|^2$ for different coupling strengths η and different reference times t'. The left column [panels (a) and (c)] shows the BCF for weak PM-bath coupling, $\eta = 0.25$, whereas the right column [panels (b) and (d)] shows a strong coupling regime, $\eta = 1.0$. In the first row [panels (a) and (b)], the reference time of the BCF is set to $t' = 0$, in the second row [panels (c) and (d)], $t' = 32.5\,\Lambda^{-1}$. Solid blue lines indicate the real part of the BCF with factorizing initial state (4.23), dashed green lines the real part of the BCF with diagonal initial state (4.26). Dotted lines show the corresponding imaginary parts. The insets in panel (c) and (d) provide a detail of the short-time dynamics, while the inset in (a) shows the SD $J_{\mathrm{EI}}(\omega)$ (dashed red line) with the position of the PM indicated by a solid vertical line. The BCFs were calculated using $T = 46\,\Lambda$ and $\Omega = 1.5\,\Lambda$.

Note that the Hamiltonian $\mathcal{H}_{\mathrm{EII}}$ is positive for all parameters employed in the numerical calculations discussed in this section, and that the finite recurrence time of the BCF is large enough to observe complete decay of the BCF.

We now evaluate the BCFs (4.24) and (4.27) with the described numerical procedure for different couplings η and times t'. Using the SD (4.28), this yields the BCFs displayed in Fig. 4.3. There, the left column [(a) and (c)] corresponds to relatively weak coupling $\eta = 0.25$ whereas the right column [(b) and (d)] to relatively strong coupling between PM and bath EI, with $\eta = 1.0$. Furthermore, the first row [(a) and (b)] shows the BCFs evaluated at $t' = 0$ while the second row [(c) and (d)] shows the BCFs evaluated at $t' = 32.5\,\Lambda^{-1}$.

As can be seen from Figs. 4.3(a) and (b), at $t' = 0$ pronounced differences emerge between the two different initial conditions (blue versus green) as the coupling η is increased. On the one hand, the damping of the BCF is increased in the presence of strong coupling $\eta = 1.0$, with the overall equilibration time of the BCF increasing as well, which results in different dynamics for the two initial states. On the other hand, the initial value $\alpha(0,0)$ of the BCFs changes, highlighting the increasing differences between the initial states that manifest themselves in the dynamics of the BCF.

Considering the BCFs evaluated at $t' = 32.5\,\Lambda^{-1}$, shown in Figs. 4.3(c) and (d), we observe that the BCFs obtained from different initial states look very similar, with the strongest difference being a transient equilibration dynamics present for factorizing initial conditions, which gets more noticeable in the case of strong coupling η. The differences found between the different initial states for $t = t' = 0$ have almost vanished at $t = t' = 32.5\,\Lambda^{-1}$ [cf. Figs. 4.3(a) and (c) and Figs. 4.3(b) and (d), respectively], due to the fact that equilibration has already taken place before $t = 32.5\,\Lambda^{-1}$.

The non-stationarity of the BCF for factorizing initial conditions is related to what is called "initial slippage" if a system is coupled to a Markovian environment. In such systems, a

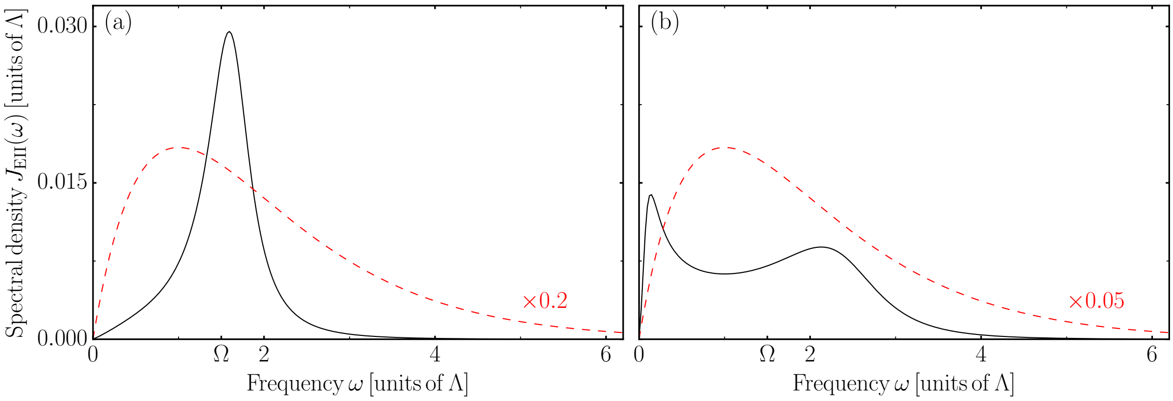

Figure 4.4: Spectral density $J_{\mathrm{EII}}(\omega)$ (black, solid line) for (a) $\eta = 0.25$ and (b) $\eta = 1.0$ obtained from Fourier transformation of the BCF (see main text for details). As the BCFs for diagonal and factorizing initial state (evaluated at $t_{\mathrm{c.m.}} = 130\,\Lambda^{-1}$) coincide, they yield identical SDs. In both panels, the red, dashed line indicates the original SD of the Ohmic bath, which has been scaled by the factor denoted in red. All other parameters are as in Fig. 4.3.

non-Markovian feature can be present at small times due to the fact that Markovian dynamics for the total system requires correlations between system and environment that are not present initially if factorizing initial conditions are employed [4, 366]. Hence, slippage of initial conditions can remedy non-Markovian dynamics introduced by an initially uncorrelated system-environment state. In the same manner, the BCFs displayed in Fig. 4.3 need some time to equilibrate for factorizing initial conditions before reaching ‘stationarity’ [364].

4.3.2 Corresponding SDs

The SD, as defined in Eq. (4.4), is fully determined by the total Hamiltonian. Consequently, it should not depend on the initial state of the environment. For a diagonal environment, the SD can be extracted straightforwardly from the BCF owing to the relation (4.9) between BCF and SD. That is, for the diagonal initial state, the SD can be obtained by Fourier transforming Eq. (4.27) with respect to the time difference τ and dividing by the factor $2\pi[n(\omega) + 1]$ [cf. Eq. (C.9)]. For factorizing initial state, we can rewrite Eq. (4.24) as a function of the center-of-mass coordinate $t_{\mathrm{c.m.}} = (t + t')/2$ and the time difference $\tau = t - t'$ and perform a Fourier transformation with respect to τ.

The spectral densities corresponding to the parameters of Fig. 4.3 are shown in Fig. 4.4. For large times $t_{\mathrm{c.m.}}$, $t_{\mathrm{c.m.}} \gtrsim 120\,\Lambda^{-1}$, the difference between the Fourier transformations obtained from the BCFs using a diagonal and a factorizing initial state, respectively, vanish. For this reason, we show only a single SD in Fig. 4.4.

The SDs obtained from the BCFs perfectly agree with the analytical result of Ref. [60], which has been obtained by direct transformation of the SD. The transformation of the BCF calculated above is thus consistent with the known transformation of the SD. Note, however, that in Ref. [60] another convention for the SD has been used, i.e., the SD is defined as $\omega^2 J(\omega)$ in our convention. For a discussion of the advantage of the convention employed in this chapter, see Ref. [363].

As shown in Fig. 4.4, for weak coupling $\eta = 0.25$, the SD exhibits only a single peak at approximately the PM frequency Ω, with a width proportional to the coupling η. For large coupling $\eta = 1.0$, the single peak is split into two and the coupling strength at the PM frequency is reduced. This illustrates that for large PM-bath coupling, the bath properties indeed become relevant for a system coupled to the PM.

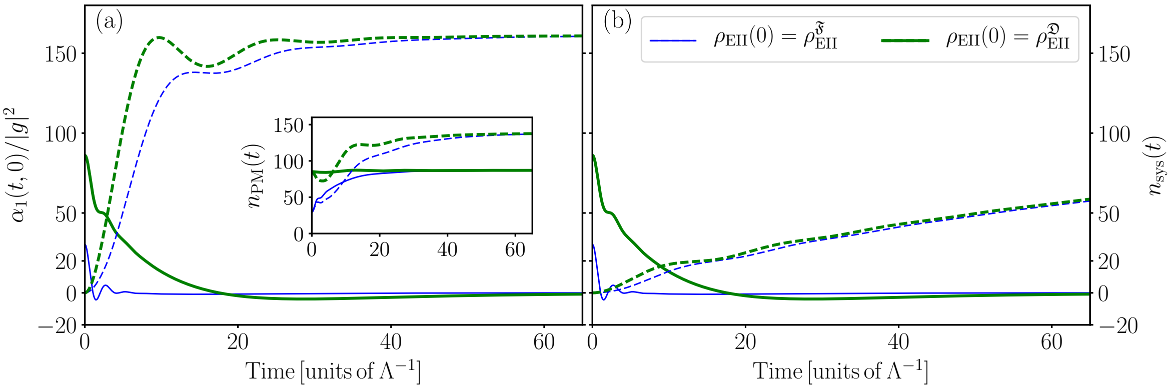

Figure 4.5: Bath correlation function $\alpha_1(t,0)/|g|^2$ (solid lines) and system mean occupation number $n_{\mathrm{sys}}(t) \equiv \langle d^\dagger(t)d(t)\rangle_{\mathrm{EII}}$ (dashed lines) for different initial conditions and different coupling strengths g. In the left panel (a), $g = 0.3\,\Lambda$, whereas the right panel (b), $g = 0.08\,\Lambda$. Thin blue lines indicate the BCF with factorizing initial state (4.23), thick green lines indicate the BCF with diagonal initial state (4.26). Only the real parts of the BCFs are shown. The inset shows the PM mean occupation number $n_{\mathrm{PM}}(t) \equiv \langle b^\dagger(t)b(t)\rangle_{\mathrm{EII}}$ for $g = 0.3\,\Lambda$ (dashed line) and $g = 0.08\,\Lambda$ (solid line) for both initial states. Except for $\eta = 1.0$ and $\Omega_{\mathrm{sys}} = 0.46\,\Lambda$, the parameters of Fig. 4.3 have been used. Note that $\alpha_1(t,0)$ is approximately $\alpha(t,0)/2$ in Fig. 4.3.

4.3.3 Corresponding system dynamics

We now turn to analyzing the effect of the features seen in Fig. 4.3 on a system observable. To that end, we specify the system operator L ($L^\dagger$) in Eq. (4.11) as the annihilation (creation) operator d ($d^\dagger$) of a harmonic oscillator with frequency Ω_{sys}, with the associated system Hamiltonian reading as

$$\mathcal{H}_{\mathrm{SII}} = \Omega_{\mathrm{sys}} d^\dagger d. \tag{4.30}$$

This particular set of non-Hermitian coupling operators allows us to conveniently evaluate the dynamics of the total system via diagonalization, as outlined in Sec. 4.2.4 and Appendix C.2. The corresponding correlation functions $\alpha_1(t,t')$ and $\alpha_2(t,t')$, defined in Eqs. (4.8a) and (4.8b), can be easily read off from Eqs. (4.24) and (4.27).

Choosing the values $\eta = 1.0$ and $\Omega_{\mathrm{sys}} = 0.46\,\Lambda$ for the above parameters, and requiring $n_{\mathrm{sys}}(0) \equiv \langle d^\dagger(0)d(0)\rangle_{\mathrm{EII}} = 0$, we obtain Fig. 4.5 for two different system-PM couplings, $g/\Lambda = 0.3$ and $g/\Lambda = 0.08$. Note that only $\alpha_1(t,t')$ is shown in Fig. 4.5 since for the parameters chosen, $\alpha_2(t,t')$ is indistinguishable from $\alpha_1(t,t')$ on the scale of the figure. The reason for choosing Ω_{sys} relatively small is that the steady-state value of $n_{\mathrm{sys}}(t)$ decreases with increasing Ω_{sys}, such that absolute differences in $n_{\mathrm{sys}}(t)$ are suppressed for large system frequencies. Likewise, we have to choose η large in order to ensure that the system dynamics, which is only indirectly coupled to the bath via the PM, is affected by the bath.

For strong coupling of the PM to both system [$g = 0.3\,\Lambda$, Fig. 4.5(a)] and bath, we observe a marked difference in the mean occupation number $n_{\mathrm{sys}}(t)$ between the results attained from using different initial states. This difference highlights that in case of a strongly-coupled PM, the initial state of the environment becomes important for the transient system dynamics. In contrast, the equilibrium values of both $n_{\mathrm{sys}}(t)$ and $n_{\mathrm{PM}}(t)$ are independent of the initial environment state [364]. If we decrease the coupling g to the system mode (or, similarly, the coupling η to the bath oscillators), the difference in the dynamics decreases [cf. Fig. 4.5(b)] and the appropriate choice of initial conditions of the environment becomes less important. The same applies for choosing Ω_{sys} large, as this results in a lower steady-state value of $n_{\mathrm{sys}}(t)$ and consequently smaller overall deviations.

Moreover, the time it takes for the system to equilibrate increases as g is decreased [cf. Fig. 4.5(b)], as the equilibration of the system only proceeds via interaction with the PM. Conversely, the PM equilibrates faster for small system-PM coupling g (cf. inset), since in this case the strong PM-bath coupling dominates the equilibration dynamics of the PM. This again illustrates that for small system-PM coupling, it is indeed valid to assume a factorized initial environment state since the differences induced by the BCF rapidly vanish from the system's point of view.

For low bath temperature, the differences in the dynamics persist, however, they become hardly observable due to the steady-state values (as well as the initial conditions) being significantly smaller as compared to high bath temperature. Hence, at low temperature, absolute deviations are reduced while relative deviations are preserved.

Our numerical simulations show for different initial environment states pronounced differences in the transient dynamics of a system that via a PM strongly couples to an Ohmic bath. Thus, any scheme sensitive to the transient behavior of the BCF crucially depends on the choice of initial conditions of the total system.

In summary, we have analytically and numerically studied the the BCFs resulting from effectively treating a harmonic oscillator (PM) linearly coupled to a harmonic bath as part of the bath, for a factorizing and a correlated initial state between PM and bath. We outlined the procedure to analytically derive the transformed BCF and discussed concrete examples for regimes in which the differences in the BCFs arising from different initial states manifest themselves in a different dynamics of the system, which we take to be a harmonic oscillator linearly coupled to the PM. This establishes a simple framework to evaluate transformed BCFs of PMs coupled to a harmonic bath. In particular, we find that in the case of a correlated, diagonal initial state, the BCF features all the properties typically assumed for a BCF (i.e., stationarity, detailed balance, and the relation (C.9) between the Fourier transform of the BCF and the SD). By contrast, for a factorizing initial state these properties do not apply, owed to the non-stationarity of the BCF in this case. Only after a transient equilibration dynamics that can induce different system dynamics, they are recovered.

Our findings highlight that (i) the differences between the BCFs for the different initial states (factorizing and diagonal initial state) are negligible for small PM-bath coupling or PM-system coupling respectively, as expected, yet (ii) these differences can have strong impact on the system dynamics if the PM is strongly coupled to both system and bath. Therefore, in case of a strongly-coupled PM, an appropriate initial state of the environment has to be used for the transformation of the BCF when considering a system's dynamics in the presence of finite temperature. This emphasizes the relevance of accounting for correlations in strongly-coupled systems, which is not specific to our particular system [360, 367]. The question as to which initial state is to be considered as appropriate cannot be answered *a priori*, but has to be answered in consideration of the specific case.

This analysis of the dependence of the BCF on different initial states arising from different system-environment partitionings complements the investigation of environment transformations (e.g., the mapping of a structured bath consisting of many harmonic oscillators to a linear chain of oscillators [37–39]), which focused on the SD. It reveals that the initial environment state has to be chosen with care when mapping different system-environment partitionings or environment structures onto each other, which may be performed for numerical convenience or for the ease of implementation [11, 41]. The caveat here comes with the assumption often-employed in open quantum system theory, namely that system and environment are initially uncorrelated. Unless the partitioning between system and environment is obvious on physical grounds, correlations between system and environment might need to be introduced to guarantee the equivalence of different system-environment partitionings.

Chapter 5

Summary and outlook

In this thesis we studied various facets of reservoir engineering in different physical platforms, using a particular, nested environment structure: our system is coupled to a finite part of the environment, which in turn is coupled to a macroscopic part. Our aim was to demonstrate the flexibility of such an environment structure for reservoir engineering, with applications ranging from quantum simulation to system-state preparation, and to investigate its limitations. We have done so by applying this nested structure in an atomic system of interacting Rydberg atoms, an optomechanical system of non-Hermitian resonators, and an open quantum system model of harmonic oscillators. With the Rydberg atomic system, we have shown that the tunable atomic environment provided by laser-driven decaying atoms allows one to realize a quantum simulator for excitation transport in the presence of a decohering environment. With the optomechanical system, we have investigated the tunability of the mechanical mode via control of the optical non-Hermitian resonator environment. Lastly, we have examined how the properties of a nested, harmonic environment depend on the initial environment state. We thereby explicated a caveat that comes with transformations between different system-environment partitionings, which are performed to cast the environment into a form that is easy to implement in numerical or quantum simulation approaches. We will first expand on the aforementioned findings and the associated further research questions before giving an overview and a personal perspective of our thesis' results.

In **Chapter 2** we showed that an aggregate of Rydberg atoms interacting with a laser-driven atomic environment, which is dissipative though its coupling to the electromagnetic continuum, can serve as a quantum simulator for excitation transport. We demonstrated that the atomic environment allows for experimentally accessible transport imaging, that is, for optical discrimination between the two Rydberg states involved in the excitation transport. We also established a link between the information on the aggregate state obtained by the environment and quantum back-action, namely dephasing of the transport. To assess the environment properties of a gas consisting of many environment atoms, for which a full numerical treatment is inhibited by the exponential increase of environment states, we derived an effective model for the aggregate dynamics by adiabatically eliminating environment states. The atomic environment essentially only enters this model through energy shifts and dephasing of the aggregate states. We showed that both dominant dephasing with Gaussian statistics and dominant energy disorder with non-Gaussian statistics can be realized in our setup, which give rise to diffusive and sub-diffusive transport dynamics respectively. Furthermore, we demonstrated that non-Markovian aggregate dynamics with a tunable degree of non-Markovianity can be achieved via control of atomic distances, laser intensities and frequencies. Lastly, we constructed a thermal environment with optically controllable temperature for the Rydberg aggregate and showed that specific aggregate states, such as Bell states, can be prepared.

Our proposal expands the toolbox available for quantum simulation of excitation transport by providing an experimentally accessible setup in which a broad range of environment effects can be achieved through the highly-controllable atomic environment. The realization of such a simulator will benefit the study of excitation transport in open systems, be it semiconductors or light-harvesting complexes, as it allows the investigation of the transition between coherent and incoherent transport, properties of non-Markovian transport dynamics, and non-equilibrium transport effects pertaining to the coupling to a thermal environment. Our findings demonstrate the high degree of control that can be attained through nested environments, here consisting of laser-driven atoms, which are coupled to a photonic continuum through spontaneous emission.

The flexibility of this nested environment for system control raises additional questions that merit further research. In particular, while we have shown that our atomic environment allows us to induce various dynamical effects, we did not classify the genericness of our environment. Answering this question requires a characterization of the environment similar to the one performed for harmonic environments through spectral density and bath correlation function. Once such a characterization has been carried out and the capabilities and limitations of our nested environment have been analyzed, it would be of great interest to investigate whether a mapping between other characterization schemes (e.g., using spectral density and bath correlation function) and the developed one could be established. If this was the case, environment models of light harvesting complexes, for example, could be directly mapped onto our quantum simulator setup, which would provide us with a fully-fledged, multipurpose quantum transport simulator.

Apart from these general questions, our setup provides fertile ground for further research. For instance, it would be interesting to investigate whether and how time-dependent laser fields, possibly even combined with feedback schemes [182], can benefit system control. Additionally, adopting a thermodynamic point of view [368] might shed more light on the connection between the energy flow from or to the system (manifested in the change in aggregate eigenstate populations) and the energy absorbed by the environment from the laser fields. Furthermore, since our effective model for the aggregate dynamics was derived via adiabatic elimination of environment states, it is not valid in parameter regimes in which adiabatic elimination cannot be performed, such as the regime in which non-Markovian aggregate dynamics arises. Accordingly, it would be highly desirable to extend the model to these parameter regimes. This would help understand the conditions under which, for example, non-Markovian aggregate dynamics is induced. In addition, it would profit the characterization of our environment and could help numerically explore the physics of large ensembles of environment atoms. Lastly, our quantum simulator might be extended to applications beyond excitation transport simulations by allowing for more than a single excitation in the Rydberg aggregate or by introducing additional microwave fields.

In **Chapter 3** we studied the tunability of the mechanical mode dynamics of an optomechanical system via its optical environment. The environment consists of two optical resonators, which are non-Hermitian due to their coupling to gain- and loss-providing environments. In particular, we analyzed the (optomechanical) enhancement of the mechanical steady-state displacement in resonators with optical gain, compared to gain-less resonators. The enhancement depends on the optical design parameters as well as the optical pumping intensities and frequencies. We showed that the steady state of the mechanical mode is rendered unstable, according to linear stability analysis, above a certain optical gain value, which leads to exponentially increasing mechanical displacement. By introducing the effect of gain saturation in the description of our system, this regime of divergent mechanical displacement was found to be regulated, and a new regime of self-sustained oscillations emerged.

Our analysis amended and clarified the findings of Ref. [59], which discussed this non-Hermitian optomechanical system in the context of a phonon laser and emphasized the advantage of balanced gain and loss, i.e., $\mathcal{PT}$ symmetry, and resonant driving for achieving a large optomechanical enhancement. In contrast, our study revealed that off-resonant driving with unbalanced gain and loss (broken $\mathcal{PT}$ symmetry) yields a larger enhancement. We found that the mechanical displacement exponentially increases in the by Ref. [59] suggested parameter regime of resonant optical pumping and balanced gain and loss, which challenges the physical meaning of the enhancement in this case. Accordingly, our investigation provides additional insight into the interplay between optical non-Hermiticity and displacement of the mechanical mode, which is relevant for designing optomechanical devices.

In our study we have focused on the classical limit of the optomechanical equations of motion, which, owing to their simplicity, allowed us to perform a comprehensive analytical and numerical investigation of the optomechanical enhancement as a function of optical design and laser parameters. A comprehensive analysis of the quantum aspects in greater detail than in Refs. [59, 369] is still lacking. In particular, it would be interesting to see whether or not the notion of phonon lasing proves useful apart from its appealing similarity to optical lasing. Additionally, the potential for, e.g., the preparation of nonclassical oscillator states [370], synchronization of mechanical oscillators [371] or generation of entanglement between the optical or mechanical modes [372] using reservoir engineering in our non-Hermitian system is still to be investigated, and could trigger exciting device applications. Lastly, an understanding of whether optomechanical systems with more than two optical resonators (and consequently higher-order exceptional points [373]) might profit engineering approaches would be valuable for designing optomechanical systems.

In **Chapter 4** we investigated the effect of different system-environment partitionings in an environment consisting of a harmonic mode coupled to a macroscopic harmonic bath. We analytically and numerically studied the transformation of the bath correlation function quantifying the effect of the environment on system dynamics under different partitionings. Differences in the bath correlation function were found to arise as a consequence of different initial state choices for the composite environment associated with the different partitionings, namely factorized and correlated initial states between mode and bath. We demonstrated that differences in the bath correlation function can lead to pronounced, transient differences in the mean occupation number of a harmonic oscillator system.

Our investigation reveals that transformations between different system-environment partitionings or environment structures, which are routinely performed in terms of the spectral density for reservoir engineering purposes, can be non-equivalent if the initial environment state is not preserved. In particular, since environment temperature enters via the initial environment state, care has to be taken in choosing appropriate initial states when transforming between different environment structures in the presence of temperature; and system-environment correlations may have to be accounted for. Our study discloses the inconsistency between the assumption of initially uncorrelated system-environment states and such transformations. The insight gained into the role of correlations between the various parts of a nested environments allows one to better assess in which cases different environment structures can yield the same action.

To supplement the results on environment transformations in terms of the spectral density [37–39, 41, 60–63] by explicit formulas for the temperature-dependent (and thus initial-state-dependent) case, it would be desirable to extend the formulas derived in this work to arbitrary environment structures. Another research direction arises from the relevance of accounting for initial system-environment correlations when describing open quantum systems (see, e.g., Refs. [356, 360, 367]), where an investigation of common physical settings that have to be described through correlated initial states would be of strong interest. In addition, further tools in open quantum system theory have to be developed and the existing ones have to be extended [374], to account for potential system-environment correlations.

The results obtained in this thesis demonstrate the high degree of system control that can be attained through a nested environment with both a finite and macroscopic part. In particular, by allowing one to admix properties of the finite environment to macroscopic environment properties, a broad range of environment effects can be realized, as illustrated, for example, in Chapter 2. This shows that nested environment structures provide valuable resources for reservoir engineering and open system control, whether for state preparation or quantum simulation.

To extend the scope of applicability of nested environments, a deeper insight into their generic features would be highly desirable. Ideally, a comprehensive characterization of nested environment properties would provide tools to map between equivalent physical system-environment structures. Given the properties of a certain environment, one could then assess which structure was able to realize these properties; and augmenting this knowledge with the qualities of different physical platforms would allow one to determine the platform best fitted for implementation. Moreover, such a theory could ease the transfer of ideas or developments between different research fields and facilitate the design of hybrid quantum devices. These interconnectable devices could push new boundaries by taking advantage of the exceptional qualities of the various physical platforms involved.

Appendix A

Supporting Information for Chapter 2

A.1 Calculation of radial Rydberg wave functions

In Sec. 2.2.1 we have briefly discussed the properties of Rydberg states of alkali atoms. Here we detail the numerical calculation of radial wave functions of rubidium Rydberg states (cf. Refs. [147, 149]). In contrast to the main part of the thesis, we employ Hartree atomic units in this section, i.e., we set $\hbar = m_e = e = 1/(4\pi\varepsilon_0) = 1$. This implies that all length scales are given in units of the Bohr radius $a_0 = 0.052917721$ nm, and all energies in units of the Hartree energy 4.359744×10^{-18} J; the Rydberg constant becomes $Ry = 1/2$ in atomic units.

Being an element of the alkali metal group, rubidium has a single valence electron. In a Rydberg state, this electron is on average located far away from the core consisting of nucleus and inner-shell electrons. The inner-shell electrons shield the nuclear charge seen by the valence electron, resulting in a hydrogen-like core potential for the highly-excited valence electron. This allows us to solve a hydrogen-like problem for the valence electron in a singly-charged core potential instead of solving the full many-electron problem for valence electron and inner-shell electrons in the potential of a multiply-charged nucleus.

In spherical coordinates (r, θ, ϕ) with r denoting the distance of the valence electron from the core and (θ, ϕ) the azimuthal and polar angle, respectively, we can hence write the Hamiltonian for the valence electron wave function $\psi_{n\ell jm_j}(r, \theta, \phi)$ as

$$\mathcal{H} = -\frac{1}{2}\boldsymbol{\nabla}^2 + V_{\text{core}}(r) + V_{\text{so}}(r), \tag{A.1}$$

with $-\boldsymbol{\nabla}^2/2$ being the kinetic energy, $V_{\text{core}}(r)$ the core potential, and $V_{\text{so}}(r)$ the spin-orbit interaction. The choice of spherical coordinates is motivated by the spherical symmetry of the core potential. Note that we approximated the reduced mass of the valence electron by one in Eq. (A.1).

Since the Hamiltonian (A.1) does not mix angular and radial degrees of freedom, we can write the wave function of the valence electron $\psi_{n\ell jm_j}(r, \theta, \phi)$ analogously to the hydrogen case as a product of radial and angular part,

$$\psi_{n\ell jm_j}(r, \theta, \phi) = R_{n\ell j}(r)\mathcal{Y}_{\ell jm_j}(\theta, \phi), \tag{A.2}$$

with $R_{n\ell j}(r)$ denoting the radial wave function and $\mathcal{Y}_{\ell jm_j}(\theta, \phi)$ the generalized spherical harmonics. The explicit form of $\mathcal{Y}_{\ell jm_j}(\theta, \phi)$ can be found in Ref. [375]. The generalized spherical harmonics are eigenfunctions of the spin-orbit coupling operator $\boldsymbol{L} \cdot \boldsymbol{S}$ with $\boldsymbol{L}$ and $\boldsymbol{S}$ denoting the operators of total orbital angular momentum respectively spin. The spin-orbit coupling operator couples angular and spin degrees of freedom, leading to the quantum numbers j and m_j associated to the total angular momentum operator $\boldsymbol{J} = \boldsymbol{L} + \boldsymbol{S}$. Note that spin-orbit interaction is important for the theoretical description of heavy alkali atoms such as rubidium [139, 144, 376].

From the full Schrödinger equation for the valence electron wave function,

$$\mathcal{H}\psi_{n\ell jm_j}(r, \theta, \phi) = E_{n\ell j}\psi_{n\ell jm_j}(r, \theta, \phi), \tag{A.3}$$

we can now extract the Schrödinger equation for the *radial* part $R_{n\ell j}(r)$ of the valence electron wave function, reading as

$$\left[-\frac{1}{2}\frac{1}{r^2}\frac{\partial}{\partial r}\left(r^2\frac{\partial}{\partial r}\right)+\frac{\ell(\ell+1)}{2r^2}+V_{\text{core}}(r)+V_{\text{so}}(r)\right]R_{n\ell j}(r)=E_{n\ell j}R_{n\ell j}(r). \tag{A.4}$$

The first term on the left hand side of Eq. (A.4) comes from the radial part of the momentum operator $-\boldsymbol{\nabla}^2/2$ in spherical coordinates. The second term, called centrifugal barrier, is obtained by applying the angular part of the momentum operator — the angular momentum operator — to the eigenfunctions of the angular Hamiltonian. The two further terms, which we discuss now, are given by the core potential $V_{\text{core}}(r)$ and the spin-orbit interaction $V_{\text{so}}(r)$.

The core potential $V_{\text{core}}(r)$ describes the effective potential seen by the valence electron, incorporating the effect of the inner-shell electrons. Far away from the core, the core potential for the valence electron is essentially given by a Coulomb potential $-1/r$, while in the vicinity of the core it is exposed to a different potential, determined by the substructure of the core. The effective core potential $V_{\text{core}}(r)$ can be quantified using a parametric model potential of the core [377], which looks Coulomb-like for large core-electron distances but is modified close to the core. In terms of the static dipole polarizability α_c of the ionic core, the radial charge $Z_\ell(r)$, and the cutoff radius r_c introduced to truncate unphysical short-range contributions, the parametric model potential reads as [377]

$$V_{\text{core}}(r)=-\frac{Z_\ell(r)}{r}-\frac{\alpha_c}{2r^4}\left(1-e^{-(r/r_c)^6}\right). \tag{A.5}$$

The radial charge $Z_\ell(r)$ depends on the nuclear charge Z ($Z=37$ for rubidium) and the angular momentum ℓ via the parameters $a_1,\ldots,a_4$,

$$Z_\ell(r)=1+(Z-1)e^{-a_1 r}-r(a_3+a_4 r)e^{-a_2 r}. \tag{A.6}$$

The parameters $a_1,\ldots,a_4$ and r_c are obtained by parametrically fitting the energy eigenvalues of the solution of the Schrödinger equation for the alkali valence electron to the empirically observed energy levels [377, 378]. Their values are listed in Ref. [377]. For a recent discussion of the quality of the model potential (A.5), see Ref. [379].

The spin-orbit interaction $V_{\text{so}}(r)$, due to which states of different total angular momentum j are shifted in energy with respect to each other, with $E_{n\ell j'}>E_{n\ell j}$ for $j'>j$, can be accounted for via the term [378]

$$V_{\text{so}}(r)=\frac{\alpha_{\text{fs}}^2}{2}\left(\boldsymbol{L}\cdot\boldsymbol{S}\right)\frac{1}{r}\frac{\mathrm{d}V_{\text{core}}(r)}{\mathrm{d}r}\left[1-\frac{\alpha_{\text{fs}}^2}{2}V_{\text{core}}(r)\right]^{-2}, \tag{A.7}$$

with α_{fs} denoting the fine structure constant, $\alpha_{\text{fs}}\approx 1/137$. The product $\boldsymbol{L}\cdot\boldsymbol{S}$ can be evaluated using the relation

$$\boldsymbol{L}\cdot\boldsymbol{S}=\frac{1}{2}\left(\boldsymbol{J}^2-\boldsymbol{L}^2-\boldsymbol{S}^2\right), \tag{A.8}$$

which evaluates to $(j(j+1)-\ell(\ell+1)-s(s+1))/2$ when applied to an electronic eigenstate $\propto\mathcal{Y}_{\ell j m_j}(\theta,\phi)$. Accordingly, the state of the valence electron is uniquely determined via the quantum numbers n,ℓ,j,m_j with n being a positive integer number, ℓ an integer number ranging from 0 to $n-1$, $j=\ell\pm s$, and m_j ranging from $-j$ to j with integer increments.

We do not consider other relativistic corrections such as the so-called Darwin term [375]. The Darwin term modifies wave functions very close to the core (for hydrogen with a Coulomb potential the Darwin correction is proportional to $\delta(\boldsymbol{r})$) and is thus not of great relevance for Rydberg states, even less if one considers overlap integrals between s states and angular momenta states with $\ell > 0$, which are mostly localized far away from the core.

To obtain the radial eigenfunctions $R_{n\ell j}(r)$, one typically solves the Schrödinger equation (A.4) using empirically determined eigenenergies $E_{n\ell j}$ as input, either by directly plugging in the observed $E_{n\ell j}$ or by making use of Eq. (2.4), in which the quantum defects are determined such that the resulting energies $E_{n\ell j}$ coincide with the empirically observed eigenenergies. Note that we do not correct the Rydberg constant in Eq. (2.4) for the finite mass of the rubidium nucleus by replacing the electron mass by the reduced electron mass, since the resulting correction is negligible for our purposes.

It is convenient to rescale the radial wave function to simplify the structure of the Schrödinger equation (A.4). A common choice is to set $R_{n\ell j}(r) = \rho_{n\ell j}(r)/r$, for which the Schrödinger equation reads as

$$\frac{\partial^2}{\partial r^2}\rho_{n\ell j}(r) + \left[2\left(E_{n\ell j} - V_{\mathrm{core}}(r) - V_{\mathrm{so}}(r)\right) - \frac{\ell(\ell+1)}{r^2}\right]\rho_{n\ell j}(r) = 0. \tag{A.9}$$

An alternative rescaling, which is designed to give an approximately constant number of points in each lobe of the wave function on an equidistant grid of the radial coordinate is obtained by making the substitutions $u = \sqrt{r}$ and $\chi = r^{3/4}R(r)$ in the Schrödinger equation [34, 380], leading to the equation

$$\frac{\partial^2}{\partial u^2}\chi(u) + \left[8u^2\left(E_{n\ell j} - V_{\mathrm{core}}(u^2) - V_{\mathrm{so}}(u^2)\right) - \frac{(2\ell+\frac{1}{2})(2\ell+\frac{3}{2})}{u^2}\right]\chi(u) = 0. \tag{A.10}$$

Note that to calculate, for instance, expectation values for the rescaled wave function $\chi(u)$ in Eq. (A.10), a transformed radial integral has to be used [380],

$$\langle r^k\rangle = \int_0^\infty R_{n\ell j}(r) r^k R_{n'\ell' j'}(r) r^2 \mathrm{d}r = \int_0^\infty \chi_{n\ell j}(u) u^{2k} \chi_{n'\ell' j'}(u) u^2 \mathrm{d}u. \tag{A.11}$$

Both equations (A.9) and (A.10) are of the type $[\frac{\partial^2}{\partial r^2} + X(r)]f(r) = 0$, which is particularly fitted to be solved using Numerov's method [381]. Following this numerical approach, the radial wave function is calculated by starting the integration outside the classically forbidden region at a radius $r_s > 2n^2$ and integrating inwards up to a inner cutoff radius r_c [34]. Subsequently, the wave function is normalized to one. In practice, we start the integration with random initial values for r and its radial derivative at $r_s = 2n(n+15)$ and end, for low ℓ states ($\ell \leq 4$) at $r_c = \sqrt[3]{\alpha_c}$ [157]. Since in the classically forbidden region the solutions of the radial Schrödinger equation are a rising and a falling exponential, the admixture of the incorrect solution is damped out exponentially while integrating inwards, such that the final, normalized result is independent of the initial condition. For high ℓ states ($\ell > 4$), we numerically determine the inner turning point and terminate the integration when the integral starts to diverge, i.e., when $r_i^2 R_{n\ell j}^2(r_i) > r_{i+1}^2 R_{n\ell j}^2(r_{i+1})$ with $r_i < r_{i+1}$. For Rydberg states of high orbital angular momentum $\ell > 4$, it is advisable to employ Eq. (A.10) rather than the 'standard' scaling (A.9) for numerical accuracy. To verify accurate numerical implementation, we compared our numerical results with the dipole moments for rubidium Rydberg states listed in Refs. [99, 165, 382, 383], finding $\lesssim 0.2$ % deviation between the listed values and the values obtained by our numerical implementation, as shown in Tab. A.1.

A.2 Derivation of an effective model for excitation transport

Here we derive the effective model for the aggregate dynamics that we discuss in Sec. 2.4.1, following Ref. [247]. We start with a derivation that ignores coupling between the aggregate

Matrix element	This work (a_0)	Literature value (a_0)	Deviation (%)	Reference
$\langle 46d_{5/2}\vert r\vert 48p_{3/2}\rangle$	1551	1548	0.2	[382]
$\langle 46d_{5/2}\vert r\vert 44f_{7/2}\rangle$	1586	1587	0.06	[382]
$\langle 46d_{5/2}\vert r\vert 47p_{3/2}\rangle$	2708	2709	0.04	[382]
$\langle 46d_{5/2}\vert r\vert 45f_{7/2}\rangle$	2694	2694	–	[382]
$\langle 50d_{5/2}\vert r\vert 52p_{3/2}\rangle$	1844	1840	0.2	[383]
$\langle 50d_{5/2}\vert r\vert 48f_{8/2}\rangle$	1893	1893	–	[383]
$\langle 35d_{5/2}\vert r\vert 37p_{3/2}\rangle$	877	875	0.2	[383]
$\langle 35d_{5/2}\vert r\vert 33f_{7/2}\rangle$	882	882	–	[383]
$\langle 58d_{3/2}\vert r\vert 56f_{5/2}\rangle$	2596	2594	0.08	[165]
$\langle 58d_{3/2}\vert r\vert 60p_{1/2}\rangle$	2565	2563	0.08	[165]
$\langle 46s_{1/2}\vert r\vert 45p_{1/2}\rangle$	1924	1924	–	[99]

Table A.1: Comparison of radial matrix elements of ^{87}Rb states with literature.

atoms and continue by extending the derivation to the case where aggregate coupling is a non-perturbative effect.

Neglecting aggregate coupling

We now formally adiabatically eliminate the "excited" states $|e\rangle$ and $|r\rangle$ of all background atoms to arrive at an evolution equation for the aggregate alone. The essential step is to divide the many-body Hilbert space into a space of interest and its complement. The former is represented by the projector

$$\mathcal{P}_g = \sum_n |\pi_n\rangle\langle\pi_n| \otimes |\boldsymbol{g}\rangle\langle\boldsymbol{g}| \,, \tag{A.12}$$

where the first part acts on the state space of the aggregate atoms and the second on that of the background atoms. The projector $|\boldsymbol{g}\rangle\langle\boldsymbol{g}|$ with $|\boldsymbol{g}\rangle = |g\ldots g\rangle$ projects on the state where all background atoms are in their ground state $|g\rangle$. The complement of the space projected onto by $\mathcal{P}_g$ is thus formed by all many-body states involving any $|e\rangle$ or $|r\rangle$ state of the background atoms, projected onto by $\mathcal{P}_e = 1 - \mathcal{P}_g$.

Segregating the total Hamiltonian $\mathcal{H} = \mathcal{H}_{\text{agg}} + \mathcal{H}_{\text{agg-bg}} + \mathcal{H}_{\text{bg}} + \mathcal{H}_{\text{bg,int}}$ (see Sec. 2.2.5) of aggregate and background atoms into segments using the projection operator formalism [247], we obtain:

$$\mathcal{H}_g = \mathcal{P}_g\mathcal{H}\mathcal{P}_g = \mathcal{P}_g\mathcal{H}_{\text{agg}}\mathcal{P}_g, \tag{A.13}$$

$$\begin{aligned}\mathcal{H}_e = \mathcal{P}_e\mathcal{H}\mathcal{P}_e = \mathcal{P}_e\Bigg[\sum_\alpha \left(\frac{\Omega_c}{2}\left[|r\rangle\langle e|\right]_\alpha + \text{H.c.}\right) - \Delta_p\left[|e\rangle\langle e|\right]_\alpha - (\Delta_p+\Delta_c)\left[|r\rangle\langle r|\right]_\alpha \\ + \mathcal{H}_{\text{agg-bg}} + \mathcal{H}_{\text{bg,int}} + \mathcal{H}_{\text{agg}}\Bigg]\mathcal{P}_e,\end{aligned} \tag{A.14}$$

$$\mathcal{C}_+ = \mathcal{P}_e\mathcal{H}\mathcal{P}_g = \mathcal{P}_e\left[\sum_\alpha \frac{\Omega_p}{2}\left[|e\rangle\langle g|\right]_\alpha\right]\mathcal{P}_g, \qquad \mathcal{C}_- = \mathcal{C}_+^\dagger. \tag{A.15}$$

After adiabatic elimination of the complement of our space of interest and to second order in $\mathcal{C}_\pm$ [247], the effective master equation for the *reduced* aggregate density matrix defined as

$\rho^{(\mathrm{agg})} = \sum_{nm} \rho_{nm} \left|\pi_n\right\rangle\!\left\langle\pi_m\right|$ reads as

$$\dot{\rho}^{(\mathrm{agg})} = -i[\mathcal{H}_g + \mathcal{H}_{\mathrm{eff}}, \rho^{(\mathrm{agg})}] + \sum_\alpha \mathcal{L}_{L^{(\alpha)}_{\mathrm{eff}}}[\rho^{(\mathrm{agg})}], \tag{A.16}$$

with the respective effective operators given by [247]

$$\mathcal{H}_{\mathrm{eff}} = -\frac{1}{2}\mathcal{C}_-[\mathcal{H}^{-1}_{\mathrm{NH}} + (\mathcal{H}^{-1}_{\mathrm{NH}})^\dagger]\mathcal{C}_+, \tag{A.17}$$

$$L^{(\alpha)}_{\mathrm{eff}} = L_\alpha \mathcal{H}^{-1}_{\mathrm{NH}}\mathcal{C}_+. \tag{A.18}$$

Here, L_α is the Lindblad operator (2.24) corresponding to the spontaneous decay of the excited state $\left|e\right\rangle_\alpha$ of atom α. Central to the effective equation are the non-Hermitian Hamiltonian $\mathcal{H}_{\mathrm{NH}} = \mathcal{H}_e - i\sum_\alpha L^\dagger_\alpha L_\alpha/2$ and its inverse $\mathcal{H}^{-1}_{\mathrm{NH}}$, which we obtain now.

It can be seen that if we neglect the interactions between background Rydberg atoms given by $\mathcal{H}_{\mathrm{bg,int}}$ as well as $\mathcal{H}_{\mathrm{agg}}$ as we do from now, the Hamiltonian $\mathcal{H}_{\mathrm{NH}}$ decomposes into the block structure

$$\mathcal{H}_{\mathrm{NH}} = \bigotimes_{n\alpha} \left[\left|\pi_n\right\rangle\!\left\langle\pi_n\right| \otimes \mathcal{H}^{(n\alpha)}_{\mathrm{NH}}\right], \tag{A.19}$$

where $\mathcal{H}^{(n\alpha)}_{\mathrm{NH}}$ acts only within the space spanned by $\left|e\right\rangle_\alpha$ and $\left|r\right\rangle_\alpha$. In that basis, $\mathcal{H}^{(n\alpha)}_{\mathrm{NH}}$ explicitly reads as

$$\mathcal{H}^{(n\alpha)}_{\mathrm{NH}} = \begin{pmatrix} -i\Gamma_p/2 - \Delta_p & \Omega_c/2 \\ \Omega_c/2 & \bar{V}_{n\alpha} - \Delta_p - \Delta_c \end{pmatrix}, \tag{A.20}$$

where $\bar{V}_{n\alpha} = V^{(pr)}_{n\alpha} + \sum_{m\neq n} V^{(sr)}_{m\alpha}$ is the overall interaction of the specific background atom α with the entire aggregate if the latter is in the state $\left|\pi_n\right\rangle$. In this basis, we further have

$$\mathcal{C}^{(n\alpha)}_+ = \begin{pmatrix} \Omega_p/2 \\ 0 \end{pmatrix}, \quad L^{(n)}_\alpha = \left(\sqrt{\Gamma_p}, 0\right). \tag{A.21}$$

Due to the block structure (A.19), we find the inverse of $\mathcal{H}_{\mathrm{NH}}$ when we find the inverse of $\mathcal{H}^{(n\alpha)}_{\mathrm{NH}}$, which is

$$\left(\mathcal{H}^{(n\alpha)}_{\mathrm{NH}}\right)^{-1} = \frac{1}{(-i\Gamma_p/2 - \Delta_p)\,\tilde{V}_{n\alpha} - \Omega_c^2/4} \begin{pmatrix} \tilde{V}_{n\alpha} & -\Omega_c/2 \\ -\Omega_c/2 & -i\Gamma_p/2 - \Delta_p \end{pmatrix}, \tag{A.22}$$

introducing the total energy shift of the Rydberg level of background atom α as $\tilde{V}_{n\alpha} = \bar{V}_{n\alpha} - \Delta_p - \Delta_c$.

Plugging the excitation and de-excitation operators (A.21) into the effective equations (A.17) and (A.18), we finally obtain

$$\dot{\rho}^{(\mathrm{agg})} = -i[\mathcal{H}_{\mathrm{agg}} + \mathcal{H}_{\mathrm{eff}}, \rho^{(\mathrm{agg})}] + \sum_\alpha \mathcal{L}_{L^{(\alpha)}_{\mathrm{eff}}}[\rho^{(\mathrm{agg})}], \tag{A.23}$$

where the effective quantities $\mathcal{H}_{\mathrm{eff}}$ and $L^{(\alpha)}_{\mathrm{eff}}$ are given by

$$\mathcal{H}_{\mathrm{eff}} = \sum_{n,\alpha} \mathcal{H}^{(n\alpha)}_{\mathrm{eff}} \left|\pi_n\right\rangle\!\left\langle\pi_n\right|, \qquad L^{(\alpha)}_{\mathrm{eff}} = \sum_n L^{(n\alpha)}_{\mathrm{eff}} \left|\pi_n\right\rangle\!\left\langle\pi_n\right|, \tag{A.24}$$

with the respective elements reading as

$$\mathcal{H}^{(n\alpha)}_{\mathrm{eff}} = \frac{\Omega_p^2 \tilde{V}_{n\alpha}(\Omega_c^2 + 4\tilde{V}_{n\alpha}\Delta_p)}{\Omega_c^4 + 8\tilde{V}_{n\alpha}\Delta_p\Omega_c^2 + 4\tilde{V}^2_{n\alpha}(\Gamma_p^2 + 4\Delta_p^2)}, \tag{A.25a}$$

$$L^{(n\alpha)}_{\mathrm{eff}} = \frac{2i\tilde{V}_{n\alpha}\sqrt{\Gamma_p}\Omega_p}{2\tilde{V}_{n\alpha}(\Gamma_p - 2i\Delta_p) - i\Omega_c^2}. \tag{A.25b}$$

In the limit $\Delta_p = \Delta_c \to 0$, we arrive at the expressions 2.70 in Sec. 2.4.1.

Note that Eq. (A.16) is obtained from a second-order perturbative expansion in $\mathcal{C}_\pm$ assuming that the "excited" states $|e\rangle$ are $|r\rangle$ are almost unpopulated and the ground state dynamics governed by $\mathcal{H}_g$ is slow compared to the "excited" state manifold, such that adiabatic elimination can be applied. The validity of these assumptions is discussed in detail in Sec. 2.4.1. In addition, we assumed in the derivation of Eq. (A.16) that interactions within the ground state manifold are much weaker than those of the "excited" states contained by $\mathcal{H}_{\text{NH}}$. Due to this assumption, we did not account for an effect of the ground state dynamics on the effective processes, such that the excited-state contribution to the effective Hamiltonian (A.17) is independent of $\mathcal{H}_g$. We will weaken this assumption now.

Beyond weak aggregate coupling

Following again Ref. [247], we now diagonalize the Hamiltonian $\mathcal{H}_g$ and include its action into the effective operators. In particular, introducing the eigenvalues E_k and the corresponding eigenvectors

$$|\varphi_k\rangle = \sum_j c_{jk} |\pi_j\rangle \,, \tag{A.26}$$

of the aggregate Hamiltonian $\mathcal{H}_{\text{agg}}$, we can define the non-Hermitian matrices $\mathcal{H}_{\text{NH}}^{(k)} = \mathcal{H}_{\text{NH}} - E_k I$, where I denotes the identity operator. The inverse of $(\mathcal{H}_{\text{NH}}^{(kn\alpha)})$, the non-Hermitian Hamiltonian in the space spanned by $|e\rangle_\alpha$ and $|r\rangle_\alpha$ belonging to state $|\pi_n\rangle$ [cf. Eq. (A.19)] reads as

$$(\mathcal{H}_{\text{NH}}^{(kn\alpha)})^{-1} = \frac{-2}{2(\tilde{V}_{n\alpha} - E_k)(2E_k + 2\Delta_p + i\Gamma_p) + \Omega_c^2} \begin{pmatrix} 2(\tilde{V}_{n\alpha} - E_k) & -\Omega_c \\ -\Omega_c & -(2E_k + 2\Delta_p + i\Gamma_p) \end{pmatrix} . \tag{A.27}$$

Applying the formalism explicated in Ref. [247] and defining $\kappa_k^{nm} = c_{nk} c_{mk}^*$, we finally obtain

$$\begin{aligned} \mathcal{H}_{\text{eff}} = \sum_{n,m} \Bigg(\sum_{\alpha,k} \frac{\kappa_k^{nm} \Omega_p^2}{2} \Bigg[& \frac{(\tilde{V}_{n\alpha} - E_k)}{2(\tilde{V}_{n\alpha} - E_k)(2E_k + 2\Delta_p + i\Gamma_p) + \Omega_c^2} \\ & + \frac{(\tilde{V}_{m\alpha} - E_k)}{2(\tilde{V}_{m\alpha} - E_k)(2E_k + 2\Delta_p - i\Gamma_p) + \Omega_c^2} \Bigg] \Bigg) |\pi_n\rangle \langle \pi_m| \,, \end{aligned} \tag{A.28a}$$

$$L_{\text{eff}}^{(\alpha)} = \sum_{n,m} \left(\sum_k \frac{-2\Omega_p \sqrt{\Gamma_p} (\tilde{V}_{n\alpha} - E_k) \kappa_k^{nm}}{2(\tilde{V}_{n\alpha} - E_k)(2E_k + 2\Delta_p + i\Gamma_p) + \Omega_c^2} \right) |\pi_n\rangle \langle \pi_m| \,, \tag{A.28b}$$

for the terms to be inserted in Eq. (A.23). In Fig. 2.15 in the main part we show that for the parameters of Tab. 2.2, this extended effective model is able to capture the occupation of the aggregate eigenstates, in contrast to the effective model given by Eqns. (A.24) and (A.25).

Appendix B

Supporting Information for Chapter 3

B.1 Rescaling of the optomechanical equations of motion

Here we show how Eqs. (3.1) can be expressed in atomic units, which is a convenient choice for numerical calculations. We start with the optomechanical equations of motion given in the form of Eqs. (40) and (41) in Ref. [58], namely

$$\partial_t a_1 = (-i\Delta + \gamma_1)a_1 - iJa_2 + \sqrt{2\mu}f_0, \tag{B.1a}$$

$$\partial_t a_2 = (-i\Delta + \gamma_2)a_2 - iJa_1 - iGa_2x, \tag{B.1b}$$

$$\partial_t^2 x = -\Gamma\dot{x} - \omega_m^2 x + \frac{\hbar G}{m}|a_2|^2. \tag{B.1c}$$

Note that the complex classical field amplitudes $a_{1,2}$ are dimensionless in Eqs. (B.1) whereas x has the dimension of length. We now re-express every frequency in units of Δ_0 (e.g. $\tilde{\Delta} = \Delta/\Delta_0$ and $\tilde{f}_0 = f_0/\sqrt{\Delta_0}$), which implies also scaling of the time, $\tilde{t} = t\Delta_0$,

$$\partial_{\tilde{t}} a_1 = (-i\tilde{\Delta} + \tilde{\gamma}_1)a_1 - i\tilde{J}a_2 + \sqrt{2\tilde{\mu}}\tilde{f}_0, \tag{B.2a}$$

$$\partial_{\tilde{t}} a_2 = (-i\tilde{\Delta} + \tilde{\gamma}_2)a_2 - i\tilde{J}a_1 - i\tilde{G}a_2x, \tag{B.2b}$$

$$\partial_{\tilde{t}}^2 x = -\tilde{\Gamma}\partial_{\tilde{t}}x - \tilde{\omega}_m^2 x + \frac{\hbar\tilde{G}}{m\Delta_0}|a_2|^2. \tag{B.2c}$$

As a next step, we express lengths in terms of the Bohr radius a_0 and masses in terms of the electron mass m_e, leading to $\tilde{x} = x/a_0$, $\tilde{g} = \tilde{G}a_0 = Ga_0/\Delta_0$, and $\tilde{m} = m/m_e$, which transforms Eqs. (B.2) into

$$\partial_{\tilde{t}} a_1 = (-i\tilde{\Delta} + \tilde{\gamma}_1)a_1 - i\tilde{J}a_2 + \sqrt{2\tilde{\mu}}\tilde{f}_0, \tag{B.3a}$$

$$\partial_{\tilde{t}} a_2 = (-i\tilde{\Delta} + \tilde{\gamma}_2)a_2 - i\tilde{J}a_1 - i\tilde{g}a_2\tilde{x}, \tag{B.3b}$$

$$\partial_{\tilde{t}}^2 \tilde{x} = -\tilde{\Gamma}\partial_{\tilde{t}}\tilde{x} - \tilde{\omega}_m^2 \tilde{x} + \frac{\tilde{g}}{\tilde{m}}|a_2|^2\frac{\hbar}{m_e\Delta_0 a_0^2}. \tag{B.3c}$$

Choosing now $\Delta_0 = E_{\text{hartree}}/\hbar = \hbar/m_e a_0^2$ leads to $\hbar/(m_e\Delta_0 a_0^2) = 1$, such that no further rescaling is needed. Thus, $P_{\text{in}} = \hbar\omega_L|f_0|^2 = \hbar\omega_L\Delta_0|\tilde{f}_0|^2$.

This shows that one can express Eqs. (B.3) in atomic units (in which Δ_0 is the frequency associated with the Hartree energy, $\Delta_0 = E_{\text{hartree}}/\hbar$) without introducing units to the amplitudes $a_{1,2}$. Equations (B.3) have been implemented numerically for the calculations of Chap. 3.

B.2 Optomechanical enhancement in the two-resonator model

In this short section we discuss the steady-state solutions of Eqs. (3.4) in more detail. In addition to the parameters of Eqs. (3.4) we further include the laser detuning Δ. According to the reasoning above Eq. (3.6), the enhancement η can be calculated from the steady-state solutions of the classical optical field amplitude a_2 via $\eta = |a_2|^2/|a_{2,\mathrm{p}}|^2$, where the subscript p again denotes the passive case with $\gamma_1 = \gamma_2 < 0$, yielding

$$\eta = \frac{J^4 + 2J^2(\gamma_2^2 - \Delta(\Delta + \Delta_x)) + (\gamma_2^2 + \Delta^2)(\gamma_2^2 + (\Delta + \Delta_x)^2)}{J^4 + 2J^2(\gamma_1\gamma_2 - \Delta(\Delta + \Delta_x)) + (\gamma_1^2 + \Delta^2)(\gamma_2^2 + (\Delta + \Delta_x)^2)}. \tag{B.4}$$

From this equation, two limits are readily obtained: For large detuning Δ, the enhancement η goes as

$$\eta \overset{|\Delta|\to\infty}{\longrightarrow} 1, \tag{B.5}$$

in agreement with Fig. 3.3 and Fig. 3.6. On the $\mathcal{PT}$ point ($\gamma_2 = -\gamma_1 = -J < 0$),

$$\eta = 1 + \frac{4\gamma_2^2}{\Delta_x^2}, \tag{B.6}$$

which is Eq. (3.6) in the main text. Note that letting $\Delta_x \to \infty$ independent of, e.g., the detuning Δ is misleading because the mechanical steady-state displacement x_s does exhibit a detuning dependence in the full model. However, the qualitative behavior of the enhancement with transmitted laser power is captured even in the simple model.

Appendix C

Supporting Information for Chapter 4

C.1 Microscopical definitions of BCF and SD

In this section we review the definition of the bath correlation function (BCF) and the spectral density (SD) on basis of the microscopic model introduced in Chapter 4. We consider the same total Hamiltonian as introduced in Eq. (4.1),

$$\mathcal{H}_{\text{tot}} = \mathcal{H}_{\text{S}} + \mathcal{H}_{\text{S-E}} + \mathcal{H}_{\text{E}}, \tag{C.1}$$

consisting of a system part $\mathcal{H}_{\text{S}}$, an environment part $\mathcal{H}_{\text{E}}$ [Eq. (4.2)], and a coupling part $\mathcal{H}_{\text{S-E}}$ [Eq. (4.3)] accounting for the interaction between system and environment.

Following Sec. 4.2.1, the BCF for a Hermitian system coupling operator L_{S} is given by [cf. Eq. (4.5)]

$$\begin{aligned}\alpha(t,t') &= \left\langle \sum_{\mu,\mu'} \left(k_\mu^* c_\mu(t) + \text{H.c.}\right) \left(k_{\mu'}^* c_{\mu'}(t') + \text{H.c.}\right) \right\rangle_{\text{E}} \\ &= \sum_\mu |k_\mu|^2 \left(\left\langle c_\mu(t) c_\mu^\dagger(t') \right\rangle_{\text{E}} + \left\langle c_\mu^\dagger(t) c_\mu(t') \right\rangle_{\text{E}} \right),\end{aligned} \tag{C.2}$$

where the second equality sign holds if the initial environment density operator $\rho_{\text{E}}(0)$ is taken to be a function of the number operators $c_\mu^\dagger c_\mu$. Here, the angle brackets denote the trace over the environment, $\langle \cdot \rangle_{\text{E}} = \text{Tr}_{\text{E}}\{\cdot \rho_{\text{E}}(0)\}$.

Thermal environment

In the following, we take the environment to be in a thermal state,

$$\rho_{\text{E}}(0) = \frac{1}{Z} e^{-\beta \sum_\mu \tilde{\omega}_\mu c_\mu^\dagger c_\mu}, \tag{C.3}$$

where Z is defined such that $\text{Tr}_{\text{E}}\{\rho_{\text{E}}(0)\} = 1$ and β is the inverse temperature, $\beta = 1/T$.

The time evolution of the environment operators c_μ can be calculated by means of the Heisenberg equations of motion (cf. Appendix C.3),

$$\partial_t c_\mu(t) = i e^{i\mathcal{H}_{\text{E}} t} [\mathcal{H}_{\text{E}}, c_\mu] e^{-i\mathcal{H}_{\text{E}} t} = -i\tilde{\omega}_\mu c_\mu(t), \tag{C.4}$$

where the time dependence refers to the interaction picture with respect to $\mathcal{H}_{\text{E}}$ and $c_\mu(t) = e^{i\mathcal{H}_{\text{E}} t} c_\mu e^{-i\mathcal{H}_{\text{E}} t}$. Using the usual commutation relation $[c_\mu, c_{\mu'}^\dagger] = \delta_{\mu\mu'}$ and evaluating the trace in Eq. (C.2) in the number basis $|n_\mu\rangle$, we find

$$\alpha(t,t') = \sum_\mu |k_\mu|^2 \left(e^{-i\tilde{\omega}_\mu (t-t')} (n(\tilde{\omega}_\mu) + 1) + e^{i\tilde{\omega}_\mu (t-t')} n(\tilde{\omega}_\mu) \right), \tag{C.5}$$

with the mean occupation number $n(\omega)$ of the environment oscillator with frequency ω defined as

$$n(\omega) \equiv \frac{1}{(e^{\beta\omega} - 1)} = \frac{\sum_n n\, e^{-\beta\omega n}}{\sum_n e^{-\beta\omega n}}. \tag{C.6}$$

Performing a Fourier transformation with respect to $\tau \equiv t - t'$, we obtain

$$\alpha(\omega) = 2\pi \sum_{\mu} |k_\mu|^2 \left[(n(\tilde{\omega}_\mu) + 1)\, \delta(\omega - \tilde{\omega}_\mu) + n(\tilde{\omega}_\mu) \delta(\omega + \tilde{\omega}_\mu) \right] \tag{C.7}$$

By means of the relation $n(-\omega) = -[n(\omega) + 1]$ and the definition

$$j(\omega) = \sum_{\mu} |k_\mu|^2 \delta(\omega - \tilde{\omega}_\mu), \tag{C.8}$$

we can rewrite Eq. (C.7), reading as

$$\alpha(\omega) = 2\pi\, (n(\omega) + 1) \left[j(\omega) - j(-\omega) \right]. \tag{C.9}$$

Following Refs. [363, 384], we now define the spectral density $J(\omega)$ as

$$J(\omega) = j(\omega) - j(-\omega) \tag{C.10}$$

and obtain, after performing the inverse Fourier transform and rearranging using $1 + 2n(\omega) = \coth[\omega/(2T)]$, the standard expression [cf. Eq. (4.9)]

$$\begin{aligned} \alpha(\tau) &= \int_{-\infty}^{\infty} \frac{d\omega}{2\pi}\, e^{-i\omega\tau} \alpha(\omega) \\ &= \int_{-\infty}^{\infty} d\omega\, J(\omega) \left[n(\omega) + 1 \right] e^{-i\omega\tau} \\ &= \int_{0}^{\infty} d\omega J(\omega) \left(\coth\left(\frac{\omega}{2T} \right) \cos(\omega\tau) - i \sin(\omega\tau) \right). \end{aligned} \tag{C.11}$$

This is the well-known result for a linearly coupled harmonic environment in thermal equilibrium, see Eq. (4.9).

C.2 Environment transformation

Here we show how the environment Hamiltonian $\mathcal{H}_{\mathrm{EII}}$ comprising both PM and bath is diagonalized. That is, following Ref. [60], we rewrite Eq. (4.19) as

$$\mathcal{H}_{\mathrm{EII}} = \bar{a}^\dagger M \bar{a}, \tag{C.12}$$

where the vector $\bar{a}$ contains all environment annihilation operators,

$$\bar{a} = (b, a_1, a_2, \ldots, a_N)^T, \tag{C.13}$$

and the matrix M all environment couplings and energies,

$$M = \begin{pmatrix} \Omega & \kappa_1^* & \kappa_2^* & \cdots & \kappa_N^* \\ \kappa_1 & \omega_1 & 0 & \cdots & 0 \\ \kappa_2 & 0 & \omega_2 & \ddots & \vdots \\ \vdots & \vdots & \ddots & \ddots & 0 \\ \kappa_N & 0 & \cdots & 0 & \omega_N \end{pmatrix}. \tag{C.14}$$

The Hermitian matrix M can be diagonalized by means of a unitary transformation,

$$M = S D S^\dagger, \tag{C.15}$$

where the diagonal matrix D contains the eigenenergies of the composite bath,

$$D = \begin{pmatrix} \tilde{\omega}_0 & & 0 \\ & \ddots & \\ 0 & & \tilde{\omega}_N \end{pmatrix}. \tag{C.16}$$

With these definitions, the new annihilation operators of the environment become $\bar{c} = S^\dagger \bar{a}$ where $\bar{c} = (c_0, c_1, \dots, c_N)^T$. The initial creation and annihilation operators are obtained from the new ones via the inverse transformation $\bar{a} = S\bar{c}$. Note that for a discrete number N of a_λ operators there are $N+1$ c_μ operators.

C.3 Alternative derivation of the transformed BCF

In this section, we review a method alternative to the one introduced in Sec. 4.2.4 to calculate the BCF for the two initial states introduced in Sec. 4.2.5 [Eqs. (4.23) and (4.26)] by calculating the time dependence of the PM operator b not via diagonalization, but rather by means of its Heisenberg equations of motion.

The Heisenberg equations of motion for the PM operator b can be easily derived by evaluating the time derivative

$$\begin{aligned} \partial_t b(t) &= i e^{i\mathcal{H}_{\mathrm{EII}} t} [\mathcal{H}_{\mathrm{EII}}, b] e^{-i\mathcal{H}_{\mathrm{EII}} t} \\ &= -i\Omega b(t) - i \sum_\lambda \kappa_\lambda^* a_\lambda(t), \end{aligned} \tag{C.17}$$

where the time dependence as before refers to the interaction picture with respect to $\mathcal{H}_{\mathrm{EII}}$, $b(t) = e^{i\mathcal{H}_{\mathrm{EII}} t}\, b\, e^{-i\mathcal{H}_{\mathrm{EII}} t}$, and $b(0) = b$. Likewise, for a_λ we have

$$\begin{aligned} \partial_t a_\lambda(t) &= i e^{i\mathcal{H}_{\mathrm{EII}} t} [\mathcal{H}_{\mathrm{EII}}, a_\lambda] e^{-i\mathcal{H}_{\mathrm{EII}} t} \\ &= -i\omega_\lambda a_\lambda(t) - i\kappa_\lambda b(t). \end{aligned} \tag{C.18}$$

Formally integrating Eq. (C.18), we find

$$a_\lambda(t) = e^{-i\omega_\lambda t} a_\lambda(0) - i\kappa_\lambda \int_0^t ds\, e^{-i\omega_\lambda (t-s)} b(s), \tag{C.19}$$

which we can insert into Eq. (C.17), yielding

$$\begin{aligned} \partial_t b(t) = -i\Omega b(t) - \int_0^t ds \sum_\lambda |\kappa_\lambda|^2 e^{-i\omega_\lambda (t-s)} b(s) \\ - i \sum_\lambda \kappa_\lambda^* e^{-i\omega_\lambda t} a_\lambda(0). \end{aligned} \tag{C.20}$$

Defining $K(t-s) \equiv \sum_\lambda |\kappa_\lambda|^2 e^{-i\omega_\lambda (t-s)}$, we can write the solution of Eq. (C.20) as

$$b(t) = U(t) b(0) - i \sum_\lambda \kappa_\lambda^* a_\lambda(0) \int_0^t ds\, U(t-s) e^{-i\omega_\lambda s}, \tag{C.21}$$

where $U(t)$ is determined from the integrodifferential equation [385]

$$\partial_t U(t) = -i\Omega\, U(t) - \int_0^t ds\, K(t-s) U(s). \tag{C.22}$$

Note that $U(t)$ is only defined for $t \geq 0$, with initial condition $U(0) = 1$. Albeit for a continuous bath spectrum an analytic calculation of $U(t)$ for specific spectral densities is possible via Laplace transforms [386], we focus on a numerical scheme for solving Eq. (C.22) in the following, relying on numerical diagonalization.

To this end, we first define auxiliary coefficients $U_\lambda(t)$ whose dependence on t is via a simple exponential and the integration boundary only,

$$U_\lambda(t) = \kappa_\lambda \int_0^t ds\, e^{-i\omega_\lambda(t-s)} U(s). \tag{C.23}$$

By means of this definition, we are able to cast Eq. (C.22) into a set of coupled equations,

$$\partial_t U(t) = -i\Omega U(t) - \sum_\lambda \kappa_\lambda^* U_\lambda(t), \tag{C.24a}$$

$$\partial_t U_\lambda(t) = \kappa_\lambda U(t) - i\omega_\lambda U_\lambda(t). \tag{C.24b}$$

Introducing the vector $\bar{u}(t) = (U(t), U_1(t), \ldots, U_N(t))^T$, we can rewrite Eqs. (C.24) as

$$\partial_t \bar{u}(t) = -iG\bar{u}(t), \tag{C.25}$$

with the matrix G given by

$$G = \begin{pmatrix} \Omega & -i\kappa_1^* & -i\kappa_2^* & \cdots & -i\kappa_N^* \\ i\kappa_1 & \omega_1 & 0 & \cdots & 0 \\ i\kappa_2 & 0 & \omega_2 & \ddots & \vdots \\ \vdots & \vdots & \ddots & \ddots & 0 \\ i\kappa_N & 0 & \cdots & 0 & \omega_N \end{pmatrix}. \tag{C.26}$$

The Hermitian matrix G can be diagonalized via the transformation $T^\dagger\, G\, T = D$, yielding the eigenvalues $\bar{\omega}_\mu$. Defining $\bar{u} = T\bar{v}$, the differential equation (C.25) becomes

$$\partial_t \bar{v}(t) = -iD\bar{v}(t), \tag{C.27}$$

which has the simple solution $\bar{v}(t) = e^{-iDt}\bar{v}(0)$ with $\bar{v}(0) = T^\dagger \bar{u}(0)$, where $\bar{u}(0) = (1, 0, \ldots, 0)^T$. Taking the first component of the full expression $\bar{u}(t) = Te^{-iDt}T^\dagger \bar{u}(0)$, which gives $U(t)$, and writing $[\bar{u}(0)]_\mu = \delta_{0\mu}$, we arrive at the simple expression

$$U(t) = \sum_\mu |T_{0\mu}|^2 e^{-i\bar{\omega}_\mu t}. \tag{C.28}$$

The above reformulation allows one to map the solution of an integrodifferential equation onto an eigenvalue problem which involves only matrix multiplication and diagonalization, which is numerically more robust with respect to the numerical time step than straightforward numerical integration of Eq. (C.22). Note that this approach requires $K(t-s)$ to be given as a sum of exponentials that reproduce when being differentiated with respect to time.

We can now employ the above results to obtain alternative analytic expressions for the BCFs of the two initial states introduced in Eqs. (4.23) and (4.26). For the factorizing initial condition (4.23), the trace in Eq. (4.22) is readily evaluated, yielding

$$\begin{aligned} \alpha(t,t')/|g|^2 = {} & U(t)U^*(t')\,(n(\Omega)+1) + U^*(t)U(t')n(\Omega) \\ & + \sum_\lambda |\kappa_\lambda|^2 \int_0^t ds \int_0^{t'} ds' \Big[U(t-s)U^*(t'-s')e^{-i\omega_\lambda(s-s')}\,(n(\omega_\lambda)+1) \\ & + U^*(t-s)U(t'-s')e^{i\omega_\lambda(s-s')} n(\omega_\lambda) \Big]. \end{aligned} \tag{C.29}$$

Here, $n(\omega)$ is the mean occupation number of the harmonic oscillator of frequency ω, as introduced in Eq. (C.6).

For the diagonal initial condition (4.26), it is advisable to first linearly transform the operators b and a_λ into the eigenbasis of the joint environment, outlined in Appendix C.2. We find

$$
\begin{aligned}
\alpha(t,t')/|g|^2 = {} & \sum_{\mu} |S_{0\mu}|^2 \left[U(t)U^*(t')\left(n(\tilde{\omega}_\mu)+1\right) + U^*(t)U(t')n(\tilde{\omega}_\mu)\right] \\
& + \sum_{\lambda,\tau,\mu} \kappa_\lambda^* \kappa_\tau S_{\lambda\mu} S_{\tau\mu}^* \int_0^t ds \int_0^{t'} ds' \Big[U(t-s)U^*(t'-s')e^{-i(\omega_\lambda s - \omega_\tau s')}\left(n(\tilde{\omega}_\mu)+1\right) \\
& \quad + U^*(t-s)U(t'-s')e^{i(\omega_\lambda s - \omega_\tau s')} n(\tilde{\omega}_\mu)\Big] \\
& + i \sum_{\lambda,\mu} S_{0\mu} S_{\lambda\mu}^* \kappa_\lambda \left[U(t) \int_0^{t'} ds\, U^*(t'-s) e^{i\omega_\lambda s}\left(n(\tilde{\omega}_\mu)+1\right)\right. \\
& \quad \left. + U(t') \int_0^t ds\, U^*(t-s) e^{i\omega_\lambda s} n(\tilde{\omega}_\mu)\right] \\
& - i \sum_{\lambda,\mu} S_{0\mu}^* S_{\lambda\mu} \kappa_\lambda^* \left[U^*(t') \int_0^t ds\, U(t-s) e^{-i\omega_\lambda s}\left(n(\tilde{\omega}_\mu)+1\right)\right. \\
& \quad \left. + U^*(t) \int_0^{t'} ds\, U(t'-s) e^{-i\omega_\lambda s} n(\tilde{\omega}_\mu)\right] .
\end{aligned}
\tag{C.30}
$$

Note that the above results assume a Hermitian system operator L of the system-PM coupling [cf. Eq. (4.11)].

The procedure allowing us to arrive at Eqs. (C.29) and (C.30) is straightforward: We (i) derived the Heisenberg equations of motion for the PM operator, (ii) linearly transformed the time-independent ($t = 0$) operators of the Heisenberg equations of motion into the operators with respect to which the initial state is diagonal (cf. Appendix C.2), and (iii) evaluated the trace of the BCF [Eq. (4.22)] in this basis. Analogously to the procedure described in Sec. 4.2.4, the scheme sketched above can be generalized to, e.g., linearly coupled chains of PMs with the last PM(s) possibly coupled to a terminating bath [37, 38], direct coupling of PMs to independent baths [363], or a combination of both [39, 41]. Since the terminating baths are usually taken to be independent, the BCFs of the PMs can be derived by successively solving the Heisenberg equations of motion following the above approach. Starting at the PM which is coupled to the system and subsequently transforming the PM and bath operators into the basis in which the initial states are diagonal, the BCFs can be evaluated with respect to the given initial states.

Bibliography

[1] I. M. Georgescu, S. Ashhab, and F. Nori, *Quantum simulation*, Rev. Mod. Phys. **86**, 153 (2014).

[2] W. Kohn, *Nobel Lecture: Electronic structure of matter–wave functions and density functionals*, Rev. Mod. Phys. **71**, 1253 (1999).

[3] H. Breuer, and F. Petruccione, *The Theory of Open Quantum Systems* (Oxford University Press, Oxford, 2002).

[4] U. Weiss, *Quantum Dissipative Systems* (World Scientific, 2008).

[5] V. May, and O. Kühn, *Charge and Energy Transfer Dynamics in Molecular Systems* (Wiley, 2011).

[6] R. P. Feynman, *Simulating physics with computers*, Int. J. Theor. Phys. **21**, 467 (1982).

[7] I. Buluta, and F. Nori, *Quantum Simulators*, Science **326**, 108 (2009).

[8] S. Lloyd, *Universal Quantum Simulators*, Science **273**, 1073 (1996).

[9] H. Weimer, M. Müller, I. Lesanovsky, P. Zoller, and H. P. Büchler, *A Rydberg quantum simulator*, Nat. Phys. **6**, 382 (2010).

[10] J. T. Barreiro, M. Müller, P. Schindler, D. Nigg, T. Monz, M. Chwalla, M. Hennrich, C. F. Roos, P. Zoller, and R. Blatt, *An open-system quantum simulator with trapped ions*, Nature **470**, 486 (2011).

[11] S. Mostame, P. Rebentrost, A. Eisfeld, A. J. Kerman, D. I. Tsomokos, and A. Aspuru-Guzik, *Quantum simulator of an open quantum system using superconducting qubits: exciton transport in photosynthetic complexes*, New J. Phys. **14**, 105013 (2012).

[12] V. M. Stojanović, T. Shi, C. Bruder, and J. I. Cirac, *Quantum Simulation of Small-Polaron Formation with Trapped Ions*, Phys. Rev. Lett. **109**, 250501 (2012).

[13] J. F. Poyatos, J. I. Cirac, and P. Zoller, *Quantum Reservoir Engineering with Laser Cooled Trapped Ions*, Phys. Rev. Lett. **77**, 4728 (1996).

[14] M. Müller, S. Diehl, G. Pupillo, and P. Zoller, in *Adv. At. Mol. Opt. Phy.* Vol. 61, edited by E. A. Paul Berman, and C. Lin, (Academic Press, 2012), pp. 1–80.

[15] J. I. Cirac, A. S. Parkins, R. Blatt, and P. Zoller, *"Dark" squeezed states of the motion of a trapped ion*, Phys. Rev. Lett. **70**, 556 (1993).

[16] A. Beige, S. Bose, D. Braun, S. F. Huelga, P. L. Knight, M. B. Plenio, and V. Vedral, *Entangling Atoms and Ions in Dissipative Environments*, J. Mod. Opt. **47**, 2583 (2000).

[17] A. R. R. Carvalho, P. Milman, R. L. de Matos Filho, and L. Davidovich, *Decoherence, Pointer Engineering, and Quantum State Protection*, Phys. Rev. Lett. **86**, 4988 (2001).

[18] B. Kraus, H. P. Büchler, S. Diehl, A. Kantian, A. Micheli, and P. Zoller, *Preparation of entangled states by quantum Markov processes*, Phys. Rev. A **78**, 042307 (2008).

[19] A. R. R. Carvalho, A. J. S. Reid, and J. J. Hope, *Controlling entanglement by direct quantum feedback*, Phys. Rev. A **78**, 012334 (2008).

[20] H. Krauter, C. A. Muschik, K. Jensen, W. Wasilewski, J. M. Petersen, J. I. Cirac, and E. S. Polzik, *Entanglement Generated by Dissipation and Steady State Entanglement of Two Macroscopic Objects*, Phys. Rev. Lett. **107**, 080503 (2011).

[21] J. Cho, S. Bose, and M. S. Kim, *Optical Pumping into Many-Body Entanglement*, Phys. Rev. Lett. **106**, 020504 (2011).

[22] K. Stannigel, P. Rabl, and P. Zoller, *Driven-dissipative preparation of entangled states in cascaded quantum-optical networks*, New J. Phys. **14**, 063014 (2012).

[23] Y. Lin, J. P. Gaebler, F. Reiter, T. R. Tan, R. Bowler, A. S. Sørensen, D. Leibfried, and D. J. Wineland, *Dissipative production of a maximally entangled steady state of two quantum bits.* Nature **504**, 415 (2013).

[24] S. Shankar, M. Hatridge, Z. Leghtas, K. M. Sliwa, A. Narla, U. Vool, S. M. Girvin, L. Frunzio, M. Mirrahimi, and M. H. Devoret, *Autonomously stabilized entanglement between two superconducting quantum bits*, Nature **504**, 419 (2013).

[25] F. Reiter, L. Tornberg, G. Johansson, and A. S. Sørensen, *Steady-state entanglement of two superconducting qubits engineered by dissipation*, Phys. Rev. A **88**, 032317 (2013).

[26] C. D. B. Bentley, A. R. R. Carvalho, D. Kielpinski, and J. J. Hope, *Detection-Enhanced Steady State Entanglement with Ions*, Phys. Rev. Lett. **113**, 040501 (2014).

[27] G. Morigi, J. Eschner, C. Cormick, Y. Lin, D. Leibfried, and D. J. Wineland, *Dissipative Quantum Control of a Spin Chain*, Phys. Rev. Lett. **115**, 200502 (2015).

[28] M. Roghani, and H. Weimer, *Dissipative Preparation of Entangled Many-Body States with Rydberg Atoms*, ArXiv e-prints (2016), arXiv:1611.09612.

[29] J. Tuorila, M. Partanen, T. Ala-Nissila, and M. Möttönen, *Efficient protocol for qubit initialization with a tunable environment*, ArXiv e-prints (2016), arXiv:1612.04160.

[30] F. Verstraete, M. M. Wolf, and J. Ignacio Cirac, *Quantum computation and quantum-state engineering driven by dissipation*, Nat. Phys. **5**, 633 (2009).

[31] S. Diehl, A. Micheli, A. Kantian, B. Kraus, H. P. Büchler, and P. Zoller, *Quantum states and phases in driven open quantum systems with cold atoms*, Nat. Phys. **4**, 878 (2008).

[32] P. Schindler, M. Müller, D. Nigg, J. T. Barreiro, E. A. Martinez, M. Hennrich, T. Monz, S. Diehl, P. Zoller, and R. Blatt, *Quantum simulation of dynamical maps with trapped ions*, Nat. Phys. **9**, 361 (2013).

[33] J. Piilo, and S. Maniscalco, *Driven harmonic oscillator as a quantum simulator for open systems*, Phys. Rev. A **74**, 032303 (2006).

[34] T. Gallagher, *Rydberg Atoms*, Cambridge Monographs on Atomic, Molecular and Chemical Physics (Cambridge University Press, Cambridge, 2005).

[35] M. Saffman, T. G. Walker, and K. Mølmer, *Quantum information with Rydberg atoms*, Rev. Mod. Phys. **82**, 2313 (2010).

[36] M. Saffman, *Quantum computing with atomic qubits and Rydberg interactions: progress and challenges*, J. Phys. B **49**, 202001 (2016).

[37] R. Martinazzo, K. Hughes, and I. Burghardt, *Unraveling a Brownian particle's memory with effective mode chains*, Phys. Rev. E **84**, 030102 (2011).

[38] M. P. Woods, R. Groux, A. W. Chin, S. F. Huelga, and M. B. Plenio, *Mappings of open quantum systems onto chain representations and Markovian embeddings*, J. Math. Phys. **55**, 032101 (2014).

[39] J. Huh, S. Mostame, T. Fujita, M.-H. Yung, and A. Aspuru-Guzik, *Linear-algebraic bath transformation for simulating complex open quantum systems*, New J. Phys. **16**, 123008 (2014).

[40] J. Roden, G. Schulz, A. Eisfeld, and J. Briggs, *Electronic energy transfer on a vibronically coupled quantum aggregate*, J. Chem. Phys. **131**, 044909 (2009).

[41] S. Mostame, J. Huh, C. Kreisbeck, A. J. Kerman, T. Fujita, A. Eisfeld, and A. Aspuru-Guzik, *Emulation of complex open quantum systems using superconducting qubits*, Quantum Inf. Process. **16**, 44 (2016).

[42] J. Roden, W. T. Strunz, and A. Eisfeld, *Non-Markovian quantum state diffusion for absorption spectra of molecular aggregates*, J. Chem. Phys. **134**, 034902 (2011).

[43] G. Ritschel, J. Roden, W. T. Strunz, and A. Eisfeld, *An efficient method to calculate excitation energy transfer in light-harvesting systems: application to the Fenna-Matthews-Olson complex*, New J. Phys. **13**, 113034 (2011).

[44] M. T. W. Milder, B. Brüggemann, R. van Grondelle, and J. L. Herek, *Revisiting the optical properties of the FMO protein*, Photosyn. Res. **104**, 257 (2010).

[45] A. Chenu, and G. D. Scholes, *Coherence in Energy Transfer and Photosynthesis*, Annu. Rev. Phys. Chem. **66**, 69 (2015).

[46] A. Eisfeld, and J. S. Briggs, *The J-band of organic dyes: lineshape and coherence length*, Chem. Phys. **281**, 61 (2002).

[47] F. Robicheaux, J. V. Hernández, T. Topçu, and L. D. Noordam, *Simulation of coherent interactions between Rydberg atoms*, Phys. Rev. A **70**, 042703 (2004).

[48] S. Westermann, T. Amthor, L. A. de Oliveira, J. Deiglmayr, M. Reetz-Lamour, and M. Weidemüller, *Dynamics of resonant energy transfer in a cold Rydberg gas*, Eur. Phys. J. D **40**, 37 (2006).

[49] O. Mülken, A. Blumen, T. Amthor, C. Giese, M. Reetz-Lamour, and M. Weidemüller, *Survival Probabilities in Coherent Exciton Transfer with Trapping*, Phys. Rev. Lett. **99**, 090601 (2007).

[50] C. S. E. van Ditzhuijzen, A. F. Koenderink, J. V. Hernández, F. Robicheaux, L. D. Noordam, and H. B. v. L. van den Heuvell, *Spatially Resolved Observation of Dipole-Dipole Interaction between Rydberg Atoms*, Phys. Rev. Lett. **100**, 243201 (2008).

[51] S. Ravets, H. Labuhn, D. Barredo, L. Beguin, T. Lahaye, and A. Browaeys, *Coherent dipole-dipole coupling between two single Rydberg atoms at an electrically-tuned Forster resonance*, Nat. Phys. **10**, 914 (2014).

[52] D. Barredo, H. Labuhn, S. Ravets, T. Lahaye, A. Browaeys, and C. S. Adams, *Coherent Excitation Transfer in a Spin Chain of Three Rydberg Atoms*, Phys. Rev. Lett. **114**, 113002 (2015).

[53] Y. R. P. Sortais, H. Marion, C. Tuchendler, A. M. Lance, M. Lamare, P. Fournet, C. Armellin, R. Mercier, G. Messin, A. Browaeys, and P. Grangier, *Diffraction-limited optics for single-atom manipulation*, Phys. Rev. A **75**, 013406 (2007).

[54] M. Schlosser, S. Tichelmann, J. Kruse, and G. Birkl, *Scalable architecture for quantum information processing with atoms in optical micro-structures*, Quantum Inf. Process. **10**, 907 (2011).

[55] F. Nogrette, H. Labuhn, S. Ravets, D. Barredo, L. Béguin, A. Vernier, T. Lahaye, and A. Browaeys, *Single-Atom Trapping in Holographic 2D Arrays of Microtraps with Arbitrary Geometries*, Phys. Rev. X **4**, 021034 (2014).

[56] L. Feng, Z. J. Wong, R.-M. Ma, Y. Wang, and X. Zhang, *Single-mode laser by parity-time symmetry breaking*, Science **346**, 972 (2014).

[57] H. Hodaei, M.-A. Miri, M. Heinrich, D. N. Christodoulides, and M. Khajavikhan, *Parity-time–symmetric microring lasers*, Science **346**, 975 (2014).

[58] M. Aspelmeyer, T. J. Kippenberg, and F. Marquardt, *Cavity optomechanics*, Rev. Mod. Phys. **86**, 1391 (2014).

[59] H. Jing, Ş. K. Özdemir, X.-Y. Lü, J. Zhang, L. Yang, and F. Nori, *$\mathcal{PT}$-Symmetric Phonon Laser*, Phys. Rev. Lett. **113**, 053604 (2014).

[60] J. Roden, W. T. Strunz, K. B. Whaley, and A. Eisfeld, *Accounting for intra-molecular vibrational modes in open quantum system description of molecular systems*, J. Chem. Phys. **137**, 204110 (2012).

[61] A. Garg, J. N. Onuchic, and V. Ambegaokar, *Effect of friction on electron transfer in biomolecules*, J. Chem. Phys. **83**, 4491 (1985).

[62] K. H. Hughes, C. D. Christ, and I. Burghardt, *Effective-mode representation of non-Markovian dynamics: A hierarchical approximation of the spectral density. I. Application to single surface dynamics*, J. Chem. Phys. **131**, 024109 (2009).

[63] R. Martinazzo, B. Vacchini, K. H. Hughes, and I. Burghardt, *Communication: Universal Markovian reduction of Brownian particle dynamics*, J. Chem. Phys. **134**, 011101 (2011).

[64] D. W. Schönleber, A. Eisfeld, M. Genkin, S. Whitlock, and S. Wüster, *Quantum Simulation of Energy Transport with Embedded Rydberg Aggregates*, Phys. Rev. Lett. **114**, 123005 (2015).

[65] M. Genkin, D. W. Schönleber, S. Wüster, and A. Eisfeld, *Non-Markovian dynamics in ultracold Rydberg aggregates*, J. Phys. B **49**, 134001 (2016).

[66] D. W. Schönleber, C. D. B. Bentley, and A. Eisfeld, *Engineering thermal reservoirs with ultracold Rydberg atoms*, ArXiv e-prints (2016), arXiv:1611.02914.

[67] R. Stebbings, and F. Dunning, *Rydberg States of Atoms and Molecules* (Cambridge University Press, 1983).

[68] D. Jaksch, J. I. Cirac, P. Zoller, S. L. Rolston, R. Côté, and M. D. Lukin, *Fast Quantum Gates for Neutral Atoms*, Phys. Rev. Lett. **85**, 2208 (2000).

[69] M. D. Lukin, M. Fleischhauer, R. Cote, L. M. Duan, D. Jaksch, J. I. Cirac, and P. Zoller, *Dipole Blockade and Quantum Information Processing in Mesoscopic Atomic Ensembles*, Phys. Rev. Lett. **87**, 037901 (2001).

[70] T. Pohl, C. S. Adams, and H. R. Sadephpour, *Cold Rydberg gases and ultra-cold plasmas*, J. Phys. B **44**, 180201 (2011).

[71] R. Löw, H. Weimer, J. Nipper, J. B. Balewski, B. Butscher, H. P. Büchler, and T. Pfau, *An experimental and theoretical guide to strongly interacting Rydberg gases*, J. Phys. B **45**, 113001 (2012).

[72] I. I. Beterov, I. I. Ryabtsev, D. B. Tretyakov, and V. M. Entin, *Quasiclassical calculations of blackbody-radiation-induced depopulation rates and effective lifetimes of Rydberg nS, nP, and nD alkali-metal atoms with $n \leq 80$*, Phys. Rev. A **79**, 052504 (2009).

[73] J. Frenkel, *On the Transformation of light into Heat in Solids. I*, Phys. Rev. **37**, 17 (1931).

[74] M. D. Lukin, and P. R. Hemmer, *Quantum Entanglement via Optical Control of Atom-Atom Interactions*, Phys. Rev. Lett. **84**, 2818 (2000).

[75] J. D. Pritchard, D. Maxwell, A. Gauguet, K. J. Weatherill, M. P. A. Jones, and C. S. Adams, *Cooperative Atom-Light Interaction in a Blockaded Rydberg Ensemble*, Phys. Rev. Lett. **105**, 193603 (2010).

[76] C. Ates, S. Sevinçli, and T. Pohl, *Electromagnetically induced transparency in strongly interacting Rydberg gases*, Phys. Rev. A **83**, 041802 (2011).

[77] G. Günter, M. Robert-de-Saint-Vincent, H. Schempp, C. S. Hofmann, S. Whitlock, and M. Weidemüller, *Interaction Enhanced Imaging of Individual Rydberg Atoms in Dense Gases*, Phys. Rev. Lett. **108**, 013002 (2012).

[78] O. Firstenberg, C. S. Adams, and S. Hofferberth, *Nonlinear quantum optics mediated by Rydberg interactions*, J. Phys. B **49**, 152003 (2016).

[79] K.-J. Boller, A. Imamoğlu, and S. E. Harris, *Observation of electromagnetically induced transparency*, Phys. Rev. Lett. **66**, 2593 (1991).

[80] M. Fleischhauer, A. Imamoğlu, and J. P. Marangos, *Electromagnetically induced transparency: Optics in coherent media*, Rev. Mod. Phys. **77**, 633 (2005).

[81] G. Günter, H. Schempp, M. Robert-de-Saint-Vincent, V. Gavryusev, S. Helmrich, C. S. Hofmann, S. Whitlock, and M. Weidemüller, *Observing the Dynamics of Dipole-Mediated Energy Transport by Interaction-Enhanced Imaging*, Science **342**, 954 (2013).

[82] B. Olmos, W. Li, S. Hofferberth, and I. Lesanovsky, *Amplifying single impurities immersed in a gas of ultracold atoms*, Phys. Rev. A **84**, 041607 (2011).

[83] I. Lesanovsky, *Liquid Ground State, Gap, and Excited States of a Strongly Correlated Spin Chain*, Phys. Rev. Lett. **108**, 105301 (2012).

[84] J. P. Hague, and C. MacCormick, *Quantum simulation of electron–phonon interactions in strongly deformable materials*, New J. Phys. **14**, 033019 (2012).

[85] J. P. Hague, and C. MacCormick, *Could optical lattices be used to simulate real materials?*, ArXiv e-prints (2015), arXiv:1506.04005.

[86] A. Dauphin, M. Müller, and M. A. Martin-Delgado, *Quantum simulation of a topological Mott insulator with Rydberg atoms in a Lieb lattice*, Phys. Rev. A **93**, 043611 (2016).

[87] N. Henkel, R. Nath, and T. Pohl, *Three-Dimensional Roton Excitations and Supersolid Formation in Rydberg-Excited Bose-Einstein Condensates*, Phys. Rev. Lett. **104**, 195302 (2010).

[88] G. Pupillo, A. Micheli, M. Boninsegni, I. Lesanovsky, and P. Zoller, *Strongly Correlated Gases of Rydberg-Dressed Atoms: Quantum and Classical Dynamics*, Phys. Rev. Lett. **104**, 223002 (2010).

[89] M. Mayle, I. Lesanovsky, and P. Schmelcher, *Dressing of ultracold atoms by their Rydberg states in a Ioffe–Pritchard trap*, J. Phys. B **43**, 155003 (2010).

[90] J. Honer, H. Weimer, T. Pfau, and H. P. Büchler, *Collective Many-Body Interaction in Rydberg Dressed Atoms*, Phys. Rev. Lett. **105**, 160404 (2010).

[91] S. Wüster, C. Ates, A. Eisfeld, and J. M. Rost, *Excitation transport through Rydberg dressing*, New J. Phys. **13**, 073044 (2011).

[92] M. Genkin, S. Wüster, S. Möbius, A. Eisfeld, and J. M. Rost, *Dipole–dipole induced global motion of Rydberg-dressed atom clouds*, J. Phys. B **47**, 095003 (2014).

[93] S. Helmrich, A. Arias, N. Pehoviak, and S. Whitlock, *Two-body interactions and decay of three-level Rydberg-dressed atoms*, J. Phys. B **49**, 03LT02 (2016).

[94] A. W. Glaetzle, M. Dalmonte, R. Nath, I. Rousochatzakis, R. Moessner, and P. Zoller, *Quantum Spin-Ice and Dimer Models with Rydberg Atoms*, Phys. Rev. X **4**, 041037 (2014).

[95] A. W. Glaetzle, M. Dalmonte, R. Nath, C. Gross, I. Bloch, and P. Zoller, *Designing Frustrated Quantum Magnets with Laser-Dressed Rydberg Atoms*, Phys. Rev. Lett. **114**, 173002 (2015).

[96] R. M. W. van Bijnen, and T. Pohl, *Quantum Magnetism and Topological Ordering via Rydberg Dressing near Förster Resonances*, Phys. Rev. Lett. **114**, 243002 (2015).

[97] H. Labuhn, D. Barredo, S. Ravets, S. de Léséleuc, T. Macrì, T. Lahaye, and A. Browaeys, *Tunable two-dimensional arrays of single Rydberg atoms for realizing quantum Ising models*, Nature **534**, 667 (2016).

[98] J. Zeiher, R. van Bijnen, P. Schausz, S. Hild, J.-y. Choi, T. Pohl, I. Bloch, and C. Gross, *Many-body interferometry of a Rydberg-dressed spin lattice*, Nat. Phys. **12**, 1095 (2016).

[99] M. Tanasittikosol, J. D. Pritchard, D. Maxwell, A. Gauguet, K. J. Weatherill, R. M. Potvliege, and C. S. Adams, *Microwave dressing of Rydberg dark states*, J. Phys. B **44**, 184020 (2011).

[100] S. Sevinçli, and T. Pohl, *Microwave control of Rydberg atom interactions*, New J. Phys. **16**, 123036 (2014).

[101] J. Holtsmark, *Über die Absorption in Na-Dampf*, Z. Phys. **34**, 722 (1925).

[102] J. Frenkel, *Zur Theorie der Resonanzverbreiterung von Spektrallinien*, Z. Phys. **59**, 198 (1930).

[103] J. Franck, and E. Teller, *Migration and Photochemical Action of Excitation Energy in Crystals*, J. Chem. Phys. **6**, 861 (1938).

[104] K. A. Safinya, J. F. Delpech, F. Gounand, W. Sandner, and T. F. Gallagher, *Resonant Rydberg-Atom-Rydberg-Atom Collisions*, Phys. Rev. Lett. **47**, 405 (1981).

[105] W. R. Anderson, J. R. Veale, and T. F. Gallagher, *Resonant Dipole-Dipole Energy Transfer in a Nearly Frozen Rydberg Gas*, Phys. Rev. Lett. **80**, 249 (1998).

[106] I. Mourachko, D. Comparat, F. de Tomasi, A. Fioretti, P. Nosbaum, V. M. Akulin, and P. Pillet, *Many-Body Effects in a Frozen Rydberg Gas*, Phys. Rev. Lett. **80**, 253 (1998).

[107] V. M. Akulin, F. de Tomasi, I. Mourachko, and P. Pillet, *Classical Chaos and its Quantum Manifestations Level-band problem and many-body effects in cold Rydberg atoms*, Physica D **131**, 125 (1999).

[108] J. S. Frasier, V. Celli, and T. Blum, *Resonant processes in a frozen gas*, Phys. Rev. A **59**, 4358 (1999).

[109] F. Robicheaux, and N. M. Gill, *Effect of random positions for coherent dipole transport*, Phys. Rev. A **89**, 053429 (2014).

[110] A. Browaeys, D. Barredo, and T. Lahaye, *Experimental investigations of dipole–dipole interactions between a few Rydberg atoms*, J. Phys. B **49**, 152001 (2016).

[111] S. Bettelli, D. Maxwell, T. Fernholz, C. S. Adams, I. Lesanovsky, and C. Ates, *Exciton dynamics in emergent Rydberg lattices*, Phys. Rev. A **88**, 043436 (2013).

[112] J. J. Balmer, *Notiz über die Spektrallinien des Wasserstoffs*, Ann. Phys. Chem. **25**, 80 (1885).

[113] J. R. Rydberg, *On the structure of the line-spectra of the chemical elements*, Philos. Mag. **29**, 331 (1890).

[114] N. Bohr, *On the constitution of atoms and molecules*, Philos. Mag. **26**, 1 (1913).

[115] E. Rutherford, *The scattering of α and β particles by matter and the structure of the atom*, Philos. Mag. **21**, 669 (1911).

[116] M. Planck, *Zur Theorie der Wärmestrahlung*, Ann. Phys. **336**, 758 (1910).

[117] H. Haken, W. Brewer, and H. Wolf, *Atomic and Quantum Physics: An Introduction to the Fundamentals of Experiment and Theory* (Springer Berlin Heidelberg, 2012).

[118] T. S. Kuhn, *Die Struktur wissenschaftlicher Revolutionen*, 2., rev. und um das Postskriptum von 1969 erg. Aufl., Suhrkamp-Taschenbuch Wissenschaft 25 (Suhrkamp, Frankfurt am Main, 1996).

[119] S. Okasha, *Philosophy of Science: A Very Short Introduction*, Very Short Introductions (OUP Oxford, 2002).

[120] N. Bohr, *Über die Anwendung der Quantentheorie auf den Atombau*, Z. Phys. **13**, 117 (1923).

[121] J. B. Balewski, A. T. Krupp, A. Gaj, D. Peter, H. P. Büchler, R. Löw, S. Hofferberth, and T. Pfau, *Coupling a single electron to a Bose-Einstein condensate*, Nature **502**, 664 (2013).

[122] M. Mack, F. Karlewski, H. Hattermann, S. Höckh, F. Jessen, D. Cano, and J. Fortágh, *Measurement of absolute transition frequencies of* ^{87}Rb *to nS and nD Rydberg states by means of electromagnetically induced transparency*, Phys. Rev. A **83**, 052515 (2011).

[123] W. Li, I. Mourachko, M. W. Noel, and T. F. Gallagher, *Millimeter-wave spectroscopy of cold Rb Rydberg atoms in a magneto-optical trap: Quantum defects of the ns, np, and nd series*, Phys. Rev. A **67**, 052502 (2003).

[124] J. Han, Y. Jamil, D. V. L. Norum, P. J. Tanner, and T. F. Gallagher, *Rb nf quantum defects from millimeter-wave spectroscopy of cold* ^{85}Rb *Rydberg atoms*, Phys. Rev. A **74**, 054502 (2006).

[125] D. B. Branden, T. Juhasz, T. Mahlokozera, C. Vesa, R. O. Wilson, M. Zheng, A. Kortyna, and D. A. Tate, *Radiative lifetime measurements of rubidium Rydberg states*, J. Phys. B **43**, 015002 (2010).

[126] X. He, B. Li, A. Chen, and C. Zhang, *Model-potential calculation of lifetimes of Rydberg states of alkali atoms*, J. Phys. B **23**, 661 (1990).

[127] M. Mayle, *Ultracold Rydberg Atoms in a Ioffe-Pritchard Trap*, PhD thesis (University of Heidelberg, 2009).

[128] R. Lutwak, J. Holley, P. P. Chang, S. Paine, D. Kleppner, and T. Ducas, *Circular states of atomic hydrogen*, Phys. Rev. A **56**, 1443 (1997).

[129] D. Comparat, and P. Pillet, *Dipole blockade in a cold Rydberg atomic sample (Invited)*, J. Opt. Soc. Am. B **27**, A208 (2010).

[130] A. Schwettmann, J. Crawford, K. R. Overstreet, and J. P. Shaffer, *Cold Cs Rydberg-gas interactions*, Phys. Rev. A **74**, 020701 (2006).

[131] J. Deiglmayr, H. Saßmannshausen, P. Pillet, and F. Merkt, *Observation of Dipole-Quadrupole Interaction in an Ultracold Gas of Rydberg Atoms*, Phys. Rev. Lett. **113**, 193001 (2014).

[132] T. G. Walker, and M. Saffman, *Consequences of Zeeman degeneracy for the van der Waals blockade between Rydberg atoms*, Phys. Rev. A **77**, 032723 (2008).

[133] N. Samboy, and R. Côté, *Rubidium Rydberg macrodimers*, J. Phys. B **44**, 184006 (2011).

[134] J. Stanojevic, R. Côté, D. Tong, E. E. Eyler, and P. L. Gould, *Long-range potentials and* $(n-1)d + ns$ *molecular resonances in an ultracold Rydberg gas*, Phys. Rev. A **78**, 052709 (2008).

[135] J. S. Cabral, J. M. Kondo, L. F. Gonçalves, V. A. Nascimento, L. G. Marcassa, D. Booth, J. Tallant, A. Schwettmann, K. R. Overstreet, J. Sedlacek, and J. P. Shaffer, *Effects of electric fields on ultracold Rydberg atom interactions*, J. Phys. B **44**, 184007 (2011).

[136] T. Pohl, and P. R. Berman, *Breaking the Dipole Blockade: Nearly Resonant Dipole Interactions in Few-Atom Systems*, Phys. Rev. Lett. **102**, 013004 (2009).

[137] D. Cano, and J. Fortágh, *Nonadditive potentials between three Rydberg atoms*, Phys. Rev. A **86**, 043422 (2012).

[138] M. Kiffner, W. Li, and D. Jaksch, *Three-Body Bound States in Dipole-Dipole Interacting Rydberg Atoms*, Phys. Rev. Lett. **111**, 233003 (2013).

[139] S. Möbius, *Intertwining Exciton Dynamics and Nuclear Motion in Rydberg Aggregates*, PhD thesis (Dresden University of Technology, 2014).

[140] A. Reinhard, T. C. Liebisch, B. Knuffman, and G. Raithel, *Level shifts of rubidium Rydberg states due to binary interactions*, Phys. Rev. A **75**, 032712 (2007).

[141] L. Marcassa, and J. Shaffer, *Interactions in Ultracold Rydberg Gases*, Adv. Atom, Mol. Opt. Phys. **63**, 47 (2014).

[142] S. Ravets, H. Labuhn, D. Barredo, T. Lahaye, and A. Browaeys, *Measurement of the angular dependence of the dipole-dipole interaction between two individual Rydberg atoms at a Förster resonance*, Phys. Rev. A **92**, 020701 (2015).

[143] S. Möbius, S. Wüster, C. Ates, A. Eisfeld, and J. M. Rost, *Adiabatic entanglement transport in Rydberg aggregates*, J. Phys. B **44**, 184011 (2011).

[144] K. Leonhardt, *Interplay of excitation transport and atomic motion in flexible Rydberg aggregates*, PhD thesis (Dresden University of Technology, 2016).

[145] P. van der Straten, and H. Metcalf, *Atoms and Molecules Interacting with Light: Atomic Physics for the Laser Era* (Cambridge University Press, 2016).

[146] H. Zoubi, A. Eisfeld, and S. Wüster, *van der Waals-stabilized Rydberg aggregates*, Phys. Rev. A **89**, 053426 (2014).

[147] J. Pritchard, *Cooperative Optical Non-Linearity in a Blockaded Rydberg Ensemble*, Springer Theses (Springer, 2012).

[148] N. Henkel, *Rydberg-dressed Bose-Einstein condensates*, PhD thesis (Dresden University of Technology, 2013).

[149] R. M. W. van Bijnen, *Quantum Engineering with Ultracold Atoms*, PhD thesis (Eindhoven University of Technology, 2013).

[150] H. Zoubi, *Van der Waals interactions among alkali Rydberg atoms with excitonic states*, J. Phys. B **48**, 185002 (2015).

[151] K. Singer, J. Stanojevic, M. Weidemüller, and R. Côté, *Long-range interactions between alkali Rydberg atom pairs correlated to the ns-ns, np-np and nd-nd asymptotes*, J. Phys. B **38**, S295 (2005).

[152] T. Vogt, M. Viteau, J. Zhao, A. Chotia, D. Comparat, and P. Pillet, *Dipole Blockade at Förster Resonances in High Resolution Laser Excitation of Rydberg States of Cesium Atoms*, Phys. Rev. Lett. **97**, 083003 (2006).

[153] J. Nipper, J. B. Balewski, A. T. Krupp, B. Butscher, R. Löw, and T. Pfau, *Highly Resolved Measurements of Stark-Tuned Förster Resonances between Rydberg Atoms*, Phys. Rev. Lett. **108**, 113001 (2012).

[154] R. Kachru, N. H. Tran, and T. F. Gallagher, *Microwave-Assisted Resonant Collisional Energy Transfer in Na Rydberg States*, Phys. Rev. Lett. **49**, 191 (1982).

[155] P. Bohlouli-Zanjani, J. A. Petrus, and J. D. D. Martin, *Enhancement of Rydberg Atom Interactions Using ac Stark Shifts*, Phys. Rev. Lett. **98**, 203005 (2007).

[156] A. Paris-Mandoki, H. Gorniaczyk, C. Tresp, I. Mirgorodskiy, and S. Hofferberth, *Tailoring Rydberg interactions via Förster resonances: state combinations, hopping and angular dependence*, J. Phys. B **49**, 164001 (2016).

[157] M. L. Zimmerman, M. G. Littman, M. M. Kash, and D. Kleppner, *Stark structure of the Rydberg states of alkali-metal atoms*, Phys. Rev. A **20**, 2251 (1979).

[158] T. J. Carroll, K. Claringbould, A. Goodsell, M. J. Lim, and M. W. Noel, *Angular Dependence of the Dipole-Dipole Interaction in a Nearly One-Dimensional Sample of Rydberg Atoms*, Phys. Rev. Lett. **93**, 153001 (2004).

[159] I. I. Ryabtsev, D. B. Tretyakov, I. I. Beterov, and V. M. Entin, *Observation of the Stark-Tuned Förster Resonance between Two Rydberg Atoms*, Phys. Rev. Lett. **104**, 073003 (2010).

[160] J. Grimmel, M. Mack, F. Karlewski, F. Jessen, M. Reinschmidt, N. Sándor, and J. Fortágh, *Measurement and numerical calculation of Rubidium Rydberg Stark spectra*, New J. Phys. **17**, 053005 (2015).

[161] P. Meystre, and M. Sargent, *Elements of Quantum Optics* (Springer, Berlin Heidelberg, 2007).

[162] H. J. Carmichael, *An open systems approach to quantum optics: lectures presented at the Université Libre de Bruxelles, October 28 to November 4, 1991* (Springer, Berlin Heidelberg, 1993).

[163] D. W. Schönleber, *Dissipative Dynamics in Many-Body Rydberg Systems*, Master Thesis (University of Heidelberg, 2013).

[164] M. Gärttner, *Heralded W-state preparation using laser-designed superatoms*, Phys. Rev. A **92**, 013629 (2015).

[165] A. Gaetan, Y. Miroshnychenko, T. Wilk, A. Chotia, M. Viteau, D. Comparat, P. Pillet, A. Browaeys, and P. Grangier, *Observation of collective excitation of two individual atoms in the Rydberg blockade regime*, Nat. Phys. **5**, 115 (2009).

[166] Y. O. Dudin, L. Li, F. Bariani, and A. Kuzmich, *Observation of coherent many-body Rabi oscillations*, Nat. Phys. **8**, 790 (2012).

[167] M. Ebert, A. Gill, M. Gibbons, X. Zhang, M. Saffman, and T. G. Walker, *Atomic Fock State Preparation Using Rydberg Blockade*, Phys. Rev. Lett. **112**, 043602 (2014).

[168] D. Barredo, S. Ravets, H. Labuhn, L. Béguin, A. Vernier, F. Nogrette, T. Lahaye, and A. Browaeys, *Demonstration of a Strong Rydberg Blockade in Three-Atom Systems with Anisotropic Interactions*, Phys. Rev. Lett. **112**, 183002 (2014).

[169] M. Gärttner, S. Whitlock, D. W. Schönleber, and J. Evers, *Collective Excitation of Rydberg-Atom Ensembles beyond the Superatom Model*, Phys. Rev. Lett. **113**, 233002 (2014).

[170] H. A. Bethe, and E. E. Salpeter, *Quantum mechanics of one- and two-electron atoms*, 1. paperback ed. (Plenum Pr., New York, 1977).

[171] C. Cohen-Tannoudji, J. Dupont-Roc, and G. Grynberg, *Atom - Photon Interactions: Basic Process and Appilcations* (Wiley-VCH Verlag, 2008).

[172] E. A. Power, and S. Zienau, *Coulomb Gauge in Non-Relativistic Quantum Electro-Dynamics and the Shape of Spectral Lines*, Phil. Trans. R. Soc. A **251**, 427 (1959).

[173] M. Scully, and S. Zubairy, *Quantum Optics* (Cambridge University Press, Cambridge, 1997).

[174] K. Rzążewski, and R. W. Boyd, *Equivalence of interaction hamiltonians in the electric dipole approximation*, J. Mod. Opt. **51**, 1137 (2004).

[175] P. Lambropoulos, and S. Smith, *Multiphoton Processes: Proceedings of the 3rd International Conference, Iraklion, Crete, Greece September 5–12, 1984*, Springer Series on Atomic, Optical, and Plasma Physics (Springer Berlin Heidelberg, 1984).

[176] S. E. Anderson, and G. Raithel, *Ionization of Rydberg atoms by standing-wave light fields*, Nat. Commun. **4**, 2967 (2013).

[177] M. Gärttner, *Many-body effects in Rydberg gases*, PhD thesis (University of Heidelberg, 2013).

[178] H. Metcalf, and P. van der Straten, *Laser Cooling and Trapping*, Graduate Texts in Contemporary Physics (Springer New York, 2012).

[179] N. Tezak, *Spectra and Excitation Dynamics of Laser-driven Lattices of Ultracold Rydberg Atoms*, Diploma Thesis (University of Heidelberg, 2010).

[180] M. Gross, and S. Haroche, *Superradiance: An essay on the theory of collective spontaneous emission*, Phys. Rep. **93**, 301 (1982).

[181] C. Gardiner, and P. Zoller, *Quantum Noise: A Handbook of Markovian and Non-Markovian Quantum Stochastic Methods with Applications to Quantum Optics*, Springer Series in Synergetics (Springer, 2004).

[182] H. Wiseman, and G. Milburn, *Quantum Measurement and Control* (Cambridge University Press, Cambridge, 2010).

[183] L. Jackman, *Dynamic Nuclear Magnetic Resonance Spectroscopy* (Elsevier Science, 2012).

[184] J. Cui, J. I. Cirac, and M. C. Bañuls, *Variational Matrix Product Operators for the Steady State of Dissipative Quantum Systems*, Phys. Rev. Lett. **114**, 220601 (2015).

[185] G. Günter, *Interfacing Rydberg atoms with light and observing their interaction driven dynamics*, eng, PhD thesis (University of Heidelberg, 2014).

[186] J. Gea-Banacloche, Y.-q. Li, S.-z. Jin, and M. Xiao, *Electromagnetically induced transparency in ladder-type inhomogeneously broadened media: Theory and experiment*, Phys. Rev. A **51**, 576 (1995).

[187] V. Gavryusev, A. Signoles, M. Ferreira-Cao, G. Zürn, C. S. Hofmann, G. Günter, H. Schempp, M. Robert-de-Saint-Vincent, S. Whitlock, and M. Weidemüller, *Density matrix reconstruction of three-level atoms via Rydberg electromagnetically induced transparency*, J. Phys. B **49**, 164002 (2016).

[188] S. G. Schirmer, and X. Wang, *Stabilizing open quantum systems by Markovian reservoir engineering*, Phys. Rev. A **81**, 062306 (2010).

[189] T. Pohl, E. Demler, and M. D. Lukin, *Dynamical Crystallization in the Dipole Blockade of Ultracold Atoms*, Phys. Rev. Lett. **104**, 043002 (2010).

[190] M. Gärttner, K. P. Heeg, T. Gasenzer, and J. Evers, *Dynamic formation of Rydberg aggregates at off-resonant excitation*, Phys. Rev. A **88**, 043410 (2013).

[191] H. Weimer, R. Löw, T. Pfau, and H. P. Büchler, *Quantum Critical Behavior in Strongly Interacting Rydberg Gases*, Phys. Rev. Lett. **101**, 250601 (2008).

[192] S. Wüster, J. Stanojevic, C. Ates, T. Pohl, P. Deuar, J. F. Corney, and J. M. Rost, *Correlations of Rydberg excitations in an ultracold gas after an echo sequence*, Phys. Rev. A **81**, 023406 (2010).

[193] I. Lesanovsky, and J. P. Garrahan, *Out-of-equilibrium structures in strongly interacting Rydberg gases with dissipation*, Phys. Rev. A **90**, 011603 (2014).

[194] R. M. W. van Bijnen, S. Smit, K. A. H. van Leeuwen, E. J. D. Vredenbregt, and S. J. J. M. F. Kokkelmans, *Adiabatic formation of Rydberg crystals with chirped laser pulses*, J. Phys. B **44**, 184008 (2011).

[195] H. Schempp, G. Günter, M. Robert-de-Saint-Vincent, C. S. Hofmann, D. Breyel, A. Komnik, D. W. Schönleber, M. Gärttner, J. Evers, S. Whitlock, and M. Weidemüller, *Full Counting Statistics of Laser Excited Rydberg Aggregates in a One-Dimensional Geometry*, Phys. Rev. Lett. **112**, 013002 (2014).

[196] P. S. M. Cheneau, M. Endres, T. Fukuhara, S. Hild, A. Omran, T. Pohl, C. Gross, S. Kuhr, and I. Bloch, *Observation of spatially ordered structures in a two-dimensional Rydberg gas*, Nature **491**, 87 (2012).

[197] P. Schauß, J. Zeiher, T. Fukuhara, S. Hild, M. Cheneau, T. Macrì, T. Pohl, I. Bloch, and C. Gross, *Crystallization in Ising quantum magnets*, Science **347**, 1455 (2015).

[198] Y. O. Dudin, and A. Kuzmich, *Strongly Interacting Rydberg Excitations of a Cold Atomic Gas*, Science **336**, 887 (2012).

[199] C. S. Hofmann, G. Günter, H. Schempp, M. Robert-de-Saint-Vincent, M. Gärttner, J. Evers, S. Whitlock, and M. Weidemüller, *Sub-Poissonian Statistics of Rydberg-Interacting Dark-State Polaritons*, Phys. Rev. Lett. **110**, 203601 (2013).

[200] A. M. Hankin, Y.-Y. Jau, L. P. Parazzoli, C. W. Chou, D. J. Armstrong, A. J. Landahl, and G. W. Biedermann, *Two-atom Rydberg blockade using direct 6S to nP excitation*, Phys. Rev. A **89**, 033416 (2014).

[201] H. van Amerongen, L. Valkunas, and R. van Grondelle, *Photosynthetic Excitons* (World Scientific, 2000).

[202] R. van Grondelle, and V. I. Novoderezhkin, *Energy transfer in photosynthesis: experimental insights and quantitative models*, Phys. Chem. Chem. Phys. **8**, 793 (2006).

[203] C. R. Kagan, C. B. Murray, and M. G. Bawendi, *Long-range resonance transfer of electronic excitations in close-packed CdSe quantum-dot solids*, Phys. Rev. B **54**, 8633 (1996).

[204] S. Kirstein, and S. Daehne, *J-aggregates of amphiphilic cyanine dyes: Self-organization of artificial light harvesting complexes*, Int. J. Photoenergy **2006**, 21 (2006).

[205] S. K. Saikin, A. Eisfeld, S. Valleau, and A. Aspuru-Guzik, *Photonics meets excitonics: natural and artificial molecular aggregates*, Nanophotonics **2**, 21 (2013).

[206] C. Ates, A. Eisfeld, and J. M. Rost, *Motion of Rydberg atoms induced by resonant dipole–dipole interactions*, New J. Phys. **10**, 045030 (2008).

[207] T. Wang, S. F. Yelin, R. Côté, E. E. Eyler, S. M. Farooqi, P. L. Gould, M. Koštrun, D. Tong, and D. Vrinceanu, *Superradiance in ultracold Rydberg gases*, Phys. Rev. A **75**, 033802 (2007).

[208] K. Singer, M. Reetz-Lamour, T. Amthor, L. G. Marcassa, and M. Weidemüller, *Suppression of Excitation and Spectral Broadening Induced by Interactions in a Cold Gas of Rydberg Atoms*, Phys. Rev. Lett. **93**, 163001 (2004).

[209] A. M. Reilly, and A. Tkatchenko, *van der Waals dispersion interactions in molecular materials: beyond pairwise additivity*, Chem. Sci. **6**, 3289 (2015).

[210] F. Karlewski, M. Mack, J. Grimmel, N. Sándor, and J. Fortágh, *State-selective all-optical detection of Rydberg atoms*, Phys. Rev. A **91**, 043422 (2015).

[211] A. Schwarzkopf, R. E. Sapiro, and G. Raithel, *Imaging Spatial Correlations of Rydberg Excitations in Cold Atom Clouds*, Phys. Rev. Lett. **107**, 103001 (2011).

[212] M. Endres, M. Cheneau, T. Fukuhara, C. Weitenberg, P. Schauß, C. Gross, L. Mazza, M. C. Bañuls, L. Pollet, I. Bloch, and S. Kuhr, *Observation of Correlated Particle-Hole Pairs and String Order in Low-Dimensional Mott Insulators*, Science **334**, 200 (2011).

[213] L. Béguin, A. Vernier, R. Chicireanu, T. Lahaye, and A. Browaeys, *Direct Measurement of the van der Waals Interaction between Two Rydberg Atoms*, Phys. Rev. Lett. **110**, 263201 (2013).

[214] V. Gavryusev, M. Ferreira-Cao, A. Kekić, G. Zürn, and A. Signoles, *Interaction Enhanced Imaging of Rydberg P states*, Eur. Phys. J. Special Topics **225**, 2863 (2016).

[215] T. Amthor, M. Reetz-Lamour, S. Westermann, J. Denskat, and M. Weidemüller, *Mechanical Effect of van der Waals Interactions Observed in Real Time in an Ultracold Rydberg Gas*, Phys. Rev. Lett. **98**, 023004 (2007).

[216] T. Amthor, J. Denskat, C. Giese, N. N. Bezuglov, A. Ekers, L. S. Cederbaum, and M. Weidemüller, *Autoionization of an ultracold Rydberg gas through resonant dipole coupling*, Eur. Phys. J. D **53**, 329 (2009).

[217] P. Hertz, *Über den gegenseitigen durchschnittlichen Abstand von Punkten, die mit bekannter mittlerer Dichte im Raume angeordnet sind*, Math. Ann. **67**, 387 (1909).

[218] P. Schauss, *High-resolution imaging of ordering in Rydberg many-body systems*, PhD thesis (University of Munich, Feb. 2015).

[219] E. Fermi, *Sopra lo Spostamento per Pressione delle Righe Elevate delle Serie Spettrali*, Il Nuovo Cimento **11**, 157 (1934).

[220] J. Dalibard, Y. Castin, and K. Mølmer, *Wave-function approach to dissipative processes in quantum optics*, Phys. Rev. Lett. **68**, 580 (1992).

[221] R. Dum, P. Zoller, and H. Ritsch, *Monte Carlo simulation of the atomic master equation for spontaneous emission*, Phys. Rev. A **45**, 4879 (1992).

[222] K. Mølmer, Y. Castin, and J. Dalibard, *Monte Carlo wave-function method in quantum optics*, J. Opt. Soc. Am. B **10**, 524 (1993).

[223] D. W. Schönleber, M. Gärttner, and J. Evers, *Coherent versus incoherent excitation dynamics in dissipative many-body Rydberg systems*, Phys. Rev. A **89**, 033421 (2014).

[224] J. Honer, R. Löw, H. Weimer, T. Pfau, and H. P. Büchler, *Artificial Atoms Can Do More Than Atoms: Deterministic Single Photon Subtraction from Arbitrary Light Fields*, Phys. Rev. Lett. **107**, 093601 (2011).

[225] A. N. Korotkov, and D. V. Averin, *Continuous weak measurement of quantum coherent oscillations*, Phys. Rev. B **64**, 165310 (2001).

[226] T. Renger, V. May, and O. Kühn, *Ultrafast excitation energy transfer dynamics in photosynthetic pigment–protein complexes*, Phys. Rep. **343**, 137 (2001).

[227] G. S. Engel, T. R. Calhoun, E. L. Read, T.-K. Ahn, T. Mancal, Y.-C. Cheng, R. E. Blankenship, and G. R. Fleming, *Evidence for wavelike energy transfer through quantum coherence in photosynthetic systems*, Nature **446**, 782 (2007).

[228] M. Mohseni, P. Rebentrost, S. Lloyd, and A. Aspuru-Guzik, *Environment-assisted quantum walks in photosynthetic energy transfer*, J. Chem. Phys. **129**, 174106 (2008).

[229] M. B. Plenio, and S. F. Huelga, *Dephasing-assisted transport: quantum networks and biomolecules*, New J. Phys. **10**, 113019 (2008).

[230] A. Olaya-Castro, C. F. Lee, F. F. Olsen, and N. F. Johnson, *Efficiency of energy transfer in a light-harvesting system under quantum coherence*, Phys. Rev. B **78**, 085115 (2008).

[231] F. Caruso, A. W. Chin, A. Datta, S. F. Huelga, and M. B. Plenio, *Highly efficient energy excitation transfer in light-harvesting complexes: The fundamental role of noise-assisted transport*, J. Chem. Phys. **131**, 105106 (2009).

[232] T. Scholak, T. Wellens, and A. Buchleitner, *The optimization topography of exciton transport*, EPL **96**, 10001 (2011).

[233] T. Scholak, T. Wellens, and A. Buchleitner, *Optimal networks for excitonic energy transport*, J. Phys. B **44**, 184012 (2011).

[234] G. D. Scholes, G. R. Fleming, A. Olaya-Castro, and R. van Grondelle, *Lessons from nature about solar light harvesting*, Nat. Chem. **3**, 763 (2011).

[235] H. Haken, and P. Reineker, *The Coupled Coherent and Incoherent Motion of Excitons and its Influence on the Line Shape of Optical Absorption*, Z. Phys. **249**, 253 (1972).

[236] H. Haken, and G. Strobl, *An exactly solvable model for coherent and incoherent exciton motion*, Z. Phys. **262**, 135 (1973).

[237] E. Schwarzer, *Coherent and incoherent exciton motion in a linear chain: Solution of the Haken-Strobl-model*, Z. Phys. B **20**, 185 (1975).

[238] P. Reineker, and R. Kühne, *Exact derivation and solution of the Nakajima-Zwanzig generalized master equation and discussion of approximate treatments for the coupled coherent and incoherent exciton motion*, Phys. Rev. B **21**, 2448 (1980).

[239] A. Eisfeld, and J. S. Briggs, *Classical master equation for excitonic transport under the influence of an environment*, Phys. Rev. E **85**, 046118 (2012).

[240] J. Roden, A. Eisfeld, W. Wolff, and W. Strunz, *Influence of Complex Exciton-Phonon Coupling on Optical Absorption and Energy Transfer of Quantum Aggregates*, Phys. Rev. Lett. **103**, 058301 (2009).

[241] F. C. Spano, *The Spectral Signatures of Frenkel Polarons in H- and J-Aggregates*, Acc. Chem. Res. **43**, 429 (2010).

[242] H. Feshbach, *The Optical Model and Its Justification*, Annu. Rev. Nucl. Sci. **8**, 49 (1958).

[243] R. Zwanzig, *Ensemble Method in the Theory of Irreversibility*, J. Chem. Phys. **33**, 1338 (1960).

[244] V. M. Kenkre, and R. S. Knox, *Generalized-master-equation theory of excitation transfer*, Phys. Rev. B **9**, 5279 (1974).

[245] E. Brion, L. H. Pedersen, and K. Mølmer, *Adiabatic elimination in a lambda system*, J. Phys. A **40**, 1033 (2007).

[246] E. M. Kessler, *Generalized Schrieffer-Wolff formalism for dissipative systems*, Phys. Rev. A **86**, 012126 (2012).

[247] F. Reiter, and A. S. Sørensen, *Effective operator formalism for open quantum systems*, Phys. Rev. A **85**, 032111 (2012).

[248] V. Čápek, *Haken-Strobl-Reineker model: its limits of validity and a possible extension*, Chem. Phys. **171**, 79 (1993).

[249] H. Fidder, J. Knoester, and D. A. Wiersma, *Optical properties of disordered molecular aggregates: A numerical study*, J. Chem. Phys. **95**, 7880 (1991).

[250] B. Kramer, and A. MacKinnon, *Localization: theory and experiment*, Rep. Prog. Phys. **56**, 1469 (1993).

[251] H. Schempp, G. Günter, S. Wüster, M. Weidemüller, and S. Whitlock, *Correlated Exciton Transport in Rydberg-Dressed-Atom Spin Chains*, Phys. Rev. Lett. **115**, 093002 (2015).

[252] E. Barkai, R. Silbey, and G. Zumofen, *Lévy Distribution of Single Molecule Line Shape Cumulants in Glasses*, Phys. Rev. Lett. **84**, 5339 (2000).

[253] J. Müller, D. Haarer, and B. Kharlamov, *Non-Lorentzian hole profiles in organic glasses caused by a distribution of optical line widths*, Phys. Lett. A **281**, 64 (2001).

[254] E. Barkai, A. V. Naumov, Y. G. Vainer, M. Bauer, and L. Kador, *Lévy Statistics for Random Single-Molecule Line Shapes in a Glass*, Phys. Rev. Lett. **91**, 075502 (2003).

[255] S. M. Vlaming, V. A. Malyshev, A. Eisfeld, and J. Knoester, *Subdiffusive exciton motion in systems with heavy-tailed disorder*, J. Chem. Phys. **138**, 214316 (2013).

[256] S. Möbius, S. M. Vlaming, V. A. Malyshev, J. Knoester, and A. Eisfeld, *One-dimensional excitonic systems with diagonal Lévy disorder: A detailed study of the absorption spectra and the disorder scaling of localization length*, ArXiv e-prints (2014), arXiv:1404.4475.

[257] F. Herrera, and R. V. Krems, *Tunable Holstein model with cold polar molecules*, Phys. Rev. A **84**, 051401 (2011).

[258] F. Herrera, K. W. Madison, R. V. Krems, and M. Berciu, *Investigating Polaron Transitions with Polar Molecules*, Phys. Rev. Lett. **110**, 223002 (2013).

[259] G. Lindblad, *On the generators of quantum dynamical semigroups*, Commun. Math. Phys. **48**, 119 (1976).

[260] D. E. Makarov, and N. Makri, *Path integrals for dissipative systems by tensor multiplication. Condensed phase quantum dynamics for arbitrarily long time*, Chem. Phys. Lett. **221**, 482 (1994).

[261] Y. Tanimura, *Stochastic Liouville, Langevin, Fokker–Planck, and Master Equation Approaches to Quantum Dissipative Systems*, J. Phys. Soc. Jpn. **75**, 082001 (2006).

[262] C. Kreisbeck, T. Kramer, M. Rodríguez, and B. Hein, *High-Performance Solution of Hierarchical Equations of Motion for Studying Energy Transfer in Light-Harvesting Complexes*, J. Chem. Theory Comput. **7**, 2166 (2011).

[263] D. Suess, A. Eisfeld, and W. T. Strunz, *Hierarchy of Stochastic Pure States for Open Quantum System Dynamics*, Phys. Rev. Lett. **113**, 150403 (2014).

[264] A. Chiuri, C. Greganti, L. Mazzola, M. Paternostro, and P. Mataloni, *Linear Optics Simulation of Quantum Non-Markovian Dynamics*, Sci. Rep. **2**, 968 (2012).

[265] J. Jin, V. Giovannetti, R. Fazio, F. Sciarrino, P. Mataloni, A. Crespi, and R. Osellame, *All-optical non-Markovian stroboscopic quantum simulator*, Phys. Rev. A **91**, 012122 (2015).

[266] F. Brito, and T. Werlang, *A knob for Markovianity*, New J. Phys. **17**, 072001 (2015).

[267] F. Mei, V. M. Stojanović, I. Siddiqi, and L. Tian, *Analog superconducting quantum simulator for Holstein polarons*, Phys. Rev. B **88**, 224502 (2013).

[268] B. M. Garraway, *Decay of an atom coupled strongly to a reservoir*, Phys. Rev. A **55**, 4636 (1997).

[269] L. Mazzola, S. Maniscalco, J. Piilo, K.-A. Suominen, and B. M. Garraway, *Pseudomodes as an effective description of memory: Non-Markovian dynamics of two-state systems in structured reservoirs*, Phys. Rev. A **80**, 012104 (2009).

[270] T. Ma, Y. Chen, T. Chen, S. R. Hedemann, and T. Yu, *Crossover between non-Markovian and Markovian dynamics induced by a hierarchical environment*, Phys. Rev. A **90**, 042108 (2014).

[271] K. Luoma, P. Haikka, and J. Piilo, *Detecting non-Markovianity from continuous monitoring*, Phys. Rev. A **90**, 054101 (2014).

[272] D. W. Schönleber, A. Croy, and A. Eisfeld, *Pseudomodes and the corresponding transformation of the temperature-dependent bath correlation function*, Phys. Rev. A **91**, 052108 (2015).

[273] H.-P. Breuer, E.-M. Laine, and J. Piilo, *Measure for the Degree of Non-Markovian Behavior of Quantum Processes in Open Systems*, Phys. Rev. Lett. **103**, 210401 (2009).

[274] Á. Rivas, S. F. Huelga, and M. B. Plenio, *Entanglement and Non-Markovianity of Quantum Evolutions*, Phys. Rev. Lett. **105**, 050403 (2010).

[275] P. Haikka, J. D. Cresser, and S. Maniscalco, *Comparing different non-Markovianity measures in a driven qubit system*, Phys. Rev. A **83**, 012112 (2011).

[276] D. Chruściński, A. Kossakowski, and Á. Rivas, *Measures of non-Markovianity: Divisibility versus backflow of information*, Phys. Rev. A **83**, 052128 (2011).

[277] H.-P. Breuer, *Foundations and measures of quantum non-Markovianity*, J. Phys. B **45**, 154001 (2012).

[278] S. Luo, S. Fu, and H. Song, *Quantifying non-Markovianity via correlations*, Phys. Rev. A **86**, 044101 (2012).

[279] P. Haikka, J. Goold, S. McEndoo, F. Plastina, and S. Maniscalco, *Non-Markovianity, Loschmidt echo, and criticality: A unified picture*, Phys. Rev. A **85**, 060101 (2012).

[280] A. Rosario, E. Massoni, and F. D. Zela, *On the relationship between non-Markovianity and entanglement protection*, J. Phys. B **45**, 095501 (2012).

[281] S. Lorenzo, F. Plastina, and M. Paternostro, *Geometrical characterization of non-Markovianity*, Phys. Rev. A **88**, 020102 (2013).

[282] A. Smirne, L. Mazzola, M. Paternostro, and B. Vacchini, *Interaction-induced correlations and non-Markovianity of quantum dynamics*, Phys. Rev. A **87**, 052129 (2013).

[283] M. J. W. Hall, J. D. Cresser, L. Li, and E. Andersson, *Canonical form of master equations and characterization of non-Markovianity*, Phys. Rev. A **89**, 042120 (2014).

[284] Á. Rivas, S. F. Huelga, and M. B. Plenio, *Quantum non-Markovianity: characterization, quantification and detection*, Rep. Prog. Phys. **77**, 094001 (2014).

[285] F. F. Fanchini, G. Karpat, B. Çakmak, L. K. Castelano, G. H. Aguilar, O. J. Farıas, S. P. Walborn, P. H. S. Ribeiro, and M. C. de Oliveira, *Non-Markovianity through Accessible Information*, Phys. Rev. Lett. **112**, 210402 (2014).

[286] D. Chruściński, and S. Maniscalco, *Degree of Non-Markovianity of Quantum Evolution*, Phys. Rev. Lett. **112**, 120404 (2014).

[287] Z. He, C. Yao, Q. Wang, and J. Zou, *Measuring non-Markovianity based on local quantum uncertainty*, Phys. Rev. A **90**, 042101 (2014).

[288] C. Addis, B. Bylicka, D. Chruściński, and S. Maniscalco, *Comparative study of non-Markovianity measures in exactly solvable one- and two-qubit models*, Phys. Rev. A **90**, 052103 (2014).

[289] S. Haseli, G. Karpat, S. Salimi, A. S. Khorashad, F. F. Fanchini, B. Çakmak, G. H. Aguilar, S. P. Walborn, and P. H. S. Ribeiro, *Non-Markovianity through flow of information between a system and an environment*, Phys. Rev. A **90**, 052118 (2014).

[290] S. C. Hou, S. L. Liang, and X. X. Yi, *Non-Markovianity and memory effects in quantum open systems*, Phys. Rev. A **91**, 012109 (2015).

[291] V. R. Overbeck, and H. Weimer, *Time evolution of open quantum many-body systems*, Phys. Rev. A **93**, 012106 (2016).

[292] B.-H. Liu, L. Li, Y.-F. Huang, C.-F. Li, G.-C. Guo, E.-M. Laine, H.-P. Breuer, and J. Piilo, *Experimental control of the transition from Markovian to non-Markovian dynamics of open quantum systems*, Nat. Phys. **7**, 931 (2011).

[293] J.-S. Tang, C.-F. Li, Y.-L. Li, X.-B. Zou, G.-C. Guo, H.-P. Breuer, E.-M. Laine, and J. Piilo, *Measuring non-Markovianity of processes with controllable system-environment interaction*, EPL **97**, 10002 (2012).

[294] J.-G. Li, J. Zou, and B. Shao, *Non-Markovianity of the damped Jaynes-Cummings model with detuning*, Phys. Rev. A **81**, 062124 (2010).

[295] S. Lloyd, and L. Viola, *Engineering quantum dynamics*, Phys. Rev. A **65**, 010101 (2001).

[296] M. Kliesch, T. Barthel, C. Gogolin, M. Kastoryano, and J. Eisert, *Dissipative quantum Church-Turing theorem*, Phys. Rev. Lett. **107**, 120501 (2011).

[297] D. Bacon, A. M. Childs, I. L. Chuang, J. Kempe, D. W. Leung, and X. Zhou, *Universal simulation of Markovian quantum dynamics*, Phys. Rev. A **64**, 062302 (2001).

[298] C. H. Tseng, S. Somaroo, Y. Sharf, E. Knill, R. Laflamme, T. F. Havel, and D. G. Cory, *Quantum simulation with natural decoherence*, Phys. Rev. A **62**, 032309 (2000).

[299] B. M. Terhal, and D. P. DiVincenzo, *Problem of equilibration and the computation of correlation functions on a quantum computer*, Phys. Rev. A **61**, 022301 (2000).

[300] D. Poulin, and P. Wocjan, *Sampling from the thermal quantum Gibbs state and evaluating partition functions with a quantum computer*, Phys. Rev. Lett. **103**, 220502 (2009).

[301] K. Temme, T. J. Osborne, K. G. Vollbrecht, D. Poulin, and F. Verstraete, *Quantum Metropolis sampling.* Nature **471**, 87 (2011).

[302] M. J. Kastoryano, and F. G. S. L. Brandão, *Quantum Gibbs Samplers: The Commuting Case*, Commun. Math. Phys. **344**, 915 (2016).

[303] S. Wüster, C. Ates, A. Eisfeld, and J. M. Rost, *Newton's Cradle and Entanglement Transport in a Flexible Rydberg Chain*, Phys. Rev. Lett. **105**, 053004 (2010).

[304] J. Johansson, P. Nation, and F. Nori, *QuTiP 2: A Python framework for the dynamics of open quantum systems*, Comput. Phys. Commun. **184**, 1234 (2013).

[305] M. Nielsen, and I. Chuang, *Quantum Computation and Quantum Information: 10th Anniversary Edition* (Cambridge University Press, Cambridge, 2010).

[306] A. Gilchrist, N. K. Langford, and M. A. Nielsen, *Distance measures to compare real and ideal quantum processes*, Phys. Rev. A **71**, 062310 (2005).

[307] M.-H. Yung, D. Nagaj, J. D. Whitfield, and A. Aspuru-Guzik, *Simulation of classical thermal states on a quantum computer: A transfer-matrix approach*, Phys. Rev. A **82**, 060302 (2010).

[308] D. W. Schönleber, A. Eisfeld, and R. El-Ganainy, *Optomechanical interactions in non-Hermitian photonic molecules*, New J. Phys. **18**, 045014 (2016).

[309] T. J. Kippenberg, and K. J. Vahala, *Cavity Optomechanics: Back-Action at the Mesoscale*, Science **321**, 1172 (2008).

[310] F. Brennecke, S. Ritter, T. Donner, and T. Esslinger, *Cavity Optomechanics with a Bose-Einstein Condensate*, Science **322**, 235 (2008).

[311] M. Aspelmeyer, T. Kippenberg, and F. Marquardt, *Cavity Optomechanics: Nano- and Micromechanical Resonators Interacting with Light*, Quantum Science and Technology (Springer Berlin Heidelberg, 2014).

[312] T. Hänsch, and A. Schawlow, *Cooling of gases by laser radiation*, Opt. Commun. **13**, 68 (1975).

[313] S. Gigan, H. R. Bohm, M. Paternostro, F. Blaser, G. Langer, J. B. Hertzberg, K. C. Schwab, D. Bauerle, M. Aspelmeyer, and A. Zeilinger, *Self-cooling of a micromirror by radiation pressure*, Nature **444**, 67 (2006).

[314] O. Arcizet, P.-F. Cohadon, T. Briant, M. Pinard, and A. Heidmann, *Radiation-pressure cooling and optomechanical instability of a micromirror*, Nature **444**, 71 (2006).

[315] A. Schliesser, P. Del'Haye, N. Nooshi, K. J. Vahala, and T. J. Kippenberg, *Radiation Pressure Cooling of a Micromechanical Oscillator Using Dynamical Backaction*, Phys. Rev. Lett. **97**, 243905 (2006).

[316] D. McClelland, N. Mavalvala, Y. Chen, and R. Schnabel, *Advanced interferometry, quantum optics and optomechanics in gravitational wave detectors*, Laser Photon. Rev. **5**, 677 (2011).

[317] D. E. Chang, A. H. Safavi-Naeini, M. Hafezi, and O. Painter, *Slowing and stopping light using an optomechanical crystal array*, New J. Phys. **13**, 023003 (2011).

[318] A. G. Krause, M. Winger, T. D. Blasius, Q. Lin, and O. Painter, *A high-resolution microchip optomechanical accelerometer*, Nat. Photon. **6**, 768 (2012).

[319] A. Sawadsky, H. Kaufer, R. M. Nia, S. P. Tarabrin, F. Y. Khalili, K. Hammerer, and R. Schnabel, *Observation of Generalized Optomechanical Coupling and Cooling on Cavity Resonance*, Phys. Rev. Lett. **114**, 043601 (2015).

[320] C. M. Bender, and S. Boettcher, *Real Spectra in Non-Hermitian Hamiltonians Having $\mathcal{PT}$ Symmetry*, Phys. Rev. Lett. **80**, 5243 (1998).

[321] R. El-Ganainy, K. G. Makris, D. N. Christodoulides, and Z. H. Musslimani, *Theory of coupled optical PT-symmetric structures*, Opt. Lett. **32**, 2632 (2007).

[322] K. G. Makris, R. El-Ganainy, D. N. Christodoulides, and Z. H. Musslimani, *Beam Dynamics in $\mathcal{PT}$ Symmetric Optical Lattices*, Phys. Rev. Lett. **100**, 103904 (2008).

[323] Z. H. Musslimani, K. G. Makris, R. El-Ganainy, and D. N. Christodoulides, *Optical Solitons in $\mathcal{PT}$ Periodic Potentials*, Phys. Rev. Lett. **100**, 030402 (2008).

[324] A. Guo, G. J. Salamo, D. Duchesne, R. Morandotti, M. Volatier-Ravat, V. Aimez, G. A. Siviloglou, and D. N. Christodoulides, *Observation of $\mathcal{PT}$-Symmetry Breaking in Complex Optical Potentials*, Phys. Rev. Lett. **103**, 093902 (2009).

[325] C. E. Rüter, K. G. Makris, R. El-Ganainy, D. N. Christodoulides, M. Segev, and D. Kip, *Observation of parity-time symmetry in optics*, Nat. Phys. **6**, 192 (2010).

[326] J. Zhang, B. Peng, Ş. K. Özdemir, Y.-x. Liu, H. Jing, X.-y. Lü, Y.-l. Liu, L. Yang, and F. Nori, *Giant nonlinearity via breaking parity-time symmetry: A route to low-threshold phonon diodes*, Phys. Rev. B **92**, 115407 (2015).

[327] W. D. Heiss, *Exceptional points of non-Hermitian operators*, J. Phys. A **37**, 2455 (2004).

[328] M. Müller, and I. Rotter, *Exceptional points in open quantum systems*, J. Phys. A **41**, 244018 (2008).

[329] R. El-Ganainy, M. Khajavikhan, and L. Ge, *Exceptional points and lasing self-termination in photonic molecules*, Phys. Rev. A **90**, 013802 (2014).

[330] R. El-Ganainy, J. I. Dadap, and R. M. Osgood, *Optical parametric amplification via non-Hermitian phase matching*, Opt. Lett. **40**, 5086 (2015).

[331] I. S. Grudinin, H. Lee, O. Painter, and K. J. Vahala, *Phonon Laser Action in a Tunable Two-Level System*, Phys. Rev. Lett. **104**, 083901 (2010).

[332] B. Peng, Ş. K. Özdemir, F. Lei, F. Monifi, M. Gianfreda, G. L. Long, S. Fan, F. Nori, C. M. Bender, and L. Yang, *Parity-time-symmetric whispering-gallery microcavities*, Nat. Phys. **10**, 394 (2014).

[333] K. J. Vahala, *Optical microcavities*, Nature **424**, 839 (2003).

[334] D. K. Armani, T. J. Kippenberg, S. M. Spillane, and K. J. Vahala, *Ultra-high-Q toroid microcavity on a chip*, Nature **421**, 925 (2003).

[335] V. Ilchenko, M. Gorodetsky, and S. Vyatchanin, *Coupling and tunability of optical whispering-gallery modes: a basis for coordinate meter*, Opt. Commun. **107**, 41 (1994).

[336] M. Bayer, T. Gutbrod, J. P. Reithmaier, A. Forchel, T. L. Reinecke, P. A. Knipp, A. A. Dremin, and V. D. Kulakovskii, *Optical Modes in Photonic Molecules*, Phys. Rev. Lett. **81**, 2582 (1998).

[337] Y. Guo, K. Li, W. Nie, and Y. Li, *Electromagnetically-induced-transparency-like ground-state cooling in a double-cavity optomechanical system*, Phys. Rev. A **90**, 053841 (2014).

[338] H. Wang, Z. Wang, J. Zhang, Ş. K. Özdemir, L. Yang, and Y.-x. Liu, *Phonon amplification in two coupled cavities containing one mechanical resonator*, Phys. Rev. A **90**, 053814 (2014).

[339] X.-Y. Lü, H. Jing, J.-Y. Ma, and Y. Wu, *$\mathcal{PT}$-Symmetry-Breaking Chaos in Optomechanics*, Phys. Rev. Lett. **114**, 253601 (2015).

[340] H. Jing, Ş. K. Özdemir, Z. Geng, J. Zhang, X.-Y. Lü, B. Peng, L. Yang, and F. Nori, *Optomechanically-induced transparency in parity-time-symmetric microresonators*, Sci. Rep. **5**, 9663 (2015).

[341] Z.-P. Liu, J. Zhang, Ş. K. Özdemir, B. Peng, H. Jing, X.-Y. Lü, C.-W. Li, L. Yang, F. Nori, and Y.-x. Liu, *Metrology with $\mathcal{PT}$-Symmetric Cavities: Enhanced Sensitivity near the $\mathcal{PT}$-Phase Transition*, Phys. Rev. Lett. **117**, 110802 (2016).

[342] S. Fan, W. Suh, and J. D. Joannopoulos, *Temporal coupled-mode theory for the Fano resonance in optical resonators*, J. Opt. Soc. Am. A **20**, 569 (2003).

[343] B. Peng, Ş. K. Özdemir, S. Rotter, H. Yilmaz, M. Liertzer, F. Monifi, C. M. Bender, F. Nori, and L. Yang, *Loss-induced suppression and revival of lasing*, Science **346**, 328 (2014).

[344] K. V. Kepesidis, T. J. Milburn, J. Huber, K. G. Makris, S. Rotter, and P. Rabl, *$\mathcal{PT}$-symmetry breaking in the steady state of microscopic gain-loss systems*, New J. Phys. **18**, 095003 (2016).

[345] H. Ramezani, T. Kottos, R. El-Ganainy, and D. N. Christodoulides, *Unidirectional nonlinear $\mathcal{PT}$-symmetric optical structures*, Phys. Rev. A **82**, 043803 (2010).

[346] S. Strogatz, *Nonlinear Dynamics and Chaos: With Applications to Physics, Biology, Chemistry, and Engineering*, Studies in Nonlinearity (Westview Press, 2014).

[347] L. Chang, X. Jiang, S. Hua, C. Yang, J. Wen, L. Jiang, G. Li, G. Wang, and M. Xiao, *Parity-time symmetry and variable optical isolation in active-passive-coupled microresonators*, Nat. Photon. **8**, 524 (2014).

[348] S. Mukamel, *Principles of nonlinear optical spectroscopy*, Oxford series in optical and imaging sciences (Oxford University Press, 1995).

[349] G. R. Fleming, and M. Cho, *CHROMOPHORE-SOLVENT DYNAMICS*, Annu. Rev. Phys. Chem. **47**, 109 (1996).

[350] B. M. Garraway, *Nonperturbative decay of an atomic system in a cavity*, Phys. Rev. A **55**, 2290 (1997).

[351] B. J. Dalton, S. M. Barnett, and B. M. Garraway, *Theory of pseudomodes in quantum optical processes*, Phys. Rev. A **64**, 053813 (2001).

[352] L. Diósi, N. Gisin, and W. T. Strunz, *Non-Markovian quantum state diffusion*, Phys. Rev. A **58**, 1699 (1998).

[353] W. T. Strunz, *Linear quantum state diffusion for non-Markovian open quantum systems*, Phys. Lett. A **224**, 25 (1996).

[354] G. Ritschel, D. Suess, S. Möbius, W. T. Strunz, and A. Eisfeld, *Non-Markovian Quantum State Diffusion for temperature-dependent linear spectra of light harvesting aggregates*, J. Chem. Phys. **142**, 034115 (2015).

[355] J. Ma, and J. Cao, *Förster resonance energy transfer, absorption and emission spectra in multichromophoric systems. I. Full cumulant expansions and system-bath entanglement*, J. Chem. Phys. **142**, 094106 (2015).

[356] J. M. Moix, J. Ma, and J. Cao, *Förster resonance energy transfer, absorption and emission spectra in multichromophoric systems. III. Exact stochastic path integral evaluation*, J. Chem. Phys. **142**, 094108 (2015).

[357] R. Kubo, M. Toda, N. Saitô, and N. Hashitsume, *Statistical Physics II: Nonequilibrium Statistical Mechanics* (Springer Berlin Heidelberg, 1991).

[358] A. Z. Chaudhry, and J. Gong, *Role of initial system-environment correlations: A master equation approach*, Phys. Rev. A **88**, 052107 (2013).

[359] C.-J. Yang, J.-H. An, H.-G. Luo, Y. Li, and C. H. Oh, *Canonical versus noncanonical equilibration dynamics of open quantum systems*, Phys. Rev. E **90**, 022122 (2014).

[360] J. Iles-Smith, N. Lambert, and A. Nazir, *Environmental dynamics, correlations, and the emergence of noncanonical equilibrium states in open quantum systems*, Phys. Rev. A **90**, 032114 (2014).

[361] N. van Kampen, *A New Approach to Noise in Quantum Mechanics*, J. Stat. Phys. **115**, 1057 (2004).

[362] V. Ambegaokar, *Equilibration of a dissipative quantum oscillator*, Ann. Phys. **16**, 319 (2007).

[363] G. Ritschel, and A. Eisfeld, *Analytic representations of bath correlation functions for ohmic and superohmic spectral densities using simple poles*, J. Chem. Phys. **141**, 094101 (2014).

[364] V. Hakim, and V. Ambegaokar, *Quantum theory of a free particle interacting with a linearly dissipative environment*, Phys. Rev. A **32**, 423 (1985).

[365] E. Pollak, J. Shao, and D. H. Zhang, *Effects of initial correlations on the dynamics of dissipative systems*, Phys. Rev. E **77**, 021107 (2008).

[366] A. Suárez, R. Silbey, and I. Oppenheim, *Memory effects in the relaxation of quantum open systems*, J. Chem. Phys. **97**, 5101 (1992).

[367] K. Modi, and E. C. G. Sudarshan, *Role of preparation in quantum process tomography*, Phys. Rev. A **81**, 052119 (2010).

[368] R. Alicki, *The quantum open system as a model of the heat engine*, J. Phys. A **12**, L103 (1979).

[369] B. He, L. Yang, and M. Xiao, *Dynamical phonon laser in coupled active-passive microresonators*, Phys. Rev. A **94**, 031802 (2016).

[370] K.-j. Huang, Y. Yan, J.-p. Zhu, Y.-f. Xiao, and G.-x. Li, *Nonclassical non-Gaussian state of a mechanical resonator via selectively incoherent damping in a three-mode optomechanical system*, Phys. Rev. A **93**, 033832 (2016).

[371] M. Zhang, G. S. Wiederhecker, S. Manipatruni, A. Barnard, P. McEuen, and M. Lipson, *Synchronization of Micromechanical Oscillators Using Light*, Phys. Rev. Lett. **109**, 233906 (2012).

[372] Y. He, and M. Jiang, *Entanglement of two optically driven quantum dots mediated by phonons in nanomechanical resonator*, Opt. Commun. **382**, 580 (2017).

[373] M. H. Teimourpour, R. El-Ganainy, A. Eisfeld, A. Szameit, and D. N. Christodoulides, *Light transport in $\mathcal{PT}$-invariant photonic structures with hidden symmetries*, Phys. Rev. A **90**, 053817 (2014).

[374] Y. Tanimura, *Reduced hierarchical equations of motion in real and imaginary time: Correlated initial states and thermodynamic quantities*, J. Chem. Phys. **141**, 044114 (2014).

[375] H. Friedrich, *Theoretical Atomic Physics (Third edition)*, Advanced Texts in Physics (Springer Berlin Heidelberg, 2006).

[376] H. Park, P. J. Tanner, B. J. Claessens, E. S. Shuman, and T. F. Gallagher, *Dipole-dipole broadening of Rb ns-np microwave transitions*, Phys. Rev. A **84**, 022704 (2011).

[377] M. Marinescu, H. R. Sadeghpour, and A. Dalgarno, *Dispersion coefficients for alkali-metal dimers*, Phys. Rev. A **49**, 982 (1994).

[378] C. H. Greene, *Photoabsorption spectra of the heavy alkali-metal negative ions*, Phys. Rev. A **42**, 1405 (1990).

[379] A. Sanayei, and N. Schopohl, *Spectrum, radial wave functions, and hyperfine splittings of the Rydberg states in heavy alkali-metal atoms*, Phys. Rev. A **94**, 012509 (2016).

[380] S. A. Bhatti, C. L. Cromer, and W. E. Cooke, *Analysis of the Rydberg character of the* $5d7d^1D_2$ *state of barium*, Phys. Rev. A **24**, 161 (1981).

[381] J. M. Blatt, *Practical points concerning the solution of the Schrödinger equation*, J. Comput. Phys. **1**, 382 (1967).

[382] W. Li, P. J. Tanner, and T. F. Gallagher, *Dipole-Dipole Excitation and Ionization in an Ultracold Gas of Rydberg Atoms*, Phys. Rev. Lett. **94**, 173001 (2005).

[383] W. Li, J. P. Tanner, Y. Jamil, and F. T. Gallagher, *Ionization and plasma formation in high* n *cold Rydberg samples*, Eur. Phys. J. D **40**, 27 (2006).

[384] S. Valleau, A. Eisfeld, and A. Aspuru-Guzik, *On the alternatives for bath correlators and spectral densities from mixed quantum-classical simulations*, J. Chem. Phys. **137**, 224103 (2012).

[385] H.-T. Tan, and W.-M. Zhang, *Non-Markovian dynamics of an open quantum system with initial system-reservoir correlations: A nanocavity coupled to a coupled-resonator optical waveguide*, Phys. Rev. A **83**, 032102 (2011).

[386] W.-M. Zhang, P.-Y. Lo, H.-N. Xiong, M. W.-Y. Tu, and F. Nori, *General Non-Markovian Dynamics of Open Quantum Systems*, Phys. Rev. Lett. **109**, 170402 (2012).

Danksagung

Am Ende dieser Arbeit möchte ich meinen Dank denen aussprechen, die mich während meiner Doktorarbeit unterstützt und begleitet haben.

Zunächst danke ich meinem Doktorvater Prof. Jan-Michael Rost für seinen Rat und für die Möglichkeit, meine Dissertation in seiner Abteilung anzufertigen.

Besonderer Dank gilt meinem Betreuer Dr. Alexander Eisfeld für seine Förderung und Unterstützung. Du hast mir viel und hilfreiche Rückmeldung gegeben, meinen kritischen Blick für Wissenschaft geschärft und bist mir nicht zuletzt in Diskussionen um meine schwäbische Identität stets zur Seite gestanden.

I thank Dr. Antoine Browaeys for being my opponent.

Besides, I owe thanks to my collaborators Sebastian Wüster, Michael Genkin, Christopher Bentley, Shannon Whitlock, Alexander Croy, Ramy El-Ganainy, Sharareh Izadnia, Aaron LaForge, Frank Stienkemeier, and Thomas Gorin for many helpful discussions. Special thanks goes to Christopher Bentley for his comments that helped improve this thesis.

I thank Pablo López and Abraham Camacho for allowing me to experience Mexican hospitality.

Meinen anfänglichen Zimmerkollegen André Scholich und Moritz Schönwetter danke ich für die freundliche Aufnahme. Meinen jetzigen Zimmerkollegen Karsten Leonhardt und Andreas Rubisch, mit denen ich die überwiegende Zeit verbracht habe, danke ich für ihre Hilfsbereitschaft, zahlreiche Gespräche und erfrischende Sticheleien. Auch Alan Celestino, Martin Winter und Armen Hayrapetyan sei hiermit für die vielen unterhaltsamen Gespräche gedankt.

Darüber hinaus haben viele Mitglieder der Abteilung durch Gespräche und Diskussionen zu der Erarbeitung dieser Dissertation beigetragen: Ulf Saalman, Thomas Pohl, Sebastian Möbius und Gerhard Ritschel. Auch Gabriele Makolies und Hubert Scherrer-Paulus möchte ich für ihre Hilfsbereitschaft bzw. ihren schnellen und fähigen technischen Support danken; sowie allen weiteren Mitgliedern und Mitarbeitern des Instituts, die für eine gute Arbeitsatmosphäre sowie einen reibungslosen Ablauf des Institutslebens gesorgt haben.

Nicht zuletzt danke ich meinen Freunden, meinen Mitbewohnern und den Leuten aus der Mennonitengemeinde für alle Unterstützung, die ich von ihnen erfahren habe. Meiner Familie und ganz besonders meinen Eltern Ina und Michael bin ich für ihre Ermutigung und tatkräftige Unterstützung sehr dankbar.

I am very grateful to have you, Mency; thank you for your great friendship, love, and support.

Versicherung

Hiermit versichere ich, dass ich die vorliegende Arbeit ohne unzulässige Hilfe Dritter und ohne Benutzung anderer als der angegebenen Hilfsmittel angefertigt habe; die aus fremden Quellen direkt oder indirekt übernommenen Gedanken sind als solche kenntlich gemacht. Die Arbeit wurde bisher weder im Inland noch im Ausland in gleicher oder ähnlicher Form einer anderen Prüfungsbehörde vorgelegt.
Die Arbeit wurde am Max-Planck-Institut für Physik komplexer Systeme in der Abteilung "Endliche Systeme" angefertigt und von Prof. Dr. Jan-Michael Rost betreut.
Ich erkenne die Promotionsordnung der Fakultät Mathematik und Naturwissenschaften der Technischen Universität Dresden vom 23.02.2011.

Datum Unterschrift